NANYANG TECHNOLOGICAL UNIVERSITY

Stability of Unsaturated Soil Slopes under Rainfall and Seismic Loading

HUANG WENGUI

School of Civil and Environmental Engineering

2017

Stability of Unsaturated Soil Slopes under Rainfall and Seismic Loading

HUANG WENGUI

School of Civil and Environmental Engineering

A thesis submitted to the Nanyang Technological University

in fulfilment of the requirements for the degree of

Doctor of Philosophy

2017

Acknowledgement

The author would like to thank his supervisor, Dr. Leong Eng Choon, for the guidance and many valuable discussions.

Besides, the author would like to thank Nanyang Technological University for providing him the research scholarship (2013 - 2017).

Last but not least, the author would like to thank his family and friends for their kind support.

Abstract

Rainfall and earthquake are the two main factors that can cause landslides in unsaturated soils. Earthquake loading is cyclic in nature. The effect of cyclic loading on the shear strength of unsaturated soils was investigated by conducting cyclic and monotonic simple shear tests. The main objective of this study is to develop equations that can easily be used for slope stability analysis considering the effects of rainfall and earthquake. To achieve the objective, an analytical framework for unsaturated slope stability analysis was developed first. More specifically, the conventional log-spiral upper bound limit analysis for dry and saturated soil slopes was extended to analyze the rotational failure of unsaturated soil slopes under rainfall. A translational failure mechanism in the context of upper bound plasticity theory was proposed to analyze the translational failure. Upper bound limit analysis can be efficiently used to develop slope stability charts. Through regression analysis of the stability numbers, stability equations were proposed for dry and saturated soil slopes, unsaturated soil slopes under rainfall and seismic loading. The accuracy of the proposed equations was validated with existing stability charts and numerical approach for a wide range of slope geometries and soil properties. Application of the proposed stability equations was illustrated by reanalyzing slope stability problems that have been solved by numerical methods and back analysis of landslides.

Table of Contents

List of Figures

List of Tables

List of Symbols

A_{est}, B_{est}, C_{est}	Curve-fit parameters estimated by Eqs. (5.2), (5.3), and (6.3), respectively
c', c	Effective cohesion and apparent cohesion of the soil
$\dot{D}_{int}$, $\dot{D}_{c'}$	Rate of internal energy dissipation
$\dot{D}_{c'}^{rot}$, $\dot{D}_{c'}^{trl}$	Rate of internal energy dissipation caused by the rotational and translational masses, respectively
d	Normal depth of the wetting front
F	Factor of safety of a slope
F_{est}	Estimated factor of safety
F_{trl}	Factor of safety for translational failure mechanism
F_{rot}^{est} , F_{trl}^{est}	Estimated factor of safety due to rotational and translational failure, respectively
F_{trl}^{IS}	Factor of safety obtained by the infinite slope model
f_1, f_2, f_3, f_4	Coefficients related to the rate of work done by soil weight (rotational component)
$f_{u_w}^{hyd}$, $f_{u_w}^{con}$	Coefficients related to the rate of work done by hydrostatic and constant negative pore-water pressures, respectively
f_{γ}^{trl}	Coefficient related to the rate of work done by soil weight (translational component)
H	Height of the slope
H_{rot}	Height of the rotational mass
H_{trl}	Height of the translational mass
H_{wt}	Vertical distance between the toe of slope and the groundwater table
$H_{ws}(\theta)$	Vertical distance between the groundwater table and the slip surface
h_{cc}	Thickness of the capillary saturated zone
h_c	Constant pore-water pressure head of the soil in the discontinuous zone

$\bar{h}_p$, $\bar{h}_c$	Average positive and negative pore-water pressure heads on the slip surface before the infiltration
$h_n^{\max}$	The maximum negative pore-water pressure head above the groundwater table
I	Rainfall intensity
i	Inclination of the groundwater table
K_o	Coefficient of earth pressure at rest
k_h	Pseudo-static coefficient for seismic slope stability analysis
k_s	Saturated permeability of the soil
L	Length of the slope at the crest intercepted by the slip surface
l	Length of the slope surface
n	Porosity of the soil
r_o	Initial radius of the log-spiral curve
$r(\theta)$	Radius of the log-spiral curve at angle θ
S	Slip surface
S_f, S_o	Final and initial degree of saturation of the soil
t	Rainfall duration
u_a	Pore-air pressure
u_w	Pore-water pressure
$(u_a - u_w)$	Matric suction
$\boldsymbol{v}$	Velocity jump vector at the slip surface
v_n	Normal component of the velocity jump vector
v_t	Tangential component of the velocity jump vector
$\bar{v}$	Average velocity of the translational mass
$\dot{W}_{\text{ext}}$	Rate of work done by the external force

$\dot{W}_{u_w}$	Rate of work done by the pore-water pressure
$\dot{W}_{u_w}^{\text{hyd}}$, $\dot{W}_{u_w}^{\text{con}}$	Rate of work done by the hydrostatic and constant negative pore-water pressures, respectively
$\dot{W}_{\gamma}$	Rate of work done by the soil weight
$\dot{W}_{\gamma}^{\text{rot}}$, $\dot{W}_{\gamma}^{\text{trl}}$	Rate of work done by the soil weight of rotational and translational components, respectively
z	Vertical distance between slope surface to sliding plane for pseudo-static analysis
z_s	Vertical distance between the top and bottom of the translational mass
z_w	Depth of the wetting front
α	Slope angle at the crest of the slope
β	Slope angle
β'	Inclination of the line from the crest point of the slope to the end point of the slip surface
$\boldsymbol{\gamma}$, γ	Unit weight vector and unit weight of the soil
γ_c	Shear strain for cyclic simple shear test
γ_w	Unit weight of water
ζ_c	Degree of contribution of matric suction (constant) to slope stability during the infiltration
ζ_h	Degree of contribution of matric suction (hydrostatic) to slope stability during the infiltration
θ_o, θ_h	Initial and final angles of the log-spiral curve
θ_{m1}, θ_{m2}	Angles at the polar coordinate corresponding to the intersection points between the groundwater table and the slip surface
θ_{w1}, θ_{w2}	Angles at the polar coordinate corresponding to the intersection points between the wetting front and the slip surface
σ	Normal stress
σ_v	Vertical stress on a simple shear test

τ	Shear stress
$\dot{\omega}$	Rate of rotation of the failed mass around the center of the log-spiral
ϕ'	Effective angle of internal friction of the soil
ϕ^b	Angle indicating the rate of increase in shear strength relative to matric suction

Chapter 1: Introduction

1.1 Background

A large number of soil slopes in nature are unsaturated, with groundwater table located at some depth below the ground surface. The pore-water pressures above the groundwater table are negative, which can increase the soil strength and enhance the slope stability (Fredlund and Rahardjo, 1993). Unsaturated soil slopes are exposed to rainfall in the rainy season, and the infiltration of rainwater can increase the pore-water pressure and decrease the shear strength of the soils. Hence, the enhancement of slope stability due to the contribution of negative pore-water pressure may be affected by climatic conditions (e.g., rainfall intensity, rainfall duration), and the extent to which the negative pore-water pressure can be relied upon depends on the magnitude of the rainfall flux, water storage capacity and permeability of the soil (Zhang et al., 2004).

The contribution of negative pore-water pressure to slope stability is usually neglected in routine geotechnical design (e.g., Vanapalli et al., 1996; Zhang et al., 2004; Fredlund et al., 2012), which may be attributed to: (1) the measurements of the parameters required for an unsaturated slope stability analysis (i.e., soil-water characteristic curve, permeability function, and unsaturated shear strength) are time-consuming, technically-demanding and costly (Vanapalli et al., 1996; Leong and Rahardjo, 1997a, 1997b; Nam et al., 2011; Zhang and Fredlund, 2015); and (2) an unsaturated slope stability analysis involves more complexity and requires more expertise than a dry/saturated slope stability analysis (Zhang et al., 2011; Vahedifard et al., 2016). Although it

may be reasonable to ignore the contribution of negative pore-water pressures for the situation where the major portion of the slip surface is below the groundwater table, it may be too conservative and unrealistic if the groundwater table is deep and the major portion of the slip surface is above the groundwater table (Fredlund and Rahardjo, 1993).

Earthquake is also an important factor that can reduce slope stability (e.g., Seed et al., 1978; Keefer, 1984, 2002). Soil behaves differently under static and earthquake loadings. Earthquake loading is cyclic in nature. The effect of cyclic loading on the shear strength of saturated soils has been widely investigated (e.g., Seed and Lee, 1966; Thiers and Seed, 1969; Idriss et al., 1978; Vucetic and Dobry, 1988; Lefebvre and Pfendler, 1996). However, only limited research has been conducted to investigate the effect of cyclic loading on the shear strength of unsaturated soils (Chu and Vucetic, 1992; Whang et al., 2004).

Stability charts provide a simple approach to assess the stability of a slope. Stability charts have been widely developed for dry soil slopes (e.g., Taylor, 1937; Michalowski, 2002; Steward et al., 2011; Gao et al., 2013) and saturated soil slopes (e.g., Bishop and Morgenstern, 1960; Michalowski, 2002; Michalowski and Nadukuru, 2013). Since stability analysis of unsaturated soil slopes is more complicated than the stability analysis of dry/saturated soil slopes, simple tools like stability charts are more essential to unsaturated soil slopes than to dry/saturated soil slopes. However, so far very limited stability charts have been developed for unsaturated soil slopes (Huat et al., 2006; Vo and Russell, 2017).

To determine the factor of safety using stability charts, stability numbers need to be read from or interpolated between the stability curves. The reading and interpolation process is tedious if numerous analyses need to be performed. It would be more convenient if factor of safety of a slope can be calculated by an explicit equation. A number of stability equations have been proposed for saturated soil slopes (Sah et al., 1994; Yang et al., 2004; Ahangar-Asr et al., 2010; Manouchehrian et al., 2014; Kostić et al., 2016), while no stability equation has been proposed for unsaturated soil slopes.

1.2 Objective and Scope

The objective of this study is to develop equations that can easily be used for slope stability analysis considering the effects of rainfall and earthquake. The scope of this study includes:

1. Investigating the effect of cyclic loading on the shear strength of unsaturated soils by conducting cyclic and monotonic simple shear tests.
2. Developing the methodology of conducting upper bound limit analysis on unsaturated soil slopes based on rotational and translational failure mechanisms.
3. Generating a large amount of dimensionless stability numbers for dry and saturated soil slopes, unsaturarted soil slopes under rainfall and seismic loading by using upper bound limit analysis.
4. Developing stability equations for dry and saturated soil slopes, unsaturated soil slopes under rainfall and seismic loading through regression analysis of the dimensionless stability numbers.
5. Illustrating the application of the stability equations using cases reported in the literature.

1.3 Organization of Thesis

This thesis consists of eight chapters. The content of each chapter is summarized briefly below.

Chapter 1 introduces the research background, objective and scope.

Chapter 2 reviews unsaturated soil mechanics, triggering mechanisms and stability analyses of rainfall and earthquake-induced landslides. The research gaps in the literature are identified.

Chapter 3 presents the methodology and results for the cyclic and monotonic simple shear tests. The test programme is designed to investigate the effect of cyclic loading on the shear strength and post-cyclic monotonic shear strength of unsaturated soils.

Chapter 4 presents the methodology of conducting upper bound limit analysis. The conventional log-spiral upper bound limit analysis for dry and saturated soil slopes is extended to analyze the rotational failure of unsaturated soil slopes under rainfall. An innovative kinematically admissible failure mode is proposed to analyze translational failure. The upper bound limit analysis is then used to generate dimensionless slope stability numbers.

Chapter 5 presents the results for unsaturated soil slopes under rainfall. The controlling factors on the failure mode of unsaturated soil slopes under rainfall are investigated first. Through regression analysis of the dimensionless stability numbers, stability equations that can explicitly calculate the factors of safety of dry soil slopes, unsaturated soil slopes under rainfall and saturated soil slopes are developed.

Chapter 6 presents the stability equations for dry and unsaturated soil slopes under seismic loading. The stability equations are further extensions of the stability equations obtained in Chapter 5. The performance of the stability equations is validated with existing stability charts and numerical approach for a wide range of slope geometries and soil properties.

Chapter 7 summarizes the slope stability equations developed in this study. The procedures to determine the required input parameters are explained. Applications of the slope stability equations are discussed and illustrated by reanalyzing slope stability problems that have been solved by numerical methods in the literature.

Chapter 8 concludes this study. The major contributions are summarized, the limitations are discussed, and recommendations for further research are made.

Chapter 2: Literature Review

In this chapter, the characteristics of unsaturated soils are reviewed first, followed by the triggering mechanisms and stability analysis methods of rainfall and earthquake-induced landslides. Finally, the slope stability charts and equations presented in the literature are summarized, and the gaps in the literature are identified.

2.1 Unsaturated Soil Mechanics

2.1.1 Saturated and Unsaturated Soils

Saturated soil has two phases: soil particles as the solid phase, and water as the liquid phase. Unsaturated soil has three phases: soil particles as the solid phase, water as the liquid phase, and air as the gaseous phase. In a soil slope, the groundwater table can be considered as the boundary which separates the saturated and unsaturated zones, as shown in Figure 2.1. The pore-water pressure in the saturated zone is positive (i.e., in a state of compression), which reduces the effective stress and hence decreases the slope stability. The pore-water pressure in the unsaturated zone is negative (i.e., in a state of tension), which increases the shearing resistances between soil particles (Figure 2.2) and hence increases the slope stability.

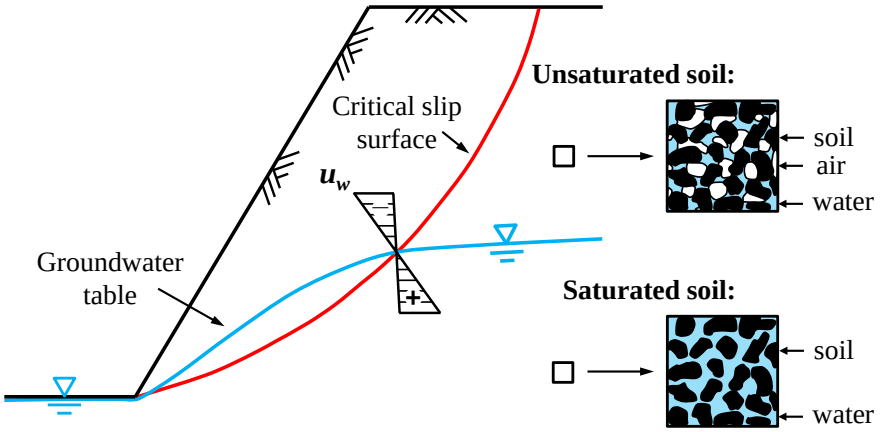

Figure 2.1 Saturated and unsaturated soil

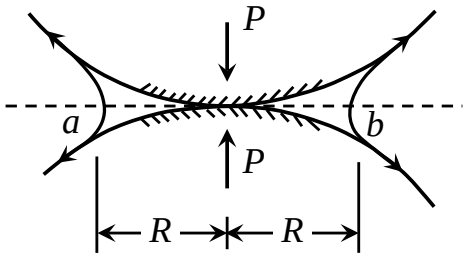

Figure 2.2 Adhesion between soil particles produced by contact moisture (from Terzaghi, 1943)

Terzaghi (1936) found that the volume change and shearing resistance of saturated soil depend exclusively on effective stress (σ'), which is equal to the difference between the total normal stress (σ) and the pore-water pressure (u_w):

$$\sigma' = \sigma - u_w \tag{2.1}$$

According to the Mohr-Coulomb failure criterion, the shear strength of saturated soil can be written as (Terzaghi, 1936):

$$\tau = c' + \sigma' \tan\phi' = c' + (\sigma - u_w)\tan\phi' \tag{2.2}$$

where τ is the shear strength, c' is the effective cohesion, ϕ' is the effective angle of internal friction.

Equations (2.1) and (2.2) are only suitable for saturated soils in which the voids are filled with water. To account for the presence of both air and water in the voids of unsaturated soils, Bishop and Blight (1963) proposed a modified form of effective stress equation:

$$\sigma' = \sigma - u_a + \chi(u_a - u_w) \tag{2.3}$$

where u_a is the pore-air pressure, χ is a parameter mainly related to the degree of saturation.

Consequently, the shear strength of unsaturated soil can be written as:

$$\tau = c' + [(\sigma - u_a) + \chi(u_a - u_w)]\tan\phi' \tag{2.4}$$

Fredlund and Morgenstern (1977) argued that Eq. (2.3) is a constitutive relationship rather than a description of the stress state, as stress state could not contain a parameter (i.e., χ) which is related to the soil property (e.g., degree of saturation). Fredlund et al. (1978) proposed net normal stress $(\sigma - u_a)$ and matric suction $(u_a - u_w)$ as independent stress state variables of unsaturated soils, and the shear strength of unsaturated soils is modified to be:

$$\tau = c' + (\sigma - u_a)\tan\phi' + (u_a - u_w)\tan\phi^b \tag{2.5}$$

where ϕ^b is an angle which indicates the rate of increase in shear strength relative to matric suction (u_a - u_w). Equation (2.5) is known as the extended Mohr-Coulomb failure criterion for unsaturated soils.

Equations (2.4) and (2.5) appear to be similar in form. For identical soils (e.g., soils compacted at the same water content and same dry density), by equating Eq. (2.4) and Eq. (2.5) the

relationship between χ and ϕ^b can be written as (Fredlund and Rahardjo, 1993; Sheng, 2011; Fredlund et al., 2012):

$$\chi = \frac{\tan \phi^b}{\tan \phi'} \tag{2.6}$$

From a practical engineering standpoint, the independent stress state variable approach may be more appealing, as it provides greater flexibility in terms of characterizing nonlinear shear strength behavior corresponding to a variety of stress paths (Fredlund and Rahardjo, 1993; Fredlund et al., 2012).

2.1.2 Unsaturated Soil Properties

The water content in an unsaturated soil is a function of the suction present in the soil (Leong and Rahardjo, 1997a). The relationship between the water content and the suction is defined by the soil-water characteristic curve (SWCC), as shown in Figure 2.3(a). The soil is essentially saturated when the suction is below the air-entry value (AEV). Between the AEV and the residual suction, water can easily be removed by increasing the suction. Above the residual suction, however, water can hardly be removed with further increase in suction.

Since water can only flow through the continuous water paths, the coefficient of permeability with respect to the water phase is related to the water content of the soil (Leong and Rahardjo, 1997b). As shown in Figure 2.3(b), the permeability of the soil (k_w) is equal to the saturated permeability (k_s) when the suction is below the AEV. Once the AEV is exceeded, air is present in the void and the water permeability is greatly reduced. Very low water permeability could be expected at high suction.

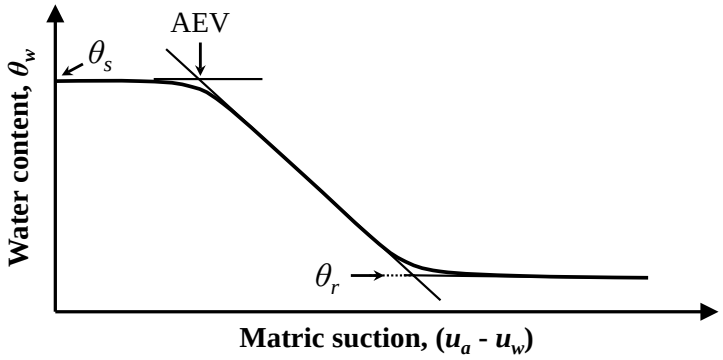

(a) Soil-water characteristic curve (SWCC)

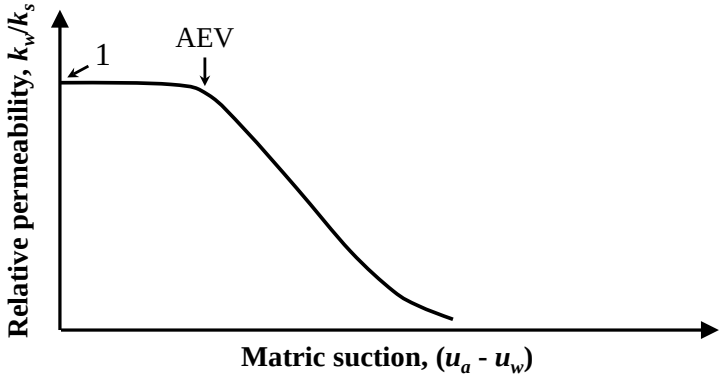

(b) Permeability function

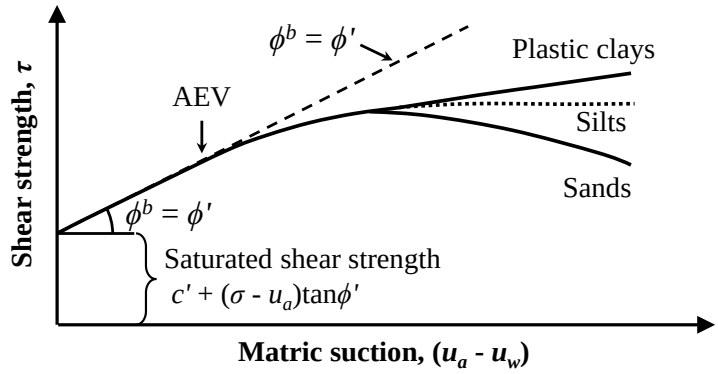

(c) Unsaturated shear strength

Figure 2.3 SWCC, permeability function and unsaturated shear strength [(a) and (b) are modified from Fredlund et al. (1994), (c) is modified from Gan and Fredlund (1996)]

The transfer of shear stress is related to the contact area between water and soil particles (Vanapalli et al., 1996). Hence, the shear strength of unsaturated soil is related to the water content and further related to the suction level, as shown in Figure 2.3(c). Below AEV, the soil particles and water are fully contacted because of the full saturation. The rate of increase in shear strength due to matric suction ϕ^b is equal to the effective angle of internal friction ϕ'. Above the AEV, the soil particles and water are not fully contacted any more. As a result, the contribution of matric suction to the shear strength is not as effective as the net normal stress (i.e., $\phi^b < \phi'$).

2.1.3 Challenge of Applying Unsaturated Soil Mechanics

It is well known that matric suction (or negative pore-water pressure) can increase the shear strength of soils and enhance the stability of geotechnical structures (Fredlund and Rahardjo, 1993). However, matric suction and its contribution to shear strength and stability may be affected by rainwater infiltration. In order to consider the contribution of matric suction in a geotechnical design, the matric suction that can be safely relied upon must be known (Zhang et al., 2004).

The water storage capacity of an unsaturated soil is determined by the soil-water characteristic curve. The rate that water can percolate in an unsaturated soil is determined by the permeability function. Hence, soil-water characteristic curve and permeability function must be known in order to conduct a transient seepage analysis. To further conduct a stability analysis incorporating matric suction, the rate of increase in shear strength relative to matric suction (ϕ^b) must be known.

The main challenge of applying unsaturated soil mechanics lies in the difficulty in measuring the soil-water characteristic curve, permeability function and shear strength parameter ϕ^b, which can be attributed to the following reasons (Fredlund and Rahardjo, 1993; Vanapalli et al., 1996; Nam et al., 2011; Zhang and Fredlund, 2015):

1) The conventional permeameter for permeability test, triaxial and direct shear apparatuses for shear strength test need to be modified in order to cater for the suction-controlled or suction-measurement requirement. Consequently, testing of unsaturated soils is more costly and technically-demanding than the testing of saturated soils.
2) In order to obtain the water content, permeability and shear strength at a wide range of suction, the soil properties at various suction levels need to be measured. It takes considerable time to establish suction equilibrium due to the low permeability of unsaturated soil. The equilibrium time could be longer in the high suction range than in the low suction range, as permeability is increasingly reduced with the increase in suction [Figure 2.3(b)].

As an alternative to direct measurements, empirical procedures have been widely developed to predict unsaturated permeability and unsaturated shear strength based on their saturated counterparts and the soil-water characteristic curve (e.g., Fredlund et al., 1994; Vanapalli et al., 1996; Leong and Rahardjo, 1997b; Goh et al., 2010; Zhai and Rahardjo, 2015), and predict the soil-water characteristic curve based on grain-size distribution and basic index properties (e.g., Fredlund et al., 2002; Perera et al., 2005; Chin et al., 2010; Li et al., 2014).

However, if all the unsaturated soil properties are predicted using empirical procedures, the results obtained from a rigorous analysis (e.g., a combined transient seepage and slope stability

analysis) also inherit the “approximate” nature and could not be considered as “rigorous” anymore. Consequently, the rigorous approach would lose its advantage of being “rigorous” while still maintain its disadvantage of involving complicated calculation. In the situation where unsaturated soil properties could not be directly measured, it is desirable to have a simplified approach that only requires easily determined parameters and involves simple calculation. Slope stability equations that fulfill the criteria will be proposed in this study. Summary and application of the proposed slope stability equations are shown in Chapter 7.

2.2 Review of Rainfall-Induced Landslides

Terzaghi (1950) listed a wide range of factors and processes that can lead to landslides, as shown in Table 2.1. According to Terzaghi (1950), landslides can be triggered by external causes, internal causes, or the intermediate causes between the external and the internal. External causes are those which can produce an increase of shearing stresses at unaltered shearing resistance of the slope material (e.g., steepening or heightening of the slope). Internal causes are those which can lead to a decrease of shearing resistance of the slope material at unaltered shearing stresses (e.g., increase of the pore-water pressure). Intermediate between the landslides due to external and internal causes are those due to rapid drawdown, to subsurface erosion, and to spontaneous liquefaction. Among the factors shown in Table 2.1, rainfall and earthquake are the two most important factors that frequently trigger landslides (Deere and Patton, 1971). Hence, only rainfall and earthquake are considered in this study. The triggering mechanisms and stability analysis methods of rainfall and earthquake-induced landslides are reviewed below.

Table 2.1 Processes leading to landslides (from Terzaghi, 1950)

A	B	C	D	E	F
Name of agent	**Event or process which brings agent into action**	**Mode of action of agent**	**Slope materials most sensitive to action**	**Physical nature of significant actions of agent**	**Effects on equilibrium conditions of slope**
Transporting agent	Construction operations or erosion	1. Increase of height or rise of slope	Every material	Changes state of stress in slope-forming material	Increases shearing stresses
			Stiff, fissured clay, shale	Changes state of stress and causes opening of joints	Increases shearing stresses and initiates process 8
Tectonic stresses	Tectonic movements	2. Large-scale deformations of earth crust	Every material	Increases slope angle	Increases of shearing stresses
Tectonic stresses or explosives	**Earthquakes** or blasting	3. High-frequency vibrations	Every material	Produces transitory change of stress	
			Loess, slightly cemented sand, and gravel	Damages intergranular bonds	Decrease of cohesion and increase of shearing stresses
			Medium or fine loose sand in saturated state	Initiates rearrangement of grains	Spontaneous liquefaction
Weight of slope-forming material	Process which created the slope	4. Creep on slope	Stiff, fissured clay, shale, remnants of old slides	Opens up closed joints, produces new ones	Reduces cohesion, accelerates process 8
		5. Creep in weak stratum below foot of slope	Rigid materials resting on plastic ones		
Water	**Rains** or melting snow	6. Displacement of air in voids	Moist sand	Increases pore-water pressure	Decrease of frictional resistance
		7. Displacement of air in open joints	Jointed rock, shale		

Table 2.1 Processes leading to landslides (Continued)

A	B	C	D	E	F
Name of agent	**Event or process which brings agent into action**	**Mode of action of agent**	**Slope materials most sensitive to action**	**Physical nature of significant actions of agent**	**Effects on equilibrium conditions of slope**
Water	**Rains** or melting snow	8. Reduction of capillary pressure associated with swelling	Stiff, fissured clay and some shales	Causes swelling	Decrease of cohesion
		9. Chemical weathering	Rock of any kind	Weakens intergranular bonds (chemical weathering)	
	Frost	10. Expansion of water due to freezing	Jointed rock	Widens existing joints, produces new ones	
		11. Formation and subsequent melting of ice layers	Silt and silty sand	Increases water content of soil in frozen top-layer	Decrease of frictional resistance
	Dry spell	12. Shrinkage	Clay	Produces shrinkage cracks	Decrease of cohesion
	Rapid drawdown	13. Produces seepage toward foot of slope	Fine sand, silt, previously drained	Produces excess pore-water pressure	Decrease of frictional resistance
	Rapid change of elevation of water table	14. Initiates rearrangement of grains	Medium or fine loose sand in saturated state	Spontaneous increase of pore-water pressure	Spontaneous liquefaction
	Rise of water table in distant aquifer	15. Causes a rise of piezometric surface in slope-forming material	Silt or sand layers between or below clay layers	Increases pore-water pressure	Decrease of frictional resistance
	Seepage from artificial source of water (reservoir or canal)	16. Seepage toward slope	Saturated silt	Increases pore-water pressure	Decrease of frictional resistance
		17. Displaces air in the voids	Moist, fine sand	Eliminates surface tension	Decrease of cohesion
		18. Removes soluble binder	Loess	Destroys intergranular bond	
		19. Subsurface erosion	Fine sand or silt	Undermines the slope	Increase of shearing stress

2.2.1 Mechanism of Rainfall-Induced Landslides

Rainfall has triggered a large number of landslides all over the world. Most of the rainfall-induced landslides were shallow with depth between 0.5 m and 2.0 m, and of small volume on slopes at angles of 25 - 50° (e.g., Toll, 2001; Dai et al., 2003; Zizioli et al., 2013). Deep-seated rotational slides were also occasionally reported (e.g., Gerscovich et al., 2006; Huat et al., 2006; Keaton et al., 2014). Terzaghi (1950) has realized that rainfall infiltration can reduce slope stability by eliminating the surface tension in the fine-grained cohesionless soils, destroying the soluble binder in loess, and decreasing the effective stress due to the rising of the groundwater table. The effect of rainfall on slope stability is conventionally analyzed by increasing the pore-water pressure in Terzaghi's effective stress equation [Eq. (2.1)], and the most critical situation would be the moment when the groundwater table rises to the ground surface (Terzaghi, 1950; Skempton and Delory, 1957). However, in most of the landslide cases there is not much evidence of a rise of the groundwater table (Fourie, 1996; Fourie et al., 1999). The failures are mainly attributed to the advance of wetting front and the reduction of shear strength due to the decrease of matric suction in the unsaturated soils (Fredlund and Rahardjo, 1993; Rahardjo et al., 1995).

Rainfall is rarely the sole cause of slope failure for a slope that had stood for a long time, as it is very likely that the slope had experienced heavy rainstorms in the past (Terzaghi, 1950). The slope failure is usually attributed to a combination of rainfall infiltration and external provocation (e.g., steepening the slope by excavation, increasing infiltration due to absence of vegetation cover) or internal change (e.g., the decrease of shearing resistance due to the aging effect or progressive weathering of the slope-forming material).

2.2.2 Numerical Seepage and Slope Stability Analyses

Infiltration of rainwater changes the pore-water pressure distribution in the soil, which in turn changes the stress state of the soil and may lead to instability of the slope. The infiltration analysis and slope stability analysis can be conducted in an "uncoupled" or "coupled" manner. In an "uncoupled" analysis, the pore pressures, stress and deformation are solved independently. In a "coupled" analysis, the pore pressures, stress and deformation are solved simultaneously (Fredlund et al., 2012). The coupled analysis is considered to be more rigorous and correct, as the changes of pore pressures, stress and deformation are strongly linked. However, the formulation for a coupled analysis is much more complicated and computational intensive than an uncoupled analysis. Hence, the uncoupled analysis that is easier to solve and sufficiently accurate for a slope stability problem is more widely adopted (Fredlund et al., 2012).

2.2.2.1 Numerical Seepage Analysis

Based on Darcy's law and flow continuity, the governing equation for two-dimensional transient flow through unsaturated soil can be written as (Richards, 1931):

$$\frac{\partial}{\partial x}\left(k_x \frac{\partial h}{\partial x}\right)+\frac{\partial}{\partial y}\left(k_y \frac{\partial h}{\partial y}\right)=-\frac{\partial \theta_w}{\partial t} \tag{2.7}$$

where k_x is the water coefficient of permeability in the x direction, k_y is the water coefficient of permeability in the y direction, h is the pressure head, and θ_w is the volumetric water content. The k_x, k_y and θ_w are all nonlinear functions of h [Figures 2.3(a) and (b)]. Permeability function [$k_x(h)$, $k_y(h)$] and soil-water characteristic curve [$\theta_w(h)$] of the soil must be known in order to solve the partial differential equation [Eq. (2.7)].

Fredlund and Morgenstern (1976) proposed the following water phase constitutive relationship for unsaturated soil:

$$\mathrm{d}\theta_w = m_1^w \mathrm{d}(\sigma - u_a) + m_2^w \mathrm{d}(u_a - u_w) \tag{2.8}$$

where σ is the normal stress, u_a is the pore-air pressure, m_1^w is the slope of the water volume versus $(\sigma - u_a)$ relationship when $\mathrm{d}(u_a - u_w)$ is zero, and m_2^w is the slope of the water storage coefficient, which is the slope of the water volume versus $(u_a - u_w)$ relationship when $\mathrm{d}(\sigma - u_a)$ is zero.

If the total stress is assumed to be constant and the pore-air pressure is assumed to be atmospheric, the seepage analysis would become "uncoupled" and Eq. (2.8) is reduced to:

$$\mathrm{d}\theta_w = m_2^w \mathrm{d}(-u_w) \tag{2.9}$$

Substituting Eq. (2.9) into Eq. (2.7) would lead to:

$$\frac{\partial}{\partial x}\left(k_x \frac{\partial h}{\partial x}\right) + \frac{\partial}{\partial y}\left(k_y \frac{\partial h}{\partial y}\right) = m_2^w \rho_w g \frac{\partial h}{\partial t} \tag{2.10}$$

where ρ_w is the density of water, g is gravitational acceleration. Equation (2.10) can readily be solved using numerical software (e.g., *SEEP/W*). The formulation for the fully coupled seepage analysis can be found in Fredlund et al. (2012).

Pore-water pressure profiles under rainfall infiltration for various soil types and various rainfall conditions can be found in the literature (e.g., Zhang et al., 2004; Lee et al., 2009). Typical pore water pressure profiles under rainfall infiltration are schematically shown in Figure 2.4. Figure 2.4(a) shows the pore-water pressure profile at steady state. According to Kisch (1959), the gradient of pore-water pressure at steady state can be written as:

$$\frac{\mathrm{d}u_w}{\mathrm{d}y} = \gamma_w \left(\frac{I}{k_s} - 1 \right) \tag{2.11}$$

where I is the infiltration rate, k_s is the saturated permeability of the soil, and γ_w is the unit weight of water. When $I = 0$, the pore-water pressure is hydrostatic. With the increase in I/k_s, pore-water pressure distribution curve shifts toward the right and approaches zero when $I/k_s = 1$. During the rainfall infiltration, the pore-water pressure is in a transient state between initial and steady states, as shown in Figures 2.4(b), (c), (d) and (e). For a rainfall event with $I/k_s < 1$, matric suction can always be maintained to some extent even if the rainfall lasts a long period of time and pore-water pressure approaches the steady state [Figures 2.4(b) and (c)]. For a rainfall event with $I/k_s \geq 1$, matric suction may still be maintained [Figures 2.4(d) and (e)], and the remaining matric suction depends on the rainfall characteristics and hydraulic properties of the soil (Zhang et al., 2004).

The idealized pore-water pressure profiles in an unsaturated residual soil slope under rainfall infiltration suggested by Rahardjo et al. (1995) are shown in Figure 2.5. Profile a represents a smooth wetting front, which tends to occur in fine-grained soils (Zhang et al., 2004; Lee et al., 2009). Profile b represents a sharp wetting front, which tends to occur in coarse-grained soils (Zhang et al., 2004; Lee et al., 2009). Profile c reveals a perched water table, which tends to occur in layered soils with a permeable layer above the wetting front and a less permeable layer below the wetting front (Cho, 2009).

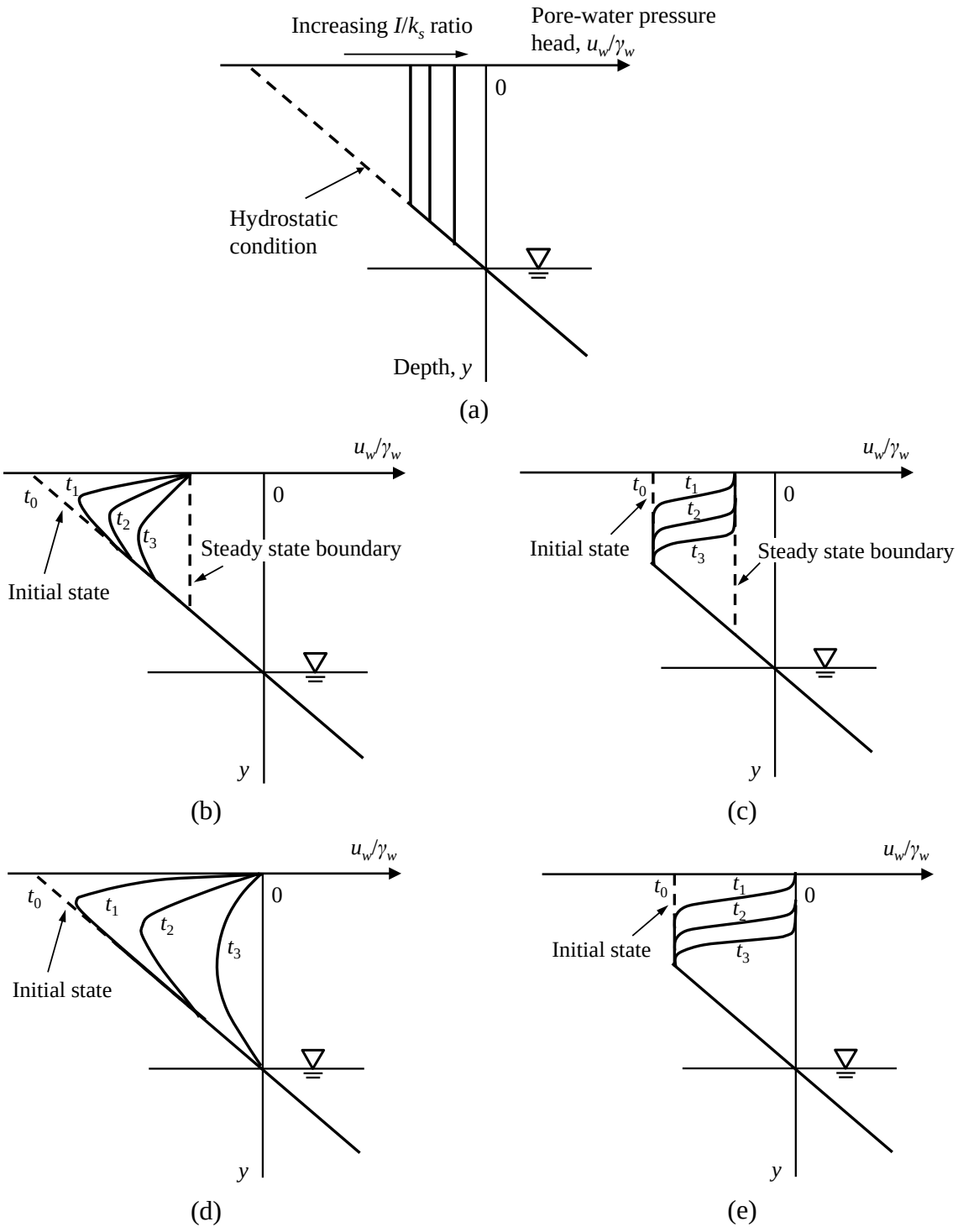

Figure 2.4 Typical pore-water pressure profiles in an unsaturated soil slope with various ground surface fluxes: (a) steady state condition; (b) and (c) transient condition, $I/k_s < 1$; (d) and (e) transient condition, $I/k_s \geq 1$ (from Zhang et al., 2011).

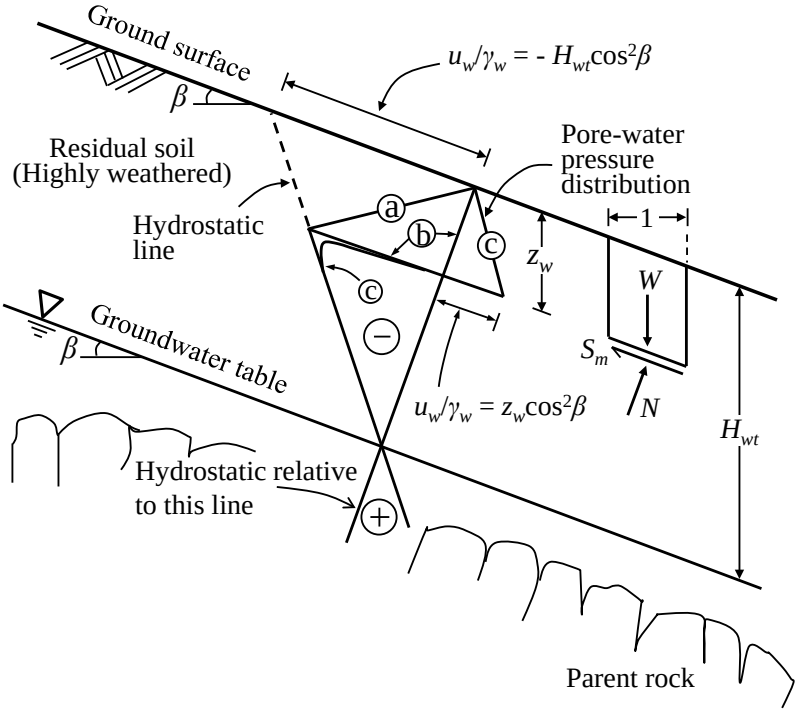

Figure 2.5 Possible pore-water pressure profiles a, b and c in an unsaturated residual soil slope under rainfall infiltration (from Rahardjo et al., 1995)

2.2.2.2 Extended Limit Equilibrium Analysis

The pore-water pressures calculated from a transient seepage analysis can readily be integrated into a slope stability analysis. Limit equilibrium methods (e.g., Bishop, 1955; Morgenstern and Price, 1965; Spencer, 1967) which discretize a failure mass into vertical slices, as illustrated in Figure 2.6, has been widely used to assess the stability of dry and saturated soil slopes. By using the extended Mohr-Coulomb failure criterion [Eq. (2.5)], the conventional limit equilibrium methods can easily be modified for unsaturated soil slopes. The factors of safety with respect to moment equilibrium (F_m) and force equilibrium (F_f) can generally be expressed as (Fredlund and Rahardjo, 1993):

$$F_m = \frac{\sum \left[c'\Delta l R + \left(N - u_w \Delta l \frac{\tan \phi^b}{\tan \phi'} \right) R \tan \phi' \right]}{\sum Wx} \tag{2.12}$$

$$F_f = \frac{\sum \left[c'\Delta l \cos\theta + \left(N - u_w \Delta l \frac{\tan \phi^b}{\tan \phi'} \right) \tan \phi' \cos\theta \right]}{\sum N \sin\theta} \tag{2.13}$$

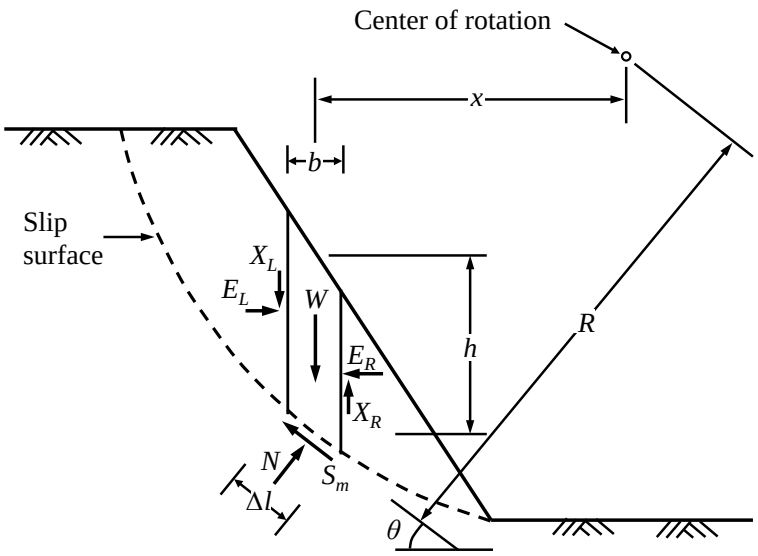

Figure 2.6 Forces acting on a slice through a sliding mass with a circular slip surface (modified from Fredlund and Rahardjo, 1993)

Commercial software packages *SEEP/W* and *SLOPE/W* are commonly adopted for the combined transient seepage and slope stability analysis (Ng and Shi, 1998; Gasmo et al., 2000; Tsaparas et al, 2002; Huat et al., 2006; Rahardjo et al., 2007, 2010; Cascini et al., 2010; Rahimi et al., 2011). More specifically, *SEEP/W* is used to calculate the transient pore-water pressure (u_w) under a rainfall infiltration, and the obtained pore-water pressure is transferred into *SLOPE/W* for the slope stability analysis [Eq. (2.12) and/or Eq. (2.13)].

Although limit equilibrium analysis generally leads to satisfactory results for design purposes, the analysis has been criticized for lack of a sound theoretical basis (Chen, 1975; Miller and Hamilton, 1989; Michalowski, 1995; Yu et al., 1998): (1) the assumed interslice forces and the forces acting across the slip surface may violate the yield condition of the soil, hence the stress field within the failure mass may not be statically admissible; and (2) the stress-strain relationship is not considered in the analysis, hence the obtained slip surface may not be kinematically admissible. The analysis conducted by Lu et al. (2012) shows that limit equilibrium analysis performs reasonably well if rotational failure is the critical failure mode; however, limit equilibrium analysis may fail to search for the potential shallow slip surface if translational failure is more critical.

2.2.2.3 Finite Element Analysis

Limit equilibrium methods are based on the principles of statics (i.e., static equilibrium of forces and/or moments), without giving any consideration to the displacement in the soil mass (Fredlund and Rahardjo, 1993). The calculated pore-water pressures from a transient seepage analysis can also be integrated into a finite element slope stability analysis. By using finite element analysis, the deformation triggered by the change of stresses is fully taken into account.

The global factor of safety of a slope can be obtained by shear strength reduction technique (Cai and Ugai, 2004; Griffiths and Lu, 2005; Huang and Jia, 2009; Le et al., 2015). As shown by Eq. (2.14), in a shear strength reduction finite element analysis, the available c (apparent cohesion) and ϕ' of the soil is incrementally divided by a shear strength reduction factor (SRF) until the

slope deforms excessively or the solution does not converge within a specified number of iterations, and the global factor of safety is equal to the final *SRF*.

$$c_d = \frac{c}{SRF},\ \phi'_d = \frac{\phi'}{SRF} \tag{2.14}$$

Alternatively, a scalar field of local factor of safety can be obtained by finite element analysis (Alonso et al., 2003; Lu et al., 2012; Robinson et al., 2017). A local factor of safety (*LFS*) at one point of the slope is defined as the ratio of the available shearing resistance τ* to the current state of shearing stress τ at that point (Lu et al., 2012), as shown by Eq. (2.15). The advantage of local factor of safety approach is that it could provide more insight if local failure is more critical (e.g., stress concentration at the toe of a vertical cut); however, it could not be used as an index to assess slope stability if global failure is more critical.

$$LFS = \frac{\tau^*}{\tau} \tag{2.15}$$

2.2.3 Simplified Slope Stability Analysis

The numerical transient seepage and slope stability analysis requires that the soil-water characteristic curve and permeability function of the soil are known. However, the measurement of soil-water characteristic curve and permeability function is costly, technically-demanding and time-consuming (Leong and Rahardjo, 1997a, 1997b; Zhang and Fredlund, 2015). As a result, the measurement is usually reserved for research studies or large projects where substantial risk may be involved (Zhang and Fredlund, 2015). The difficulty in obtaining the required input parameters, the complexity involved in the analysis and the level of expertise required by the analysis have limited the application of the rigorous numerical methods (Vahedifard et al., 2016). Simplified slope stability analysis that consists of conceptual infiltration model and infinite slope

analysis is widely used to assess slope stability based on translational failure mechanism (Pradel and Raad, 1993; Cho and Lee, 2002; Lu and Godt, 2008; Godt et al., 2012; Zizioli et al., 2013).

2.2.3.1 Conceptual Infiltration Models

Conceptual infiltration models use the concept of wetting front, and involve a simplification of the pore-water pressure profile above the wetting front. The models proposed by Green and Ampt (1911) and Lumb (1962) have been widely used and continuously improved to estimate the depth of wetting front.

Green-Ampt Model

The Green-Ampt model is illustrated in Figure 2.7. The model is established on the following assumptions: (1) the soil is initially unsaturated with volumetric water content equals to θ_o, the downward flow of water saturates the soil, produces a sharp wetting front of depth z_w, and increases the volumetric water content from θ_o to θ_f; and (2) the permeability of the soil above the wetting front, k_s, is a constant, and there is a constant capillary pressure head, h_c, ahead of the wetting front. Because of the ponded water, there is excess supply of water on the ground surface. Hence, the rate that water entering the soil is always equal to the infiltration capacity of the soil. According to Darcy's law, the infiltration capacity of the soil, I_p, can be expressed as:

$$I_p = k_s \frac{z_w + h_c + h_p}{z_w} \tag{2.16}$$

The rate that water entering the soil can be calculated by:

$$v = \left(\theta_f - \theta_o\right)\frac{\mathrm{d}z_w}{\mathrm{d}t} \tag{2.17}$$

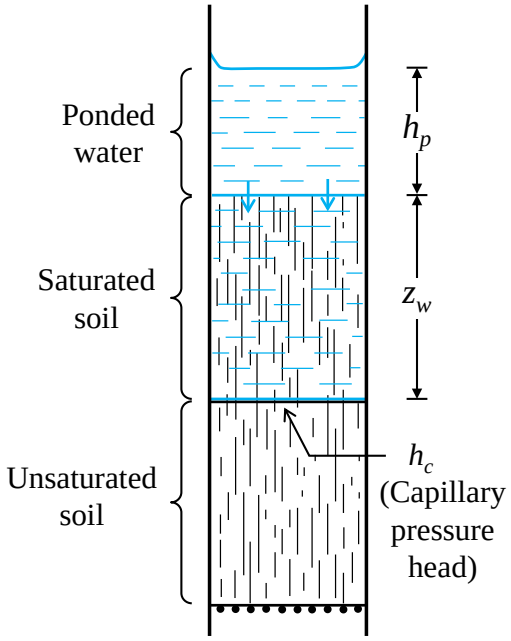

Figure 2.7 Downward flow of water through soil (modified from Green and Ampt, 1911)

By equating Eq. (2.16) and Eq. (2.17) with the boundary condition that $z_w = 0$ at $t = 0$, the depth of wetting front, z_w, can be expressed as:

$$z_w = \frac{k_s t}{(\theta_f - \theta_o)} + (h_c + h_p)\ln\frac{h_c + h_p + z_w}{h_c + h_p} \tag{2.18a}$$

Alternatively, the time, t, to reach z_w can be calculated by:

$$t = \frac{\theta_f - \theta_o}{k_s}\left[z_w - (h_c + h_p)\ln\frac{h_c + h_p + z_w}{h_c + h_p}\right] \tag{2.18b}$$

The capillary pressure head h_c was found to have physical significance and can be written as:

$$h_c = \int_0^{z_w} \frac{k_w}{k_s} dz \tag{2.19}$$

Eq. (2.19) was first suggested by Bouwer (1966) and theoretically verified by Neuman (1976). Bouwer (1966) suggested that h_c can be approximated as half of the air-entry value of the drying

SWCC. Philip (1957) approximated h_c as the height of capillary rise. During infiltration, air may be entrapped in the soil. As a result the soil above the wetting front may not be fully saturated and the permeability of the soil above the wetting front is usually less than the saturated permeability, k_s. Bouwer (1966) suggested that the k_s in Eqs. (2.16) and (2.18) is replaced by $0.5k_s$ based on field and laboratory measurements.

In Eq. (2.16), I_p tends to infinity when z_w approaches to zero. Hence, in the initial stage ($t \rightarrow 0$, $z_w \rightarrow 0$) of a rainfall event, the rate of water entering the soil is controlled by the rainfall intensity I rather than the infiltration capacity I_p of the soil. Mein and Larson (1973) proposed a two-stage infiltration model: in the first stage ($I \leq I_p$), the infiltration rate [Eq. (2.17)] is equal to the rainfall intensity I, and there is no ponding or runoff; in the second stage ($I > I_p$), the infiltration rate [Eq. (2.17)] is equal to the infiltration capacity of the soil I_p, and ponding or runoff starts to occur.

The z_w in Eq. (2.18a) appears on both the left and right sides of the equation. Hence, iteration is required to calculate z_w using Green-Ampt model. The time t to reach z_w can be calculated explicitly according to Eq. (2.18b). Hence, Green-Ampt model is more commonly presented as Eq. (2.18b), and it is usually used to estimate the t required to reach a critical z_w at which an infinite slope is on the verge of failure (Pradel and Raad, 1993; Cho and Lee, 2002).

Lumb's Wetting Band Equation

According to Lumb (1962), the soil under a heavy rainfall is fully saturated near the surface, and near-saturated (S_f = 0.8 to 0.9) down to a depth of z_w, as shown in Figure 2.8. Below the wetting

front the degree of saturation drops abruptly to the initial value, S_o. The analytical solution to calculate z_w for the one-dimensional Richard's equation provided by Lumb (1962) is:

$$z_w = \sqrt{Dt} + \frac{k_s t}{n\left(S_f - S_o\right)} \tag{2.20}$$

where D is a diffusion term, and n is the soil porosity. The diffusion D decreases rapidly with time and it can be considered as zero for prolonged and heavy rainfall. Hence, Eq. (2.20) can be simplified to:

$$z_w = \frac{k_s t}{n\left(S_f - S_o\right)} \tag{2.21}$$

Eq. (2.21) enables the explicit calculation of z_w. Hence, it is commonly used to estimate the depth of wetting front and the rise of groundwater table (Koo, 1998; Sun et al., 1998).

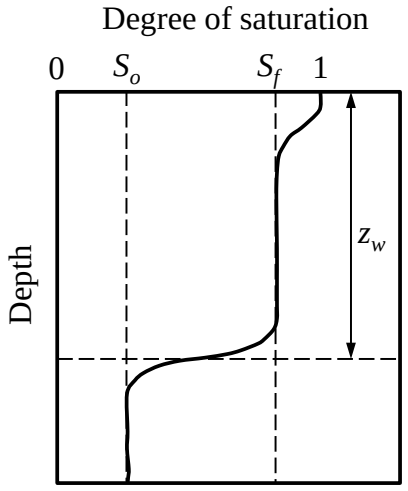

Figure 2.8 Variation of degree of saturation with depth during infiltration (from Lumb, 1962)

Eq. (2.21) is suitable for the situation where $I \geq k_s$. For the situation where $I < k_s$, Sun et al. (1998) suggested that z_w can be calculated by:

$$z_w = \frac{It}{n\left(S_f - S_o\right)} \tag{2.22}$$

The denominator of Eqs. (2.21) and (2.22) [i.e., $n(S_f - S_o)$] is essentially the water storage capacity of the soil. Antecedent rainfall could substantially increase S_o, and reduce the time t required to saturate the soil to a specified depth at which a slope failure may be initiated (Fourie et al., 1999). The z_w estimated by the "wetting band equations", Eqs. (2.21) and (2.22), agree reasonably well with those obtained by the finite element transient seepage analysis (Sun et al., 1998; Lee et al., 2009) and field measurement (Li et al., 2005).

2.2.3.2 Infinite Slope Analysis

Infinite slope model has two assumptions (Taylor, 1948; Duncan et al., 2014): (1) strata of different strengths exist, and the sliding surface is more likely to pass through the stratum of lower shear strength; and (2) the depth of the sliding surface is much less than the length of slope, so that the boundary effects are negligible. Due to rainwater infiltration, the matric suction above the wetting front is greatly reduced. The wetted soil can be considered as a weak layer compared with the underlying unsaturated soil. Field monitoring shows that the infiltration depth is usually less than 2 m and rarely exceeds 4 m even under a heavy rainfall of long duration (Li et al., 2005; Tu et al., 2009), and most of the rainfall-induced landslide cases were reported to be shallow compared with its length (Dai et al., 2003; Zizioli et al., 2013). Hence, the two assumptions are satisfied for a potential rainfall-induced translational slide.

In the infinite slope analysis, the groundwater table and sliding surface are usually assumed to be parallel to the slope surface, as shown in Figure 2.5. By adopting the extended Mohr-Coulomb

failure criterion [Eq. (2.5)] and applying limit equilibrium method to a vertical slice of unit width, the factor of safety can be expressed as (Cho and Lee, 2002):

$$F = \frac{c'}{\gamma z_w \sin\beta\cos\beta} + \frac{\tan\phi'}{\tan\beta} + \frac{(u_a - u_w)\tan\phi^b}{\gamma z_w \sin\beta\cos\beta} \tag{2.23}$$

where γ is the unit weight of the soil, and β is the slope angle. Different forms of infinite slope equations are presented in the literature, but they can generally be reduced to Eq. (2.23). The differences are in how the $(u_a - u_w)$ and ϕ^b are defined.

For the pore-water pressure profiles a, b and c shown in Figure 2.5, the $(u_a - u_w)$ at the sliding plane is equal to $\gamma_w(H_{wt} - z_w)$, 0 and $-\gamma_w z_w \cos^2\beta$, respectively. By substituting the $(u_a - u_w)$ to Eq. (2.23), the factor of safety F can be calculated by (Rahardjo et al., 1995):

$$F = \begin{cases} \dfrac{c'}{\gamma z_w \sin\beta\cos\beta} + \dfrac{\tan\phi'}{\tan\beta} + \dfrac{\gamma_w}{\gamma}\left(\dfrac{H_{wt}}{z_w} - 1\right)\dfrac{\tan\phi^b}{\tan\beta}, \text{ for profile a} & \text{(2.24a)} \\ \dfrac{c'}{\gamma z_w \sin\beta\cos\beta} + \dfrac{\tan\phi'}{\tan\beta}, \text{ for profile b} & \text{(2.24b)} \\ \dfrac{c'}{\gamma z_w \sin\beta\cos\beta} + \dfrac{\tan\phi'}{\tan\beta} - \dfrac{\gamma_w}{\gamma}\dfrac{\tan\phi'}{\tan\beta}, \text{ for profile c} & \text{(2.24c)} \end{cases}$$

The equation presented by Iverson (2000) is:

$$F = \frac{c'}{\gamma_t z_w \sin\beta\cos\beta} + \frac{\tan\phi'}{\tan\beta} - \frac{\gamma_w h_p \tan\phi'}{\gamma \sin\beta\cos\beta} \tag{2.25}$$

where h_p is the pressure head at the slip surface. Comparing Eq. (2.25) with Eq. (2.23), it can be found that $(u_a - u_w) = -\gamma_w h_p$ and $\phi^b = \phi'$.

The equation presented by Lu and Godt (2008) is:

$$F = \frac{c'}{\gamma z_w \sin\beta\cos\beta} + \frac{\tan\phi'}{\tan\beta} - \frac{\sigma^s \tan\phi'}{\gamma z_w \sin\beta\cos\beta} \tag{2.26}$$

where $\sigma^s = \Theta(u_a - u_w)$ is the suction stress. Comparing Eq. (2.26) with Eq. (2.23), it can be found that $\tan\phi^b = \Theta\tan\phi'$.

The equation presented by Travis et al. (2010) is:

$$F = \frac{c' + \bar{\gamma}(z) z\cos\beta\tan\phi' + \psi(z)\tan\left[\phi^b(z)\right]}{\bar{\gamma}(z) z\sin\beta} \tag{2.27}$$

where $\bar{\gamma}(z)$ is the average soil unit weight, which is a function of *z*. The suction ψ and angle ϕ^b are also functions of *z*.

Infinite slope model provides a simple approach to assess the stability of an unsaturated soil slope under rainfall due to translational failure. However, if rotational failure is more critical, infinite slope model would fail to predict the slope failure. Besides, infinite slope analysis is only accurate when the depth of the slip is much less than the length of the slip (Taylor, 1948). The errors caused by the neglect of boundary effects become increasingly considerable with the increase in depth/length ratio of the translational slip (Griffiths et al., 2011a; Milledge et al., 2012).

2.3 Review of Earthquake-Induced Landslides

Earthquake triggered a large number of landslides, in both rock and soil, natural and engineered slopes (e.g., Seed et al., 1978; Keefer, 1984, 2002; Rodríguez et al., 1999). Based on the type of material, type of landslide movement, degree of internal disruption of the landslide mass, and geologic environment, Keefer (1984) classified earthquake-induced landslides into three main categories (i.e., disrupted landslides, coherent landslides, and lateral spreads and flows) and fourteen individual types (rock falls, rock avalanches, disrupted soil slides, soil slumps, etc.). The focus of this study is on soil slopes, especially unsaturated soil slopes. Hence, rock slope failures under earthquake loading will not be considered.

2.3.1 Mechanism of Earthquake-Induced Landslides

Earthquake reduces slope stability by increasing the shearing stress in the slope. Soil slope failure during earthquake is usually associated with a substantial decrease in the shearing resistance (e.g., liquefaction) of the soil. Seed et al. (1978) and Seed (1979) examined dam failures caused by earthquake in the United States and Japan from the 1900s to the 1970s, and found that dams which have suffered complete failure or slope failures are those which have been constructed primarily with saturated sand shells or on saturated sand foundations, while dams constructed of clay soils on clay or rock foundations have withstood extremely strong shaking ranging from 0.35 to 0.8g from an earthquake of magnitude 8.25 (Richter scale) with no apparent damage.

Harder (1991) examined the performance of earth dams during the Loma Prieta earthquake that occurred in Northern California on 17 October 1989, and found that most of the dams performed

satisfactory as major portions of the dams were unsaturated due to the low reservoir water levels. The potential damages for unsaturated embankments under earthquake loading are settlements and the induced cracks below the slope crest, which may affect the serviceability of the structures that are built on the embankments (Harder, 1991; Stewart et al., 2004).

The performance of slopes under earthquake loading strongly depends on the material of the slope. Terzaghi (1950) insightfully described this phenomenon as follows.

"The most stable materials are clays with a low degree of sensitivity, in a plastic state (Terzaghi and Peck, 1948, p. 1931), dense sand either above or below the water table, and loose sand above the water table. The most sensitive materials are slightly cemented grain aggregates such as loess and submerged or partly submerged loose sand. If a violent earthquake shock strikes a slope on plastic clay with low sensitivity, it will hardly have any effect beyond the formation of tension cracks along the upper edge associated with a slight bulging of the slope, because the viscosity of the clay interferes with more extensive displacements under impact. The slopes of earth dams or dikes, consisting of sand, may bulge slightly, and the crest of the fills may settle, but the slopes will not fail, provided the fills rest on a rough and stable base. After the earthquake, the fills will be more stable than before, because the earthquake vibrations tend to compact the material."

2.3.2 Effect of Seismic Loading on Soil Properties

2.3.2.1 Saturated Soils

Loose sand tends to contract while dense sand tends to dilate when subjected to ground vibrations. For loose saturated sands under seismic loading, if drainage is unable to occur, the

tendency to contract would result in an increase in pore-water pressure. If the pore-water pressure builds to the point at which it is equal to the overburden pressure, the effective stress becomes zero. As a result, the loose sand would lose strength completely and reach a liquefied state. The tests conducted by Seed and Lee (1966) show that loose saturated sand could liquefy under less than 10 cycles of cyclic loading, while dense saturated sand only partially liquefies under more than 800 cycles of cyclic loading. After the cyclic shearing, the dense saturated sand could mobilize its monotonic strength at a much smaller deformation than loose saturated sand.

Cohesive soils have tendency to gain strength under rapid load application due to the viscous nature of the cohesion component, which is manifested concurrently with the tendency to lose strength due to the cyclic nature of the load application (Ishihara, 1996). Hence, cyclic strength may be larger or smaller than the static strength, depending on the degree of strength degradation under cyclic loading. Seed and Chan (1966) conducted cyclic triaxial tests on various undisturbed and compacted clays, and found that the cyclic strength is generally greater than, approximately equal to, or 10-15% less than the static strength after 10, 30 and 100 cycles of cyclic loading, respectively.

Thiers and Seed (1969) investigated the influence of cyclic loading on the post-cyclic static strength of undisturbed and remolded clays using triaxial and simple shear apparatuses. They found that the strength degradation caused by cyclic loading can be expressed as a function of the ratio of the peak cyclic strain to the static failure strain, and the test results reveal that clayey soils could retain at least 80% of their original static strength after 200 cycles of loading if the peak cyclic strain is less than one half the static failure strain. The cyclic degradation of saturated

cohesive soils would increase with the increase in number of cycles and magnitude of cyclic shear strain (Idriss et al., 1978), and decrease significantly with the increase in overconsolidation ratio of the soil (Vucetic and Dobry, 1988).

Boulanger and Idriss (2007) proposed procedures to estimate the cyclic strength of saturated silts and clays as a function of monotonic undrained shear strength, earthquake magnitude and initial shear stress in the sloping ground. Extensive charts were presented by Andersen (2015) to determine the cyclic strength of clay for offshore foundation and slope stability design.

2.3.2.2 Unsaturated Soils

Unsaturated soils have three phases (i.e., soil particle, water and air), in contrast to the two phases of saturated soils (i.e., soil particle and water). As air is easier to compress than water, the air phase of unsaturated soils would be compressed first under cyclic loading. Hence, unsaturated soils would experience densification, in contrast to the buildup of pore-water pressure in saturated soils. The densification would manifest the dilatancy effect and lead to strength hardening (Ishihara, 1996).

Silver and Seed (1971) conducted cyclic simple shear tests on dry sand and found that the shear modulus of dry sand would increase with the increase in number of cycles, which was also observed by Kovacs and Leo (1981) and Amer et al. (1984). Jafarzadeh and Sadeghi (2012) conducted cyclic simple shear tests on both saturated and unsaturated sands, and found that saturated sand would experience liquefaction, while unsaturated sands regardless of the degree of saturation would experience hardening under cyclic loading.

Chu and Vucetic (1992) conducted cyclic simple shear tests on a compacted clay. For the clay compacted at dry of optimum and at optimum moisture content, the clay would experience hardening with the increase in number of cycles. For the clay compacted at a moisture content which is significantly above the optimum, the clay still experiences hardening in the first few cycles, after which the clay becomes saturated and starts to degrade due to the buildup of pore-water pressure. The cyclic simple shear tests conducted by Whang et al. (2004) shows that unsaturated compacted clay would experience hardening in the first few cycles and then the shear modulus would gradually stabilize after 10 cycles of loading.

2.3.3 Slope Stability Analysis Methods

2.3.3.1 Pseudo-Static Analysis

The pseudo-static analysis method has been used to evaluate the stability of slopes under earthquake since the 1940s or even earlier (Seed, 1979), and it was first documented by Terzaghi (1950). In the analysis, the effects of an earthquake on a slope are represented by an equivalent static horizontal force determined as the product of seismic coefficient, k_h, and the weight of the potential sliding mass, W, as shown in Figure 2.9. For a rotational failure [Figure 2.9(a)], the factor of safety can be expressed as:

$$F = \frac{s l_{\widehat{ac}} R}{W l_H + k_h W l_V} \tag{2.28}$$

where s is the average shearing resistance per unit area of the sliding surface; $l_{\widehat{ac}}$ and R are the length and radius of the sliding surface, respectively; l_H and l_V are the horizontal and vertical

distances between the center of rotation O and center of gravity O_1 of the sliding mass, respectively.

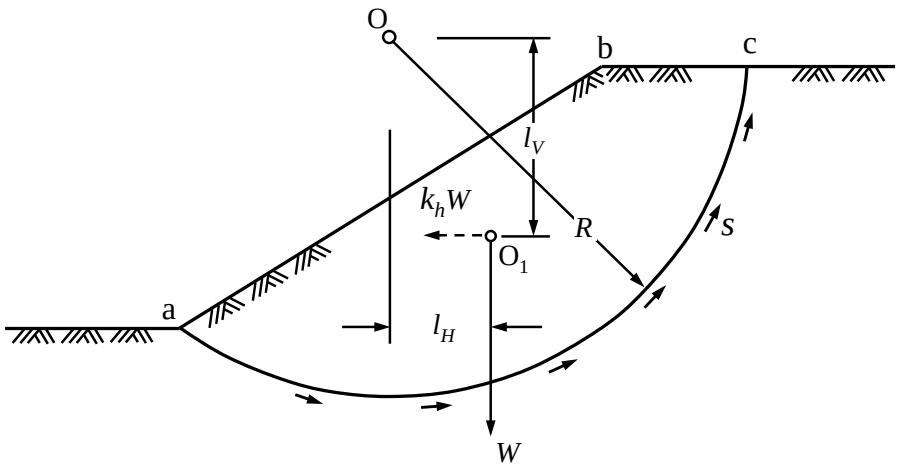

(a) Analysis of a rotational failure (from Terzaghi, 1950)

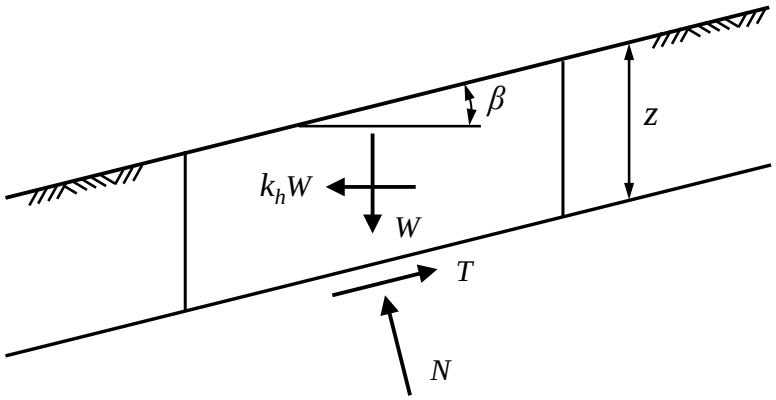

(b) Infinite slope analysis (modified from Duncan et al., 2014)

Figure 2.9 Conventional method for computing effect of earthquake on slope stability

For a shallow translational failure, the factor of safety *F* can be calculated using the infinite slope model [Figure 2.9(b)]:

$$F = \frac{c'}{\gamma z \sin\beta \cos\beta + k_h \gamma z \cos^2\beta} + \frac{1 - k_h \tan\beta}{k_h + \tan\beta} \tan\phi' \qquad (2.29)$$

where z is the vertical depth of the sliding plane.

It is a crude assumption to simplify a transient and complex earthquake shaking as a permanent and unidirectional body force. Terzaghi (1950) stated that "the concept it conveys of earthquake effects on slopes is very inaccurate". The seismic coefficient is generally selected to be some fraction of the peak acceleration to account for the fact that the peak acceleration acts only briefly and does not represent a long and more sustained acceleration of the landslide mass (Jibson, 2011).

Selection of an appropriate seismic coefficient (k_h) is the most important, and most difficult, aspect of a pseudo-static analysis (Kramer, 1996; Jibson, 2011). Terzaghi (1950) originally suggested that k_h = 0.1 for severe (Rossi-Forel IX) earthquakes, k_h = 0.2 for violent and destructive (Rossi-Forel X) earthquakes, and k_h = 0.5 for catastrophic earthquakes. For the soils which do not lose more than 15% of their original strength during earthquake, Seed (1979) suggested k_h = 0.1 for earthquakes of M = 6.25 and k_h = 0.15 for earthquakes of M = 8.25, and $F \geq 1.15$ to ensure that displacements will be acceptably small. Hynes-Griffin and Franklin (1984) applied the Newmark sliding block analysis to over 350 accelerograms and concluded that earth dams with $k_h = 0.5PGA/g$ (where PGA denotes peak ground acceleration) and $F \geq 1$ would not develop "dangerously large" deformations.

The selection of k_h usually lacks rational basis and depends heavily on past precedents (Seed and Martin, 1966; Kramer, 1996). Two recent studies have attempted to rationalize the selection.

Stewart et al. (2003) developed a site screening procedure which calculates k_h as a function of maximum horizontal ground acceleration, earthquake magnitude, source distance, and allowable displacement. Bray and Travasarou (2009) presented an analytical equation which calculates k_h as a function of allowable displacement, earthquake magnitude, and spectral acceleration.

Because seismic loading is of short duration, the undrained shear strength is usually recommended for a pseudo-static analysis. For compacted dam-construction materials and many natural soil strata, the dynamic shearing resistance is generally about the same as or slightly greater than the static shearing resistance (Newmark, 1965). Based on various cyclic triaxial and simple shear tests, Makdisi and Seed (1978) concluded that under typical earthquake loading conditions the dynamic yield strength of non-liquefiable soils would appear to be not less than 80% of the static undrained strength. Lefebvre and Pfendler (1996) conducted cyclic simple shear tests on a slightly overconsolidated clay and concluded that the undrained shear strength determined in monotonic tests is a conservative estimate of the dynamic yield strength, at least for slightly overconsolidated clay, for a pseudo-static analysis.

Federal Highway Administration (FHWA, 2011) suggested that the static undrained strength is generally considered to be an upper bound on the undrained strength that should be used in a seismic stability analysis, and for saturated cohesive soils of low to intermediate sensitivity the static strength may be reduced by 10-15% to account for the strength degradation in large magnitude earthquakes ($M > 7$). Duncan et al. (2014) pointed out that reductions in strength of up to 20% caused by cyclic loading during an earthquake are probably offset by the effects of a

higher loading rate during an earthquake compared to normal loading rates in static tests, hence there is some basis for not reducing the shear strength used in pseudo-static analyses.

For soils which do not lose significant strength during earthquakes (e.g., clays and clayey soils, dry or partially saturated cohesionless soils or extremely dense cohesionless soils), pseudo-static analyses generally provide a reasonable assessment of the seismic performance of embankments and slopes (Seed, 1979). The major limitation of pseudo-static analysis is that it only assesses a slope to be "stable" or "failed". Field records show that many slopes assessed to fail by pseudo-static analysis may still survive with limited amount of permanent displacement (Wilson and Keefer, 1983). However, pseudo-static analysis provides no information about the deformation if the slope is assessed to be "failed" (Jibson, 1993, 2011).

2.3.3.2 Stress-Deformation Analysis

For soils which may lose substantial strength under earthquake loading (e.g., sensitive clays, loose to medium dense saturated sands), pseudo-static analysis may not be appropriate due to the difficulty involved in the consideration of strength reduction. In order to determine the strength reduction under seismic loading accurately, advanced laboratory testing and numerical modeling are required. The essential procedures for a stress-deformation analysis can be found in Seed (1979). Kramer (1996) provided a good summary of the various methods and their associated studies. The advantage of stress-deformation analysis is that it gives the most accurate picture of what actually happens in the slope during an earthquake. The drawback of the stress-deformation analysis is that it uses highly complex models that, to be worthwhile, requires a high density of

high-quality data, which are reserved for critical projects where substantial risk may be involved (Jibson, 2011).

2.3.3.3 Permanent Displacement Analysis

Pseudo-static analysis is easy to use, while it is difficult to select a rational seismic coefficient (k_h) and the analysis provides no further information if the slope is assessed to fail. Stress-deformation analysis is accurate, while it is too costly and complicated for general application. Permanent displacement analysis bridges the gap between overly simplistic pseudo-static analysis and overly complex stress-deformation analysis; hence, it has gained increasing popularity among research and practicing community (Jibson, 2011).

Permanent displacement analysis was initially proposed by Newmark (1965) and it models a potential sliding mass as a block which has a known yield acceleration (= $k_y g$, where k_y is the yield coefficient, and g is the acceleration of gravity). The yield coefficient k_y is defined as the seismic coefficient k_h that could bring the slope to the verge of failure (F = 1). Hence, by rearranging Eq. (2.28) and Eq. (2.29) with the condition that F = 1, k_y for rotational failure and infinite slope model (i.e., translational failure) can be expressed as Eq. (2.30) and Eq. (2.31), respectively.

$$k_y = \frac{s l_{\widehat{ac}} R - W l_H}{W l_V} \tag{2.30}$$

$$k_y = \frac{\dfrac{c'}{\gamma z \cos^2 \beta} + \tan\phi' - \tan\beta}{1 + \tan\phi' \tan\beta} \tag{2.31}$$

The basic idea of permanent displacement analysis is that the ground motion that temporary exceeds the yield acceleration would not bring the slope to failure; instead, it causes permanent displacement of the slope. In a permanent displacement analysis, an earthquake motion record of interest is selected. As illustrated in Figure 2.10, the acceleration that exceeds the yield acceleration is integrated with respect to time to obtain the velocity-time history, and double integrated to obtain the displacement-time history. The cumulative displacement is a useful design index, as it indicates the potential damage to a slope during an earthquake.

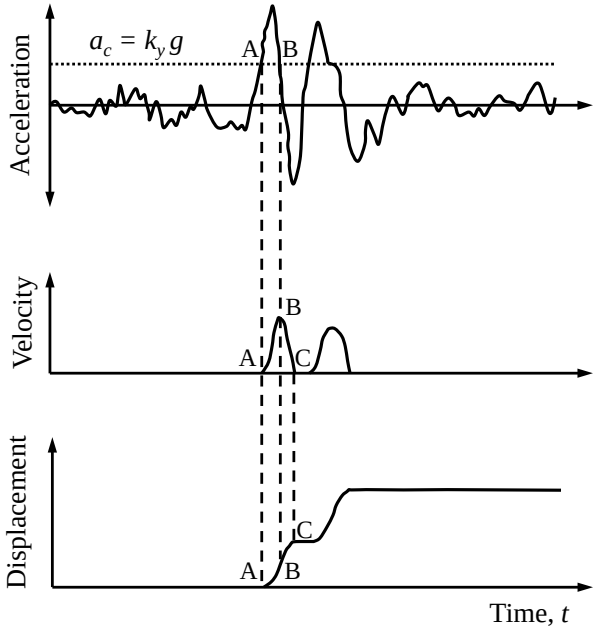

Figure 2.10 Illustration of the Newmark integration algorithm (modified from Wilson and Keefer, 1983)

In the procedure proposed by Newmark (1965), the sliding mass is assumed to be a rigid block, which is appropriate if the sliding mass is relatively shallow and stiff, as shown in Figure 2.11. The acceleration-time (a - t) history of the rigid block is equal to that at the base of the sliding

mass. Most of the earthquake-induced landslides in natural slopes generally satisfy this assumption (Keefer, 1984, 2002). However, earth structures like dams and embankments are constructed largely of ductile fine-grained soils, and deep rotational failure is usually the critical failure mode due to the homogeneous properties (Jibson, 2007, 2011). Hence, it is not reasonable to assume these engineered earth structures as rigid sliding mass under earthquake loading.

Makdisi and Seed (1978) modified Newmark's procedure to account for the deformable response of earth structures. In the modified procedure, a dynamic analysis assuming that the failure surface does not exist is conducted first to obtain the seismic coefficient-time (k - t) history, which is then transferred to a sliding block analysis to calculate the permanent displacement. The procedure developed by Makdisi and Seed (1978) is a decoupled analysis, as the calculation of dynamic response and plastic slip are performed separately, and the procedure has been extended to fully coupled analysis (Lin and Whitman, 1983; Rathje and Bray, 1999, 2000).

The approaches for computing earthquake-induced permanent displacements for rigid and flexible sliding masses are shown in Figure 2.11. A number of displacement predictive models have been proposed for rigid block analysis (Ambraseys and Menu, 1988; Jibson, 1993, 2007; Romeo, 2000; Saygili and Rathje, 2008), decoupled analysis (Makdisi and Seed, 1978) and coupled analysis (Bray and Travasarou, 2007). The displacement models can generally be expressed as:

$$D = f\left(k_y, \text{GM1}, \text{GM2}, \text{etc.}\right) \tag{2.32}$$

where D is the seismic displacement, GM1 and GM2 are ground motion parameters.

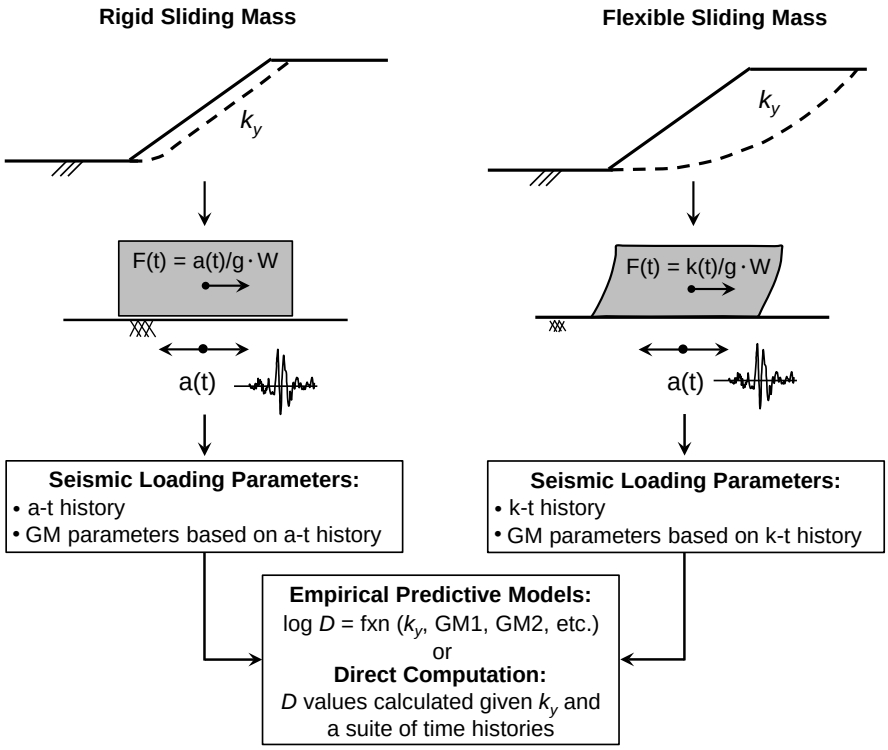

Figure 2.11 Approaches for computing earthquake-induced sliding displacements for rigid and flexible sliding masses (from Rathje and Antonakos, 2011)

Typical displacement predictive models are shown in Table 2.2. The ground motion parameters GM are used to characterize the amplitude (e.g., *PGA*), frequency content (e.g., S_a and T_s) and duration of the ground motion, which can be further correlated to the magnitude of the earthquake (*M*) and distance from the source to the site being considered (Kramer, 1996). The displacement predictive models are usually not recommended for use in site-specific design, but they are useful for preliminary screening of sites or regional seismic landslide hazard mapping (Romeo, 2000; Jibson et al., 2000; Dreyfus et al., 2013; Jibson, 2014).

Table 2.2 Typical predictive models for permanent displacement analysis

Reference	Models	Equation	
Ambraseys and Menu (1988)	Rigid block	$\log D = 0.9 + \log\left[\left(1-\frac{k_y g}{PGA}\right)^{2.53}\left(\frac{k_y g}{PGA}\right)^{-1.09}\right] \pm 0.30$	(2.33)
Jibson (2007)		$\log D = -2.710 + \log\left[\left(1-\frac{k_y g}{PGA}\right)^{2.335}\left(\frac{k_y g}{PGA}\right)^{-1.478}\right] + 0.424M \pm 0.454$	(2.34)
Bray and Travasarou (2007)	Coupled flexible block	$\log D = -1.10 - 2.83\log k_y - 0.333(\log k_y)^2 + 0.566(\log k_y)[\log S_a(1.5T_s)] + 3.04\log[S_a(1.5T_s)] - 0.244[\log S_a(1.5T_s)]^2 + 1.50T_s + 0.278(M-7) \pm \varepsilon$	(2.35)

from Eq. (2.33) to Eq. (2.35), D is the seismic displacement (unit: cm); PGA is the peak ground acceleration; M is the earthquake magnitude; T_s is the initial fundamental period of the sliding mass; $S_a(1.5T_s)$ is the spectral acceleration of the input ground motion at a period of $1.5T_s$.

The regional seismic landslide hazard mapping usually involves the following procedures (Jibson, 2000): (1) the geologic map is rasterized, and in each grid cell soil properties and ground motion records are assigned; (2) the k_y and ground motion parameters for each grid cell are calculated; and (3) the permanent displacement for each grid cell is calculated through a predictive model [e.g., Eq. (2.34)]. In the second step, the k_y is usually calculated by an explicit equation, as it is cumbersome to run numerous limit equilibrium or finite element analyses during the mapping.

The k_y is commonly explicitly calculated by the infinite slope equation [Eq. (2.31)] (Jibson et al., 2000; Dreyfus et al., 2013; Jibson, 2014). Infinite slope model is accurate when the depth/length ratio of the slip is small (Taylor, 1948), while it may increasingly underestimate k_y with the

increase in depth/length ratio due to the neglect of boundary effects. Rotational failure is usually not considered in regional seismic landslide mapping. The primary reason is that rotational failure is usually not as common as translational failure for natural slopes under earthquake (Keefer, 1984, 2002). Another reason may be due to the limited tools that can explicitly calculate k_y for rotational failure (Chien and Tsai, 2017).

In this study, equations which could calculate k_y explicitly for translational failure (i.e., rigid sliding mass) and rotational failure (i.e., flexible sliding mass) are proposed. The equation to calculate k_y for translational failure has considered the boundary effects, through which the influence of depth/length ratio on the accuracy of k_y obtained by infinite slope model can be investigated. The equation to calculate k_y for rotational failure can be integrated into the regional seismic landslide hazard mapping to identify potential rotational landslides.

2.4 Slope Stability Charts and Equations

2.4.1 Slope Stability Charts

Stability charts provide a simple and rapid approach to assess the stability of a slope. They are useful for preliminary design despite the availability of many sophisticated slope stability software (Duncan, 1996; Eid, 2014). A large number of stability charts have been developed for dry soil slopes, dry soil slopes under pseudo-static condition, saturated soil slopes with $u_w = r_u \gamma z$, and saturated soil slopes under rapid drawdown condition, as shown in Table 2.3. Limit equilibrium methods and upper bound limit analysis are the two common methods used to develop the stability charts, as summarized in Table 2.4. However, so far very limited stability

charts have been developed for unsaturated soil slopes. Huat et al. (2006) developed stability charts for typical unsaturated residual soil slopes in Malaysia under certain rainfall intensity and duration. The prerequisites on the slope geometries, soil properties and rainfall characteristics limit the applicability of the stability charts. Vo and Russell (2017) developed stability charts for unsaturated curvilinear slopes under no infiltration condition.

Table 2.3 Classification of stability charts according to the applicable soil conditions

Dry Soil Slopes		**Saturated Soil Slopes**	
Static condition	**Pseudo-static condition**	$u_w = r_u \gamma z$	**Rapid drawdown**
Taylor, 1937; Chen, 1975; Michalowski, 2002; Baker, 2003; Steward et al., 2011	Leshchinsky and San, 1994; Michalowski, 2002; Baker et al., 2006; Gao et al., 2013	Bishop and Morgenstern, 1960; Spencer, 1967; Michalowski, 2002; Michalowski and Nadukuru, 2013	Morgenstern, 1963; Viratjandr and Michalowski, 2006; Gao et al., 2014;

Table 2.4 Classification of stability charts according to the developing methods

Limit equilibrium methods	**Upper bound limit analysis**
Bishop and Morgenstern, 1960; Morgenstern, 1963; Spencer, 1967; Steward et al., 2011	Chen, 1975; Michalowski, 2002; Viratjandr and Michalowski, 2006; Michalowski and Nadukuru, 2013; Gao et al., 2013, 2014

2.4.2 Slope Stability Equations

To determine the factor of safety using stability charts, stability numbers need to be read from or interpolated between the stability curves. The reading and interpolation process is tedious if a large number of analyses need to be performed. It would be more convenient if factor of safety of a slope can be calculated by an explicit equation.

Table 2.5 Summary of the existing stability equations

References	Stability Equations	
Sah *et al*. (1994)	$F = 2.27\dfrac{c'}{\gamma H \sin\beta} + 1.54\left(1 - r_u\right)\dfrac{\tan\phi'}{\tan\beta}$	(2.36)
Yang *et al*. (2004)	$F = \dfrac{1}{H}\left(1.406 + 0.039c'\csc^2\phi'\right) + 1.25\left(1 - r_u\right)\dfrac{\tan\phi'}{\tan\beta} + \dfrac{0.156}{\cos\phi'} + \dfrac{0.011}{\gamma\sin\beta}$	(2.37)
Ahangar-Asr *et al*. (2010)	$F = -\dfrac{1.49H}{\gamma^2} - 1.8r_u^2 + \tan\phi'\left(2.59 - 2.18\tan\beta\right) + 0.014c' - 5.19\times10^{-5}c'^2 + 0.817$	(2.38)
Manouchehrian *et al*. (2014)	$F = 1.979 + 3.25\times10^{-7}\sqrt{\exp\left(\gamma\right)} + 0.083\sqrt{c'} - \dfrac{1.372}{\left[\exp\left(\tan\phi'\right)\right]^2} - 0.673\ln\left(\tan\beta\right) - 0.19\ln\left(H\right) - 3.515\left(r_u\right)^3$	(2.39)
Kostić *et al*. (2016)	$F = 0.2049 - 0.004H - 0.0375\beta + 0.0046\gamma + 0.1617c' + 0.0871\phi' + 0.4981r_u - 0.0061Hc' - 0.0003\beta c' - 0.001\beta\phi' - 0.0024\gamma c' + 0.0003c'\phi' - 0.067\phi' r_u + 0.0005\beta^2 - 0.0002c'^2$	(2.40)

Stability equations available in the literature, as summarized in Table 2.5, are developed for saturated soil slopes ($r_u \geq 0$), while no stability equation has been proposed for unsaturated soil slopes. The stability equations in Table 2.5 were obtained by regressing databases that consist of

known c', ϕ', γ, H, β and r_u as input variables and F as the output variable. The range and mean values of the input and output variables, the size of the database and the adopted regression techniques are summarized in Table 2.6. The performance of the slope stability equations listed in Table 2.5 will be evaluated critically in Section 5.4.1.

Table 2.6 Parameter ranges and regression methods for the existing stability equations

	Sah *et al*. (1994)	Yang *et al*. (2004)	Ahangar-Asr *et al*. (2010)	Manouchehrian *et al*. (2014)	Kostić *et al*. (2016)
β (°)	16 – 53 (32.93)	16 – 53 (32.93)	16 – 53 (32.41)	16 – 53 (33.05)	25 – 70 (47.50)
H (m)	3.66 – 214 (43.91)	3.66 – 214 (43.91)	3.66 – 214 (44.15)	3.66 – 214 (41.76)	6 – 10 (8.00)
γ (kN/m^3)	12 – 28.44 (19.72)	12 – 28.44 (19.72)	12 – 28.44 (19.71)	12 – 28.44 (19.93)	16 – 20 (18.00)
c' (kPa)	0 – 150.05 (20.48)	0 – 150.05 (20.48)	0 – 150.05 (22.12)	0 – 50 (10.45)	0 – 50 (25.00)
ϕ' (°)	0 – 45 (27.51)	0 – 45 (27.51)	0 – 45 (26.26)	0 – 45 (25.84)	10 – 50 (30.00)
r_u	0 – 0.5 (0.17)	0 – 0.5 (0.17)	0 – 0.5 (0.20)	0 – 0.5 (0.20)	0 – 0.5 (0.25)
F	0.63 – 2.05 (1.24)	0.63 – 2.05 (1.24)	0.63 – 2.31 (1.29)	0.63 – 2.31 (1.28)	0.028 – 4.79 (1.81)
$c'/\gamma H$	0 – 0.30 (0.04)	0 – 0.30 (0.04)	0 – 0.30 (0.05)	0 – 0.23 (0.03)	0.06 – 0.88 (0.29)
Number of cases	46	46	67	103	48
Regression technique	Maximum likelihood method	Genetic algorithm	Evolutionary polynomial regression	Genetic algorithm	Design of experiments

(The number in brackets are the mean values for the range of data)

2.5 Summary of the Research Gaps

Stability of an unsaturated soil slope under rainfall can be assessed by a combined transient seepage and slope stability analysis, or by a simplified infiltration and infinite slope analysis. A

combined transient seepage and slope stability analysis requires that the soil-water characteristic curve and permeability function are known. The difficulties in obtaining the unsaturated soil properties and the complexity involved in the numerical analysis have limited the application of the combined transient seepage and slope stability analysis in practice. On the other hand, simplified infiltration and infinite slope analysis is easy to conduct, but it can only be used to analyze translational failure and the analysis becomes increasingly conservative with the increase in depth/length ratio.

For slope stability analysis considering earthquake, dynamic shear strength should be used in seismic stability analysis. The effect of cyclic loading on the shear strength of saturated soils has been widely investigated, while only limited research has been conducted to investigate the effect of cyclic loading on unsaturated soils. In regional seismic landslide hazard mapping, the pseudo-static factors of safety or yield coefficients for permanent displacement analysis need to be calculated explicitly, and so far only infinite slope model can be used for such purposes. However, infinite slope model can only assess slope stability based on translational failure mechanism, and it is not accurate when the depth/length ratio of the slip is large.

Slope stability charts provide a simple approach for slope stability analysis. Stability charts have been widely developed for dry and saturated soil slopes, while very limited stability charts have been developed for unsaturated soil slopes. By using slope stability charts, stability numbers need to be read from or interpolated between the stability curves. It would be more convenient if factor of safety of a slope can be calculated by an explicit equation. A number of stability equations have been proposed for saturated soil slope. However, the performance of the existing

slope stability equations has not been evaluated objectively and comprehensively. Besides, no stability equation has been proposed for unsaturated soil slopes.

The above research gaps will be addressed in the following chapters.

Chapter 3: Simple Shear Tests on Unsaturated Soils

Soil behaves differently under static and dynamic loadings, and dynamic shear strength instead of static shear strength should be used in seismic slope stability analysis. However, very limited research has been conducted to investigate the effect of cyclic loading on the shear strength of unsaturated soils. The effect is investigated by conducting cyclic and monotonic simple shear tests in this chapter. An overview of simple shear test, test methodology and test results are presented below.

3.1 Overview of Simple Shear Test

Simple shear tests are often preferred over triaxial tests for field problems which involved smooth and continuous rotation of the principal stress directions (Franke et al., 1979; Boulanger et al., 1993; Rutherford and Biscontin, 2013). There are two general configurations of the simple shear apparatus: the NGI-type apparatus which tests a short circular specimen (Kjellman, 1951; Bjerrum and Landva, 1966), and Cambridge-type apparatus which tests a cuboidal specimen (Roscoe, 1953). The Cambridge-type is not as commonly used as NGI-type due to the difficulty in mounting undisturbed field specimens (Boulanger et al., 1993). The essential requirement for a simple shear test is that the soil specimen should be uniformly strained in simple shear and plane strain (Bjerum and Landva, 1966). For a NGI-type simple shear apparatus, the requirement is commonly fulfilled by confining the specimen by a wire-reinforced membrane (e.g., Bjerum and Landva, 1966; Ladd and Edgers, 1972; Airey and Wood, 1987) or by stacked rings (e.g., Amer et al., 1987; Hubler et al., 2017). Undrained simple shear tests on high plasticity clay and

low plasticity organic silt (Baxter et al., 2010; McGuire, 2011) and drained simple shear tests on dry sand (Kwan and El Mohtar, 2014) show that reinforced membrane and stacked rings can lead to comparable stress-strain relationship and strength if appropriate system correction is applied to the measured shear stresses.

Back-pressure saturation is usually not possible for a conventional NGI-type simple shear device, as back pressure may lead to bulging of the membrane. Franke et al. (1979) designed a simple shear device in which the specimen is enclosed in a latex rubber membrane and laterally confined by cell pressure. Similar to a triaxial test, back-pressure saturation can be performed due to the existence of cell pressure. The device developed by Franke et al. (1979) is elaborately instrumented. Any tendency to change the specimen height is prevented through automatic regulation of the cell pressure. Hence, during the consolidation and shearing stages, the cell pressure is a variable which is automatically adjusted to ensure the plane strain condition.

Boulanger et al. (1993) suggested that for an undrained constant volume stress-controlled cyclic simple shear test, the cell pressure can be a constant ($= K_o \sigma_v$, where K_o is the coefficient of earth pressure at rest, and σ_v is the vertical stress on the specimen) throughout the consolidation and shearing stages if the membrane compliance is negligible. The advantage of such a boundary condition is that the lateral effective stress can be easily and inexpensively measured as the difference between the external cell pressure and the internal pore-water pressure (Boulanger et al., 1993; Joer et al, 2011). If the cell pressure is maintained constant throughout the consolidation and shearing stages, the instrumentation used by Franke et al. (1979) can be considerably simplified. Cyclic and monotonic simple shear tests have been increasingly

conducted with specimen enclosed by latex rubber membrane and confined by constant cell pressure (Reyno et al., 2005; Joer et al. 2010; Kang et al., 2015, 2016).

Despite the increasing popularity of confining the specimen with latex rubber membrane and constant cell pressure in simple shear test, very limited research has been conducted to investigate whether the constant cell pressure could provide sufficient confinement and lead to same test results as a specimen that is laterally confined by either reinforced membrane or stacked rings. Recently, Acharya and Airey (2017) performed monotonic undrained simple shear tests on a normally consolidated clay, and found that similar undrained strength is obtained for the specimens confined by either reinforced membrane or constant cell pressure. For dry and unsaturated soils, simple shear tests are usually conducted at drained and under constant vertical stress conditions (Silver and Seed, 1971; Chu and Vucetic, 1992; Whang et al., 2004). However, no research was conducted to investigate whether constant cell pressure can provide sufficient confinement for drained simple shear tests.

3.2 Test Objective

The effect of seismic loading on saturated and unsaturated soil properties has been reviewed comprehensively in Section 2.3.2, which reveals that unsaturated soils would experience hardening in contrast to the degradation of saturated soils under earthquake loading. However, experimental data that clearly demonstrate the cyclic hardening effect in unsaturated soils are still limited. Section 3.1 shows that simple shear tests have been increasingly conducted with specimens laterally confined by constant cell pressure. However, whether constant cell pressure could provide sufficient confinement for the simple shear tests conducted at drained and under

constant normal stress conditions remains uncertain. Hence, before performing cyclic and monotonic simple shear tests to investigate the cyclic hardening effect, the effectiveness of lateral confinement by constant cell pressure is examined first in order to choose the correct lateral confinement method.

3.3 Test Equipment

An NGI-type cyclic simple shear apparatus manufactured by GCTS Testing System, USA, was used. The apparatus provides chamber pressure control which allows back-pressure saturation. Lateral constraint of the vertical piston is imposed via a cross-beam to minimize top-cap rocking and reduce the mechanical compliance. The apparatus has been slightly modified since its initial acquisition to cater for the suction-controlled requirement of unsaturated soil testing (Chin et al., 2009; Chin, 2011). The details of the modification can be found in Chin (2011).

The instruments in the simple shear apparatus include measuring devices for shear displacement, shear load, axial displacement and axial load. The instrumentations were calibrated before they were used. The calibration data are shown in Appendix A. The specimens were laterally confined by reinforced membranes fabricated in-house. The procedure to make the reinforced membrane is: (1) a stainless steel wire mesh of 20 mm height and 71 mm diameter is cut and attached on the surface of the latex rubber membrane, as shown in Figure 3.1(a); (2) a layer of PVC cement is applied to bond the mesh to the latex rubber membrane; (3) the PVC cement is left to dry for more than 24 hours, after which a reinforced membrane is formed, as shown in Figure 3.1(b). In Step 1, the size of mesh opening is about 1 mm × 1 mm, the diameter of the wire is 0.15 mm, and the wire is wound at 10 turns per centimeter of height.

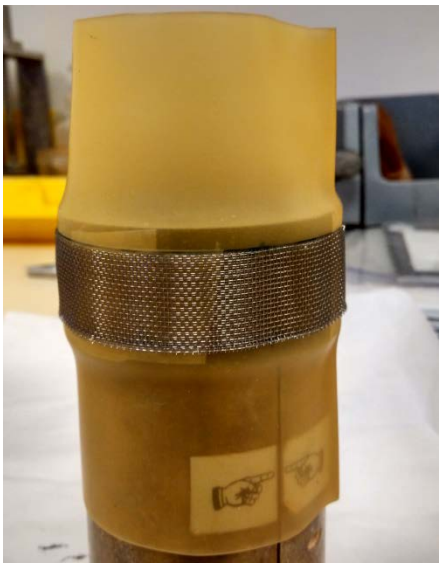

(a) Mesh

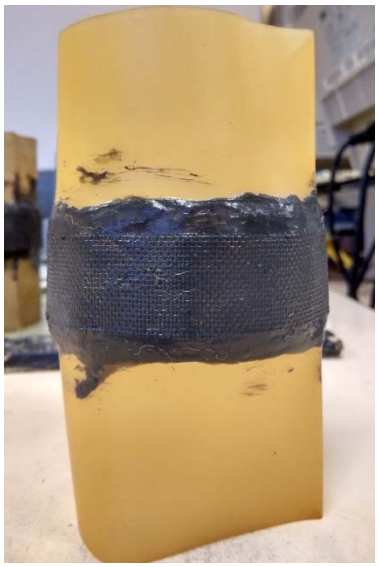

(b) Reinforced membrane

Figure 3.1 Reinforced membrane used in this study

The performance of the simple shear apparatus and the reinforced membrane was tested using dry Ottawa sand 20-30, and the results are compared with those presented by Amer et al. (1987). The grain size distribution and basic soil properties of Ottawa sand 20-30 are shown in Figure 3.2. To enabe comparison of test results, the sample preparation method and testing conditions of Ottawa sand 20-30 in this study are consistent with those used by Amer et al. (1987). More specifically, the dry Ottawa sand specimens were prepared by air pluviation method, tested at a dense state (void ratio e = 0.537, relative density D_r = 73%), under a constant vertical stress of 47.9 kPa, and subjected to sinusoidal loading at a frequency of 0.5 Hz and shear strain levels of 0.1, 1.0 and 5%. During the cyclic shearing, axial load was controlled, axial displacement, shear displacement and shear load were measured. The shear moduli for 1st and 300th cycles obtained by Amer et al. (1987) and this study are compared in Figure 3.3. In the calculation, the measured shear loads have been corrected for the membrane resistance and friction in the loading ram and

the slide table, as per ASTM D6528-07. It can be seen that the shear moduli obtained in this study agree reasonably well with those presented in Amer et al. (1987).

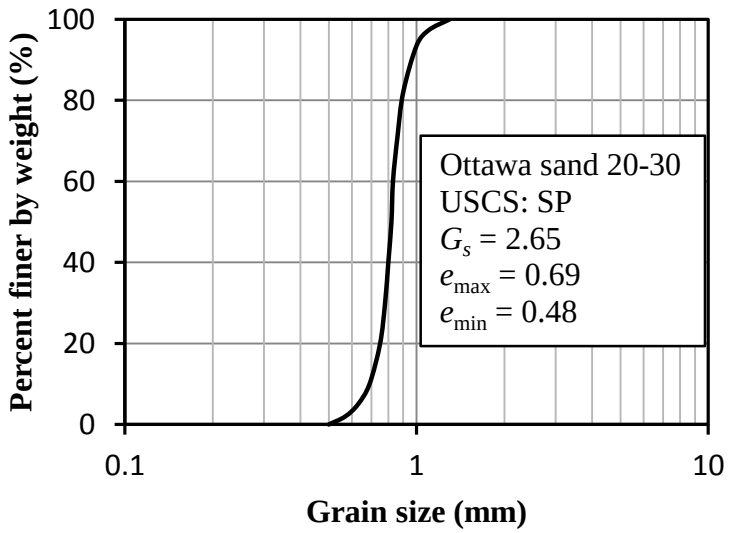

Figure 3.2 Grain size distribution and basic properties of Ottawa sand 20-30

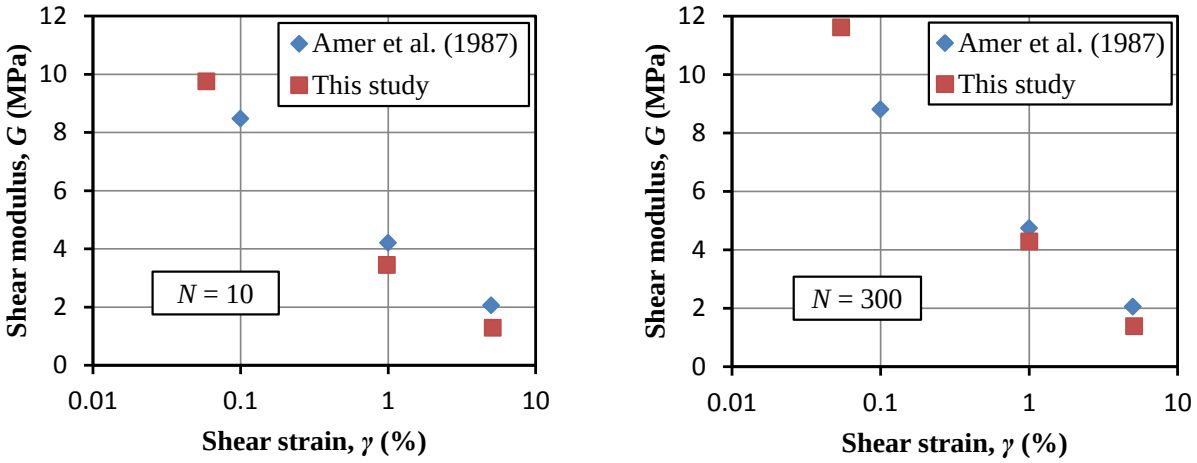

Figure 3.3 Comparison of cyclic simple shear test results on Ottawa sand 20-30 for device validation

3.4 Effectiveness of Lateral Confinement by Constant Cell Pressure

3.4.1 Test Materials and procedure

To investigate the effectiveness of lateral confinement provided by constant cell pressure, cyclic and monotonic drained simple shear tests were conducted on dry Ottawa sand 20-30 (Figure 3.2) with lateral confinement provided by either constant cell pressure or reinforced membrane. The diameter of the specimen is 71 mm, and the height is about 20 mm. All the specimens were initially prepared in a loose state (e = 0.62, D_r = 33%) using air pluviation technique, after which the specimens were consolidated under a vertical stress (σ_v) of 50 kPa, 100 kPa or 200 kPa. For the specimens enclosed in latex rubber membranes and confined by constant cell pressure (= $K_o\sigma_v$), the K_o value was determined by Jaky relationship $K_o = 1 - \sin\phi'$ (Terzaghi et al., 1996). Pilot tests showed that ϕ' of the Ottawa sand is about 40°, consequently K_o = 0.36. Following the consolidation stage, cyclic and monotonic drained simple shear tests were conducted on the specimen with the vertical stress maintained constant throughout the tests. The loading frequency for cyclic simple shear testing was selected to be 0.5 Hz, which is commonly adopted for sandy soils (e.g., Amer et al., 1987; Chin, 2011; Jafarzadeh and Sadeghi, 2012). In order to produce a "loose" specimen for the monotonic drained simple shear test, the specimen was incrementally subjected to a total of 9 cycles of sinusoidal cyclic loading and strain amplitudes of 0.03%, 0.15% and 1% (3 cycles at each strain amplitude). Similarly, in order to produce a "dense" specimen, the specimen was incrementally subjected to a total of 90 cycles of sinusoidal cyclic loading at strain amplitudes of 0.03%, 0.15% and 1% (30 cycles at each strain amplitude). The numbers of loading cycles, which could lead to desirable relative densities, were chosen after a number of trial tests. After the cyclic simple shearing, the specimens were monotonically sheared at a

constant deformation rate of 0.2 mm/min, as suggested by Kang et al. (2015). The tests were stopped when the shear strains reached 25%.

3.4.2 Results of the Drained Simple Shear Tests

A summary of the drained simple shear test program is shown in Table 3.1. In the "test code", the first two letters denote the lateral confinement method ("RM" for reinforced membrane, "CP" for cell pressure), the number in the middle denotes the normal stress level (50, 100 or 200 kPa), and the last letter denotes the relative density state of the specimen for monotonic drained simple shear test ("D" for dense, "L" for loose). The symbol e_0 denotes the void ratio after the consolidation. The symbol e_1 denotes the void ratio after the cyclic simple shearing and also the initial void ratio for the monotonic simple shearing. The symbol e_2 denotes the void ratio after the monotonic simple shearing. Before consolidation, all the specimens were prepared at a void ratio of 0.62. The void ratio decreased from 0.62 to e_0 after the consolidation. The e_0 generally decreases with the increase in vertical stress as expected. The e_1 at dense state is less than the e_1 at loose state, as the specimens in the dense state have been subjected to 90 cycles of cyclic shearing in contrast to 9 cycles of cyclic shearing for the specimens in the loose state.

The cyclic shear moduli obtained from the cyclic simple shearing were calculated as per ASTM D6528-07 and shown in Figure 3.4. At small strain level of γ = 0.03%, which is close to the threshold volumetric strain of dry sand (Hsu and Vucetic, 2004), the shear moduli are sensitive to the measured shear load and show some scatter. At shear strains γ_c = 0.03% and 0.15%, higher shear moduli were measured if the specimen was confined by the K_o cell pressure, while the difference between the two confinement methods decreases with increasing number of cycles.

This phenomenon is mainly attributed to the fact that cell pressure provides active confinement from the beginning of the test, while the reinforced membrane and the specimen may not be in good contact at the beginning and the confinement was increasingly activated with increasing number of cycles. At shear strain γ_c = 1%, the shear moduli for the specimen confined by reinforced membrane are in better agreement with the specimen confined by K_o cell pressure. The mobilization of lateral confinement provided by the reinforced membrane may be accompanied by slight bulging (i.e., increase in cross-sectional area) and consequently higher axial strain was measured. In the calculation of the void ratio, the cross-sectional area of the specimen is assumed to be constant throughout the consolidation and shearing stages. As a result, e_1 for the specimen confined by reinforced membrane is generally smaller than the e_1 for the specimen confined by K_o cell pressure in Table 3.1.

Table 3.1 Summary of the drained simple shear test programme

Confinement method	Test code	e_0	e_1	e_2	τ_h/σ_v	ϕ' (°)
Reinforced Membrane	RM50D	0.616	0.514	0.554	1.080	47.2
	RM50L	0.611	0.572	0.570	0.888	41.6
	RM100D	0.589	0.517	0.551	0.930	42.9
	RM100L	0.613	0.575	0.576	0.850	40.4
	RM200D	0.564	0.515	0.538	0.760	37.2
	RM200L	0.571	0.548	0.549	0.675	34.0
Latex Membrane with Cell Pressure (K_o = 0.36)	CP50D	0.585	0.531	0.497	0.507 (0.842)	26.9 (40.1)
	CP50L	0.604	0.590	0.552	0.502 (0.571)	26.7 (29.8)
	CP100D	0.566	0.536	0.504	0.440 (0.690)	23.7 (34.6)
	CP100L	0.578	0.562	0.523	0.440 (0.524)	23.7 (27.7)
	CP200D	0.567	0.550	0.531	0.470 (0.621)	25.2 (31.8)
	CP200L	0.566	0.562	0.534	0.470 (0.512)	25.2 (27.1)

(Note: τ_h is taken as the peak shear stress (in Figure 3.5) for the ratio τ_h/σ_v and friction angle ϕ' shown in brackets; otherwise τ_h is taken as the shear stress τ when the shear strain γ = 20%.)

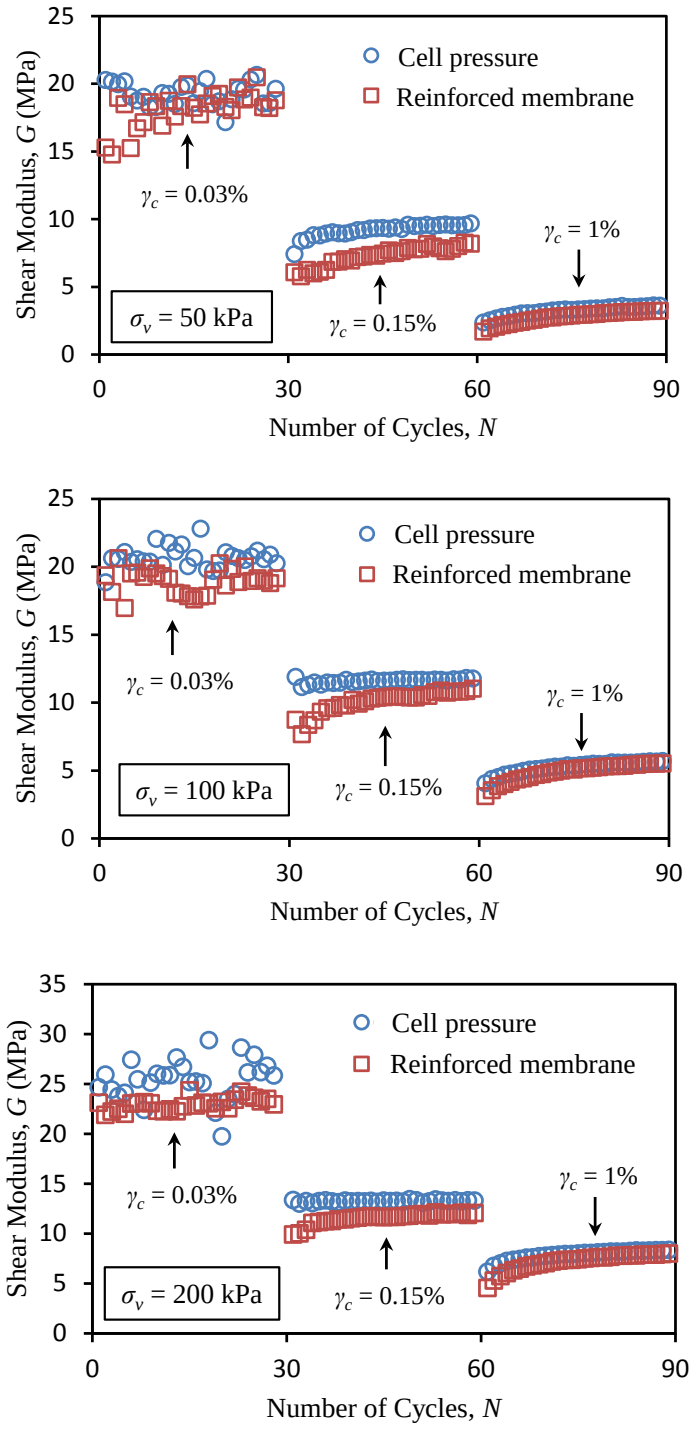

Figure 3.4 Small-strain cyclic shear modulus for Ottawa sand 20-30 obtained by different confinement methods

After the cyclic simple shearing stage, the specimens were subjected to monotonic shearing. The monotonic shear stress-strain relationships are summarized in Figure 3.5. It can be seen that the specimens confined by reinforced membrane consistently have higher peak shear stresses compared to those specimens confined by K_o cell pressure regardless of the initial void ratio and the normal stress level.

The void ratios after the monotonic simple shearing stage are shown in Table 3.1 as e_2. For the specimens confined by reinforced membrane, the specimens experienced dilation ($e_2 > e_1$) if the specimens were initially dense (e_1 = 0.514~0.517, D_r = 82~84%). The shearing occurred under almost constant volume condition ($e_2 \approx e_1$) if the specimens were initially loose (e_1 = 0.548~0.575, D_r = 55~68%). For the specimens confined by K_o cell pressure, the specimens could bulge considerably at large shear strain, which was measured by Kang et al. (2015) and also observed in this study. The lateral bulging could induce additional axial strain. In the calculation of void ratios, the cross-sectional area of the specimen is assumed to be constant. As a result, e_2 for the specimens confined by cell pressure are smaller than the e_2 for the specimens confined by reinforced membrane in Table 3.1.

For the drained monotonic simple shear test on dry sand, it is generally reasonable to assume that the rupture plane is horizontal. When τ_h is at its maximum value, the frictional strength is fully mobilized, and the friction angle ϕ' can be calculated by (Rutherford and Biscontin, 2013; Kwan and El Mohtar, 2014):

$$\frac{\tau_h}{\sigma_v} = \tan\phi' \tag{3.1}$$

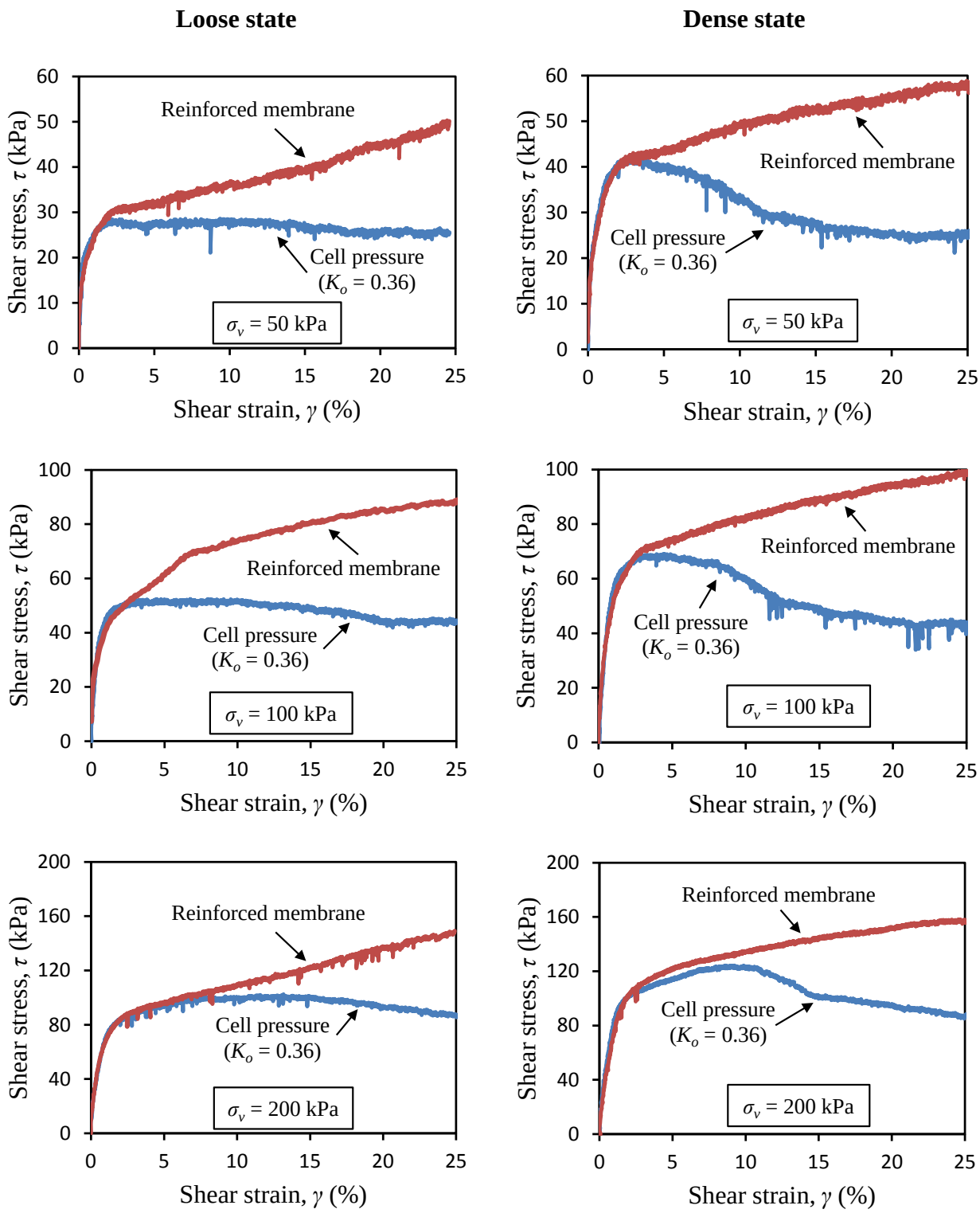

Figure 3.5 Monotonic shear stress-strain relationships for Ottawa sand 20-30 obtained by different confinement methods

For the specimens confined by reinforced membrane, no peak shear stress is shown before γ = 25% in Figure 3.5. In such situation shear strength (τ_h) is commonly taken as the shear stress at γ = 20% (e.g., Seed and Chan, 1959). Consequently, the ratios τ_h/σ_v and friction angles ϕ' calculated by Eq. (3.1) are shown in Table 3.1. It can be seen that ϕ' decreases with the increase in σ_v, and ϕ' in the dense state is larger than ϕ' in the loose state. The average ϕ' in the dense state is 42.4°, and the average ϕ' in the loose state is 38.7°.

For the specimens confined by K_o cell pressure, strain softening is observed in Figure 3.5 if the specimens were prepared in dense state, while the differences between peak shear stresses and residual shear stresses are small if the specimens were prepared in loose state. If the shear stress-strain curves for dense and loose states are plotted together, the curves essentially merge together at large shear strain (e.g., $\gamma \geq$ 15%). Hence, if τ_h is taken as the shear stress at γ = 20%, the ratios τ_h/σ_v and friction angles ϕ' calculated by Eq. (3.1), as summarized in Table 3.1, are mainly affected by σ_v and not affected by the density state ("loose" or "dense") of the specimens. The average ϕ' for various σ_v at residual state is 25.2°. If τ_h is taken as the peak shear stress, the ratio τ_h/σ_v and friction angle ϕ' are shown in brackets in Table 3.1. The average ϕ' for various σ_v is 35.5° for the dense state, and 28.2° for the loose state.

Kang et al. (2015) conducted drained monotonic simple shear tests on dry silica sand with lateral confinement provided by stacked rings or by K_o cell pressure (K_o = 0.5 and K_o = 1) to investigate the influence of K_o values on the radial strain behaviors. The shear stress-strain data presented by Kang et al. (2015) were digitized and reinterpreted, as shown in Figure 3.6. The specimens of Kang et al. (2015) were initially prepared at a relative density of 80%. Hence, the specimens

were tested at a dense state. Similar to Figure 3.5, Figure 3.6 shows that the specimen confined by stacked rings has the highest peak shear stress, followed by the specimen confined by cell pressure with K_o = 1 and K_o = 0.5. The test results presented in Figure 3.6 are also interpreted by Eq. (3.1) with τ_h taken as the peak shear stress. The results are summarized in Table 3.2. The magnitudes and trends of ϕ' shown in Table 3.2 are in good agreement with the ϕ' presented in Table 3.1.

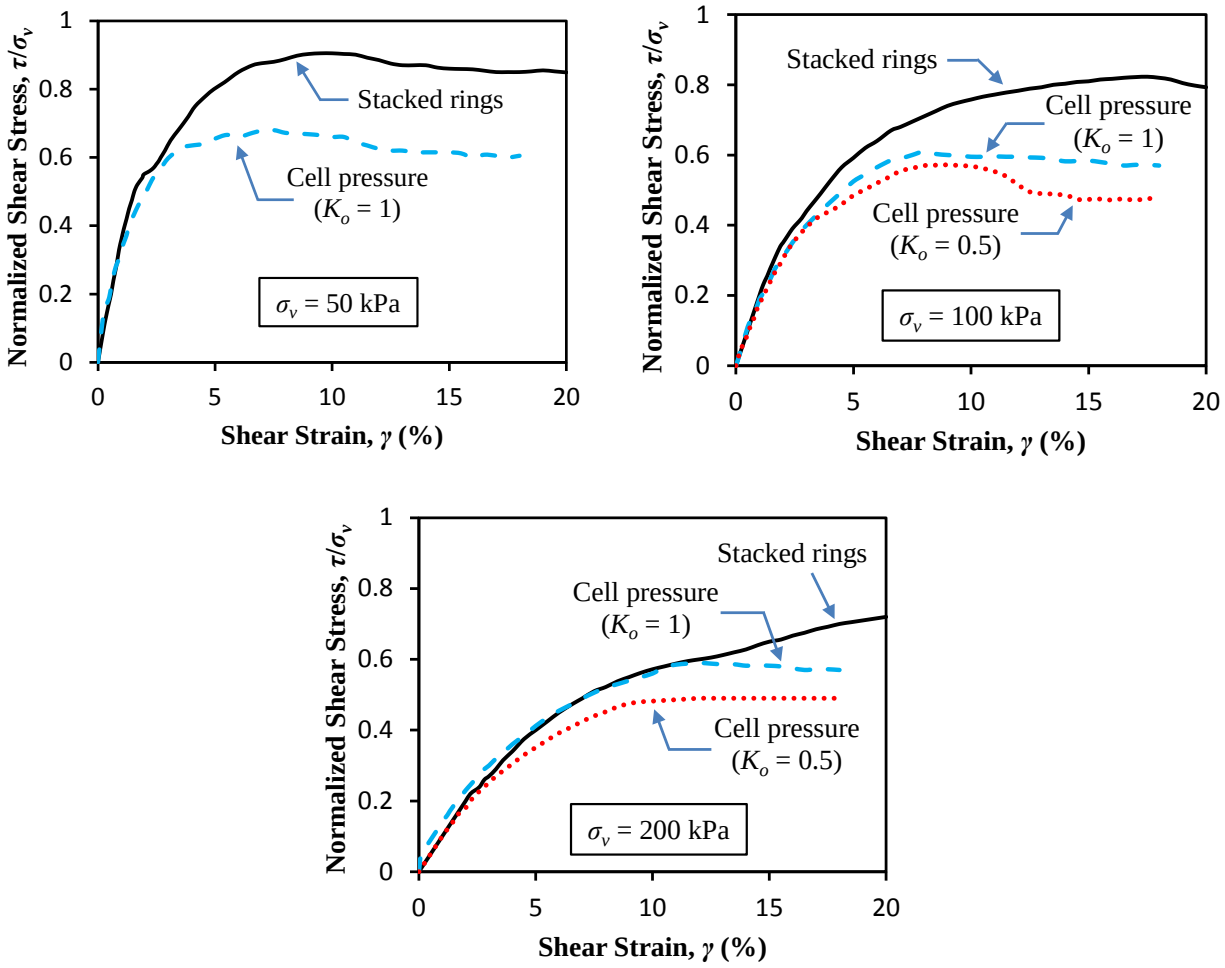

Figure 3.6 Shear stress-strain relationships for silica sand obtained by different lateral confinement methods (data are taken from Kang et al., 2015)

Table 3.2 Friction angles for the data from Kang et al. (2015)

Lateral Confinement	σ_v = 50 kPa		σ_v = 100 kPa		σ_v = 200 kPa	
	τ/σ_v	ϕ' (°)	τ/σ_v	ϕ' (°)	τ/σ_v	ϕ' (°)
Stacked rings	0.90	42.00	0.82	39.35	0.72	35.75
Cell pressure (K_o = 1)	0.68	34.21	0.61	31.38	0.59	30.54
Cell pressure (K_o = 0.5)	-	-	0.57	29.68	0.49	26.11

From Tables 3.1 and 3.2, it can be seen that ϕ' for the specimens confined by constant cell pressure are generally less than 30° and lower than the value expected (i.e., in the order of 40°) for dry sand. The differences in peak shear stresses (Figures 3.5 and 3.6) and friction angles (Tables 3.1 and 3.2) can be explained by the different stress conditions of the rigid and flexible confinement methods, as illustrated in Figure 3.7. During the consolidation stage, for both rigid and flexible lateral confinements the major principal stress (σ_1) is vertical and equal to the vertical stress (σ_v), the minor principal stress (σ_3) is horizontal and equal to $K_o\sigma_v$. In the shearing stage, the vertical stress σ_v maintains constant. The horizontal stress σ_h due to rigid confinement increases with the increase in shear strain. Experimental evidence can be found in Budhu (1984), who observed that the horizontal stress imposed by reinforced membrane for a dry sand under monotonic shearing increases from about $0.4\sigma_v$ at the consolidation stage to a value close to $2\sigma_v$ at the failure strain. However, for the specimen confined by cell pressure, the horizontal stress is a constant ($=K_o\sigma_v$) throughout the consolidation and shearing stages. Hence, during the shearing stage the mean effective stress is higher in the specimen confined by rigid boundary than in the specimen confined by constant cell pressure. Since shear strength is directly related to the mean effective stress (Wroth, 1984), it is not surprising that higher peak shear stresses (Figures 3.5 and

3.6) and friction angles (Tables 3.1 and 3.2) are obtained for the specimens confined by reinforced membrane and stacked rings than the specimens confined by constant cell pressure.

Reyno et al. (2005) and Joer et al. (2011) pointed out that if lateral confinement is provided by a constant cell pressure, the failure plane is not a horizontal rupture. Instead, it is a diagonal failure which is similar to the failure mode under triaxial compression. Hence, ϕ' cannot be interpreted by Eq. (3.1) for the specimen confined by a constant cell pressure (Joer et al., 2011). However, simple shear test aims to test a thin layer of soil which is essentially sheared horizontally (Bjerum and Landva, 1966). It is argued that if the lateral confinement cannot lead to a horizontal rupture plane, the lateral confinement does not provide the correct boundary condition for a simple shear test.

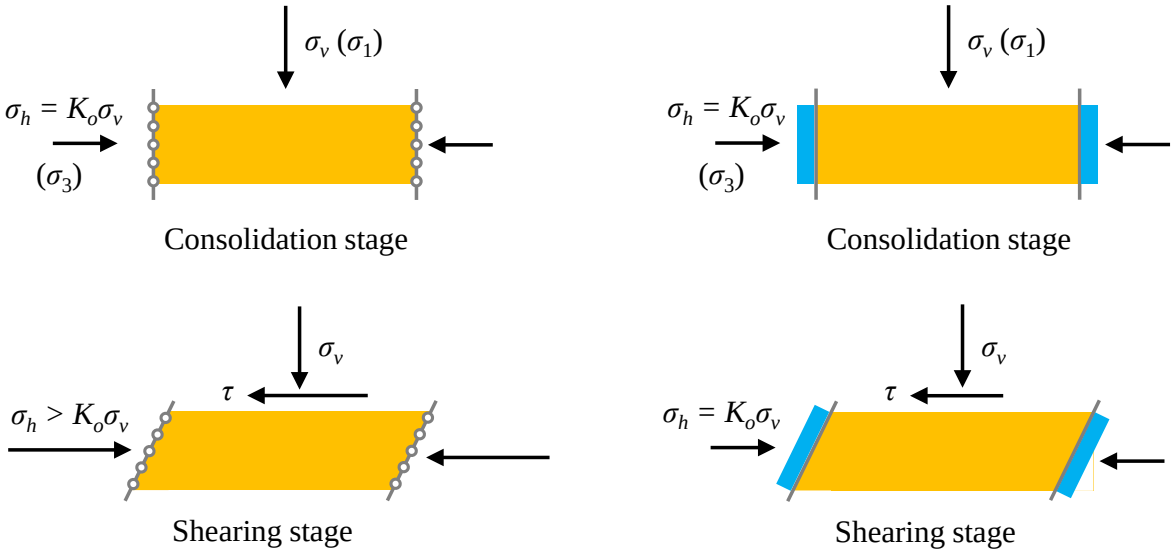

(a) Rigid confinement (reinforced membrane or stacked rings)

(b) Flexible confinement (cell pressure)

Figure 3.7 Illustration of horizontal and vertical stresses for different confinement methods

3.4.3 Choice of the Lateral Confinement Method

For the cyclic simple shear test conducted at small shear strain (e.g., $\gamma \leq 1\%$), K_o cell pressure with latex membrane can generally provide effective lateral confinement. If reinforced membrane is used as lateral confinement, good contact between the reinforced membrane and soil needs to be ensured before the shearing test, otherwise the shear modulus may be underestimated, especially at the first few cycles. For a monotonic drained simple shear test, the constant cell pressure with latex membrane could not ensure plane strain condition and lead to lower peak shear stress. As a result, shear strength parameters are underestimated. Hence, for the subsequent cyclic and monotonic simple shear tests described in Section 3.5, reinforced membrane and K_o cell pressure were applied together, consequently these two confinement methods can complement each other in providing effective lateral confinement at the beginning of the cyclic simple shear test and plane strain condition in the monotonic simple shear test.

3.5 Effect of Cyclic Loading on Shear Strength of Unsaturated soils

3.5.1 Test Materials and Procedure

In Singapore two thirds of the land area is covered by residual soils, and the residual soils at shallow depth are usually unsaturated (Chin, 2011). The soil tested is a residual soil from the Bukit Timah Granite taken from a construction site in the northern part of Singapore. The basic soil properties are: liquid limit LL = 59%, plastic limit PL = 34%, plasticity index I_P = 25% and specific gravity G_S = 2.64. The soil is categorized as MH according to the USCS classification. The grain size distribution of the soil is shown in Figure 3.8. The soil consists of 47% sand, 37%

silt and 16% clay. The standard Proctor compaction curve of the residual soil is shown in Figure 3.9. The optimum water content is 22.5% and the maximum dry density is 1.56 Mg/m^3.

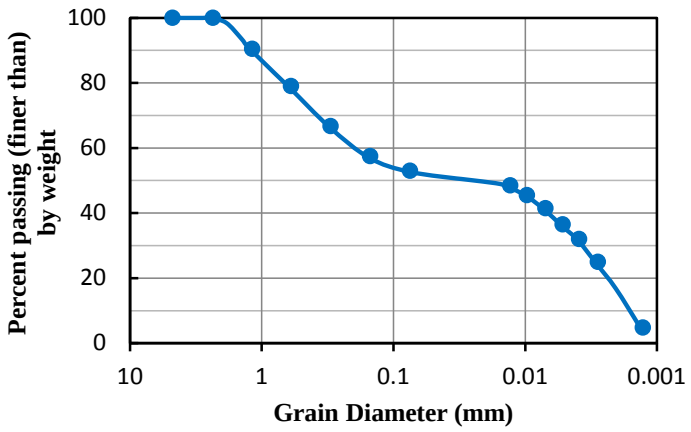

Figure 3.8 Grain size distribution of the residual soil

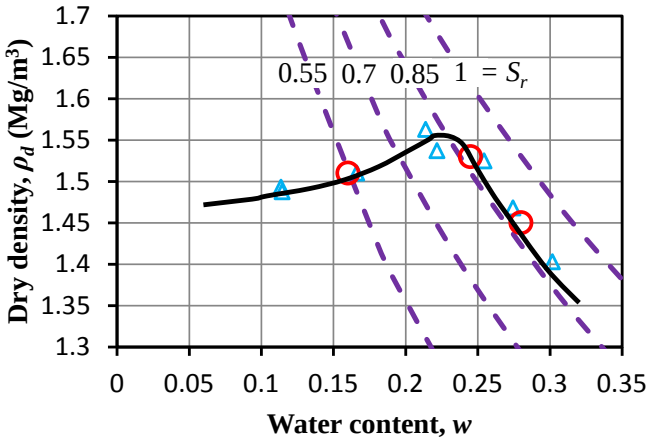

Figure 3.9 Compaction curve of the residual soil

The soil was air-dried first, and then sieved through a No. 4 Sieve. The target water contents of the compacted soil specimens were 16.2%, 24.5% and 27.2%; hence, the soil specimens were tested at both dry and wet of optimum. The soils were mixed with given amount of water and cured at least one day in a zip-locked bag placed in a humidity cupboard for moisture

equilibrium. The soil specimens were prepared by static compaction, and the dry densities were determined from the standard Proctor curve, as shown by the circles in Figure 3.9. The height of the specimen is about 20 mm, and the diameter is 71 mm.

The compacted soil specimens were tested under constant water content and constant vertical stress conditions. The reason to adopt constant water content and constant vertical stress is that these conditions replicate field conditions more realistically. The reinforced membrane and K_o cell pressure were applied together as previously explained. All the specimens were consolidated and tested under vertical stress of 100 kPa and cell pressure of 50 kPa (pilot tests showed that ϕ' of the compacted soil is about 30°, therefore $K_o = 1 - \sin\phi' = 0.5$). After the consolidation, strain-controlled cyclic simple shear tests were performed first. Cyclic simple shear tests on compacted soils were commonly conducted with 25 – 40 cycles of sinusoidal cyclic loading at a frequency of 0.3 – 1 Hz (Chu and Vucetic, 1991; Whang et al., 2004). In this study, the specimens were subjected to 50 cycles of sinusoidal cyclic loading at a frequency of 0.5 Hz. Besides, the cyclic shear strain of 1% was selected. According to Makdisi and Seed (1978), cyclic shear strain of 1% could be considered as the maximum strain that could be induced by a magnitude 8.25 earthquake with a base acceleration of 0.75g.

After the cyclic simple shearing stage, the specimens were subjected to monotonic simple shearing. The obtained shear strength is considered as post-cyclic static shear strength. As a reference, monotonic simple shear tests were conducted on compacted soil specimens prepared at the same initial dry densities and moisture contents. The obtained shear strength is considered

as the static shear strength. All the monotonic simple shear tests were conducted at a strain rate of 5%/min, as suggested by Thiers and Seed (1969) for the testing of silty clay.

3.5.2 Results of Cyclic Simple Shear Tests

The cyclic shear stress-strain loops at cycle number N = 1, 5 and 50 for various compacted water contents are show in Figure 3.10. With the increase in number of cycles, the stress-strain loop becomes increasingly steeper. The shear modulus and vertical strain for various compaction water content are shown in Figure 3.11. The shear modulus was calculated as per ASTM D6528-07. Figures 3.11(a) and 3.11(b) show that the shear modulus and vertical strain increase with the increase in number of cycles regardless of the compaction water content. The increase of shear modulus is especially obvious in the first 5 cycles, as revealed in both Figures 3.10 and 3.11(a). The majority of the vertical strain occurs during the first 10 cycles. Similar observation was made by Whang et al. (2004).

The soil compacted at w = 24.5% shows higher shear moduli and higher vertical strains than the soil compacted at w = 27.2%. The soils compacted at w = 24.5% and w = 27.2% have similar degree of saturation ($S_r \approx 0.9$ in Figure 3.9), hence the higher shear moduli may be mainly attributed to the higher dry density. The soil compacted at w = 16.2% (dry of optimum) was expected to have higher shear moduli and larger vertical strains than the soils compacted at w = 24.5% and w = 27.2%, as the former has higher suction (i.e., higher shear strength) and more voids filled with air (i.e., higher compressibility) (Whang et al., 2004). The soils compacted at w = 16.2% only shows slightly higher shear moduli [Figure 3.11(a)] and much less vertical strain than the soils compacted at other water contents [Figure 3.11(b)]. These phenomena can be

attributed to the fact that the soils compacted at w = 16.2% were very stiff, and they may have experienced boundary sliding during the cyclic and monotonic shearing. More detailed discussion is given below.

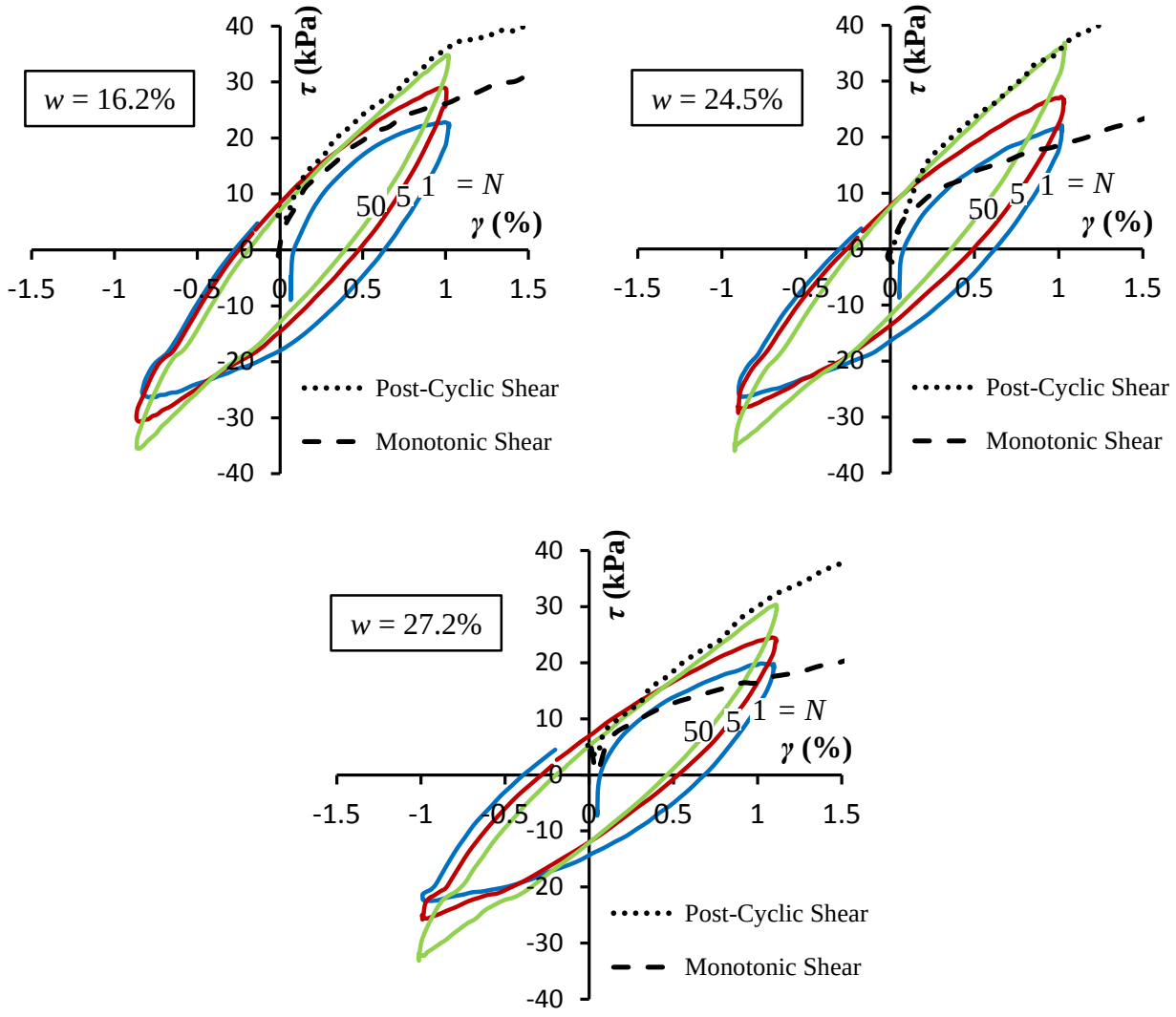

Figure 3.10 Cyclic shear stress-strain loops

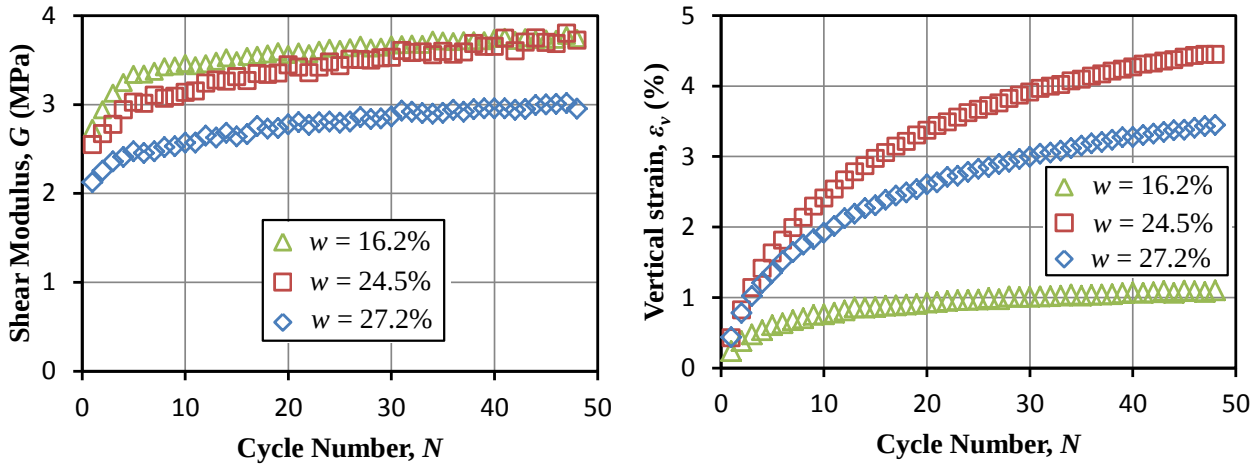

(a) Shear modulus (b) Vertical strain

Figure 3.11 Shear modulus and vertical strain for different compacted water contents

3.5.3 Results of Post-Cyclic Monotonic Simple Shear Tests

The results of post-cyclic monotonic simple shear tests and monotonic simple shear tests on compacted soil specimens are shown in Figure 3.10 for the small shear strain range (γ = 0 ~ 1.5%), and shown in Figure 3.12 for the full shear strain range (γ = 0 ~ 25%).

Figure 3.10 shows that the initial portion of the stress-strain curve for post-cyclic monotonic shearing would merge with the first quarter of the cyclic stress-strain loop at the last cycle (N = 50) of cyclic shearing, while the stress-strain curve for the monotonic shearing of intact samples would agree closely with the first quarter of the cyclic stress-strain loop at N = 1. For w = 24.5% and 27.2%, cyclic shear stresses at N = 1 and γ = 1% are slightly larger than the corresponding monotonic shear stresses, which can be attributed to the fact that cyclic simple shear test has a higher loading rate (equivalent to 24 mm/min) than the monotonic simple shear test (1 mm/min). For w = 16.2%, the cyclic shear stress at N = 1 and γ = 1% is slightly lower than the

corresponding monotonic shear stress. This phenomenon reveals that boundary slippage may have occurred during the cyclic shearing stage, as slippage is more likely to occur at a higher loading rate and leads to a lower measured shear stress.

Figure 3.12 shows that the post-cyclic monotonic shear strength for w = 24.5% and 27.2% are larger than the corresponding monotonic shear strength, as the unsaturated compacted soil specimens have been further compacted during the cyclic shearing. For w = 16.2%, at small shear strain (e.g., $\gamma \leq 1\%$) the post-cyclic monotonic simple shearing still mobilizes higher shearing stress than the monotonic simple shearing, while the difference becomes increasingly smaller with further increase in shear strain. At large shear strain ($\gamma \geq 10\%$) the difference is essentially zero, which reveals that the soil specimens for both post-cyclic monotonic and monotonic simple shear experienced pure boundary sliding due to the high stiffness of the specimen.

The soil specimen for w = 16.2% after the cyclic and monotonic shearing is shown in Figure 3.13. It can be seen that the specimen remains intact and no rupture plane can be found. If the soil specimen has experienced simple shear with a strain up to 25%, a rupture plane should have been shown. The intact specimen supports the speculation that stiff specimen mainly experienced boundary slippage during the cyclic and monotonic shearing.

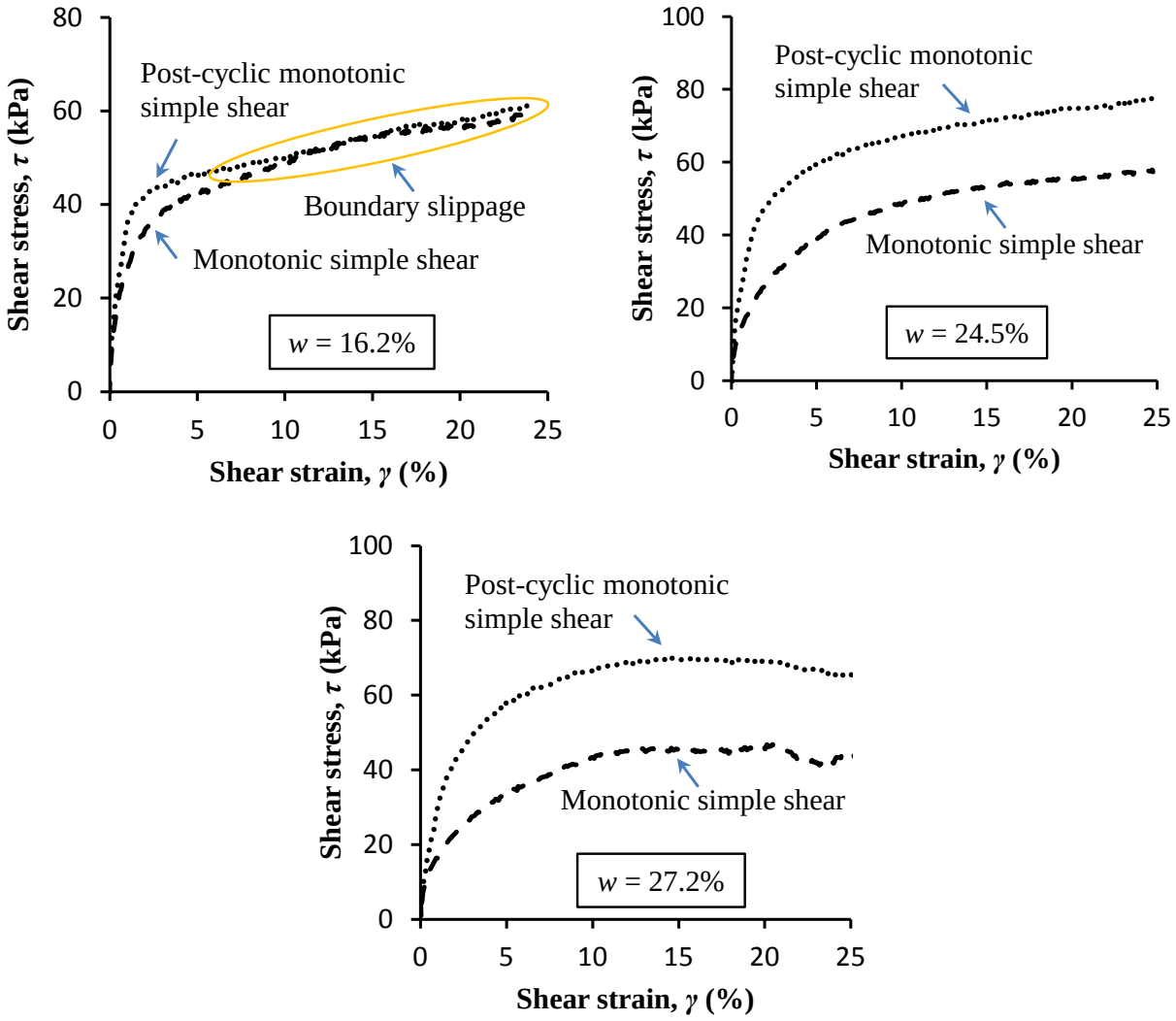

Figure 3.12 Post-cyclic monotonic and monotonic simple shear tests

Figure 3.13 Soil specimen (w = 16.2%) after the cyclic and monotonic shearing

Two monotonic simple shear tests were conducted on the same soil compacted at w = 16% and 12% to further investigate the slippage during monotonic shearing. As shown in Figure 3.14, the shear stress-strain curves for w = 16% essentially merges with the shear stress-strain curve for w = 12%. If the shearing occurred between soil particles, the test results should have been affected by the compacted water content of the soil specimen. However, the test results are independent of the compacted water content, which reveals that the shearing occurred at the boundary between the soil and the platens rather than the internal shearing between soil particles.

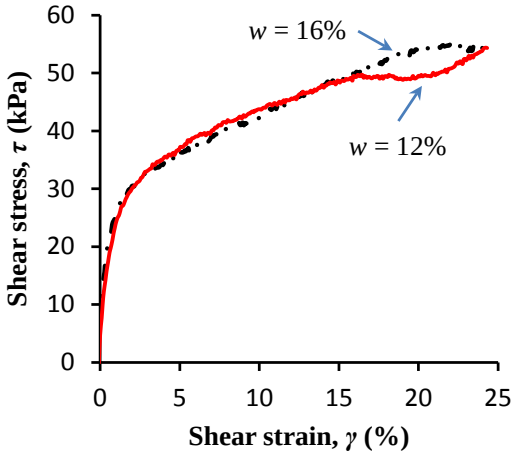

Figure 3.14 Monotonic simple shear tests for soils compacted dry of optimum

3.6 Shear Strength Parameters for Seismic Slope Stability Analysis

Static shear strength is more commonly measured than dynamic shear strength. However, dynamic shear strength should be the one being used in a seismic stability analysis. The relationship between static and dynamic shear strengths of saturated soils has been widely investigated (e.g., Makdisi and Seed, 1978; Lefebvre and Pfendler, 1996; Duncan et al., 2014). By knowing the relationship and static shear strength, dynamic shear strength can readily be

estimated. Federal Highway Administration (FHWA, 2011) suggested that for saturated cohesive soils the static undrained strength is generally considered to be an upper bound of the undrained strength that should be used in a seismic stability analysis, and for saturated cohesive soils of low to intermediate sensitivity the static shear strength may be reduced by 10-15% to account for the strength degradation in large magnitude earthquakes ($M > 7$).

Unsaturated soils would experience hardening rather than degradation under cyclic loading, as has been found by other researchers (e.g., Chu and Vucetic, 1992; Ishihara, 1996; Whang et al., 2004) and in this study. Hence, it may be concluded that for unsaturated soils the static shear strength can be considered as a lower bound on the dynamic strength that should be used in a seismic stability analysis.

3.7 Summary

Simple shear apparatus was used to investigate the effect of cyclic loading on the shear strength of unsaturated soils. There are several lateral confinement methods for the simple shear tests. Hence, the effect of lateral confinement methods was investigated first in order to choose the right lateral confinement method. It was found that constant cell pressure may not provide sufficient lateral confinement and underestimate shear strength parameters for monotonic drained simple shear test at large strain level. For the cyclic simple shear test at small shear strain level, the shear modulus may be underestimated if the soil specimen was confined by reinforced membrane due to the poor contact condition between soil specimen and reinforced membrane. Hence, in this study the soil specimens were confined by both reinforced membrane and cell pressure, so that these two confinement methods can complement each other. The cyclic simple

shear tests on unsaturated residual soil shows that unsaturated soil would experience hardening under cyclic loading. In the strain-controlled cyclic simple shear tests, both the shear modulus and the vertical strain increase with the increase in number of cycles. The increase in shear modulus is especially obvious in the first five cycles, and the majority of the vertical strain accumulates during the first 10 cycles. Due to the densification caused by the cyclic shearing, post-cyclic monotonic shear strength is larger than the monotonic shear strength. Hence, for unsaturated soils the static shear strength can be considered as a conservative estimate to the dynamic strength that should be used in a seismic stability analysis.

Chapter 4: Upper Bound Limit Analysis

Upper bound limit analysis has been widely used to develop slope stability charts for dry and saturated soil slopes, as shown in Tables 2.2 and 2.3, due to its sound theoretical basis and high computational efficiency (Chen, 1975; Michalowski, 1995; Chen et al., 2001). This chapter presents the methodology for conducting upper bound limit analysis on unsaturated soil slopes based on rotational and translational failure mechanisms. The proposed methodology will be used to develop slope stability charts and equations shown in Chapters 5 and 6. In the following sections, the conventional log-spiral upper bound limit analysis for dry and saturated soil slopes is reviewed first. The analysis is then extended to incorporate matric suction and rainfall infiltration for the analysis of unsaturated soil slopes. In addition, a kinematically admissible failure mode, which can consider the boundary resistance of a translational slip, is proposed to analyze the translational failure. Finally, a procedure that can be efficiently used to produce slope stability charts is suggested.

4.1 Conventional Log-Spiral Upper Bound Limit Analysis

In the upper bound limit analysis, the soil is assumed to be perfectly plastic and the deformation is assumed to follow the associated flow rule (Chen, 1975). Kinematic admissibility requires that the velocity jump vector at the slip surface must be inclined to the slip surface at an angle ϕ' (effective friction angle of the soil). Two kinematically admissible failure modes (i.e., wedge failure and log-spiral rotational failure) which were first proposed by Drucker and Prager (1952) are shown in Figures 4.1(a) and (b). In Figure 4.1(b), the log-spiral slip surface can be described

by Eq. (4.1), in which $r(\theta)$ is the radius of the log-spiral at angle θ, r_o is the initial radius, θ_o and θ_h are the initial and final angles of the log-spiral, respectively. For a homogeneous slope, rotational failure is always more critical than wedge failure (Taylor, 1948; Chen, 1975) and log-spiral slip surface is the most efficient slip surface, which can be justified by upper bound plasticity theorem (Chen, 1975) and variational calculus (Baker and Garber, 1978).

$$r(\theta) = r_o \exp\left[(\theta - \theta_o)\tan\phi'\right] \tag{4.1}$$

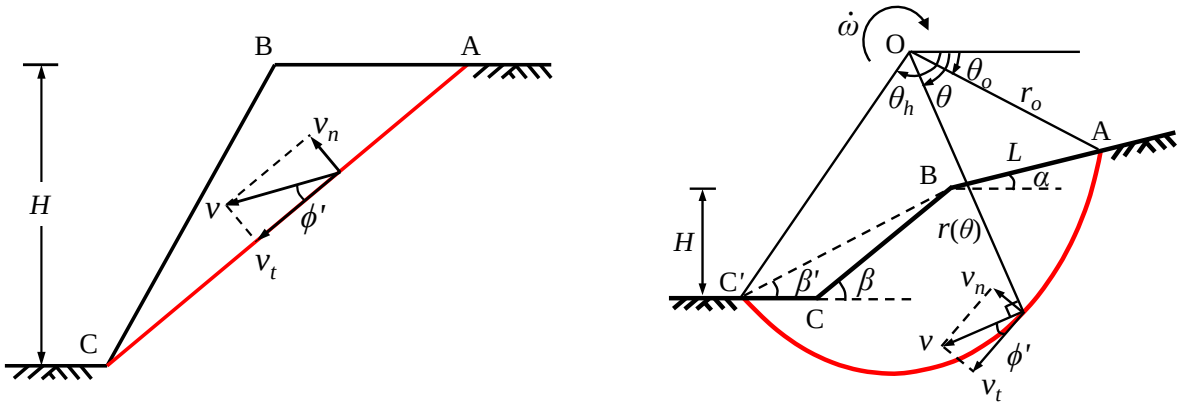

(a) Wedge failure (b) Log-spiral rotational failure

Figure 4.1 Wedge failure and log-spiral rotational failure [(a) is modified from Drucker and Prager (1952), (b) is modified from Chen (1975)]

Soil mass would fail if the rate of work done by external forces exceeds the rate of internal energy dissipation. Hence, equating the rate of work done by external force $\dot{W}_{\text{ext}}$ to the rate of internal energy dissipation $\dot{D}_{\text{int}}$ gives an unsafe upper bound on the collapse or limit load (Chen, 1975):

$$\dot{W}_{\text{ext}} = \dot{D}_{\text{int}} \tag{4.2}$$

4.1.1 Dry Soil Slopes

For a dry soil slope with soil weight as the only external force, Eq. (4.2) can be written as:

$$\dot{W}_\gamma = \dot{D}_{\text{int}} \tag{4.3}$$

where $\dot{W}_\gamma$ is the rate of work done by soil weight. The calculation procedures of $\dot{W}_\gamma$ and $\dot{D}_{\text{int}}$ can be found in Chen (1975) and the final expressions are shown below:

$$\dot{W}_\gamma = \int_A \boldsymbol{\gamma} \bullet \mathbf{v} \mathrm{d}A = \dot{\omega}\gamma r_o^3 \left(f_1 - f_2 - f_3 - f_4 \right) \tag{4.4}$$

$$\dot{D}_{\text{int}} = \int_S c' v_t \mathrm{d}S = \frac{c' \dot{\omega} r_o^2}{2 \tan \phi'} \left\{ \exp\left[2\left(\theta_h - \theta_o \right) \tan \phi' \right] - 1 \right\} \tag{4.5}$$

where A denotes the cross-sectional area of the failing soil mass, S denotes the slip surface, $\boldsymbol{\gamma}$ is the unit weight vector, $\mathbf{v}$ is the velocity jump vector, v_t is the tangential component of the velocity jump vector, γ is the unit weight of the soil, c' is the effective cohesion of the soil, $\dot{\omega}$ is the rate of rotation of the failing soil mass, the functions f_1, f_2, f_3 and f_4 are defined as (Chen, 1975):

$$f_1 = \frac{1}{3\left(1 + 9\tan^2 \phi'\right)} \left\{ \left(3\tan\phi' \cos\theta_h + \sin\theta_h \right) \exp\left[3\left(\theta_h - \theta_o \right) \tan\phi' \right] - \left(3\tan\phi' \cos\theta_o + \sin\theta_o \right) \right\} \tag{4.6}$$

$$f_2 = \frac{1}{6}\frac{L}{r_o} \left(2\cos\theta_o - \frac{L}{r_o}\cos\alpha \right) \sin\left(\theta_o + \alpha \right) \tag{4.7}$$

$$f_3 = \frac{1}{6} \exp\left[\left(\theta_h - \theta_o \right) \tan\phi' \right] \left[\sin\left(\theta_h - \theta_o \right) - \frac{L}{r_o} \sin\left(\theta_h + \alpha \right) \right] \left\{ \exp\left[\left(\theta_h - \theta_o \right) \tan\phi' \right] \cos\theta_h + \cos\theta_o - \frac{L}{r_o}\cos\alpha \right\} \tag{4.8}$$

$$f_4 = \frac{1}{2} \left(\frac{H}{r_o} \right)^2 \frac{\sin\left(\beta - \beta' \right)}{\sin\beta \sin\beta'} \left(\cos\theta_o - \frac{L}{r_o}\cos\alpha - \frac{1}{3}\frac{H}{r_o} \left(\cot\beta' + \cot\beta \right) \right) \tag{4.9}$$

From Eq. (4.7) to Eq. (4.9), L/r_o and H/r_o are further calculated by:

$$\frac{L}{r_o}=\frac{\sin\left(\beta'+\theta_o\right)}{\sin\left(\beta'-\alpha\right)}-\frac{\sin\left(\beta'+\theta_h\right)}{\sin\left(\beta'-\alpha\right)}\exp\left[\left(\theta_h-\theta_o\right)\tan\phi'\right] \tag{4.10}$$

$$\frac{H}{r_o}=\frac{\sin\beta'}{\sin\left(\beta'-\alpha\right)}\left\{\sin\left(\theta_h+\alpha\right)\exp\left[\left(\theta_h-\theta_o\right)\tan\phi'\right]-\sin\left(\theta_o+\alpha\right)\right\} \tag{4.11}$$

Substituting Eqs. (4.4) and (4.5) to Eq. (4.3) gives:

$$\frac{\gamma H}{c'}=\frac{H}{r_o}\frac{\exp\left[2\left(\theta_h-\theta_o\right)\tan\phi'\right]-1}{2\tan\phi'\left(f_1-f_2-f_3-f_4\right)} \tag{4.12}$$

Minimum value of $\gamma H/c'$ can be obtained for given α, β and ϕ' through optimization, with θ_o, θ_h and β' being the variables. Stability charts for dry soil slopes developed based on Eq. (4.12) can be found in Chen et al. (1969) and Chen (1975).

4.1.2 Dry Soil Slopes under Seismic Loading

The effect of seismic loading on slope stability can be analyzed through a pseudo-static approach (Terzaghi, 1950), namely that a horizontal pseudo-static force k_hW (k_h is the pseudo-static coefficient, W is the weight of the failure mass) which try to pull the soil away from the slope is imposed on the slope. Chang et al. (1984) incorporated the pseudo-static force into the log-spiral upper bound limit analysis, and Eq. (4.3) is modified to be:

$$\dot{W}_\gamma+\dot{W}_s=\dot{D}_{\text{int}} \tag{4.13}$$

where $\dot{W}_s$ is the rate of work done by pseudo-static force, and it can be calculated by:

$$\dot{W}_s=\int_A \mathbf{k_h}\gamma\bullet\mathbf{v}\mathrm{d}A=\dot{\omega}\gamma r_o^3k_h\left(f_1^s-f_2^s-f_3^s-f_4^s\right) \tag{4.14}$$

The functions f_1^s, f_2^s, f_3^s and f_4^s in Eq. (4.14) can be calculated by (Chang et al., 1984):

$$f_1^s = \frac{1}{3\left(1+9\tan^2\phi'\right)}\left\{\left(3\tan\phi'\sin\theta_h-\cos\theta_h\right)\exp\left[3\left(\theta_h-\theta_o\right)\tan\phi'\right]-3\tan\phi'\sin\theta_o+\cos\theta_o\right\} \tag{4.15}$$

$$f_2^s = \frac{1}{6}\frac{L}{r_o}\left(2\sin\theta_o+\frac{L}{r_o}\sin\alpha\right)\sin\left(\theta_o+\alpha\right) \tag{4.16}$$

$$f_3^s = \frac{1}{6}\exp\left[\left(\theta_h-\theta_o\right)\tan\phi'\right]\left[\sin\left(\theta_h-\theta_o\right)-\frac{L}{r_o}\sin\left(\theta_h+\alpha\right)\right]\left\{\exp\left[\left(\theta_h-\theta_o\right)\tan\phi'\right]\sin\theta_h+\sin\theta_o+\frac{L}{r_o}\sin\alpha\right\} \tag{4.17}$$

$$f_4^s = \frac{1}{2}\left(\frac{H}{r_o}\right)^2\frac{\sin\left(\beta-\beta'\right)}{\sin\beta\sin\beta'}\left(\sin\theta_o+\frac{L}{r_o}\sin\alpha+\frac{2}{3}\frac{H}{r_o}\right) \tag{4.18}$$

The work rate balance equation can finally be written as:

$$\frac{\gamma H}{c'} = \frac{H}{r_o}\frac{\exp\left[2\left(\theta_h-\theta_o\right)\tan\phi'\right]-1}{2\tan\phi'\left[\left(f_1-f_2-f_3-f_4\right)+k_h\left(f_1^s-f_2^s-f_3^s-f_4^s\right)\right]} \tag{4.19}$$

4.1.3 Saturated Soil Slopes

Positive pore-water pressures have been widely incorporated into the upper bound limit analysis (Miller and Hamilton, 1989; Michalowski, 1995; Viratjandr and Michalowski, 2006; Michalowski and Nadukuru, 2013; Gao et al., 2014). If positive pore-water pressure is considered as external force, Eq. (4.2) can be written as:

$$\dot{W}_\gamma + \dot{W}_{u_w} = \dot{D}_{\text{int}} \tag{4.20}$$

where $\dot{W}_{u_w}$ is the rate of work done by positive pore-water pressure, and it can be calculated by (Miller and Hamilton, 1989; Michalowski, 1995):

$$\dot{W}_{u_w} = \int_S u_w v_n \mathrm{d}S \tag{4.21}$$

The final expression of $\dot{W}_{u_w}$ can generally be written as:

$$\dot{W}_{u_w} = \dot{\omega}\gamma r_o^3 f_{u_w} \tag{4.22}$$

and Eq. (4.20) can be rearranged to be:

$$\frac{\gamma H}{c'} = \frac{H}{r_o}\frac{\exp\left[2\left(\theta_h - \theta_o\right)\tan\phi'\right]-1}{2\tan\phi'\left(f_1 - f_2 - f_3 - f_4 + f_{u_w}\right)} \tag{4.23}$$

The f_{u_w} in Eqs. (4.22) and (4.23) is a function related to the rate of work done by pore-water pressure. The f_{u_w} for the two and three-dimensional slope analyses with $u_w = r_u\gamma h$ can be found in Michalowski (1995) and Michalowski and Nadukuru (2013), respectively. The f_{u_w} for the two and three-dimensional slopes subjected to water drawdown can be found in Viratjandr and Michalowski (2006) and Gao et al. (2014), respectively.

4.1.4 Accuracy of Log-Spiral Upper Bound Limit Analysis

The commonly used slope stability analysis methods and their key features are summarized in Table 4.1. In order to examine the accuracy of a stability analysis method, the solution obtained by the method must be compared with the exact solution. Unfortunately, an exact solution is usually not available for a slope stability problem (Michalowski, 1995; Yu et al., 1998). The limit equilibrium methods and finite element method which have been widely used in practice generally do not fulfill the requirements of static and kinematic admissibility, hence the solutions are neither lower bound nor upper bound, and not necesarry between the bounds. The stress field in lower bound limit analysis is statically admissible, and the velocity field in upper bound limit analysis is kinematically admissible. Hence, it is believed that the exact solution is bounded by the lower and upper bound limit analyses from below and above (e.g., Kim et al., 1999).

Yu et al. (1998) and Kim et al. (1999) conducted numerical lower and upper bound limit analyses on dry and saturated soil slopes, respectively. They found that the maximum difference between numerical upper and lower bound solutions is less than 5% if $\beta \leq 45°$ and less than 10% if $\beta > 45°$. The log-spiral upper bound solution is generally less than the numerical upper bound solution (Loukidis et al., 2003; Gao et al., 2013). Hence, the difference between log-spiral upper bound and numerical lower bound solutions would be expected to be smaller.

Loukidis et al. (2003) conducted pseudo-static analysis for simple homogeneous slopes using all the methods listed in Table 4.1. They found that the yield coefficients and slip surfaces obtained by the various methods are in excellent agreement. The difference of the yield coefficients obtained by numerical upper and lower bound analyses is less than 8%, 12% and 20% for β = 20°, 30° and 45°, respectively. The yield coefficients obtained by log-spiral upper bound are generally the average of the numerical bounds, or closer to the numerical lower bound. The difference between log-spiral upper bound and numerical lower bound solutions is less than 4%, 6% and 6% for β = 20°, 30° and 45°, respectively. Besides, very close solutions are shown between log-spiral upper bound and Spencer's method.

Gao et al. (2013) presented stability curves for three-dimensional homogeneous slopes obtained by log-spiral upper bound, numerical lower and upper bound. The stability curves developed by log-spiral upper bound are generally in the middle of the stability curves developed by numerical lower and upper bounds, or slightly closer to the stability curves developed by numerical lower bound.

Table 4.1 Comparison of slope stability analysis methods (from Sloan, 2013)

Property	Limit equilibrium analysis	Upper bound limit analysis	Lower bound limit analysis	Displacement finite element analysis
Assumed failure mechanism?	Yes	Yes	-	No
Equilibrium satisfied everywhere?	No (globally)	-	Yes	No (nodes only)
Flow rule satisfied everywhere?	No	Yes	-	No (integration points only)
Complex loading and boundary conditions possible?	No	Yes	Yes	Yes
Complex soil models possible?	No	No	No	Yes
Coupled analysis possible?	No	No	No	Yes
Error estimate?	No	Yes (with LB)	Yes (with UB)	No

Statically admissible stress field usually needs to be constructed numerically, while kinematically admissible velocity field can be constructed analytically (e.g., log-spiral failure mechanism). Therefore, upper bound limit analysis is more widely used than the lower bound limit analysis (Chen, 1975). In the upper bound limit analysis, the failure mass satisfies both force and moment equilibrium. Hence, an upper bound limit analysis solution can be considered as a special limit equilibrium solution, but not vice versa (Chen, 1975; Michalowski, 1989). The efficiency of log-spiral failure mechanism for homogeneous slopes has been proven by Chen (1975) using plasticity theorem and Baker and Garber (1978) through variational calculus. It is generally believed that the log-spiral upper bound solution is very close to the exact solution for a homogenous slope, and log-spiral upper bound limit analysis is commonly used to benchmark

the limit equilibrium methods (e.g., Michalowski, 1995) and finite element method (e.g., Dawson et al., 1999).

4.2 Extended Log-Spiral Upper Bound Limit Analysis of Unsaturated Soil Slopes

In order to extend the log-spiral upper bound limit analysis for unsaturated soil slopes, the equation to calculate the rate of work done by negative pore-water pressure is derived, rational pore-water pressure profiles for unsaturated soil slopes before and after rainfall infiltration are suggested, and the work rate balance equations are established.

4.2.1 Rate of Work Done by Negative Pore-Water Pressure

The equation to calculate the rate of work done by positive pore-water pressure has been provided by Miller and Hamilton (1989) and Michalowski (1995), as shown in Eq. (4.21). The equation to calculate the rate of work done by negative pore-water pressure, which has not been given in the literature, is first derived in this study. It is demonstrated below that both positive and negative pore-water pressures can be considered in the same framework.

For saturated soils, the shear strength can be described using the Mohr-Coulomb failure criterion and the effective stress concept (Terzaghi, 1943):

$$\tau = c' + \left(\sigma - u_w\right)\tan\phi' \quad (u_w \geq 0) \tag{4.24}$$

where τ is the shear strength, c' is the effective cohesion, σ is the normal stress and u_w is the pore-water pressure.

For unsaturated soils, the shear strength can be determined by the extended Mohr-Coulomb failure criterion (Fredlund et al., 1978):

$$\tau = c' + (\sigma - u_a)\tan\phi' + (u_a - u_w)\tan\phi^b \quad (u_w < 0) \tag{4.25a}$$

where u_a is the pore-air pressure, and ϕ^b is an angle which indicates the rate of increase in shear strength relative to matric suction (u_a - u_w). If u_a is considered to be atmospheric pressure and equal to zero, Eq. (4. 25a) can be rearranged to be:

$$\tau = c' + \sigma\tan\phi' - u_w\tan\phi^b \quad (u_w < 0) \tag{4.25b}$$

The original equation to calculate $\dot{D}_{\text{int}}$ given by Drucker and Prager (1952) and Chen (1975) is:

$$\dot{D}_{\text{int}} = \int_S (\tau v_t - \sigma v_n)\mathrm{d}S \tag{4.26}$$

where v_t and v_n are the tangential and normal components of the velocity jump vector at the slip surface, respectively.

Substitution of Eqs. (4.24) and (4.25b) into Eq. (4.26) gives:

$$\dot{D}_{\text{int}} = \begin{cases} \int_S (c' v_t - u_w v_n)\mathrm{d}S, (u_w \geq 0) & \text{(4.27a)} \\ \int_S \left(c' v_t - \dfrac{\tan\phi^b}{\tan\phi'} u_w v_n\right)\mathrm{d}S, (u_w < 0) & \text{(4.27b)} \end{cases}$$

In the formulation of upper bound limit analysis, pore-water pressure u_w can be considered as either part of the system or external to the system (Miller and Hamilton, 1990). In the first approach, u_w leads to internal energy dissipation [Eq. (4.27)] and the work rate balance equation is written as Eq. (4.3). In the second approach, u_w is considered as external force (buoyancy and seepage), and the work rate balance equation is written as:

$$\dot{W}_\gamma + \dot{W}_{u_w} = \dot{D}_{c'} \tag{4.28}$$

where $\dot{W}_{u_w}$ and $\dot{D}_{c'}$ can be calculated by Eq. (4.29) and Eq. (4.30), respectively.

$$\dot{W}_{u_w} = \begin{cases} \int_S u_w v_n \mathrm{d}S, u_w \geq 0 & \text{(4.29a)} \\ \int_S \frac{\tan\phi^b}{\tan\phi'} u_w v_n \mathrm{d}S, u_w < 0 & \text{(4.29b)} \end{cases}$$

$$\dot{D}_{c'} = \int_S c' v_t \mathrm{d}S \quad \text{(4.30)}$$

If u_w is considered as part of the system, positive u_w in Eq. (4.27a) produces negative energy dissipation. Similarly, negative u_w in Eq. (4.29b) produces negative work rate if it is considered as external force. The terms of negative energy dissipation and negative work rate may lead to physical disputes (Miller and Hamilton, 1990; Michalowski, 1995). Hence, it may be more physically correct to treat positive u_w as external force [Eq. (4.29a)] and negative u_w as internal force [Eq. (4.27b)]. However, the work rate balance equations and the solutions are identical whether u_w is considered as internal or external to the system (Miller and Hamilton, 1990), as the term that considers u_w has a negative sign [Eq. (4.27)] if it appears on the right-hand side of the work rate balance equation [Eq. (4.3)] and the sign changes to positive if the term is moved to the left-hand side [Eq. (4.28)]. Positive pore-water pressure is commonly treated as external force and the work rate balance equation is written as Eq. (4.28) in the literature (Michalowski, 1995; Kim et al., 1999; Viratjandr and Michalowski, 2006; Michalowski and Nadukuru, 2013; Gao et al., 2014). In order to simplify the derivation and to be consistent with the existing literature, both positive and negative u_w are considered as external force in this study.

4.2.2 Pore-Water Pressure Profiles

For an unsaturated soil slope which is currently stable, the soil in the slope has undergone numerous cycles of wetting and drying (e.g., infiltration and evaporation, rise and fall of the

groundwater table). Due to rainwater percolation and/or elevated groundwater table in the past, the relationship between degree of saturation and negative pore-water pressure (matric suction) of the soil above the groundwater table is more likely to be governed by a drainage process (e.g., Lambe, 1951).

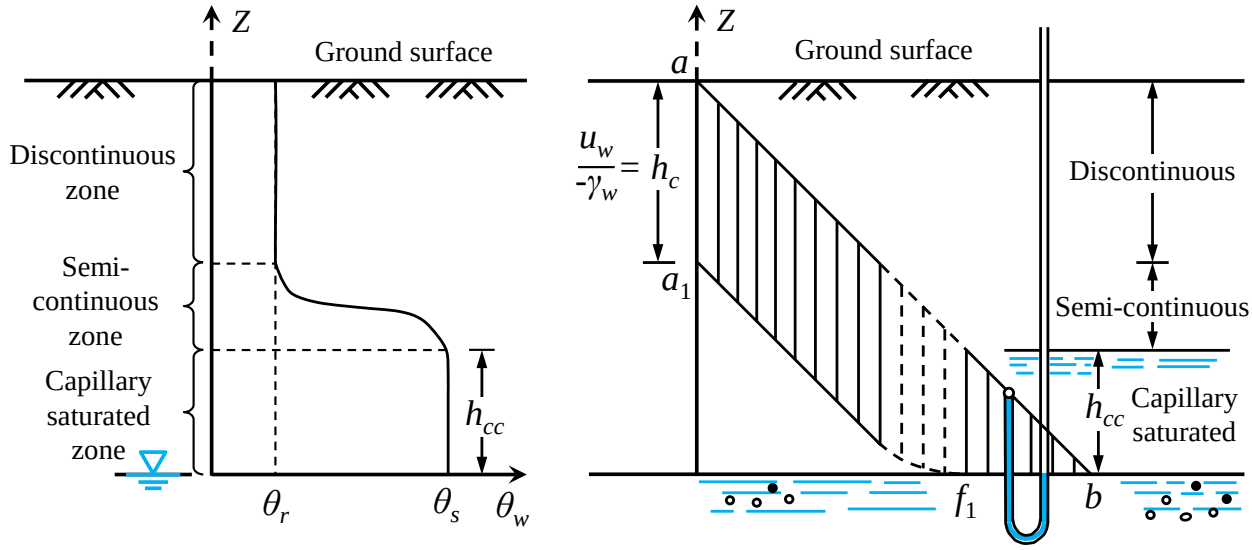

(a) Water content distribution (b) Pore-water pressure distribution

Figure 4.2 Water content and pore-water pressure distribution in the soil after drainage (modified from Terzaghi, 1943)

Figure 4.2(a) shows the distribution of water in the soil after drainage. The ground can be categorized into three zones (Terzaghi, 1943): capillary saturated zone, in which all the pores are filled with water; semi-continuous zone, in which only the narrowest pore channels and the grooves between the grains are filled with water; and discontinuous zone, in which the pores are filled with discontinuous moisture. The thickness of the capillary saturated zone h_{cc} depends on

the largest pore in the soil, while the distance from the groundwater table to the top of the semi-continuous zone is controlled by the smallest pore in the soil.

In Figure 4.2(b), the pore-water pressure distribution in the soil is visualized by making a section *ab* which is inclined to the horizontal at an angle of 45°. The pore-water pressure heads are equal to the vertical distances between *ab* and a_1f_1b. In the capillary saturated zone, the pore-water pressure increases hydrostatically. In the discontinuous zone the pore-water pressure is relatively constant and equals to $-\gamma_w h_c$ ($h_c > h_{cc}$), this was first found by Terzaghi (1943) through laboratory determination of the apparent cohesion of drained sand, and has been widely confirmed by field monitoring of matric suction at the shallow depth (e.g., Rahardjo et al., 2000; Zhan et al., 2007; Tu et al., 2009). In the semi-continuous zone, the pore-water pressure would gradually transit from $-\gamma_w h_{cc}$ to $-\gamma_w h_c$.

The supplement of rainwater would produce a wetting front and change the pore-water pressure distribution in the soil. The depth of wetting front is a function of rainfall intensity, rainfall duration and soil hydrological properties, and it can readily be estimated by conceptual infiltration models (Green and Ampt, 1911; Lumb, 1962; Mein and Larson, 1973; Sun et al., 1998), as reviewed in Section 2.2.3.1. The idealized pore-water pressure profiles a, b and c for the soil above the wetting front suggested by Rahardjo et al. (1995) are shown in Figure 4.3. Profile a represents the situation where the matric suction is reduced to zero at the ground surface and increases with depth until it reaches the initial hydrostatic (Figure 4.3a) or constant matric suction (Figure 4.3b) at the wetting front. Profile b represents the situation where matric suction above the wetting front is reduced to zero. Profile c corresponds to the situation where a perched

water table is generated over the wetting front. Research shows that profile a tends to occur in fine-grained soils, profile b tends to occur in coarse-grained soils (Zhang et al., 2004; Lee et al., 2009) and profile c tends to occur in layered soils with a permeable layer above the wetting front and a less permeable layer below the wetting front (Cho, 2009).

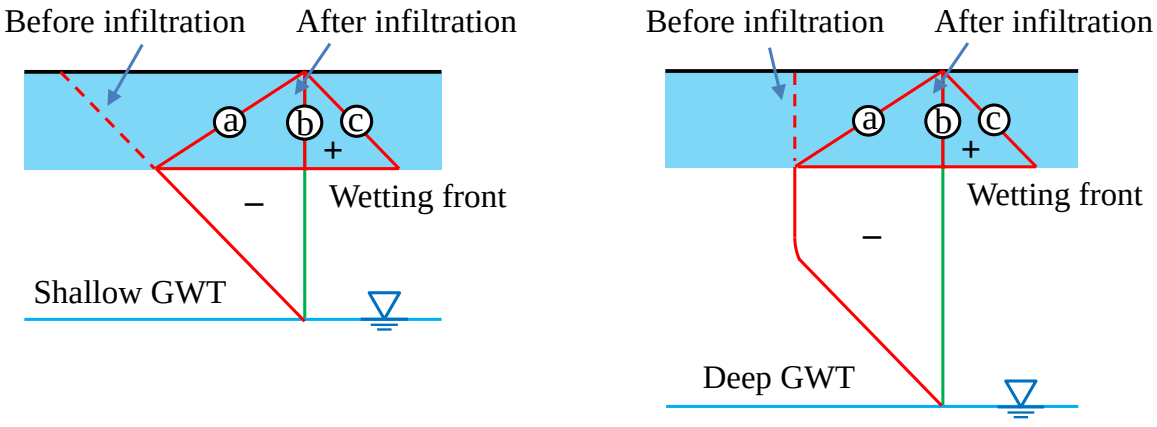

(a) Shallow groundwater table (GWT) (b) Deep groundwater table (GWT)

Figure 4.3 Pore-water pressure profiles a, b and c (modified from Rahardjo et al., 1995)

Based on the pore-water pressure profiles conceptualized in Figures 4.2 and 4.3, the geometry of an unsaturated soil slope under rainfall is shown in Figure 4.4. The groundwater table of an unsaturated soil slope is generally below the toe of the slope and can be approximated by a plane (Zhang et al., 2004; Rahardjo et al., 2007; Tu et al., 2009). The vertical distance between the toe of the slope and the groundwater table is denoted as H_{wt} and the inclination of the groundwater table is denoted as i. Under rainfall infiltration, a distinct wetting front which is parallel to the ground surface with depth z_w is assumed. Although some soils may not have a distinct wetting front, the assumption is useful due to its simplicity and satisfactory results have been obtained with the assumption (e.g., Green and Ampt, 1911; Mein and Larson, 1973; Pradel and Raad,

1993). The pore-water pressure above the wetting front is assumed to be zero (profile b in Figure 4.3), which is a reasonable assumption for coarse-grained soils and conservative for fine-grained soils (Zhang et al., 2004; Lee et al., 2009).

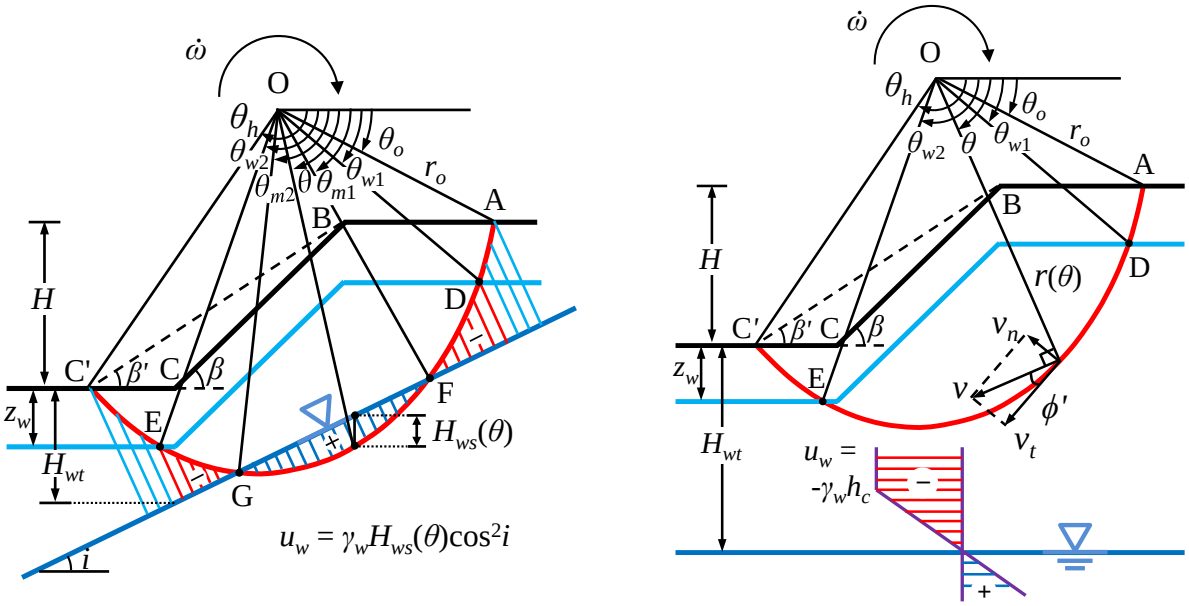

(a) Hydrostatic pore-water pressure (b) Constant negative pore-water pressure

Figure 4.4 Rotational failure of an unsaturated soil slope under rainfall infiltration

4.2.3 Work Rate Balance Equations

To construct the mathematical model, the Cartesian coordinate system is adopted, and the toe of the slope is chosen as the origin of the coordinate system. The coordinates of the centre of the log-spiral can be expressed as:

$$x_o = -r_0 \exp\left[\left(\theta_h - \theta_o\right)\tan\phi'\right]\cos\theta_h - \frac{H\sin\left(\beta-\beta'\right)}{\sin\beta\sin\beta'} \tag{4.31}$$

$$y_o = r_o \exp\left[\left(\theta_h - \theta_o\right)\tan\phi'\right]\sin\theta_h \tag{4.32}$$

The coordinates of a point on the slip surface can be expressed as:

$$x_s(\theta) = x_o + r_o \exp\left[(\theta - \theta_o)\tan\phi'\right]\cos\theta \tag{4.33}$$

$$y_s(\theta) = y_o - r_o \exp\left[(\theta - \theta_o)\tan\phi'\right]\sin\theta \tag{4.34}$$

The function of the ground surface can be expressed as:

$$g_{AB}(\theta) = H\left(1 - \tan\alpha / \tan\beta\right) + x_s(\theta)\tan\alpha,\ x_s(\theta) > H / \tan\beta \tag{4.35a}$$

$$g_{BC}(\theta) = x_s(\theta)\tan\beta,\ 0 \le x_s(\theta) \le H / \tan\beta \tag{4.35b}$$

$$g_{CC'}(\theta) = 0,\ x_s(\theta) < 0 \tag{4.35c}$$

The function of the wetting front can be expressed as:

$$w_f^1(\theta) = g_{AB}(\theta) - z_w,\ x_s(\theta) > H / \tan\beta \tag{4.36a}$$

$$w_f^2(\theta) = g_{BC}(\theta) - z_w,\ 0 \le x_s(\theta) \le H / \tan\beta \tag{4.36b}$$

$$w_f^3(\theta) = g_{CC'}(\theta) - z_w,\ x_s(\theta) < 0 \tag{4.36c}$$

The function of the groundwater table can be expressed as:

$$w_t(\theta) = x_s(\theta)\tan i - H_{wt} \tag{4.37}$$

According to Eqs. (4.29a) and (4.29b), the rate of work done by u_w for a log-spiral failure mechanism can be calculated by:

$$\dot{W}_{u_w} = \begin{cases} \int_S u_w \dot{\omega} r(\theta)\sin\phi' \dfrac{r(\theta)\mathrm{d}\theta}{\cos\phi'} = \int_S u_w \dot{\omega} r^2(\theta)\tan\phi'\mathrm{d}\theta,\ u_w \ge 0 & (4.38a) \\ \int_S \dfrac{\tan\phi^b}{\tan\phi'} u_w \dot{\omega} r(\theta)\sin\phi' \dfrac{r(\theta)\mathrm{d}\theta}{\cos\phi'} = \int_S u_w \dot{\omega} r^2(\theta)\tan\phi^b\mathrm{d}\theta,\ u_w < 0 & (4.38b) \end{cases}$$

If the groundwater table is shallow (e.g., $H_{wt} < h_{cc}$), as shown in Figure 4.4(a), the potential slip surface is mainly located in the capillary saturated zone or below (Figure 4.2), u_w is assumed to be hydrostatic relative to the groundwater table before the infiltration:

$$u_w(\theta) = \gamma_w H_{ws}(\theta)\cos^2 i \tag{4.39}$$

where γ_w is the unit weight of water, $H_{ws}(\theta)$ is the vertical distance between the groundwater table and the slip surface:

$$H_{ws}(\theta) = w_t(\theta) - y_s(\theta) \tag{4.40}$$

$H_{ws}(\theta)$ is positive if the groundwater table is above the slip surface and negative if the groundwater table is below the slip surface.

The derivative of $H_{ws}(\theta)$ with respect to θ is:

$$\frac{\mathrm{d}H_{ws}(\theta)}{\mathrm{d}\theta} = r_o \exp\left[(\theta - \theta_o)\tan\phi'\right]\cos\theta\left(\tan\phi' - \tan i\right)\left[\tan\theta - \frac{1}{\tan(i-\phi')}\right] \tag{4.41}$$

Hence, $H_{ws}(\theta)$ obtains its maximum value at:

$$\theta_m = 90^\circ + \phi' - i \tag{4.42}$$

After the infiltration, the rate of work done by $u_w(\theta)$ is denoted as $\dot{W}_{u_w}^{\mathrm{hyd}}$ and calculated by:

$$\dot{W}_{u_w}^{\mathrm{hyd}} = \int_{\theta_{w1}}^{\theta_{m1}} u_w(\theta)\dot{\omega}r^2(\theta)\tan\phi^b \mathrm{d}\theta + \int_{\theta_{m1}}^{\theta_{m2}} u_w(\theta)\dot{\omega}r^2(\theta)\tan\phi' \mathrm{d}\theta + \int_{\theta_{m2}}^{\theta_{w2}} u_w(\theta)\dot{\omega}r^2(\theta)\tan\phi^b \mathrm{d}\theta \tag{4.43a}$$

where θ_{w1} and θ_{w2} are the angles corresponding to the intersection points between the wetting front and the slip surface, θ_{m1} and θ_{m2} are the angles corresponding to the intersection points between the groundwater table and the slip surface, as shown in Figure 4.4(a). The angle θ_{w1} can be numerically solved by $y_s(\theta) = w_f^1(\theta)$, θ_{w2} can be numerically solved by $y_s(\theta) = w_f^2(\theta)$ for toe failure or $y_s(\theta) = w_f^3(\theta)$ for base failure, where $y_s(\theta)$ and $w_f^i(\theta)$ (i = 1, 2, 3) are indicated in Eq. (4.34) and Eq. (4.36), respectively. If $H_{ws}(\theta_m) > 0$, θ_{m1} and θ_{m2} are the two roots of $H_{ws}(\theta) = 0$ ($\theta_{m1} < \theta_{m2}$). If $H_{ws}(\theta_m) \le 0$, $\theta_{m1} = \theta_{m2} = \theta_m$. Bisection method can be efficiently used to solve for

θ_{w1}, θ_{w2}, θ_{m1} and θ_{m2}, and the implementation in Excel through Visual Basic Application (VBA) programming can be found in Appendix B.

It is well recognized that $\phi^b = \phi'$ when the matric suction is below the air-entry value or the soil is fully saturated, and ϕ^b decreases nonlinearly with a further increase in matric suction or decrease in degree of saturation (e.g., Gan et al. 1988; Vanapalli et al. 1996; Goh et al. 2010). Since the potential slip surface is mainly located in the capillary saturated zone or below where the soil is fully saturated (Figure 4.2), it is reasonable to assume ϕ^b as a constant (e.g., $\phi^b = \phi'$). Hence, Eq. (4.43a) can be rearranged to be:

$$\dot{W}_{u_w}^{\text{hyd}} = \tan\phi^b \int_{\theta_{w1}}^{\theta_{m1}} u_w(\theta)\dot{\omega}r^2(\theta)\mathrm{d}\theta + \tan\phi' \int_{\theta_{m1}}^{\theta_{m2}} u_w(\theta)\dot{\omega}r^2(\theta)\mathrm{d}\theta + \tan\phi^b \int_{\theta_{m2}}^{\theta_{w2}} u_w(\theta)\dot{\omega}r^2(\theta)\mathrm{d}\theta \quad (4.43b)$$

Substituting Eq. (4.39) into Eq. (4.43b) leads to:

$$\dot{W}_{u_w}^{\text{hyd}} = \dot{\omega}\gamma_w \cos^2 i \tan\phi' \left[\frac{\tan\phi^b}{\tan\phi'} \int_{\theta_{w1}}^{\theta_{m1}} H_{ws}(\theta)r^2(\theta)\mathrm{d}\theta + \int_{\theta_{m1}}^{\theta_{m2}} H_{ws}(\theta)r^2(\theta)\mathrm{d}\theta + \frac{\tan\phi^b}{\tan\phi'} \int_{\theta_{m2}}^{\theta_{w2}} H_{ws}(\theta)r^2(\theta)\mathrm{d}\theta \right] \quad (4.43c)$$

Finally, $\dot{W}_{u_w}^{\text{hyd}}$ can be written as:

$$\dot{W}_{u_w}^{\text{hyd}} = \dot{\omega}\gamma r_o^3 f_{u_w}^{\text{hyd}} \quad (4.43d)$$

where $f_{u_w}^{\text{hyd}}$ can be calculated by:

$$f_{u_w}^{\text{hyd}} = \frac{\gamma_w}{\gamma} \cos^2 i \tan\phi' \left[\frac{\tan\phi^b}{\tan\phi'} \int_{\theta_{w1}}^{\theta_{m1}} \frac{H_{ws}(\theta)r^2(\theta)}{r_o^3}\mathrm{d}\theta + \int_{\theta_{m1}}^{\theta_{m2}} \frac{H_{ws}(\theta)r^2(\theta)}{r_o^3}\mathrm{d}\theta + \frac{\tan\phi^b}{\tan\phi'} \int_{\theta_{m2}}^{\theta_{w2}} \frac{H_{ws}(\theta)r^2(\theta)}{r_o^3}\mathrm{d}\theta \right] \quad (4.44)$$

The integration in Eq. (4.44) can be calculated analytically by:

$$\int \frac{H_{ws}(\theta) r^2(\theta)}{r_o^3} \mathrm{d}\theta = \frac{(\sin\theta + 3\tan\phi'\cos\theta)\tan i - \cos\theta + 3\tan\phi'\sin\theta}{1 + 9\tan^2\phi'} \exp\left[3(\theta - \theta_o)\tan\phi'\right] + \frac{x_o \tan i - y_o - H_{wt}}{r_o} \frac{\exp\left[2(\theta - \theta_o)\tan\phi'\right]}{2\tan\phi'} \tag{4.45}$$

In Eq. (4.45), x_o and y_o can be calculated by Eq. (4.31) and Eq. (4.32), respectively. The ratio H/r_o can be further calculated by Eq. (4.11). For a slope stability analysis, the function $f_{u_w}^{\mathrm{hyd}}$ depends on the given conditions α, β, i, γ_w/γ, H_{wt}/H, z_w/H, ϕ' and $\tan\phi^b/\tan\phi'$, and variables θ_o, θ_h and β'.

If the groundwater table is deep (e.g., $H_{wt} >> h_{cc}$), as shown in Figure 4.4(b), the potential slip surface is mainly located in the discontinuous zone (Figure 4.2), constant u_w is assumed along the entire slip surface before the infiltration:

$$u_w = -\gamma_w h_c \tag{4.46}$$

where h_c is the constant pore-water pressure head of the soil in the discontinuous zone.

After the infiltration, the rate of work done by u_w is denoted as $\dot{W}_{u_w}^{\mathrm{con}}$ and can be calculated by:

$$\dot{W}_{u_w}^{\mathrm{con}} = \int_{\theta_{w1}}^{\theta_{w2}} -\gamma_w h_c \dot{\omega} r^2(\theta)\tan\phi^b \mathrm{d}\theta \tag{4.47a}$$

where the angles θ_{w1} and θ_{w2} are denoted in Figure 4.4(b). The angle θ_{w1} can be numerically solved by $y_s(\theta) = w_f^1(\theta)$, θ_{w2} can be numerically solved by $y_s(\theta) = w_f^2(\theta)$ for toe failure or $y_s(\theta) = w_f^3(\theta)$ for base failure.

As the pore-water pressure is relatively constant in the discontinuous zone [Figure 4.2(b)], it is reasonable to assume ϕ^b as a constant. Hence, Eq. (4.47a) can be rearranged to be:

$$\dot{W}_{u_w}^{\text{con}} = -\gamma_w h_c \tan\phi^b \int_{\theta_{w1}}^{\theta_{w2}} \dot{\omega} r^2(\theta) \mathrm{d}\theta \tag{4.47b}$$

Substituting Eq. (4.1) into Eq. (4.47b) yields:

$$\dot{W}_{u_w}^{\text{con}} = -\dot{\omega}\gamma r_o^3 \frac{\gamma_w}{\gamma}\frac{h_c}{H}\frac{H}{r_o}\tan\phi^b \frac{\exp\left[2(\theta_{w2}-\theta_o)\tan\phi'\right]-\exp\left[2(\theta_{w1}-\theta_o)\tan\phi'\right]}{2\tan\phi'} = \dot{\omega}\gamma r_o^3 f_{u_w}^{\text{con}} \tag{4.47c}$$

where $f_{u_w}^{\text{con}}$ can be calculated by:

$$f_{u_w}^{\text{con}} = -\frac{\gamma_w h_c \tan\phi^b}{\gamma H \tan\phi'}\frac{H}{r_o}\frac{\exp\left[2(\theta_{w2}-\theta_o)\tan\phi'\right]-\exp\left[2(\theta_{w1}-\theta_o)\tan\phi'\right]}{2} \tag{4.48}$$

For a slope stability analysis, the function $f_{u_w}^{\text{con}}$ depends on the given conditions α, β, z_w/H, $\left(\gamma_w h_c \tan\phi^b\right)/\left(\gamma H \tan\phi'\right)$ and ϕ', and variables θ_o, θ_h and β'.

Factor of safety F of a slope is commonly defined as the ratio of the shear strength available to the shear stress mobilized (Duncan, 1996). For an unsaturated soil slope, F can be expressed as:

$$F = \frac{c'}{c'_d} = \frac{\tan\phi'}{\tan\phi'_d} = \frac{\tan\phi^b}{\tan\phi_d^b} \tag{4.49}$$

where c'_d, ϕ'_d and ϕ_d^b are the shear strength parameters that are required to bring the slope to the limit state of failure.

Substitute Eq. (4.4), Eq. (4.30), Eq. (4.43d) or Eq. (4.47c) into Eq. (4.28), the work rate balance equation for an unsaturated soil slope due to log-spiral failure mechanism can be written as:

$$\frac{\gamma H}{c'} = \frac{H}{r_o}\frac{\exp\left[2(\theta_h-\theta_o)\tan\phi'\right]-1}{2\tan\phi'\left(f_1 - f_2 - f_3 - f_4 + f_{u_w}\right)} \tag{4.50}$$

in which f_{u_w} is $f_{u_w}^{\text{hyd}}$ [Eq. (4.44)] for hydrostatic pore-water pressure assumption, and $f_{u_w}^{\text{con}}$ [Eq. (4.48)] for constant negative pore-water pressure assumption. Minimum value of $\gamma H/c'$ can be obtained for given conditions by optimization, with θ_o, θ_h and β' being the variables (Chen, 1975).

Alternatively, Eq. (4.50) can be presented as:

$$\frac{c'}{\gamma H \tan\phi'} = \frac{r_o}{H}\frac{2\left(f_1 - f_2 - f_3 - f_4 + f_{u_w}\right)}{\exp\left[2\left(\theta_h - \theta_o\right)\tan\phi'\right] - 1} \tag{4.51}$$

Instead of searching for minimum $\gamma H/c'$ in Eq. (4.50), maximum $c'/\gamma H\tan\phi'$ in Eq. (4.51) is searched. In order to ensure the physical feasibility of the slip surface, the variables θ_o, θ_h and β' are subjected to the following constraints: $0 < \beta' \le \beta$, $\phi' \le \theta_o \le \frac{\pi}{2} + \phi'$, $\theta_o < \theta_h$, $\frac{\pi}{2} + \phi' - \beta \le \theta_h \le \pi + \phi' - \beta$ for toe failure or $\frac{\pi}{2} + \phi' \le \theta_h < \pi$ for base failure.

In the objective function [Eq. (4.50) or Eq. (4.51)], c' is denoted as c'_d. In the given conditions, ϕ' is denoted as ϕ'_d, and ϕ^b is denoted as ϕ^b_d. According to Eq. (4.49), the parameter group $c'/\gamma H\tan\phi'$ is independent of F (Bell, 1966):

$$\frac{c'_d}{\gamma H \tan\phi'_d} = \frac{c'/F}{\gamma H \tan\phi'/F} = \frac{c'}{\gamma H \tan\phi'} \tag{4.52}$$

Similarly, $\tan\phi^b/\tan\phi'$ is also independent of F:

$$\frac{\tan\phi^b_d}{\tan\phi'_d} = \frac{\tan\phi^b/F}{\tan\phi'/F} = \frac{\tan\phi^b}{\tan\phi'} \tag{4.53}$$

Hence, in the given conditions $\tan\phi^b_d$ is normalized to $\tan\phi'_d$ as $\tan\phi^b_d / \tan\phi'_d$ (= $\tan\phi^b/\tan\phi'$), and a given ϕ'_d [$= \arctan\left(\tan\phi'/F\right)$] corresponds to an optimized $c'_d / \gamma H \tan\phi'_d$ (= $c'/\gamma H \tan\phi'$).

Therefore, the solutions of Eq. (4.51) can be conveniently presented as charts, in which $F/\tan\phi'$ is expressed as a function of $c'/\gamma H\tan\phi'$. The advantage of the stability charts presented in this format is that factor of safety F can be obtained without iteration for a slope with known c', γ, H, ϕ' and β etc. (Bell, 1966; Michalowski, 2002; Viratjandr and Michalowski, 2006; Gao et al., 2013, 2014).

For a specific slope stability problem with given c', γ, H, ϕ' and ϕ^b etc., the parameter group $c'/\gamma H\tan\phi'$ is known while ϕ'_d is unknown. In this situation, the procedure to obtain F is the reverse of the procedure to develop stability charts. More specifically, the ratio $\tan\phi_d^b / \tan\phi'_d$ is fixed (= $\tan\phi^b/\tan\phi'$), and an interative procedure is conducted to search for ϕ'_d which could lead to $c'_d / \gamma H \tan\phi'_d = c' / \gamma H \tan\phi'$. Consequently, F can be calculated according to Eq. (4.49), i.e., $F = \tan\phi' / \tan\phi'_d$.

4.3 Proposed Translational Upper Bound Limit Analysis

4.3.1 Static Stability Analysis

For an unsaturated soil slope under rainfall, a shallow translational failure may be more critical than a global rotational failure. Hence, a kinematically admissible translational failure mode is proposed to analyze the translational failure, as shown in Figure 4.5(a). The translational slip consists of an intermediate translational component DEFG which is a parallelogram and two rotational components ABDE (at the crest) and CFG (at the toe) which take the boundary effects into account. The two rotational components can be combined into a complete log-spiral rotational mass ABC, as shown in Figure 4.5(b), by connecting the side DE to the side GF. In

order to be kinematically admissible, the log-spirals AE and CF are tangent to the plane EF at points E and F, and the velocity jump vectors are shown as arrows in Figure 4.5. The vertical height of the translational mass H_{trl} and log-spiral rotational mass H_{rot} satisfy the relationship below:

$$H_{\text{trl}} + H_{\text{rot}} = H \tag{4.54}$$

In Eq. (4.54) and the following equations, the subscript (or superscript) "trl" denotes "translational" and "rot" denotes "rotational".

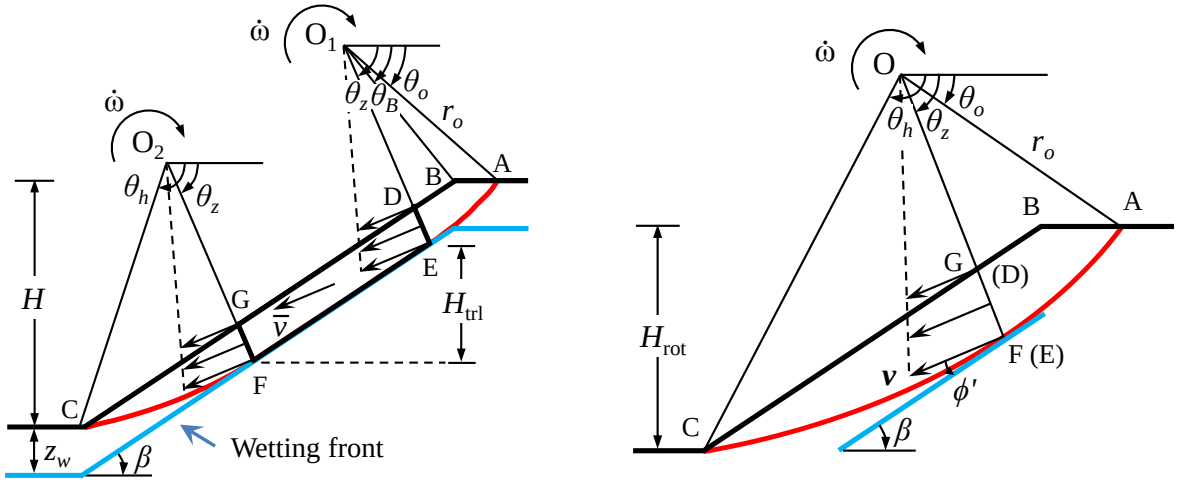

(a) Proposed translational slip (b) Log-spiral rotational mass

Figure 4.5 Proposed translational failure mode

If the pore-water pressure above the wetting front is zero, there is no need to consider the rate of work done by pore-water pressure. The work rate balance equation can be written as:

$$\dot{W}_{\gamma}^{\text{rot}} + \dot{W}_{\gamma}^{\text{trl}} = \dot{D}_{c'}^{\text{rot}} + \dot{D}_{c'}^{\text{trl}} \tag{4.55}$$

The rate of work done by the weight of the rotational mass $\dot{W}_{\gamma}^{\text{rot}}$ is calculated by:

$$\dot{W}_{\gamma}^{\text{rot}} = \int_{A_{\text{rot}}} \boldsymbol{\gamma} \bullet \mathbf{v} \mathrm{d}A_{\text{rot}} = \dot{\omega}\gamma r_o^3 \left(f_1 - f_2 - f_3 \right) \tag{4.56}$$

where f_1, f_2 and f_3 can still be calculated by Eq. (4.6) – Eq. (4.11), with slight modification that $\beta' = \beta$ and H is replaced by H_{rot}.

The rate of work done by the weight of the translational mass $\dot{W}_{\gamma}^{\text{trl}}$ is calculated by:

$$\dot{W}_{\gamma}^{\text{trl}} = \int_{A_{\text{trl}}} \boldsymbol{\gamma} \bullet \mathbf{v} \mathrm{d}A_{\text{trl}} = \gamma A_{\text{trl}} \bar{v} \cos\theta_z = \gamma \frac{H_{\text{trl}} z_s}{\tan\beta} \bar{v} \cos\theta_z \tag{4.57}$$

where $\bar{v}$ is the average velocity of the translational mass and it is calculated by:

$$\bar{v} = \dot{\omega} \left\{ r_o \exp\left[\left(\theta_z - \theta_o \right) \tan\phi' \right] - \frac{z_s \cos\beta}{2\cos\phi'} \right\} \tag{4.58}$$

In Eqs. (4.57) and (4.58), z_s denotes the vertical distance between the top (DG) and bottom (EF) of the translational mass, and θ_z denotes the angle at which the log-spirals AE and CF are tangent to the plane EF, as shown in Figure 4.5(a). According to the geometric relationship, z_s and θ_z can be calculated by Eq. (4.59) and Eq. (4.60), respectively.

$$\frac{z_s}{r_o} = \left(\cos\theta_z \tan\beta + \sin\theta_z \right) \exp\left[\left(\theta_z - \theta_o \right) \tan\phi' \right] - \left(\cos\theta_h \tan\beta + \sin\theta_h \right) \exp\left[\left(\theta_h - \theta_o \right) \tan\phi' \right] \tag{4.59}$$

$$\theta_z = 90^\circ - \beta + \phi' \tag{4.60}$$

Substitute Eq. (4.58) into Eq. (4.57), $\dot{W}_{\gamma}^{\text{trl}}$ can finally be expressed as:

$$\dot{W}_{\gamma}^{\text{trl}} = \dot{\omega}\gamma r_o^3 f_{\gamma}^{\text{trl}} \tag{4.61}$$

where f_{γ}^{trl} can be calculated by:

$$f_{\gamma}^{\text{trl}} = \frac{H_{\text{trl}}}{r_o} \frac{z_w}{r_o} \left\{ \exp\left[\left(\theta_z - \theta_o \right) \tan\phi' \right] - \frac{z_s \cos\beta}{2 r_o \cos\phi'} \right\} \frac{\cos\theta_z}{\tan\beta} \tag{4.62}$$

The energy dissipation caused by the rotational mass $\dot{D}_{c'}^{\text{rot}}$ is calculated by:

$$\dot{D}_{c'}^{\text{rot}} = \int_{S_{\text{rot}}} c' v_t \mathrm{d}S_{\text{rot}} = \dot{\omega}\gamma r_o^3 \frac{c'}{\gamma H \tan\phi'} f_{c'}^{\text{rot}} \tag{4.63}$$

where $f_{c'}^{\text{rot}}$ can be expressed as:

$$f_{c'}^{\text{rot}} = \frac{1}{2}\frac{H}{r_o}\left\{\exp\left[2(\theta_h - \theta_o)\tan\phi'\right] - 1\right\} \tag{4.64}$$

The energy dissipation caused by the translational mass $\dot{D}_{c'}^{\text{trl}}$ is calculated by:

$$\dot{D}_{c'}^{\text{trl}} = \int_{S_{\text{trl}}} c' v_t \mathrm{d}S_{\text{trl}} = \dot{\omega}\gamma r_o^3 \frac{c'}{\gamma H \tan\phi'} f_{c'}^{\text{trl}} \tag{4.65}$$

where $f_{c'}^{\text{trl}}$ can be expressed as:

$$f_{c'}^{\text{trl}} = \frac{H}{r_o}\frac{H_{\text{trl}}}{r_o}\exp\left[(\theta_z - \theta_o)\tan\phi'\right]\frac{\sin\phi'}{\sin\beta} \tag{4.66}$$

Substituting Eqs. (4.57), (4.58c), (4.61) and (4.63) into Eq. (4.56) gives:

$$\frac{c'}{\gamma H \tan\phi'} = \frac{f_1 - f_2 - f_3 + f_\gamma^{\text{trl}}}{f_{c'}^{\text{rot}} + f_{c'}^{\text{trl}}} \tag{4.67}$$

In Eq. (4.67), maximum $c'/\gamma H\tan\phi'$ ($c_d'/\gamma H\tan\phi_d'$) can be obtained for given values of α, β, ϕ' (ϕ_d') and z_w/H, with θ_o, θ_h and H_{trl}/H being the variables. In order to ensure the physical feasibility of the slip surface, the optimization is subjected to the following constraints: $0 \le H_{\text{trl}}/H < 1$, $z_s \le z_w$, $\phi' \le \theta_o \le \theta_B$, $\theta_B \le \theta_z$, and $\theta_z < \theta_h \le \pi + \phi' - \beta$. The angle θ_B is denoted in Figure 4.5(a) and can be calculated by:

$$\tan\theta_B = \frac{\sin\beta\sin(\theta_0 + \alpha) - \sin\alpha\sin(\theta_h + \beta)\exp\left[(\theta_h - \theta_0)\tan\phi'\right]}{-\cos\beta\sin(\theta_0 + \alpha) + \cos\alpha\sin(\theta_h + \beta)\exp\left[(\theta_h - \theta_0)\tan\phi'\right]} \tag{4.68}$$

The procedures to develop stability chart and obtain factor of safety have been discussed at the end of Section 4.2.3, and would not be repeated here.

4.3.2 Seismic Stability Analysis

Shallow translational and deep rotational slips, as shown in Figure 2.11, are the two common failure modes for a dry soil slope under seismic loading (Rathje and Antonakos, 2011). The upper bound pseudo-static limit analysis of rotational failure has been given by Chang et al. (1984), as reviewed in Section 4.1.2. The upper bound pseudo-static limit analysis of translational failure is proposed below. By incorporating the pseudo-static force, the work rate balance equation, Eq. (4.55), is modified to be:

$$\dot{W}_{\gamma}^{\text{rot}} + \dot{W}_{\gamma}^{\text{trl}} + \dot{W}_{s}^{\text{rot}} + \dot{W}_{s}^{\text{trl}} = \dot{D}_{c'}^{\text{rot}} + \dot{D}_{c'}^{\text{trl}} \tag{4.69}$$

where $\dot{W}_{s}^{\text{rot}}$ and $\dot{W}_{s}^{\text{trl}}$ denote the rate of work done by the seismic force imposed on the rotational component and translational component, respectively, and they can be calculated by:

$$\dot{W}_{s}^{\text{rot}} = \int_{A_{\text{rot}}} \mathbf{k_h}\gamma \bullet \mathbf{v}\mathrm{d}A_{\text{rot}} = \dot{\omega}\gamma r_o^3 k_h \left(f_1^{\,s} - f_2^{\,s} - f_3^{\,s} \right) \tag{4.70}$$

$$\dot{W}_{s}^{\text{trl}} = \int_{A_{\text{trl}}} \mathbf{k_h}\gamma \bullet \mathbf{v}\mathrm{d}A_{\text{trl}} = \dot{\omega}\gamma r_o^3 k_h f_s^{\,\text{trl}} \tag{4.71}$$

In Eq. (4.70), the functions $f_1^{\,s}$, $f_2^{\,s}$ and $f_3^{\,s}$ can still be calculated by Eq. (4.15) – Eq. (4.17), with slight modification that $\beta' = \beta$ and $H = H_{\text{rot}}$. In Eq. (4.71), $f_s^{\,\text{trl}}$ can be calculated by:

$$f_s^{\,\text{trl}} = \frac{H_{\text{trl}}}{r_o}\frac{z_s}{r_o}\left\{ \exp\left[\left(\theta_z - \theta_o \right) \tan\phi' \right] - \frac{1}{2}\frac{z_s}{r_o}\frac{\cos\beta}{\cos\phi'} \right\} \frac{\sin\theta_z}{\tan\beta} \tag{4.72}$$

The work rate balance equation Eq. (4.69) can finally be written as:

$$\frac{c'}{\gamma H \tan\phi'} = \frac{f_1 - f_2 - f_3 + f_{\gamma}^{\,\text{trl}} + k_h \left(f_1^{\,s} - f_2^{\,s} - f_3^{\,s} + f_s^{\,\text{trl}} \right)}{f_{c'}^{\,\text{rot}} + f_{c'}^{\,\text{trl}}} \tag{4.73}$$

Maximum value of $c'/\gamma H\tan\phi'$ ($c'_d/\gamma H\tan\phi'_d$) can be obtained for given α, β, ϕ' (ϕ'_d) and z/H, with θ_o, θ_h and H_{trl}/H being the variables. Stability chart can be presented by expressing $F/\tan\phi'$ ($1/\tan\phi'_d$) as a function of $c'/\gamma H\tan\phi'$.

Alternatively, Eq. (4.72) can be presented as:

$$k_h = \frac{\dfrac{c'}{\gamma H\tan\phi'}\left(f_{c'}^{\,rot} + f_{c'}^{\,trl}\right) - \left(f_1 - f_2 - f_3 + f_\gamma^{\,trl}\right)}{f_1^{\,s} - f_2^{\,s} - f_3^{\,s} + f_s^{\,trl}} \tag{4.74}$$

Minimum value of k_h (= k_y, yield coefficient of the slope) can be obtained for given α, β, ϕ', $c'/\gamma H$ and z/H, with θ_o, θ_h and H_{trl}/H being the variables.

In order to ensure that the slip surface is physically feasible, the optimization of both Eq. (4.73) and Eq. (4.74) is subjected to the following constraints: $0 \le H_{trl}/H < 1$, $z_s \le z$, $\phi' \le \theta_o \le \theta_B$, $\theta_B \le \theta_z$, $\theta_z < \theta_h \le \pi + \phi' - \beta$.

4.4 Procedure to Develop Slope Stability Charts

The upper bound limit analysis proposed in Sections 4.2 and 4.3 can be efficiently used to develop slope stability charts, and the details are summarized in Table 4.2. For a set of given conditions, a maximum $c'/\gamma H\tan\phi'$ (or minimum k_h) can be searched. By varying the values of ϕ'_d in the given conditions, various $(c'/\gamma H\tan\phi')_{max}$ (or k_h^{min}) can be obtained. Hence, a stability curve is produced by plotting $F/\tan\phi'$ (or k_y) as a function of $c'/\gamma H\tan\phi'$.

Table 4.2 Summary of the details for the upper bound limit analyses

Failure Mode	Given conditions	Variables	Objective function
Rotational failure (Hydrostatic u_w)	α, β, i, γ_w/γ, H_{wt}/H, z_w/H, $\tan\phi^b/\tan\phi'$, ϕ' (ϕ'_d)	β', θ_o, θ_h	$c'/\gamma H\tan\phi'$ [Eq. (4.51)]
Rotational failure (Constant u_w)	α, β, z_w/H, $\left(\gamma_w h_c \tan\phi^b\right)/\left(\gamma H \tan\phi'\right)$, ϕ' (ϕ'_d)		
Translational failure	α, β, z_w/H, ϕ' (ϕ'_d)	θ_o, θ_h, H_{trl}/H	$c'/\gamma H\tan\phi'$ [Eq. (4.67)]
Pseudo-static analysis of translational failure	α, β, z/H, k_h, ϕ' (ϕ'_d)	θ_o, θ_h, H_{trl}/H	$c'/\gamma H\tan\phi'$ [Eq. (4.73)]
	α, β, z/H, $c'_d/\gamma H$, ϕ'_d		k_h [Eq. (4.74)]

In the given conditions the value of ϕ'_d can be selected manually. However, manual selection would be tedious and not efficient if a large number of stability charts need to be developed. A procedure which enables the automatic determination of ϕ'_d by computer program is suggested below:

1) The $\phi_d^{\max}$ that satisfies the target condition [e.g., $0 < \left(c'/\gamma H \tan\phi'\right)_{\max} < 1.0\times10^{-6}$] is searched;

2) The $\phi_d^{\min}$ that satisfies the target condition (e.g., $1/\tan\phi_d^{\min} = 14$) is searched;

3) The value of ϕ_d^i is exponentially distributed between $\phi_d^{\min}$ and $\phi_d^{\max}$, and calculated by $\phi_d^i = \left(\phi_d^{\min}\right)^{\frac{i-1}{n-1}} \times \left(\phi_d^{\max}\right)^{\frac{n-i}{n-1}}$ (i = 1, 2, …, n), where n denotes the number of data points on a stability curve (n is usually taken as 10 in this study);

4) For a specific ϕ_d^i , the objective function is optimized (maximum $c'/\gamma H\tan\phi'$, or minimum k_h);

5) The $F/\tan\phi'$ (k_y) is plotted against $c'/\gamma H\tan\phi'$ ($c_d / \gamma H \tan\phi_d'$), and a smooth curve is used to connect the n data points.

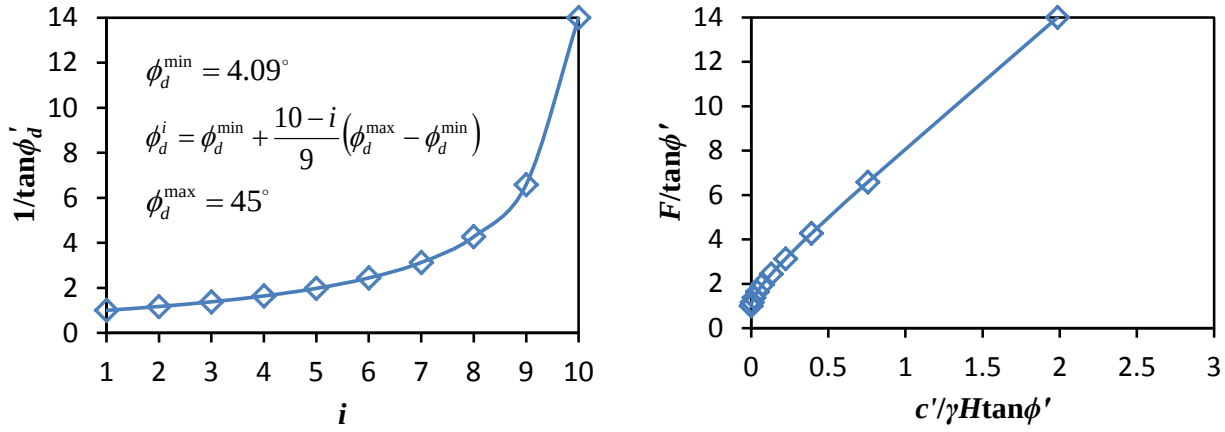

(a) Linear distribution of ϕ_d^i

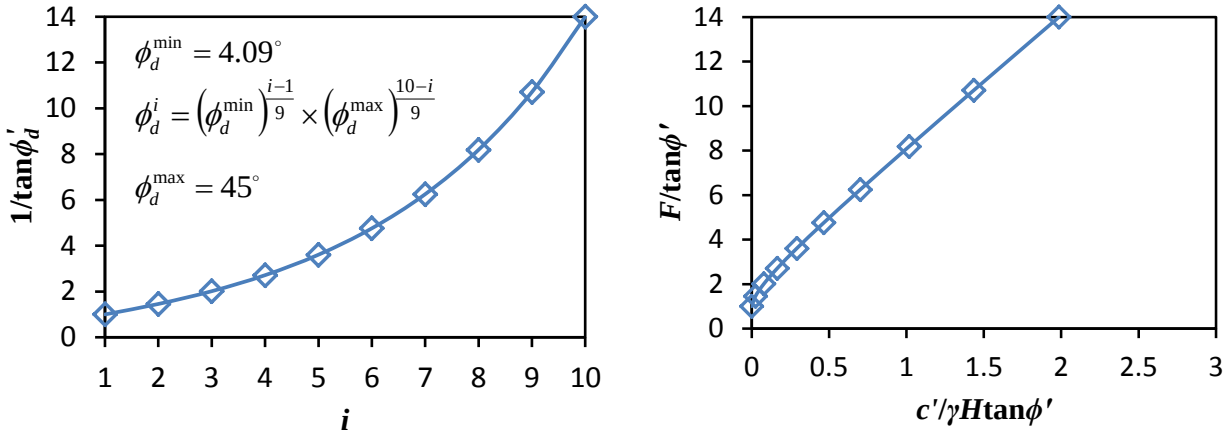

(b) Exponential distribution of ϕ_d^i

Figure 4.6 Distribution of data points on a stability curve (Rotational failure for dry soil slopes with $\alpha = 0°$, $\beta = 45°$, $\phi^b = 0$)

In step 3, exponential distribution of ϕ_d^i is adopted. To explain this selection, stability curves based on linear and exponential distribution of ϕ_d^i are compared in Figure 4.6. If ϕ_d^i is linearly

distributed between $\phi_d^{\min}$ and $\phi_d^{\max}$, most data points are obtained at small $c'/\gamma H\tan\phi'$ [Figure 4.6(a)]. If ϕ_d^i is exponentially distributed, the data points are more evenly distributed in the entire range of $c'/\gamma H\tan\phi'$ [Figure 4.6(b)]. In Chapters 5 and 6, stability curves will be curve-fitted by equations. To ensure that the curve-fitting coefficients are representative for the entire range of $c'/\gamma H\tan\phi'$, the value of ϕ_d^i is exponentially distributed between $\phi_d^{\min}$ and $\phi_d^{\max}$.

Excel spreadsheet can be efficiently used to perform the upper bound limit analysis (Sections 4.2 and 4.3) and develop the stability charts using the procedure outlined above. A typical Excel Spreadsheet and Visual Basic Application (VBA) codes are shown in Appendix B.

4.5 Summary

In this chapter, the conventional log-spiral upper bound limit analysis for dry and saturated soil slopes was reviewed first, and the analysis was then extended to unsaturated soil slopes. More specifically, the equation to calculate the rate of work done by negative pore-water pressure was derived, the pore-water pressure profiles before and after rainfall infiltration were conceptualized, and the work rate balance equations for the log-spiral failure mechanism of unsaturated soil slopes were established. In addition, a kinematically admissible failure mode which can consider the boundary resistance of a translational slip was proposed to analyze the translational failure both statically and pseudo-statically. Finally, a procedure which can be incorporated into a computer program and enable automatic generation of dimensionless slope stability numbers was proposed.

Chapter 5: Stability Equations for Unsaturated Soil Slopes under Rainfall

Upper bound limit analysis of unsaturated soil slopes under rainfall based on rotational and translational failure mechanisms is shown in Chapter 4. The upper bound limit analysis is used to develop slope stability charts and equations in this chapter. More specifically, the controlling factors on the failure mode of unsaturated soil slopes under rainfall are investigated by using the dimensionless slope stability charts. Through careful selection of the functional forms and regression analysis of the dimensionless slope stability numbers, slope stability equations that can explicitly calculate the factors of safety of unsaturated soil slopes under rainfall and saturated soil slopes are proposed.

5.1 Controlling Factors on the Failure Mode

Stability charts for unsaturated soil slopes under rainfall due to rotational and translational failures can be developed according to Eq. (4.51) and Eq. (4.67), respectively. For example, in Figures 5.1(a) and (b), the dash curves are obtained for translational failure mechanism with given conditions $\alpha = 0°$, $\beta = 45°$, $z_w/H = 0.1$. In Figure 5.1(a), the solid curves are obtained for rotational failure mechanism (hydrostatic pore-water pressure assumption) with given conditions $\alpha = 0°$, $\beta = 45°$, $z_w/H = 0.1$, $\gamma_w/\gamma = 0.5$, $H_{wt}/H = 0.2$, $i = 0°$, and $\tan\phi^b/\tan\phi'$ ranging from 0 to 1. In Figure 5.1(b), the solid curves are obtained for rotational failure mechanism (constant negative pore-water pressure assumption) with given conditions $\alpha = 0°$, $\beta = 45°$, $z_w/H = 0.1$, and

($\gamma_w h_c \tan\phi^b$)/($\gamma H \tan\phi'$) ranging from 0 to 0.5. For a specific slope, the parameter group $c'/\gamma H \tan\phi'$ is calculated first, the corresponding $F/\tan\phi'$ can be checked from the charts, F can hence be calculated.

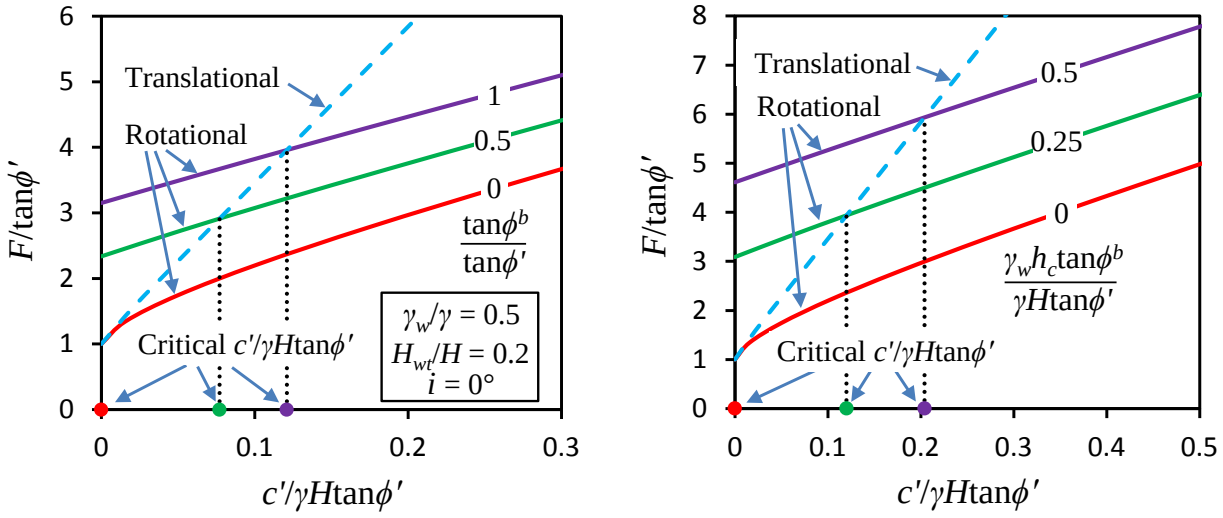

(a) Hydrostatic pore-water pressure (b) Constant negative pore-water pressure

Figure 5.1 Stability charts for unsaturated soil slopes under rainfall (α = 0°, β = 45°, z_w/H = 0.1)

Figures 5.1(a) and (b) show that there is an intersection between the stability curves of rotational and translational failure mechanisms for a given shear strength increment due to matric suction. The corresponding $c'/\gamma H \tan\phi'$ of the intersection point is defined as the critical $c'/\gamma H \tan\phi'$, below which translational failure mechanism would give a lower factor of safety and govern the failure mode, above which rotational failure mechanism would give a lower factor of safety and govern the failure mode. For a slope, the larger the critical $c'/\gamma H \tan\phi'$, the wider the range of soil properties in which translational failure is the governing failure mode.

The influences of infiltration depth (z_w/H), contribution of matric suction ($\tan\phi^b/\tan\phi'$) and slope angle (β) on the critical $c'/\gamma H\tan\phi'$ were investigated and shown in Figure 5.2. Figures 5.2(a), (b) and (c) are obtained based on the assumption that the groundwater table is shallow and the pore-water pressure is hydrostatic [Figure 4.4(a)]. Figures 5.2(d), (e) and (f) are obtained based on the assumption that the groundwater table is very deep and the negative pore-water pressure is a constant [Figure 4.4(b)].

Figures 5.2(a) and (d) illustrate the influence of z_w/H on the critical $c'/\gamma H\tan\phi'$. When there is no infiltration ($z_w/H = 0$), the critical $c'/\gamma H\tan\phi'$ equals to zero and rotational failure is the governing failure mode for any soil slope with $c' > 0$. With the increase in z_w/H, the critical $c'/\gamma H\tan\phi'$ increases correspondingly, the slope becomes increasingly prone to translational failure. A dilemma of infinite slope analysis is highlighted here: when z_w/H is small (e.g., $z_w/H \rightarrow 0$), the boundary effects are negligible and infinite slope analysis is accurate, but rotational failure is more likely to be the governing failure mode; when z_w/H is large (e.g., $z_w/H = 0.2$), although translational failure may become the governing failure mode, infinite slope analysis is inaccurate because the boundary effects become considerable. A kinematic analysis of translational failure in the context of upper bound plasticity theory is presented in Section 4.3.1. The boundary effects are always taken into account in the kinematic analysis. Hence, the dilemma of infinite slope analysis can be avoided if upper bound limit analysis with the proposed translational failure mechanism is used instead.

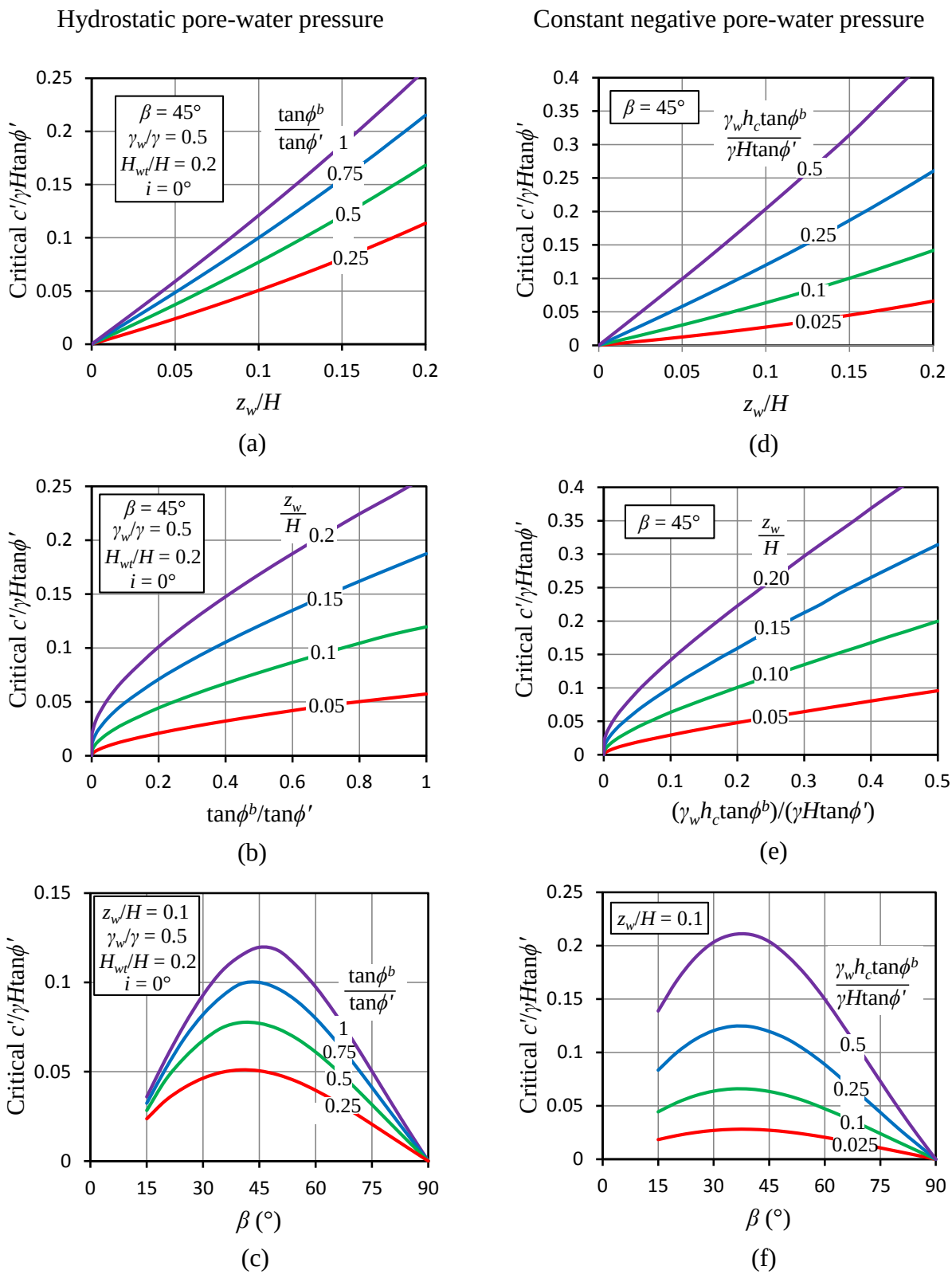

Figure 5.2 Influence of z_w/H, $\tan\phi^b/\tan\phi'$ and β on the critical $c'/\gamma H\tan\phi'$ ($\alpha = 0°$)

Figures 5.2(b) and (e) illustrate the influence of shear strength contribution from matric suction on the critical $c'/\gamma H\tan\phi'$. When the shear strength contribution from matric suction is zero ($\tan\phi^b/\tan\phi' = 0$), rainfall infiltration would not further reduce the slope stability, the critical $c'/\gamma H\tan\phi'$ is equal to zero and rotational failure is the governing failure mode if $c' > 0$. With the increase in $\tan\phi^b/\tan\phi'$ (or $\gamma_w h_c \tan\phi^b/\gamma H\tan\phi'$), the critical $c'/\gamma H\tan\phi'$ increases for a given z_w/H, the slope becomes increasingly susceptible to translational failure.

Figures 5.2(c) and (f) illustrate the influence of β on the critical $c'/\gamma H\tan\phi'$. The critical $c'/\gamma H\tan\phi'$ first increases and then decreases with the increase in β. In Figure 5.2(c), the critical $c'/\gamma H\tan\phi'$ peaks when β is about 45°. In Figure 5.2(f), the critical $c'/\gamma H\tan\phi'$ peaks when β is about 37.5°. The maximum critical $c'/\gamma H\tan\phi'$ suggests the widest range of soil properties in which translational failure is the governing failure mode. A decrease in critical $c'/\gamma H\tan\phi'$ implies a decreasing possibility of translational failure. When $\beta = 90°$, the critical $c'/\gamma H\tan\phi'$ equals to zero and rotational failure is the governing failure mode if $c' > 0$. In Figure 5.2(c), when $\beta = 15°$, the increase of critical $c'/\gamma H\tan\phi'$ is small due to the increase in $\tan\phi^b/\tan\phi'$. The reason is that the critical slip surface for $\beta = 15°$ would pass below the groundwater table (i.e., $H_{wt}/H = 0.2$, $i = 0°$), and the critical slip surface goes deeper with the increase in $\tan\phi^b/\tan\phi'$. Hence, the increasing shear strength contribution from matric suction is partially offset by the increase in positive pore-water pressure.

Most of the rainfall-induced landslides were shallow translational and occurred in the terrains with slope angles between 25° and 50° (e.g., Toll 2001; Dai et al. 2003; Zizioli et al. 2013).

Rainfall rarely triggered slope failures in very gentle and steep terrains. An explanation to this phenomenon is that steep slopes (> 50°) are usually limited by weathering due to the downslope removal of regolith under gravity, while moderately steep slopes (30° - 40°) are often weathered at shallow depth (Dai et al. 2003). Figs. 7(c) and (f) show that even for unsaturated homogeneous slopes which have no variation in degree of weathering with depth, moderately steep slopes are more susceptible to shallow translational failure than gentle and steep slopes. This phenomenon can be attributed to the fact that the loss of matric suction is greater in moderately steep slopes than in gentle and steep slopes for a given amount of rainwater infiltration. Quantitative evidence can be found in Figure 5.7 and will be explained in detail later, while qualitative reasons are provided as follows: 1) rainfall infiltrates into a steep slope mainly from the slope crest, while rainfall infiltrates into a moderately steep slope from both the slope crest and the slope surface; 2) although rainfall can also infiltrate into a gentle slope from both the slope crest and slope surface, the portion of slip surface saturated by rainfall water is less for a gentle slope than for a moderately steep slope, as the slip surface passes below the toe for a gentle slope while it passes through the toe for a moderately steep slope (Baker 2003). The above discussion reveals that apart from the different degrees of weathering with depth, the different degrees of loss in matric suction with slope angle can also contribute to the frequent occurrence of shallow translational slide in moderately steep terrains.

5.2 Stability Equations for Rotational Failure Mechanism

In order to cover a wide range of slope geometries, soil properties and rainfall characteristics, a large number of stability charts like those shown in Figure 5.1 need to be presented. By using charts, stability numbers need to be read from or interpolated between the stability curves. Due

to the number of parameters involved in the stability charts, interpolation between multiple stability curves may be often required for a slope stability problem. It would be more convenient if factor of safety of a slope can be explicitly calculated as a function of slope geometries, soil properties and rainfall characteristics. In the following sections, a stability equation for dry soil slopes is proposed first. The equation is then extended to unsaturated soil slopes considering rotational failure mechanism.

5.2.1 Dry Soil Slopes

For a dry soil slope which is not affected by pore-water pressure (both positive and negative), rotational failure is the critical failure mode (Taylor, 1948; Chen, 1975). The stability charts presented by Taylor (1937) and Michalowski (2002) are shown in Figures 5.3(a) and (b). For a slope with known $c'/\gamma H$, β and ϕ', F can be deduced from both charts. However, the procedure of evaluating F from the chart in Figure 5.3(a) is iterative (except for the case of $\phi' = 0$), as F is applied to both c' and $\tan\phi'$ (e.g., Spencer, 1967). The iteration can be avoided if Figure 5.3(b) is used. Hence, stability charts are commonly presented in the format shown in Figure 5.3(b) (e.g., Steward et al., 2011; Gao et al., 2013, 2014).

Figure 5.3(b) shows a nonlinear relationship between $F/\tan\phi'$ and $c'/\gamma H\tan\phi'$, and the nonlinearity is especially obvious when $c'/\gamma H\tan\phi'$ is small. Michalowski and Nadukuru (2013) used a power function, as shown in Eq. (5.1a), to approximate the stability curves of dry and saturated soil slopes with parameters A, B and G.

$$\frac{F}{\tan\phi'} = A\left(\frac{c'}{\gamma H\tan\phi'}\right)^{B} + G \tag{5.1a}$$

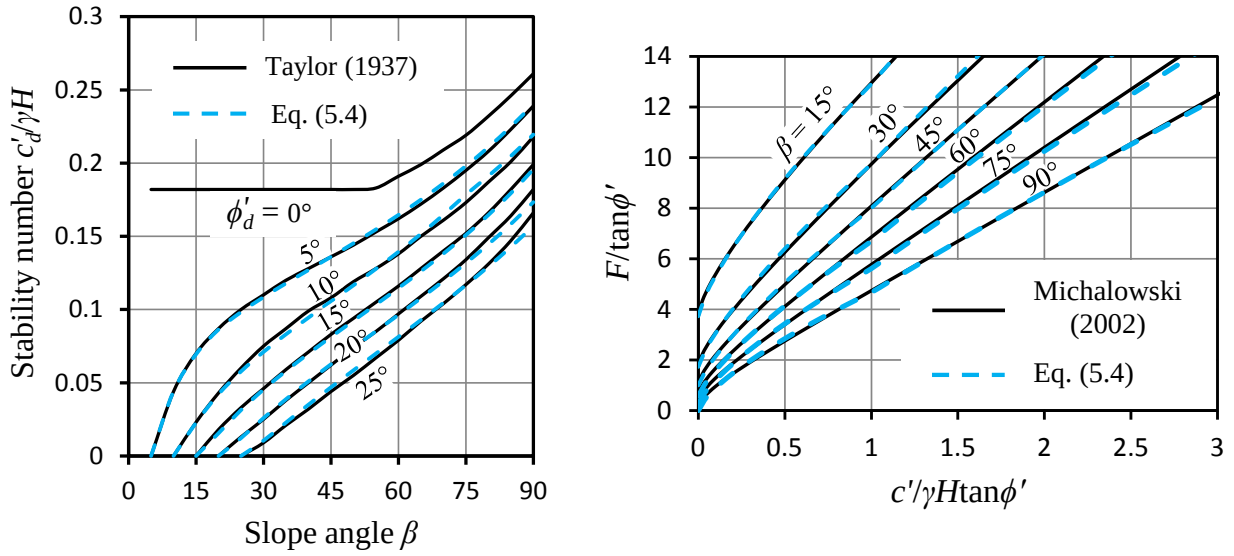

(a) Taylor (1937) (b) Michalowski (2002)

Figure 5.3 Stability charts for dry soil slopes

For a dry cohesionless slope (c' = 0), the critical slip surface is a plane parallel to the slope surface, and F is equal to $\tan\phi'/\tan\beta$ according to the infinite slope model (Taylor, 1948). Hence, G is equal to $1/\tan\beta$ for dry soil slopes. Consequently, the number of curve-fit parameters in Eq. (5.1a) would be reduced from three (A, B and G) to two (A and B):

$$\frac{F}{\tan\phi'} = A\left(\frac{c'}{\gamma H\tan\phi'}\right)^B + \frac{1}{\tan\beta} \tag{5.1b}$$

In this study, stability charts of the same format as Figure 5.3(b) were developed for dry soil slopes with β ranging from 15° to 90° at intervals of 5°. Upper bound limit analysis with a log-spiral failure mechanism, as shown in Section 4.1.1, was adopted to develop the stability charts. The stability curve for each β was curve-fitted by Eq. (5.1b), and the coefficients A and B obtained for various β are summarized in Figure 5.4.

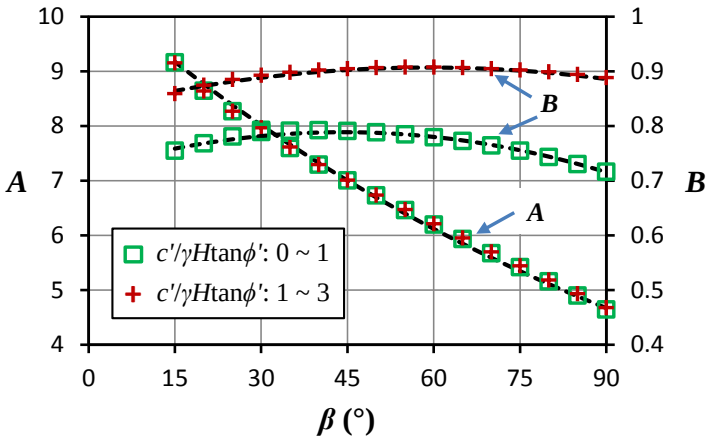

Figure 5.4 Summary of coefficients of A and B

Figure 5.4 shows that parameter A is insensitive to the curve-fitting range of $c'/\gamma H\tan\phi'$ ($0 \le c'/\gamma H\tan\phi' \le 3$), and it can be estimated by:

$$A_{\text{est}} = 10.50\exp(-0.009\beta) \tag{5.2}$$

However, parameter B is sensitive to the curve-fitting range of $c'/\gamma H\tan\phi'$, and it can be estimated by:

$$B_{\text{est}} = \begin{cases} 0.72 - 3.5\times10^{-5}\beta^2 + 0.0031\beta, \text{ if } 0 \le \dfrac{c'}{\gamma H\tan\phi'} \le 1 & \text{(5.3a)} \\ 0.83 - 2.2\times10^{-5}\beta^2 + 0.0026\beta, \text{ if } 1 < \dfrac{c'}{\gamma H\tan\phi'} \le 3 & \text{(5.3b)} \end{cases}$$

In Eqs. (5.2) and (5.3), the slope angle β is input as degree (°). For cohesive-frictional slopes encountered in practice, $c'/\gamma H\tan\phi'$ is usually between 0 and 1 and rarely exceeds 3. Therefore, B_{est} is calculated by Eq. (5.3a) for most situations.

Hence, for a dry soil slope with known β, c', γ, H and ϕ', F can be explicitly estimated by:

$$F_{est} = A_{est}\left(\frac{c'}{\gamma H \tan\phi'}\right)^{B_{est}} \tan\phi' + \frac{\tan\phi'}{\tan\beta} \tag{5.4}$$

where A_{est} and B_{est} are calculated by Eqs. (5.2) and (5.3), respectively.

The performance of Eq. (5.4) is compared with the stability charts given by Taylor (1937) and Michalowski (2002) in Figure 5.3. Good agreements are shown between the stability curves (solid) presented in the charts and the stability curves (dash) determined from Eq. (5.4). The difference between the F_{est} calculated by Eq. (5.4) and the F obtained by the stability charts is generally within ±2%. As will be shown later, Eq. (5.4) can easily be modified to assess the stability (based on rotational failure mechanism) of unsaturated soil slopes under rainfall and seismic loading.

5.2.2 Unsaturated Soil Slopes

The pore-water pressure profiles and stability of unsaturated soil slopes are greatly affected by the location of groundwater table. Hence, the stability equation for slopes with deep and shallow groundwater table is considered separately before proposing a general stability equation.

5.2.2.1 Deep Groundwater Table

For an unsaturated soil slope, if the groundwater table is deep (e.g., $H_{wt} > H$, where H_{wt} is the vertical distance between the toe of the slope and the groundwater table), as shown in Figure 5.5(a), the critical slip surface which produces the minimum factor of safety is mainly located in the moisture discontinuous zone (Figure 4.2). The pore-water pressure u_w along the slip surface

can be assumed to be a constant before the infiltration ($u_w = -\gamma_w h_c$, where γ_w is the unit weight of water, h_c is the constant pore-water pressure head in the discontinuous zone). The infiltration of rainwater can produce a wetting front and reduce the matric suction above the wetting front. The wetting front is assumed to be parallel to the ground surface with vertical depth z_w, and the matric suction above the wetting front is assumed to be zero (profile b in Figure 4.3), which is a conservative assumption for fine-grained soils and a reasonable assumption for coarse-grained soils (Lee et al., 2009).

If the contribution of matric suction to slope stability is eliminated (e.g., the entire critical slip surface is saturated by rainwater water), factor of safety of the slope can be calculated by Eq. (5.4). However, under a rainfall event the critical slip surface may only be partially saturated by rainwater, i.e., the major portion of the critical slip surface still pass through unsaturated zone in which the matric suction is not affected and contributes to slope stability. Fredlund and Rahardjo (1993) demonstrated that matric suction can readily be incorporated into conventional slope stability analysis (e.g., limit equilibrium analysis) by using "total cohesion" method, i.e., effective cohesion (c') is replaced by total cohesion [$c = c' + (u_a - u_w)\tan\phi^b$]. In this study, Eq. (5.4) is proposed for dry soil slopes, it is also extended to unsaturated soil slopes by using "total cohesion" method.

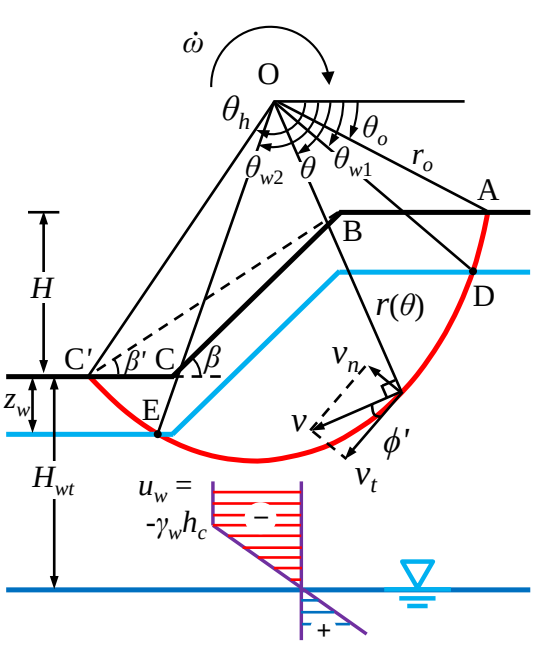

(a) Deep groundwater table

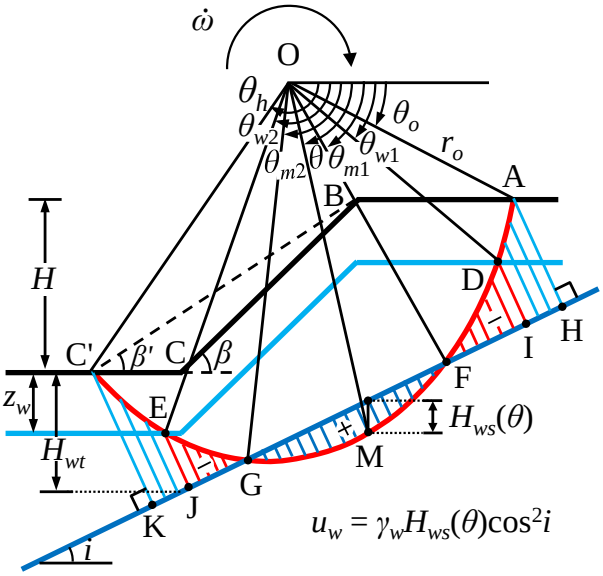

(b) Shallow groundwater table

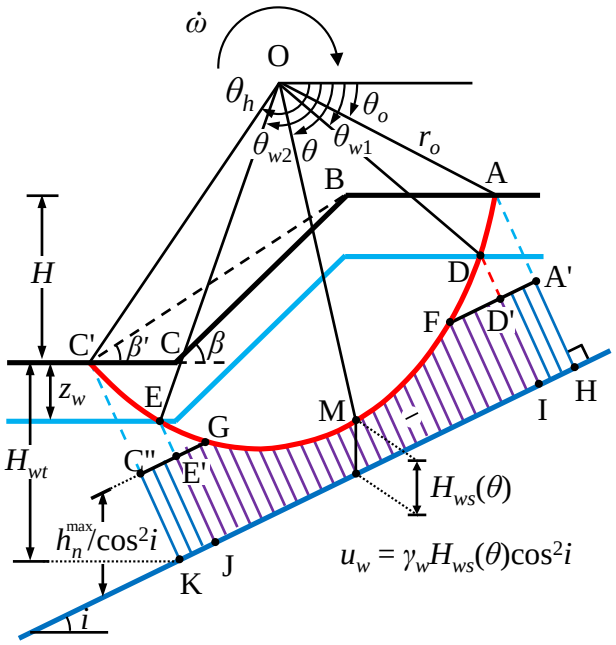

(c) Moderately deep groundwater table

Figure 5.5 Rotational failure of unsaturated soil slopes

For an unsaturated soil slope with deep groundwater table, the total cohesion during the rainfall infiltration can be calculated as:

$$c = c' + \zeta_c \gamma_w h_c \tan\phi^b \tag{5.5}$$

where ζ_c denotes the degree of contribution of matric suction to slope stability. The parameter $\zeta_c = 1$ when there is no infiltration and $\zeta_c = 0$ when the entire slip surface is saturated by rainwater.

Log-spiral upper bound limit analysis of unsaturated soil slopes under rainfall is shown in Section 4.2. In the framework of log-spiral upper bound limit analysis, the parameter ζ_c can be calculated as:

$$\zeta_c = \frac{\int_{\theta_{w1}}^{\theta_{w2}} \frac{\tan\phi^b}{\tan\phi'} u_w v_n \mathrm{d}S}{\int_{\theta_o}^{\theta_h} \frac{\tan\phi^b}{\tan\phi'} u_w v_n \mathrm{d}S} \tag{5.6a}$$

In Eq. (5.6a), the numerator and denominator denote the rate of work done by pore-water pressure ($u_w = -\gamma_w h_c$) after and before the infiltration, respectively; θ_o and θ_h are the initial and final angles of the log-spiral slip surface S; θ_{w1} and θ_{w2} are the angles corresponding to the intersection points between the wetting front and the slip surface; v_n is the normal component of the velocity vector at the slip surface. The symbols θ_o, θ_h, θ_{w1}, θ_{w2} and v_n can be found in Figure 5.5(a).

For given conditions of β, $c'/\gamma H\tan\phi'$, $(\gamma_w h_c \tan\phi^b)/(\gamma H\tan\phi')$ and z_w/H, the critical slip surface of the slope can be searched with β', θ_o and θ_h being the variables. The parameter ζ_c is then

calculated using Eq. (5.6a). It was found that ζ_c can also be obtained graphically for the critical slip surface:

$$\zeta_c^g = \frac{l_{\widehat{DE}}}{l_{\widehat{AC'}}} \tag{5.6b}$$

where $l_{\widehat{DE}}$ is the length of the slip surface not saturated by rainwater [arc DE in Figure 5.5(a)], and $l_{\widehat{AC'}}$ is the total length of the slip surface [arc AC′ in Figure 5.5(a)]. For a given log-spiral slip surface, the graphical parameter ζ_c^g can be calculated analytically, as shown in Appendix C. In Figure 5.6, ζ_c calculated by Eq. (5.6a) are compared with ζ_c^g obtained by Eq. (5.6b) for slopes of given β (= 15°, 30°, …, 90°), ϕ_d' [= 5°, 10°, …, min(β - 5°, 40°)], $\left(\gamma_w h_c \tan\phi^b\right)/\left(\gamma H \tan\phi'\right)$ (= 0.025, 0.1, 0.5) and z_w/H (= 0, 0.1, …, 1). Good agreements are shown between ζ_c^g and ζ_c with coefficient of determination R^2 = 0.9998. Hence, the parameter ζ_c in Eq. (5.5) can be estimated graphically when a theoretical approach is not available.

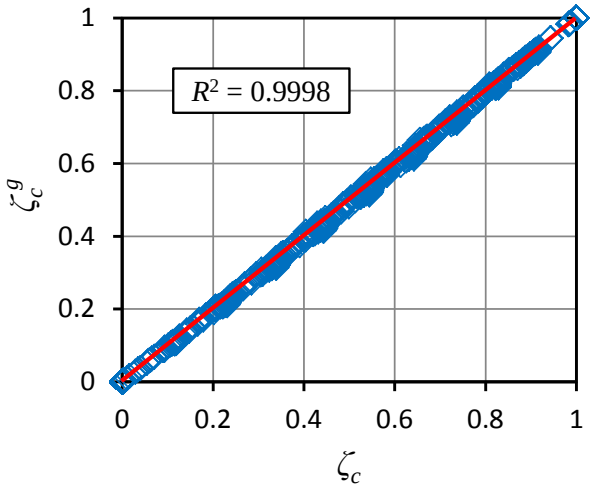

Figure 5.6 Comparison of ζ_c obtained by Eq. (5.6a) and ζ_c^g obtained by Eq. (5.6b)

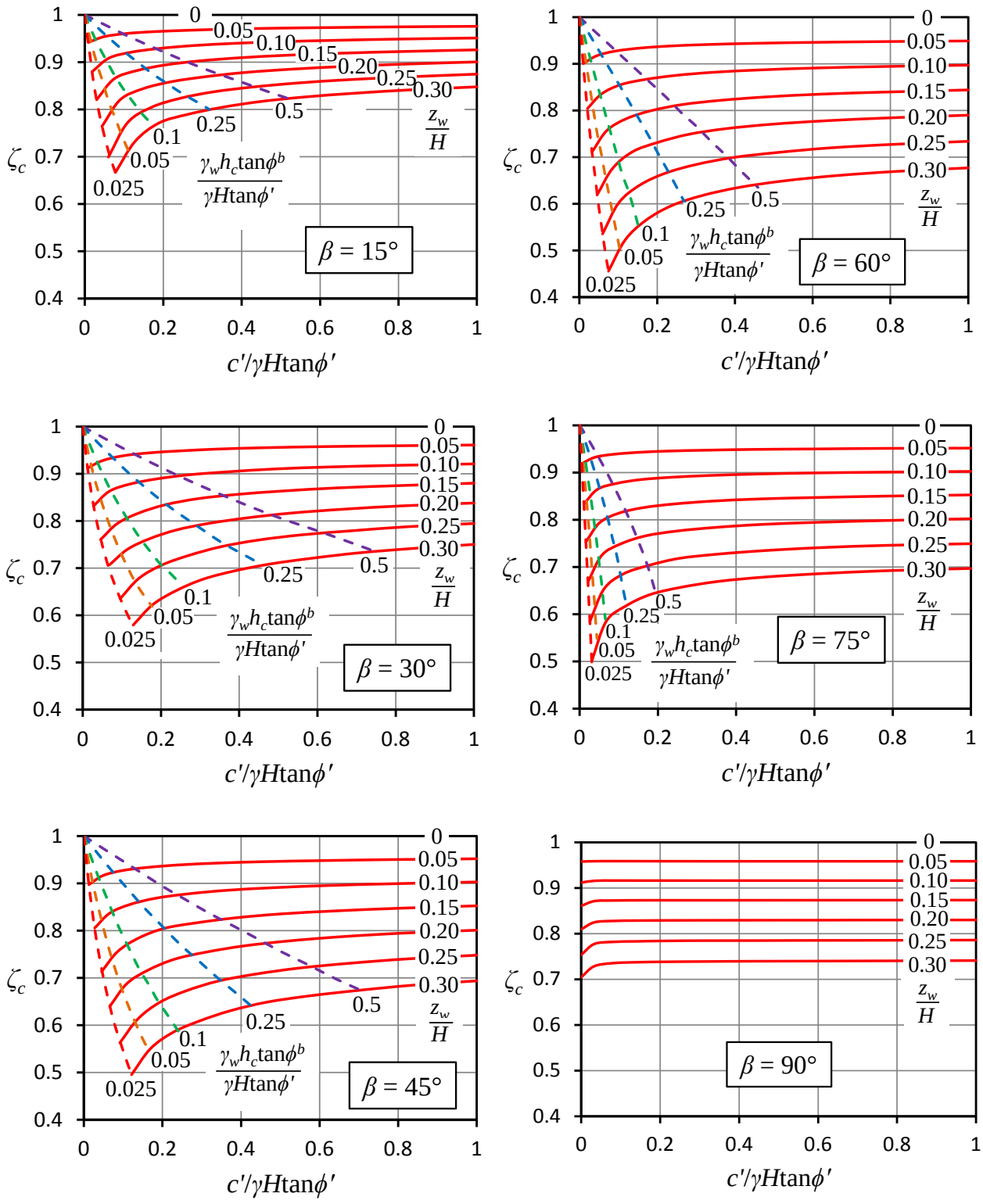

Figure 5.7 Charts of ζ_c for various conditions

The parameter ζ_c is rarely affected by $(\gamma_w h_c \tan\phi^b)/(\gamma H \tan\phi')$ and mainly dependent on β, z_w/H and $c'/\gamma H \tan\phi'$. The charts of ζ_c obtained by Eq. (5.6a) are shown in Figure 5.7. The parameter ζ_c can be obtained for given β, $c'/\gamma H \tan\phi'$ and z_w/H using the charts. The governing failure mode of an unsaturated soil slope under rainfall infiltration can also be determined using the charts provided in Figure 5.7. For a given β ($\beta < 90°$), a solid curve can be obtained according to the given z_w/H, and a dash curve can be obtained according to the given $(\gamma_w h_c \tan\phi^b)/(\gamma H \tan\phi')$. The two curves intersect and the corresponding $c'/\gamma H \tan\phi'$ of the intersection point is the critical $c'/\gamma H \tan\phi'$, below which translational failure is the governing failure mode and above which rotational failure is the governing failure mode. For $\beta = 90°$, the critical $c'/\gamma H \tan\phi'$ is equal to zero and rotational failure is the governing failure mode for any soil slope with $c' > 0$.

Figure 5.7 shows that ζ_c increases with the increase in $c'/\gamma H \tan\phi'$. The reason is that the slip surface goes deeper with the increase in $c'/\gamma H \tan\phi'$ (Jiang and Yamagami, 2006), as a result $l_{\widehat{DE}}$ increases while $\left(l_{\widehat{AC'}} - l_{\widehat{DE}}\right)$ is relatively constant for a given z_w/H. Figure 5.7 also shows that for fixed values of $c'/\gamma H \tan\phi'$ and z_w/H, ζ_c of moderately steep slope (e.g., $\beta = 45°$ and $60°$) is smaller than the ζ_c for gentle slope (e.g., $\beta = 15°$) and steep slope (e.g., $\beta = 90°$). The reasons are explained as follows. For steep and moderately steep slopes, the critical slip surfaces would usually pass through the toe, i.e., $\beta' = \beta$ (Baker, 2003). Rainfall infiltrates into a steep slope mainly from the slope crest ($l_{\widehat{AD}} > 0$, $l_{\widehat{C'E}} \to 0$), while rainfall infiltrates into a moderately steep slope from both the slope crest and the slope surface ($l_{\widehat{AD}} > 0, l_{\widehat{C'E}} > 0$). Although rainfall can

also infiltrate into a gentle slope from both the slope crest and the slope surface, the critical slip surface of a gentle slope would usually pass below the toe, i.e., $\beta' < \beta$ (Baker, 2003). The length of the slip surface $l_{\widehat{AC'}}$ for a gentle slope is larger than the $l_{\widehat{AC'}}$ for a moderately steep slope which has the same height *H*. According to Eq. (5.6b), the ζ_c is smaller (the loss of matric suction is greater) in moderately steep slopes than in gentle and steep slopes for the same amount of rainwater infiltration. This may explain the phenomenon that rainfall-induced landslides occur frequently in moderately steep terrains and rarely in gentle and steep terrains (Toll, 2001; Dai et al., 2003).

5.2.2.2 Shallow Groundwater Table

If the groundwater table of the unsaturated soil slope is shallow (e.g., H_{wt} = 0), as shown in Figure 5.5(b), the slip surface is mainly located in the capillary saturated zone or below. The pore-water pressure can be assumed to be hydrostatic relative to the groundwater table before the infiltration [$u_w(\theta) = \gamma_w H_{ws}(\theta)\cos^2 i$, where $H_{ws}(\theta)$ is the vertical distance between the groundwater table and the slip surface and it is a function of θ in the polar coordinates, *i* is the inclination of the groundwater table. $H_{ws}(\theta)$ is positive if the groundwater table is above the slip surface, and it is negative if the groundwater table is below the slip surface].

During the infiltration, Eq. (5.5) can be modified to be:

$$c = c' - \gamma_w \bar{h}_p \tan\phi' + \zeta_h \gamma_w \bar{h}_c \tan\phi^b \tag{5.7}$$

where $\overline{h}_p$ and $\overline{h}_c$ are the average positive and negative pore-water pressure heads on the slip surface before the infiltration, and ζ_h denotes the degree of contribution of matric suction (hydrostatic) to the slope stability. The parameter $\zeta_h = 1$ when there is no infiltration, ζ_h decreases during the infiltration, and $\zeta_h = 0$ when the matric suction in the unsaturated zone is eliminated. If the groundwater table rises during the infiltration, the rising groundwater table can be taken into account by increasing the value of $\overline{h}_p$.

In the framework of upper bound limit analysis, $\overline{h}_p$ and $\overline{h}_c$ can be considered as the equivalent pore-water pressure heads that can lead to the same amount of work done by positive and negative pore-water pressures, respectively:

$$\overline{h}_p = \frac{\int_{\theta_{m1}}^{\theta_{m2}} u_w(\theta) v_n \mathrm{d}S}{\gamma_w \int_{\theta_{m1}}^{\theta_{m2}} v_n \mathrm{d}S} \tag{5.8a}$$

$$\overline{h}_c = -\frac{\int_{\theta_o}^{\theta_{m1}} u_w(\theta) v_n \mathrm{d}S + \int_{\theta_{m2}}^{\theta_h} u_w(\theta) v_n \mathrm{d}S}{\gamma_w \int_{\theta_o}^{\theta_{m1}} v_n \mathrm{d}S + \gamma_w \int_{\theta_{m2}}^{\theta_h} v_n \mathrm{d}S} \tag{5.8b}$$

Parameter ζ_h can be calculated as the ratio of the rate of work done by negative pore-water pressure after the infiltration to the rate of work done by negative pore-water pressure before the infiltration:

$$\zeta_h = \frac{\int_{\theta_{w1}}^{\theta_{m1}} u_w(\theta) v_n \mathrm{d}S + \int_{\theta_{m2}}^{\theta_{w2}} u_w(\theta) v_n \mathrm{d}S}{\int_{\theta_o}^{\theta_{m1}} u_w(\theta) v_n \mathrm{d}S + \int_{\theta_{m2}}^{\theta_h} u_w(\theta) v_n \mathrm{d}S} \tag{5.8c}$$

In Eqs. (5.8a), (5.8b) and (5.8c), θ_{m1} and θ_{m2} are the angles corresponding to the intersection points between the groundwater table and the slip surface, as shown in Figure 5.5(b).

For given conditions of β, $c'/\gamma H\tan\phi'$, γ_w/γ, H_{wt}/H, i, $\tan\phi^b/\tan\phi'$ and z_w/H, the critical slip surface of the slope can be searched with β', θ_o and θ_h being the variables. The parameters $\bar{h}_p$, $\bar{h}_c$ and ζ_h are then calculated by Eqs. (5.8a), (5.8b) and (5.8c), respectively. It was found that $\bar{h}_p$, $\bar{h}_c$ and ζ_h can also be obtained graphically for the critical slip surface:

$$\bar{h}_p^g = \frac{A_{\mathrm{GMF}}}{l_{\mathrm{GF}}}\cos i \tag{5.8d}$$

$$\bar{h}_c^g = \frac{A_{\mathrm{C'GK}} + A_{\mathrm{AFH}}}{l_{\mathrm{KG}} + l_{\mathrm{FH}}}\cos i \tag{5.8e}$$

$$\zeta_h^g = \frac{A_{\mathrm{EGJ}} + A_{\mathrm{DFI}}}{A_{\mathrm{C'GK}} + A_{\mathrm{AFH}}} \tag{5.8f}$$

where A denotes area, l denotes length, and the subscripts of A and l denote the location of the regions and planes shown in Figure 5.5(b). For example, in Eq. (5.8d) A_{GMF} denotes the area of the region GMF and l_{GF} denotes the length of the plane GF. For a given log-spiral slip surface, the parameters $\bar{h}_p^g$, $\bar{h}_c^g$ and ζ_h^g can be calculated analytically, as shown in Appendix C.

In order to compare the $\bar{h}_p$, $\bar{h}_c$ and ζ_h obtained theoretically and graphically, parametric studies were conducted with β (= 15°, 30°, …, 90°), H_{wt}/H (= 0, 0.2, 0.5), i/β (= 0, 0.2, 0.4), γ_w/γ (= 0.5), $\phi_d^b = \phi_d'$ [= 5°, 10°, …, min(β - 5°, 40°)] and z_w/H = (0, 0.1, …, 1). The results are summarized in Figure 5.8. In Figures 5.8(a) and (b), $\bar{h}_p$ and $\bar{h}_c$ are normalized by H. It is shown that the

graphical $\bar{h}_p^g$ obtained by Eq. (5.8d) generally agree well with the theoretical $\bar{h}_p$ obtained by Eq. (5.8a). Graphical approaches tend to underestimate $\bar{h}_c$ and overestimate ζ_h, while it was found that the underestimation and overestimation would cancel each other out when the obtained $\bar{h}_c^g/H$ and ζ_h^g are substituted into Eq. (5.9), as demonstrated in Figure 5.8(d). Hence, the graphical approaches from Eq. (5.8d) to Eq. (5.8f) can be conveniently and reliably used when rigorous approaches are not available.

For a slope with $\beta \geq 45°$, the slip surface is usually a shallow toe circle (Baker, 2003). For $\beta \geq 45°$, $H_{wt} \geq 0$ and $i = 0°$, the slip surface would generally not pass below the groundwater table, and the parameter $\bar{h}_p$ is equal to (or can be approximated by) zero. For a slope with $\beta < 45°$, the slip surface is usually a deep toe circle or base circle (Baker, 2003), and the slip surface goes deeper with the increase in $c'/\gamma H\tan\phi'$ and $\tan\phi^b/\tan\phi'$.

According to Eqs. (5.8a), (5.8b) and (5.8c), charts are provided in Figure 5.9 for $\bar{h}_p$, $\bar{h}_c$ and ζ_h. In Figure 5.9(a), the values of $\bar{h}_p/H$ are given for $\beta = 15°$ and 30°, with $i = 0°$, $\phi^b = \phi'$ and $c'/\gamma H\tan\phi' = 0$, 0.2 and 0.5. It can be seen that $\bar{h}_p/H$ increases with the increase in $c'/\gamma H\tan\phi'$, and $\bar{h}_p/H$ decreases with the increase in H_{wt}/H. The parameter $\bar{h}_c$ is mainly affected by β, H_{wt} and i. In Figure 5.9(b), the values of $\bar{h}_c/H$ are given for various β and H_{wt}/H with $i = 0°$. For $\beta \geq 50°$, $\bar{h}_c/H$ linearly increases with the increase in H_{wt}/H, while the influence of H_{wt}/H on the $\bar{h}_c/H$ of the gentle slope (e.g., $\beta = 15°$) is slight.

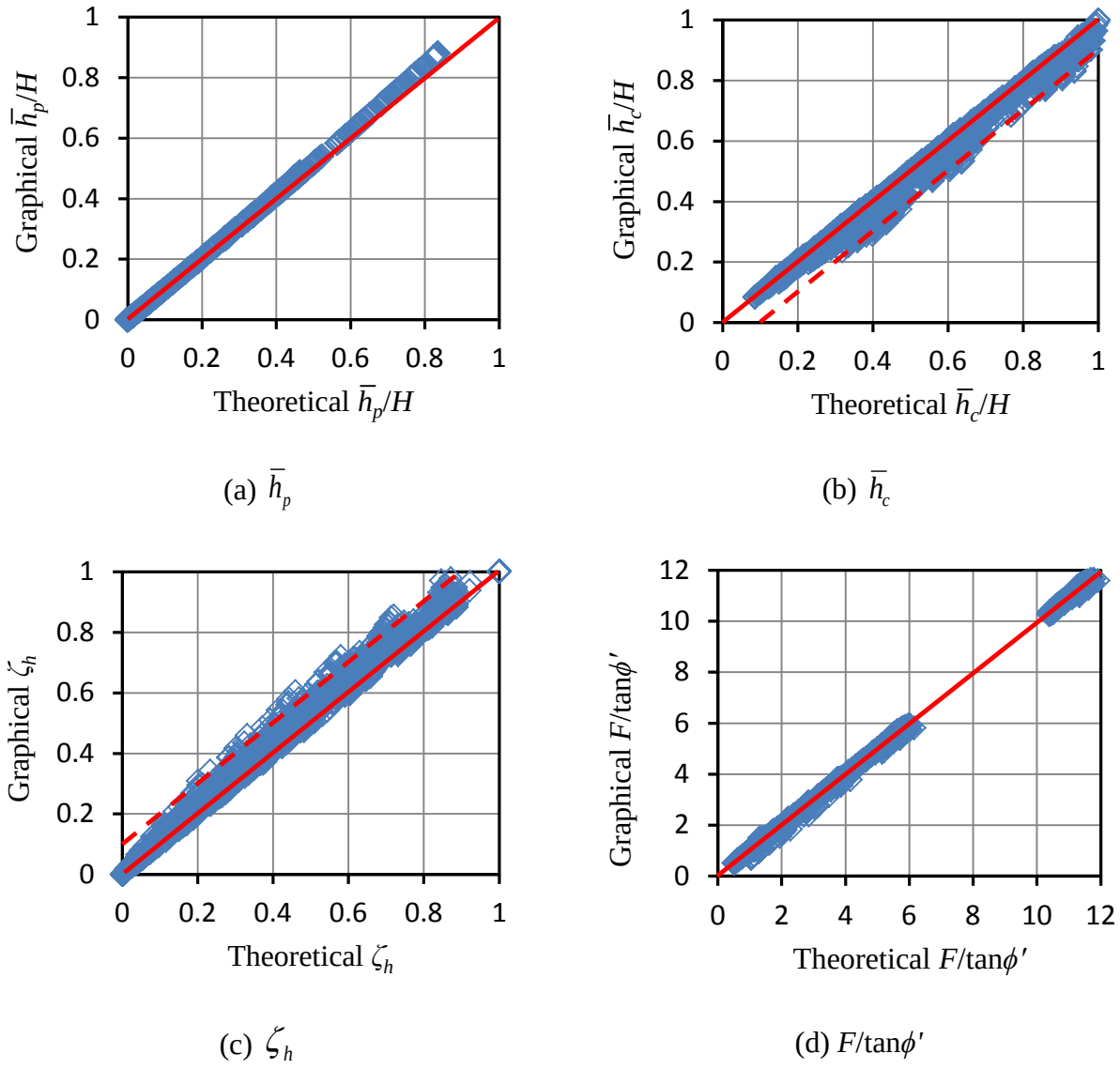

(a) $\bar{h}_p$ (b) $\bar{h}_c$

(c) ζ_h (d) $F/\tan\phi'$

Figure 5.8 Comparisons of $\bar{h}_p$, $\bar{h}_c$, ζ_h and $F/\tan\phi'$ obtained theoretically and graphically

The parameter ζ_h mainly depends on z_w/H. A large number of parametric studies were performed with various β (= 15° ~ 90°), $c'/\gamma H\tan\phi'$ (= 0 ~ 1), γ_w/γ (= 0.5), H_{wt}/H (= 0 ~ 0.5), i (= 0 ~ 0.2β), $\tan\phi^b/\tan\phi'$ (= 1/3 ~ 1) and z_w/H (= 0 ~ 0.7) as given conditions. The obtained mean, upper and lower bound values of ζ_h are plotted against z_w/H, as shown in Figure 5.9(c). A

highly linear relationship is shown between ζ_h and z_w/H. The parameter ζ_h can be approximated by:

$$\zeta_h = 1 - 1.4\frac{z_w}{H} \tag{5.8g}$$

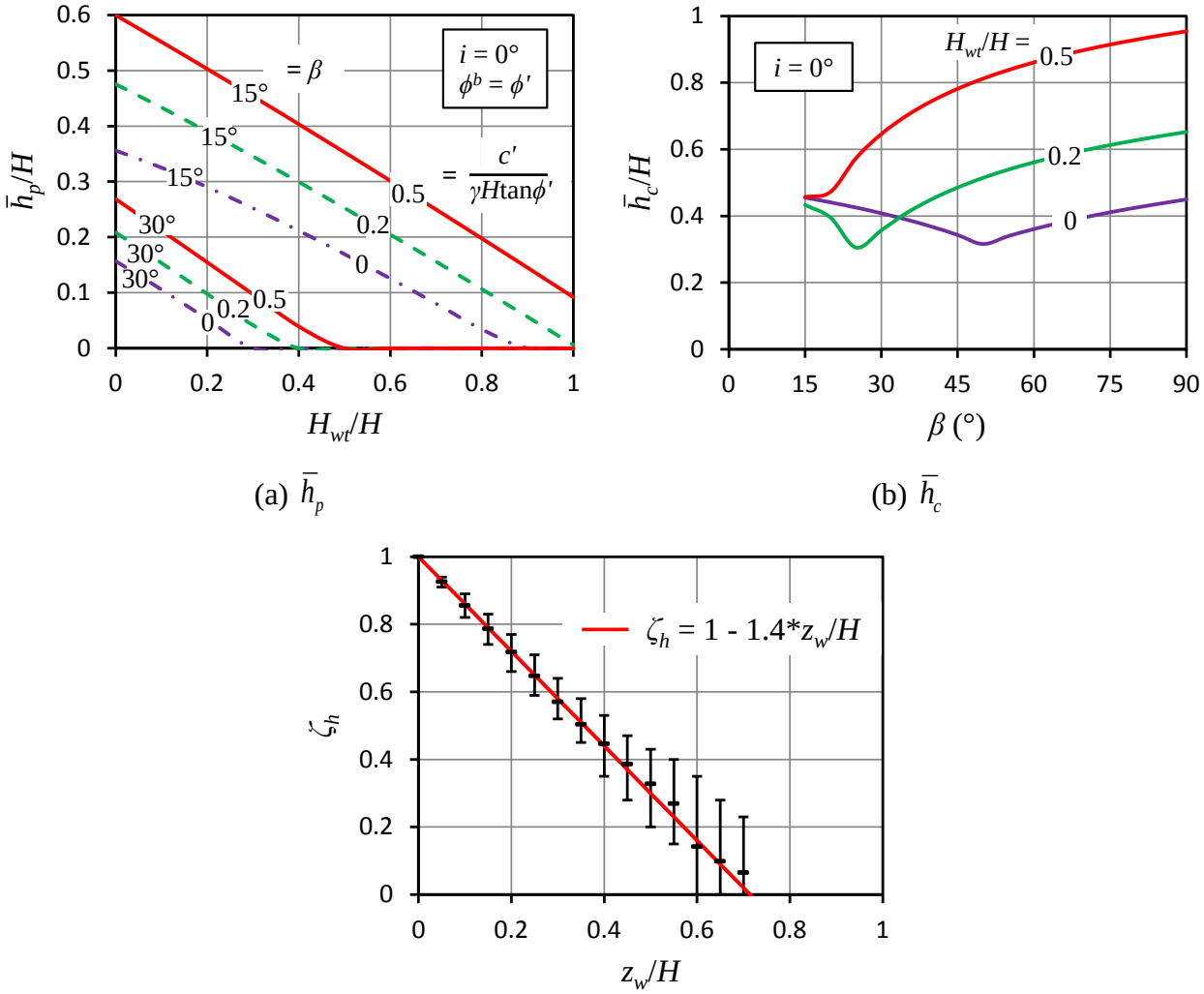

(a) $\bar{h}_p$

(b) $\bar{h}_c$

(c) ζ_h

Figure 5.9 Charts for $\bar{h}_p$, $\bar{h}_c$ and ζ_h

5.2.2.3 General Stability Equation

Factors of safety of dry soil slopes can be calculated by Eq. (5.4). By using the "total cohesion" method (Fredlund and Rahardjo, 1993), i.e., the effective cohesion c' is replaced by the total cohesion c [Eq. (5.5) or Eq. (5.7)], Eq. (5.4) is extended to calculate the factors of safety of unsaturated soil slopes under rainfall based on rotational failure mechanism:

$$F_{\text{rot}}^{\text{est}} = A_{\text{est}}\left(\frac{c'}{\gamma H \tan\phi'} - \frac{\gamma_w h_p \tan\phi'}{\gamma H \tan\phi'} + \zeta \frac{\gamma_w h_c^* \tan\phi^b}{\gamma H \tan\phi'}\right)^{B_{\text{est}}} \tan\phi' + \frac{\tan\phi'}{\tan\beta} \qquad (5.9)$$

In Eq. (5.9), for a slope with deep groundwater table [Figure 5.5(a)], $h_p = 0$, $\zeta = \zeta_c$ and $h_c^* = h_c$. For a slope with shallow groundwater table [Figure 5.5(b)], $h_p = \bar{h}_p$, $\zeta = \zeta_h$ and $h_c^* = \bar{h}_c$.

For a slope with moderately deep groundwater table, as shown in Figure 5.5(c), the slip surface passes through both the capillary saturated zone and the discontinuous zone. The pore-water pressure distributes hydrostatically before a maximum negative pore-water pressure head $h_n^{\max}$ is reached. Upper bound limit analysis for a slope with moderately deep groundwater table is not given in Chapter 4. Hence, no theoretical approach is available to calculate the parameters h_p, ζ and h_c^* at the moment. However, Sections 5.2.2.1 and 5.2.2.2 have shown that graphical approaches can be used to estimate the required input parameters in Eq. (5.9). The graphical approaches are extended to the situation where the groundwater table is moderately deep. If the slip surface passes below the groundwater table, $\bar{h}_p$ can be estimated by Eq. (5.8d). The graphical approaches to estimate $\bar{h}_c$ [Eq. (5.8e)] and ζ_h [Eq. (5.8f)] are modified to be Eq. (5.10a) and Eq. (5.10b), respectively. The subscripts of *A* and *l* can be found in Figure 5.5(c).

$$\bar{h}_c^g = \frac{A_{\text{C''KHA'FMG}}}{l_{\text{KH}}} \cos i \tag{5.10a}$$

$$\zeta_h^g = \frac{A_{\text{E'JID'FMG}}}{A_{\text{C''KHA'FMG}}} \tag{5.10b}$$

5.3 Stability Equation for Translational Failure Mechanism

For an unsaturated soil slope under rainfall infiltration, shallow translational failure above the wetting front may be more critical than the global rotational failure shown in Figure 5.5. A kinematically admissible translational failure mode has been proposed in Chapter 4. As shown in Figure 5.10, the translational slip consists of a translational component DEFG which is a parallelogram and two log-spiral rotational components ABDE (at the crest) and CFG (at the toe). The spirals $\overset{\frown}{\text{AE}}$ and $\overset{\frown}{\text{CF}}$ are tangent to the plane EF at points E and F, respectively. The plane EF is coincident with or is located above the wetting front. For given conditions of β, $c'/\gamma H$, ϕ' and z_w/H, the critical translational slip surface can be searched with θ_o, θ_h and H_{trl}/H (H_{trl} is the vertical height of the translational component) being the variables, and the obtained factor of safety F_{trl} has considered the boundary effects.

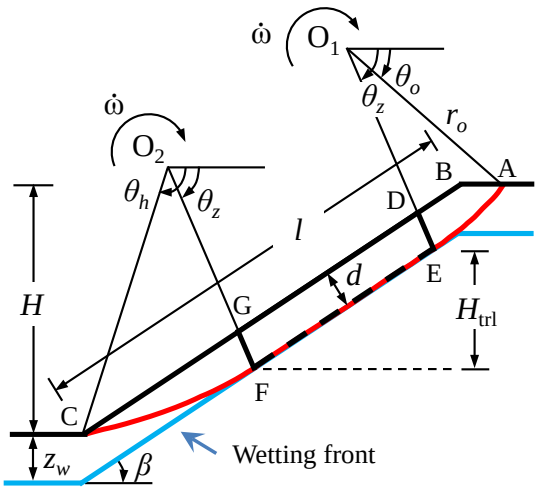

Figure 5.10 Translational failure of an unsaturated soil slope

5.3.1 Stability Equation

Stability chart for unsaturated soil slopes under rainfall infiltration due to translational failure can be developed according to Eq. (4.67). Stability charts were developed with β ranging from 15° to 85° at intervals of 5° and z_w/H ranging from 0.02 to 0.3 at intervals of 0.02. Hence, 15 × 15 = 225 stability curves have been produced. As an example, stability curves for β = 45° with z_w/H equals to 0.1, 0.2 and 0.3 are shown in Figure 5.11. The stability curves show high linearity. Hence, each stability curve was fitted by Eq. (5.11) with curve-fitting parameter a and coefficient of determination R^2. An R^2 value of 1 gives the best agreement, and an R^2 value of 0 indicates no correlation at all. The coefficient of determination R^2 is generally larger than 0.999.

$$\frac{F_{\text{trl}}}{\tan\phi'} = a\frac{c'}{\gamma H\tan\phi'} + \frac{1}{\tan\beta} \tag{5.11}$$

The obtained coefficients a are partially shown in Table 5.1. Through regression analysis it was found that parameter a can be estimated by:

$$a_{\text{est}} = \frac{H}{z_w}\frac{1}{\sin\beta\cos\beta} + 5.0\exp\left(-0.008\beta\right) \tag{5.12}$$

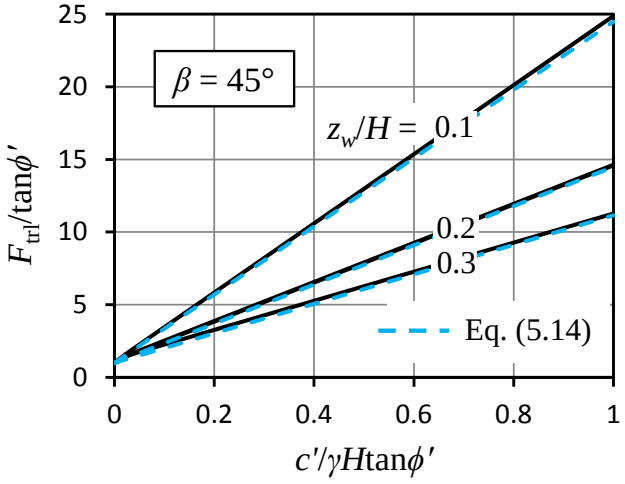

Figure 5.11 Stability chart for translational failure

Table 5.1 Summary of the curve-fit parameter *a*

	z_w/H = 0.02		z_w/H = 0.10		z_w/H = 0.20		z_w/H = 0.30	
β	*a*	R^2	*a*	R^2	*a*	R^2	*a*	R^2
15°	207.9368	1	45.3781	1	24.8072	0.9999	18.0065	0.9995
30°	121.6437	1	27.5107	1	15.6851	0.9996	11.8733	0.9982
45°	105.4178	1	23.9233	1	13.7075	0.9995	10.4212	0.9979
60°	120.6985	1	26.7400	1	14.9066	0.9997	11.0255	0.9988
75°	205.8726	1	43.7308	1	23.2440	1	16.3990	0.9998

In Figure 5.10, the ratios d/l and z_w/H are related as follows:

$$\frac{d}{l} = \frac{z_w}{H}\sin\beta\cos\beta \tag{5.13}$$

According to Eqs. (5.11), (5.12) and (5.13), the factor of safety of an unsaturated soil slope under rainfall infiltration due to translational failure can be estimated by:

$$F_{\text{trl}}^{\text{est}} = \left[\frac{l}{d} + 5.0\exp\left(-0.008\beta\right)\right]\frac{c'}{\gamma H} + \frac{\tan\phi'}{\tan\beta} \tag{5.14}$$

Eq. (5.14) can be applied reliably within the range $0 < z_w/H \leq 0.3$ and $15° \leq \beta < 90°$. The dash curves shown in Figure 5.11 are obtained by Eq. (5.14). Good agreement can be found between the stability chart and Eq. (5.14). The differences between $F_{\text{trl}}^{\text{est}}$ and F_{trl} are mostly within 3% ($F_{\text{trl}}^{\text{est}}/F_{\text{trl}} = 0.97 \sim 1$) and generally within 10% ($F_{\text{trl}}^{\text{est}}/F_{\text{trl}} = 0.90 \sim 1$).

For $0.3 < z_w/H \leq 0.6$, the failure mode is no longer purely translational, and it is usually a compound of translational and rotational failure. If Eq. (5.14) is used, the underestimation of F_{trl} is generally within 10% and can be up to 25%. For $z_w/H > 0.6$, the failure mode would generally be pure rotational and Eq. (5.9) should be used instead of Eq. (5.14).

5.3.2 Accuracy of the Infinite Slope Model

For an unsaturated soil slope with $u_w = 0$ above the wetting front, factor of safety due to translational failure can also be obtained by infinite slope analysis with the neglect of boundary effects. It is denoted as F_{trl}^{IS} and calculated by:

$$F_{\text{trl}}^{IS} = \frac{c'}{\gamma z_w \sin\beta\cos\beta} + \frac{\tan\phi'}{\tan\beta} \tag{5.15a}$$

Eq. (5.15a) can be rearranged to be:

$$F_{\text{trl}}^{IS} = \frac{c'}{\gamma H}\frac{H}{z_w}\frac{1}{\sin\beta\cos\beta} + \frac{\tan\phi'}{\tan\beta} = \frac{c'}{\gamma H}\frac{l}{d} + \frac{\tan\phi'}{\tan\beta} \tag{5.15b}$$

It has been pointed out by Taylor (1948) that infinite slope model is only accurate when d/l is small, and it increasingly underestimates the stability of a slope with the increase in d/l. Griffiths

et al. (2011a) conducted finite element analysis and infinite slope analysis on "long" slopes of various d/l. They found that the factors of safety obtained by infinite slope analysis (neglect the boundary effects) are always conservative, and only at small d/l the factors of safety obtained by finite element analysis (consider the boundary effects) approach the infinite slope solutions.

The accuracy of infinite slope model may also be affected by the slope geometry and soil properties. Milledge et al. (2012) investigated the influence of c', ϕ', γ, z_w, β and u_w on the accuracy of infinite slope model, and found that the accuracy is affected by β while the influences of other parameters are not clear. The latter may due to the fact that the parameters c', ϕ', γ, etc. were investigated separately, rather than being investigated as a dimensionless group, e.g., $c'/\gamma H\tan\phi'$.

If the $F_{\text{trl}}^{\text{est}}$ obtained by Eq. (5.14), which has considered the boundary effects, is treated as a benchmark solution, the difference between $F_{\text{trl}}^{\text{est}}$ and F_{trl}^{IS} can be considered as the underestimation caused by the neglect of boundary effects. The error (underestimation) caused by the infinite slope analysis can be calculated as:

$$\text{Error}(\%)=\frac{F_{\text{trl}}^{\text{est}}-F_{\text{trl}}^{IS}}{F_{\text{trl}}^{\text{est}}}=\frac{5.0\exp(-0.008\beta)}{5.0\exp(-0.008\beta)+\dfrac{l}{d}+\dfrac{\gamma H\tan\phi'}{c'}\dfrac{1}{\tan\beta}}\times 100\% \qquad (5.16)$$

From Eq. (5.16), it can be seen that the accuracy of infinite slope analysis is not only affected by d/l, but also affected by $c'/\gamma H\tan\phi'$ and β. The error is negligible when d/l is small ($d/l \rightarrow 0$) or the soil is cohesionless ($c'/\gamma H\tan\phi' \rightarrow 0$), and it increases with the increase in d/l and $c'/\gamma H\tan\phi'$, as illustrated in Figure 5.12 for $\beta = 45°$. In order to limit the underestimation (e.g., 10%), d/l must be limited for given $c'/\gamma H\tan\phi'$ and β, as shown in Figure 5.13. It can be seen that the

limiting value of d/l generally decreases with the increase in β for a specific $c'/\gamma H\tan\phi'$. For a given β, the limiting value of d/l decreases with the increase in $c'/\gamma H\tan\phi'$.

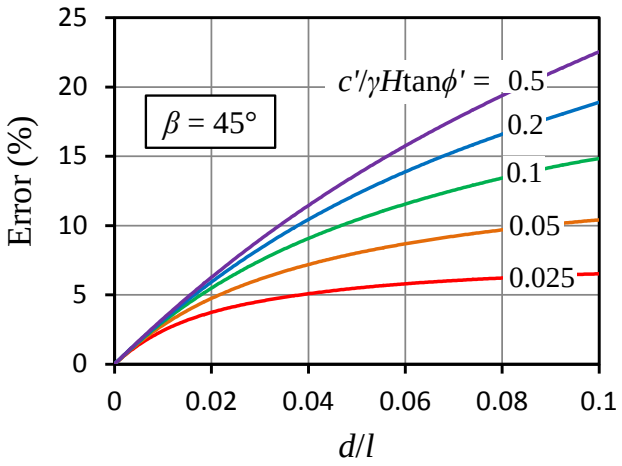

Figure 5.12 The error caused by infinite slope analysis

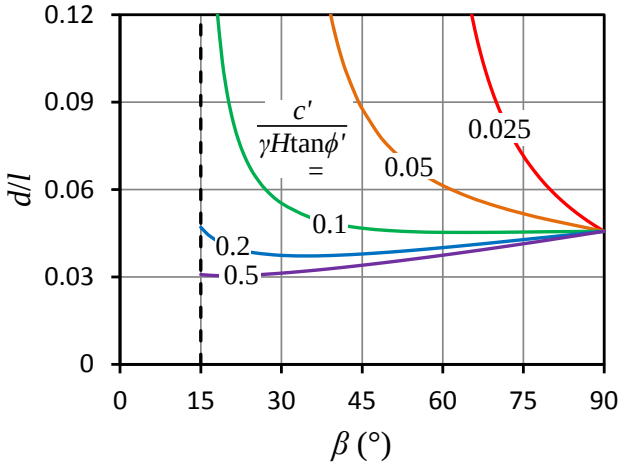

Figure 5.13 Limits of d/l for 10% error in infinite slope analysis

5.4 Stability Equations for Saturated Soil Slopes

An unsaturated soil slope may change from unsaturated to saturated state under a rainfall of high intensity and prolonged duration. The pore-water pressure ratio r_u proposed by Bishop and Morgenstern (1960) is widely used to describe the pore-water pressure condition of a saturated soil slope:

$$r_u = \frac{u_w}{\gamma h} \tag{5.17}$$

where u_w is the magnitude of pore-water pressure at a point, γ is the bulk unit weight of the soil, and h is the vertical distance between the point on the slip surface and the ground surface, as shown in Figure 5.14.

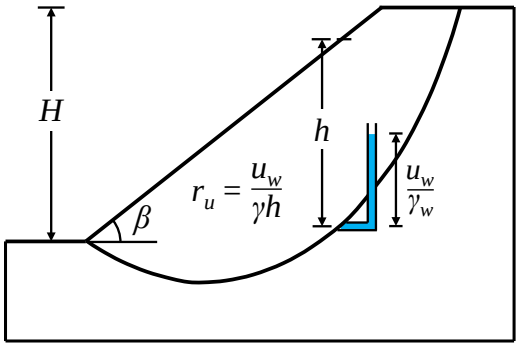

Figure 5.14 Geometry of a saturated soil slope (modified from Bishop and Morgenstern, 1960)

5.4.1 Gentle and Moderately Steep Slopes

Bishop and Morgenstern (1960) found that there is a linear relationship between F and r_u for certain ranges of β and $c'/\gamma H\tan\phi'$:

$$F = m - nr_u \tag{5.18}$$

where m and n are stability coefficients. The linear relationship has later been confirmed and extended to wider ranges of β and $c'/\gamma H\tan\phi'$ by other researchers, as summarized in Table 5.2.

Table 5.2 Valid range for the linear relationship between F and r_u

	Bishop and Morgenstern (1960)	O'Connor and Mitchell (1977)	Chandler and Peiris (1989)	Barnes (1991)
β	11.3° - 26.6°	11.3° - 26.6°	11.3° - 63.4°	11.3° - 63.4°
$c'/\gamma H$	0 - 0.05	0.075 - 0.10	0 - 0.15	0 - 0.15
ϕ'	10° - 40°	20° - 40°	20° - 40°	20° - 45°
$c'/\gamma H\tan\phi'$	0 - 0.2836	0.0894 - 0.2748	0 - 0.4121	0 - 0.4121

For a saturated cohesionless slope ($c' = 0$), the critical slip surface is a plane parallel to the slope surface and F can be calculated by the infinite slope model (Bishop and Morgenstern, 1960):

$$F = \frac{\tan\phi'}{\tan\beta}\left(1 - r_u \sec^2\beta\right) \tag{5.19}$$

Factor of safety of a dry soil slope ($r_u = 0$) can be explicitly calculated by Eq. (5.4). The stability equation Eq. (5.4) is extended to saturated soil slopes ($r_u > 0$). According to Eq. (5.18), F is a linear function of r_u. The extended equation should be transformed into Eq. (5.19) when $c' = 0$, and Eq. (5.4) when $r_u = 0$. An equation which satisfies all the above conditions is given below:

$$F_{\text{est}} = A_{\text{est}}\left(\frac{c'}{\gamma H\tan\phi'}\right)^{B_{\text{est}}}\tan\phi' + \frac{\tan\phi'}{\tan\beta} - \left(\frac{c'}{\gamma H}\frac{1}{\tan\beta} + \frac{\tan\phi'}{\sin\beta\cos\beta}\right)r_u \tag{5.20}$$

A number of stability equations have been suggested in the literature for saturated soil slopes, as summarized in Table 2.5. The performance of Eq. (5.20) and the existing slope stability equations listed from Eq. (2.36) to Eq. (2.40) are evaluated with the stability charts presented by Barnes (1991). For a combination of β, $c'/\gamma H$ and ϕ' listed in Table 5.3, a pair of m and n can be

found in Barnes (1991), and F can be calculated by Eq. (5.18) for a given r_u (= 0, 0.25 and 0.5). By substituting β, $c'/\gamma H$, ϕ' and r_u into Eq. (5.20) or the existing stability equations in Table 2.5, F_{est} can be calculated. In the calculations of Eqs. (2.37) – (2.40), the values of γ and H are fixed to be the mean values of the respective training data sets which can be found in Table 2.6 (the numbers in the brackets), and c' is back calculated from a given $c'/\gamma H$. A total of 882 (= 7×7×6×3) calculations for F and F_{est} have been carried out. The obtained F_{est} are plotted against F in Figure 5.15, which show that the F_{est} calculated by Eq. (5.20) consistently agree well with the F, while the F_{est} calculated by the existing stability equations may considerably overestimate or underestimate the F.

Table 5.3 Valid range for the tabulated coefficients m and n in Barnes (1991)

β (°) :	11.3, 14.0, 18.4, 26.6, 33.7, 45.0, 63.4
$c'/\gamma H$:	0, 0.025, 0.050, 0.075, 0.100, 0.125, 0.150
ϕ' (°) :	20, 25, 30, 35, 40, 45

The performance of Eq. (5.20) and the existing stability equations are quantitatively assessed through the coefficient of determination (R^2):

$$R^2 = 1 - \frac{\sum_{i=1}^{N}\left(F^i - F_{est}^i\right)^2}{\sum_{i=1}^{N}\left(F^i - \overline{F}\right)^2} \tag{5.21}$$

where F^i is the factor of safety calculated by Eq. (5.18) with coefficients m and n checked from the tables presented in Barnes (1991); F_{est}^i is the factor of safety calculated by a stability equation; $\overline{F}$ is the average of the factors of safety calculated by Eq. (5.18), and N (= 882) is the number of the cases.

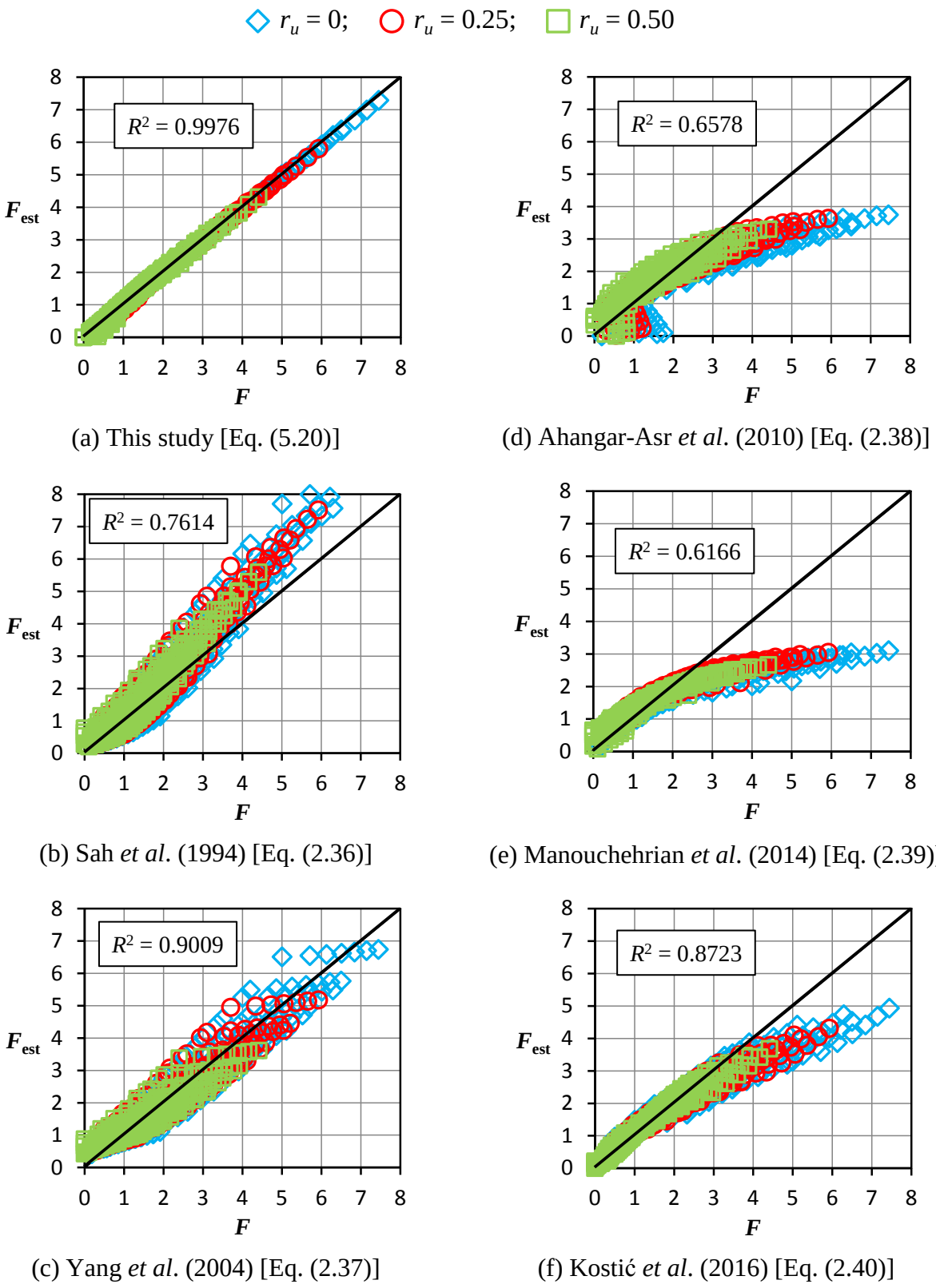

(a) This study [Eq. (5.20)]

(d) Ahangar-Asr *et al*. (2010) [Eq. (2.38)]

(b) Sah *et al*. (1994) [Eq. (2.36)]

(e) Manouchehrian *et al*. (2014) [Eq. (2.39)]

(c) Yang *et al*. (2004) [Eq. (2.37)]

(f) Kostić *et al*. (2016) [Eq. (2.40)]

Figure 5.15 Evaluation of the stability equations for saturated soil slopes

As labelled in Figure 5.15, the R^2 for the existing stability equations ranges from 0.6166 to 0.9009, compared to 0.9976 for Eq. (5.20) proposed in this study.

For a cohesionless slope, r_u must be less than $\cos^2\beta$ so that F calculated by Eq. (5.19) can be greater than zero and frictional resistance can be mobilized (Bishop and Morgenstern, 1960). In order to ensure the F_{est} calculated by Eq. (5.20) is greater than zero, r_u must satisfy the following relationship:

$$r_u < \frac{A_{est}\left(\frac{c'}{\gamma H \tan\phi'}\right)^{B_{est}} \sin\beta\cos\beta + \cos^2\beta}{\frac{c'}{\gamma H \tan\phi'}\cos^2\beta + 1} \tag{5.22}$$

The right-hand side of Eq. (5.22) is an increasing function of $c'/\gamma H\tan\phi'$; it has a minimum value of $\cos^2\beta$ when $c' = 0$. Hence, the constraint of r_u for Eq. (5.20) can be safely approximated by $r_u \leq \cos^2\beta$. This constraint mainly affects the slopes that are steeper than 45°, as is also noted by Barnes (1991).

5.4.2 Steep Slopes

Equation (5.20) can estimate the F of gentle and moderately steep slopes accurately. However, it may severely underestimate the F of steep slopes, as shown in Figure 5.17 and will be explained later. The F of unsaturated soil slopes under rainfall based on rotational failure mechanism can be calculated by Eq. (5.9). Saturated soil slopes can be considered as special cases of unsaturated soil slopes when the negative pore-water pressure approaches zero. Consequently, Eq. (5.9) is modified to be:

$$F_{\text{est}} = A_{\text{est}}\left(\frac{c'}{\gamma H \tan\phi'} - \frac{r_u \gamma \bar{h} \tan\phi'}{\gamma H \tan\phi'}\right)^{B_{\text{est}}} \tan\phi' + \frac{\tan\phi'}{\tan\beta} \tag{5.23}$$

In Figure 5.14, the vertical distance h is a variable that depends on the location at the slip surface. The $\bar{h}$ in Eq. (5.23) can be considered as the average vertical distance and it can be calculated by:

$$\bar{h} = \frac{\int_{\theta_o}^{\theta_h} u_w v_n \mathrm{d}S}{r_u \gamma \int_{\theta_o}^{\theta_h} v_n \mathrm{d}S} \tag{5.24a}$$

Finally, Eq. (5.24a) can be written as:

$$\frac{\bar{h}}{H} = \frac{2 f_5}{\frac{H}{r_o}\left\{\exp\left[2(\theta_h - \theta_o)\tan\phi'\right] - 1\right\}} \tag{5.24b}$$

where the function f_5 can be found in Michalowski (1995) and calculated by:

$$f_5 = \tan\phi' \int_{\theta_o}^{\theta_h} \frac{h}{r_o} \exp\left[2(\theta - \theta_o)\tan\phi'\right] \mathrm{d}\theta \tag{5.24c}$$

the ratio H/r_o can be found in Chen (1975) and shown in Eq. (4.11).

The ratios $\bar{h}/H$ calculated by Eq. (5.24b) for various $c'/\gamma H\tan\phi'$ and β are shown in Figure 5.16. With the increase in $c'/\gamma H\tan\phi'$, the ratio $\bar{h}/H$ converges to the value of 0.5, regardless of the slope angle β. Hence, the $\bar{h}/H$ in Eq. (5.23) can be taken as 0.5:

$$F_{\text{est}} = A_{\text{est}}\left(\frac{c'}{\gamma H \tan\phi'} - 0.5 r_u\right)^{B_{\text{est}}} \tan\phi' + \frac{\tan\phi'}{\tan\beta} \tag{5.25}$$

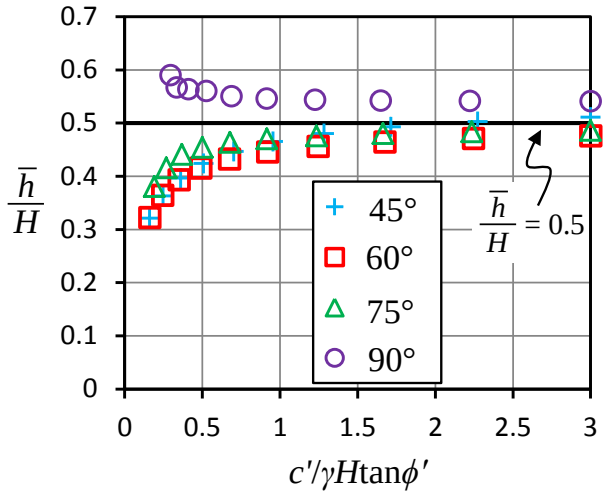

Figure 5.16 Influence of $c'/\gamma H\tan\phi'$ and β on $\bar{h}/H$

At r_u = 0, both Eqs. (5.20) and (5.25) can be transformed into Eq. (5.4). The comparisons of Eq. (5.20) and Eq. (5.25) at r_u = 0.25 and 0.50 are shown in Figure 5.17. Very close estimations are obtained by Eq. (5.20) and Eq. (5.25) for $\beta \le 60°$ and $c'/\gamma H\tan\phi' \ge 0.5$ despite their different forms. Equation (5.20) may severely underestimate F when $\beta > 60°$. Equation (5.25) is ill-defined when $c'/\gamma H\tan\phi' < 0.5r_u$, but it generally provides good estimation of F when $\beta > 60°$. Therefore, Eqs. (5.20) and (5.25) are suggested to be applied for $\beta \le 60°$ and $\beta > 60°$, respectively:

$$F_{\text{est}} = \begin{cases} A_{\text{est}}\left(\dfrac{c'}{\gamma H\tan\phi'}\right)^{B_{\text{est}}}\tan\phi' + \dfrac{\tan\phi'}{\tan\beta} - \left(\dfrac{c'}{\gamma H}\dfrac{1}{\tan\beta} + \dfrac{\tan\phi'}{\sin\beta\cos\beta}\right)r_u, \text{ if } \beta \le 60^\circ & \text{(5.26a)} \\ A_{\text{est}}\left(\dfrac{c'}{\gamma H\tan\phi'} - 0.5r_u\right)^{B_{\text{est}}}\tan\phi' + \dfrac{\tan\phi'}{\tan\beta}, \text{ if } \beta > 60^\circ & \text{(5.26b)} \end{cases}$$

The performance of Eqs. (5.26a) and (5.26b) at r_u = 0.25 and 0.5 is further evaluated with the stability charts presented in Michalowski (2002), as shown in Figure 5.18. It is shown that Eq. (5.26a) [or Eq. (5.20)] performs well, especially when $0 \le c'/\gamma H\tan\phi' \le 0.5$, which is consistent with the evaluation presented in Figure 5.15(a). For β = 15°, r_u = 0.5 and $c'/\gamma H\tan\phi' > 0.5$, Eq.

(5.26a) may underestimate F with error up to 10%. Equation (5.26b) predicts F reasonably well for steep slopes ($\beta > 60°$).

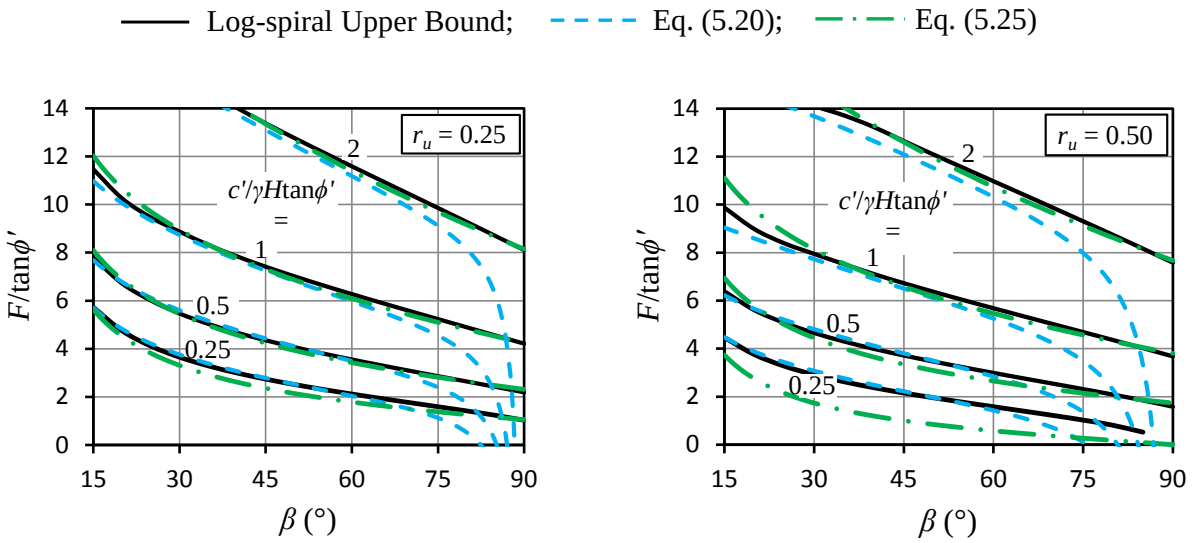

(a) r_u = 0.25 (b) r_u = 0.50

Figure 5.17 Comparisons of Eq. (5.20) and Eq. (5.25)

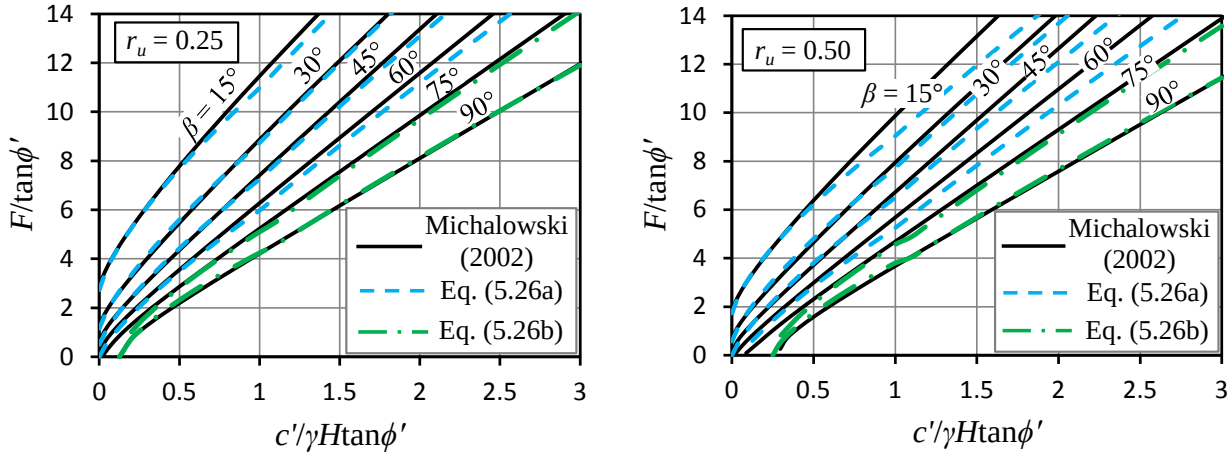

(a) r_u = 0.25 (b) r_u = 0.50

Figure 5.18 Performance of the stability equations for saturated soil slopes

5.5 Summary

The controlling factors on the failure mode of unsaturated soil slopes under rainfall were investigated through dimensionless slope stability charts. It was found that the governing failure mode of an unsaturated soil slope under rainfall is closely related to the parameter group $c'/\gamma H\tan\phi'$. An unsaturated soil slope is increasingly prone to translational failure with the increase in infiltration depth and contribution of matric suction to the soil strength in the unsaturated zone. Moderately steep slopes are more susceptible to translational failure than gentle and steep slopes.

Through regression analysis of the dimensionless slope stability numbers, a general stability equation [Eq. (5.9)] was proposed to assess the stability of unsaturated soil slopes under rainfall due to rotational failure. Graphical approaches and charts were provided to estimate the required input parameters in Eq. (5.9). In addition, an equation [Eq. (5.14)] was proposed to estimate the factors of safety of unsaturated soil slopes under rainfall due to translational failure. The factor of safety obtained by Eq. (5.14) has considered the boundary effects of the translational slip. Hence, by benchmarking the factor of safety obtained by infinite slope analysis with the one obtained by Eq. (5.14), the accuracy of infinite slope analysis was investigated. An unsaturated soil slope may change from unsaturated to saturated after a prolonged and heavy rain storm. Hence, stability equations [Eqs. (5.26a) and (5.26b)] were also proposed to assess the stability of saturated soil slopes.

Chapter 6: Stability Equations for Unsaturated Soil Slopes under Seismic Loading

The stability equations for dry, unsaturated and saturated soil slopes under static condtion are presented in Chapter 5. The slope stability equations that consider seismic loading are presented in this chapter.

6.1 Saturated, Unsaturated and Dry Soil Slopes under Seismic Loading

So far all the stability charts that have considered seismic loading summarized in Table 2.3 were only developed for dry soil slopes. No attempt has been made to develop stability charts for saturated soil slopes under seismic loading. This phenomenon could be attributed to the different responses of dry and saturated soils under seismic loading. As reviewed in Section 2.3.2, under seismic loading dry soils would experience strength hardening (Silver and Seed, 1971; Kovacs and Leo, 1981; Amer et al., 1984), while saturated soils would experience strength degradation and may even be susceptible to liquefaction (Seed and Lee, 1966; Idriss et al., 1978; Ishihara, 1996). For the charts that were developed for pseudo-static slope stability analysis, the error is on the safe side for dry soil slopes due to the cyclic hardening effect, while the error is on the unsafe side for saturated soil slopes due to strength degradation. Hence, stability charts that were developed for pseudo-static analysis of saturated soil slopes would be inappropriate, as they may overestimate seismic stability, especially for liquefiable soils (Michalowski, 2002). Due to the

same concern, neither chart nor equation is developed for saturated soil slopes under seismic loading in this study.

For an unsaturated soil slope with shallow groundwater table [Figure 4.4(a)], the critical slip surface may pass below the groundwater table and liquefaction may occur under seismic loading. However, for an unsaturated soil slope with deep groundwater table [Figure 4.4(b)], liquefaction is unlikely to occur and the critical slip surface only passes through the unsaturated zone. Similar to dry soils, unsaturated soils would experience densification and hardening under cyclic loading, as has been found by other researchers (e.g., Chu and Vucetic, 1992; Ishihara, 1996; Whang et al., 2004) and confirmed by the experiments conducted in Chapter 3. Hence, it may be reasonable to develop slope stability equations for the pseudo-static analysis of unsaturated soil slopes with deep groundwater table, as the error is on the safe side due to the cyclic hardening effect.

In the following sections, stability equations for dry soil slopes under seismic loading based on rotational and translational failure mechanisms are proposed first. The equations are then extended to unsaturated soil slopes.

6.2 Stability Equations for Dry Soil Slopes under Seismic Loading

Rotational and translational failures are the two common failure modes for a dry soil slope under seismic loading, as illustrated in Figure 6.1. Rotational failure is the critical failure mode when the slope is relatively homogeneous (e.g., Jibson, 2011). Translational failure usually occurs in heterogeneous slopes, for example, soil at shallow depth is highly weathered and underlain by

less weathered soil or bedrock (e.g., Duncan et al., 2014). The stability equations for dry soil slopes under seismic loading based on rotational and translational failure mechanisms are given below.

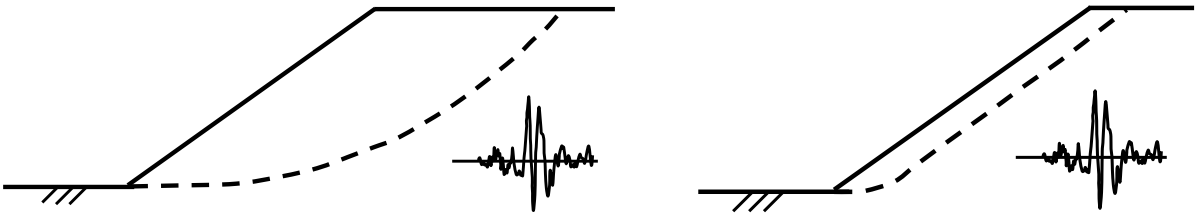

(a) Rotational failure (b) Translational failure

Figure 6.1 Slope failure modes under earthquake (modified from Rathje and Antonakos, 2011)

6.2.1 Rotational Failure

6.2.1.1 Factor of Safety

The factor of safety of a dry soil slope under static condition can be calculated by Eq. (5.4). For a cohesionless slope under seismic loading, the critical slip surface is a plane parallel to the slope surface, and factor of safety can be calculated by the infinite slope model (e.g., Duncan et al., 2014):

$$F = \frac{1 - k_h \tan\beta}{k_h + \tan\beta} \tan\phi' \tag{6.1}$$

The extended equation for pseudo-static analysis of dry soil slopes must be transformed into Eq. (5.4) when $k_h = 0$, and transformed into Eq. (6.1) when $c' = 0$. In addition, the extended equation should enable explicit expression of k_h when $F = 1$ (i.e., $k_h = k_y$). A functional form which satisfies all the above conditions is given below:

$$F = A_{\text{est}}\left(1-\frac{k_h \tan\beta}{k_h+\tan\beta}C\right)\left(\frac{c'}{\gamma H \tan\phi'}\right)^{B_{\text{est}}} \tan\phi' + \frac{1-k_h \tan\beta}{k_h+\tan\beta}\tan\phi' \qquad (6.2)$$

where A_{est} and B_{est} can be calculated by Eq. (5.2) and Eq. (5.3), respectively; C is the only unknown parameter and the determination of which is explained below.

Upper bound pseudo-static limit analysis with a log-spiral failure mechanism, the details of which can be found in Section 4.1.2, was adopted to develop a large number of stability charts. The charts were presented in the similar format as Figure 6.2 (Michalowski, 2002). The pseudo-static coefficient k_h = 0.1, 0.2 and 0.3, while the slope angle β ranges from 15° to 90° at intervals of 5°. Each stability curve was fitted by Eq. (6.2), consequently a coefficient C was back-calculated. The coefficients C for various β and k_h are summarized in Figure 6.3, which shows that C is insensitive to the value of k_h and can be estimated by:

$$C_{\text{est}} = \frac{60}{\beta} \qquad (6.3)$$

By substituting Eq. (6.3) into Eq. (6.2), the stability equation for pseudo-static analysis of dry soil slopes based on rotational failure mechanism is obtained:

$$F_{\text{dyn}}^{\text{rot}} = A_{\text{est}}\left(1-\frac{k_h \tan\beta}{k_h+\tan\beta}\frac{60}{\beta}\right)\left(\frac{c'}{\gamma H \tan\phi'}\right)^{B_{\text{est}}} \tan\phi' + \frac{1-k_h \tan\beta}{k_h+\tan\beta}\tan\phi' \qquad (6.4)$$

In Figure 6.2, the dash curves are determined from Eq. (6.4). Good agreements are shown between the dash and solid curves when k_h = 0.1 and k_h = 0.2. For k_h = 0.3, Eq. (6.4) could overestimate the factor of safety when β = 60° and $c'/\gamma H\tan\phi' > 1.5$, but the error is less than 7%. Hence, Eq. (6.4) can generally provide satisfactory assessment for the pseudo-static analysis of dry soil slopes.

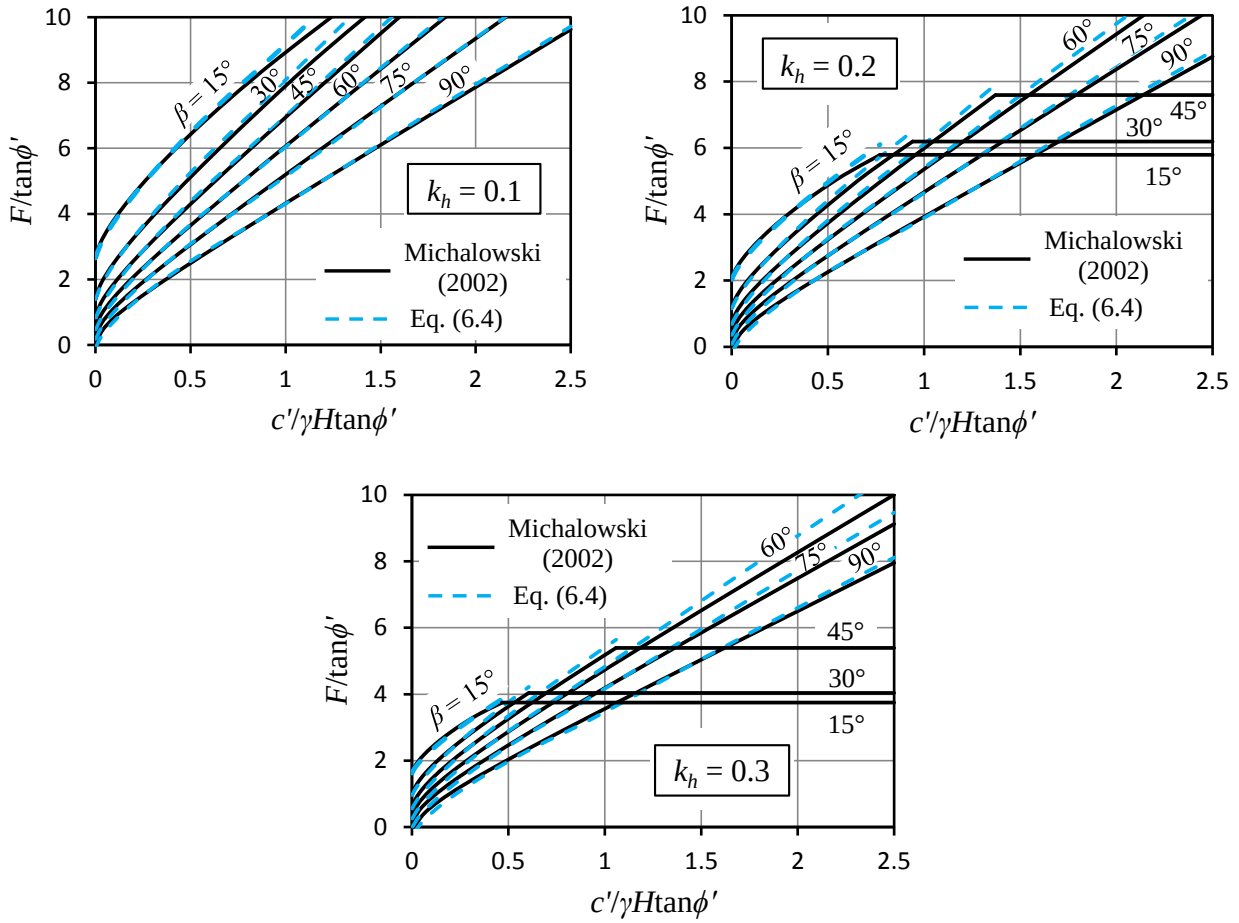

Figure 6.2 Stability charts and equation for pseudo-static slope stability analysis

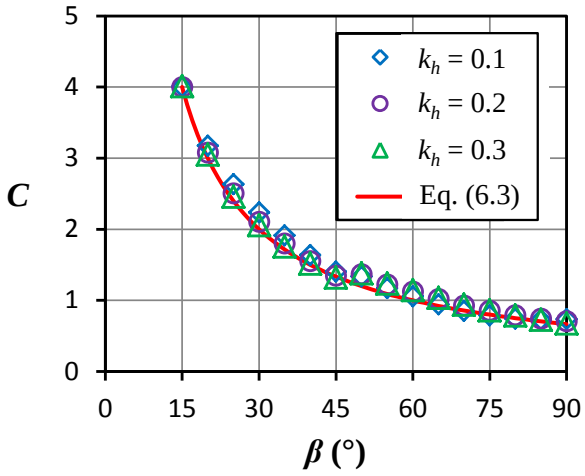

Figure 6.3 Summary of coefficients *C*

6.2.1.2 Yield Coefficient

The yield coefficient, k_y, is equal to the pseudo-static coefficient, k_h, which could bring the slope to the verge of failure ($F_{\text{dyn}}^{\text{rot}} = 1$). On the condition that $F_{\text{dyn}}^{\text{rot}} = 1$ and by rearranging Eq. (6.4), the yield coefficient k_y can be expressed explicitly as:

$$k_y^{\text{rot}} = \frac{\dfrac{1}{\tan\beta} - \dfrac{1}{\tan\phi'} + A_{\text{est}}\left(\dfrac{c'}{\gamma H \tan\phi'}\right)^{B_{\text{est}}}}{1 + \dfrac{1}{\tan\beta\tan\phi'} + A_{\text{est}}\left(\dfrac{60}{\beta} - \dfrac{1}{\tan\beta}\right)\left(\dfrac{c'}{\gamma H \tan\phi'}\right)^{B_{\text{est}}}} \tag{6.5}$$

The efficiency of Eq. (6.4) has been demonstrated in Figure 6.2. In other words, the efficiency of Eq. (6.5), which is derived from Eq. (6.4), has already been shown. The efficiency of Eq. (6.5) is further validated with rigorous numerical approach.

Loukidis et al. (2003) conducted log-spiral upper bound limit analysis, finite element analysis and limit equilibrium analysis on dry soil slopes, and found that the yield coefficients obtained by these methods are in excellent agreement. Log-spiral upper bound limit analysis, the detail of which can be found in Chang et al. (1984), is adopted to validate Eq. (6.5) due to its computational efficiency.

The k_y obtained by log-spiral upper bound limit analysis and Eq. (6.5) are compared comprehensively for $15° \leq \beta \leq 90°$, as shown in Figure 6.4. For a given pair of β and k_h and to ensure a factor of safety of unity ($k_y = k_h$), the $c'/\gamma H$ and hence $c'/\gamma H \tan\phi'$ need to be relatively large when ϕ' is small (e.g., = 10°), and relatively small when ϕ' is large (e.g., = 30°). Figure 6.4

shows that Eq. (6.5) provides good estimation of k_y when $\phi' = 20°$. Eq. (6.5) may overestimate k_y when $\phi' = 10°$ and underestimate k_y when $\phi' = 30°$. The error can be up to 20%, but in most practical cases the error is less than 10%.

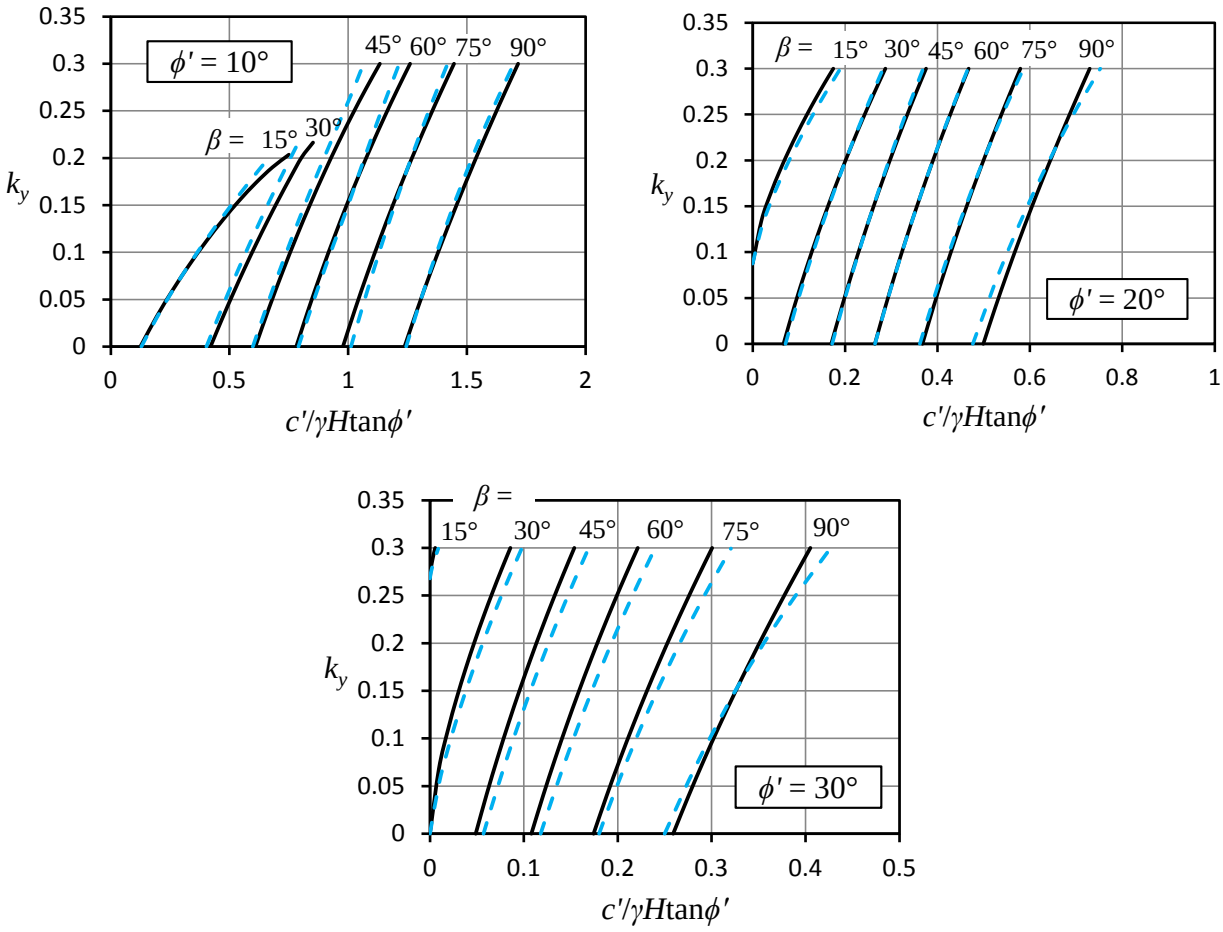

Figure 6.4 Comparison of k_y obtained by upper bound limit analysis (solid curve) and Eq. (6.15) (dash curve)

The yield coefficient k_y is a key parameter for a permanent displacement analysis, and Eq. (6.5) can readily be incorporated into the existing displacement models (e.g., the models summarized in Table 2.2) for preliminary screening of sites and regional seismic stability analysis. The existing displacement models, which express seismic displacement as a function of k_y and

ground motion parameters, commonly have standard deviations up to ±0.5 log units and yield a range of displacements spanning an order of magnitude. This broad range results largely from the stochastic nature of seismic shaking and the difficulty in characterizing the shaking using a few ground motion parameters (Jibson, 2007). Considering the uncertainty inherited in the displacement models, the errors caused by Eq. (6.5) shown in Figure 6.4 can be considered as acceptable.

6.2.2 Translational Failure

6.2.2.1 Factor of Safety

For a cohesive-frictional (c' - ϕ') slope, if translational failure is the critical failure mode, factor of safety of the slope is commonly calculated by the infinite slope model (e.g., Duncan et al., 2014):

$$F_{\text{trl}}^{IS} = \frac{c'}{\gamma z \cos^2\beta\left(k_h + \tan\beta\right)} + \frac{1 - k_h \tan\beta}{k_h + \tan\beta}\tan\phi' \tag{6.6}$$

However, it is widely known that infinite slope model may underestimate the stability of a slope due to the neglect of boundary effects (e.g., Taylor, 1948).

The factor of safety of a dry soil slope under static condition (k_h = 0) based on translational failure mechanism can be calculated by Eq. (5.14). The factor of safety obtained by Eq. (5.14) has considered the boundary effects. In this section, Eq. (5.14) is extended to consider the effect of seismic loading (k_h > 0). The extended equation should be transformed into Eq. (6.1) when c' = 0, and transformed into Eq. (5.14) when k_h = 0. An equation which satisfies the above conditions is given below:

$$F_{\text{trl}} = \frac{\dfrac{c'}{\gamma H}\left[\dfrac{H}{z\sin\beta\cos\beta} + 5.0\exp\left(-0.008\beta\right)\right]\tan\beta + \left(1 - k_h\tan\beta\right)\tan\phi'}{k_h + \tan\beta} \tag{6.7}$$

The pseudo-static factor of safety of a dry soil slope based on translational failure mechanism can be accurately obtained by translational upper bound limit analysis, as shown in Section 4.3.2. The stability curves determined from Eq. (6.7), infinite slope analysis [Eq. (6.6)], and translational upper bound limit analysis for various β, z/H and k_h are shown in Figure 6.5.

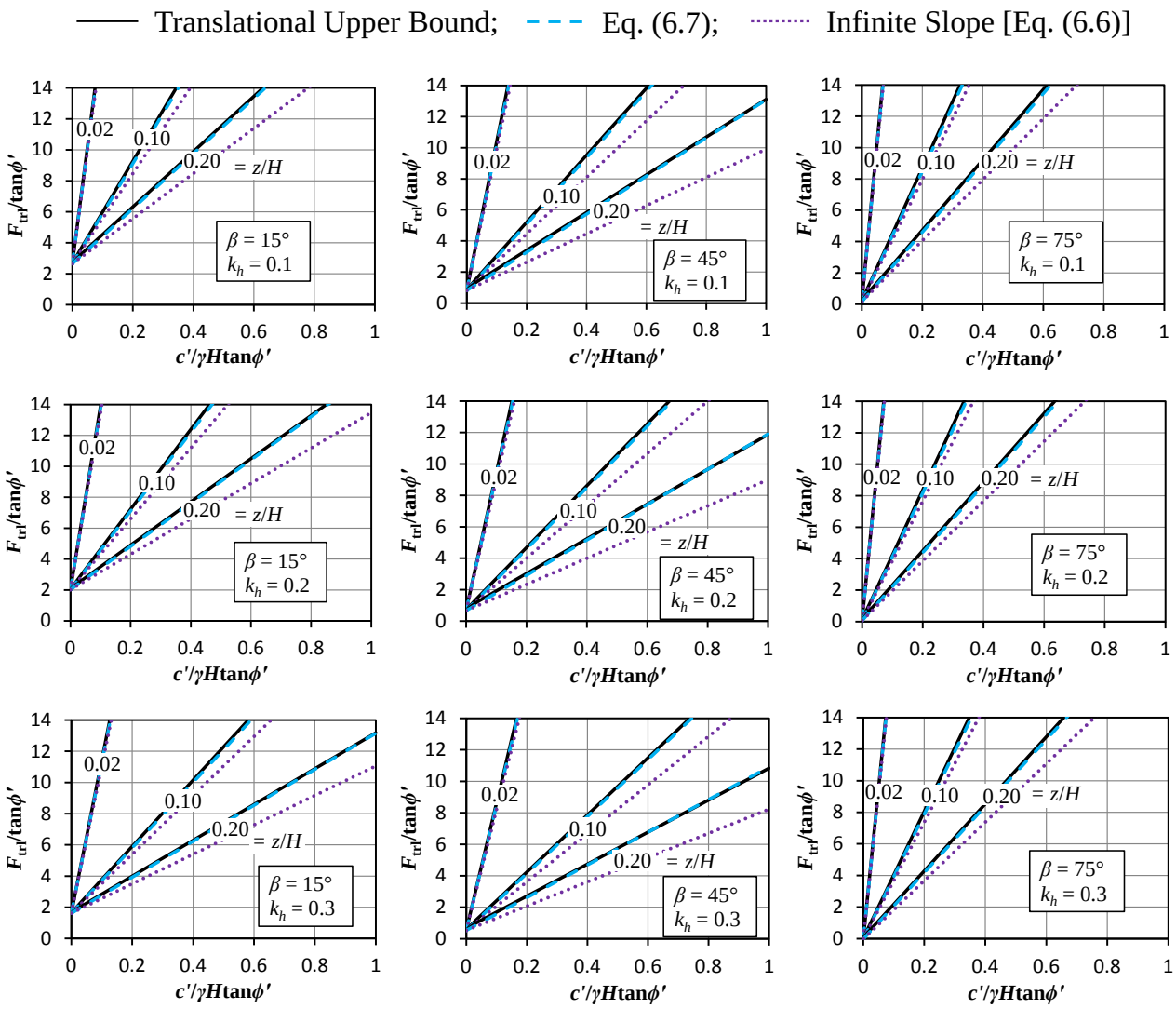

Figure 6.5 Stability charts for pseudo-static translational failure obtained by various methods

Figure 6.5 shows that the stability curves determined from Eq. (6.7) agree well with those obtained by translational upper bound limit analysis regardless of the magnitude of β, z/H and k_h. Infinite slope analysis performs well when z/H is small (e.g., $z/H = 0.02$). However, the factor of safety obtained by infinite slope analysis becomes increasingly conservative with the increase of z/H. If the factor of safety obtained by Eq. (6.7) is treated as a benchmark solution, the error (underestimation) caused by infinite slope model can be calculated by:

$$\text{Error}(\%) = \frac{F_{\text{trl}} - F_{\text{trl}}^{IS}}{F_{\text{trl}}} = \frac{5.0\exp(-0.008\beta)}{5.0\exp(-0.008\beta) + \frac{l}{d} + \frac{\gamma H \tan\phi'}{c'}\left(\frac{1}{\tan\beta} - k_h\right)} \tag{6.8}$$

According to Eq. (6.8), the error caused by the infinite slope model is not only affected by d/l, but also affected by $c'/\gamma H\tan\phi'$, β and k_h. The error is negligible when d/l is small ($d/l \rightarrow 0$) or the soil is cohesionless ($c'/\gamma H\tan\phi' \rightarrow 0$). The error increases with the increase in d/l and $c'/\gamma H\tan\phi'$, as shown in Figure 6.6 for $\beta = 45°$ and $k_h = 0.2$. Equation (6.8) would reduce to Eq. (5.16) when $k_h = 0$. With the increase in k_h, the denominator of Eq. (6.8) decreases, consequently the error increases. The error caused by infinite slope analysis with $\beta = 45°$ at static condition (i.e., $k_h = 0$) is shown in Figure 5.12. By comparing Figure 6.6 with Figure 5.12, it can be found that the influence of k_h on the error obtained is small. The error is increased by about 1% at $d/l = 0.1$ if k_h increases from 0 to 0.2.

In order to limit the error caused by the pseudo-static infinite slope analysis (e.g., 10%), d/l must be limited for given $c'/\gamma H\tan\phi'$, β and k_h, as illustrated in Figure 6.7. Similar to the results presented in Figure 5.13, the limiting value of d/l generally decreases with the increases in β for a specific $c'/\gamma H\tan\phi'$. Figure 6.7 shows that all the curves intersect when $\beta = \tan^{-1}(1/k_h)$ (β =

78.69° for k_h = 0.2). At this particular slope angle, the error calculated by Eq. (6.8) is independent of $c'/\gamma H\tan\phi'$.

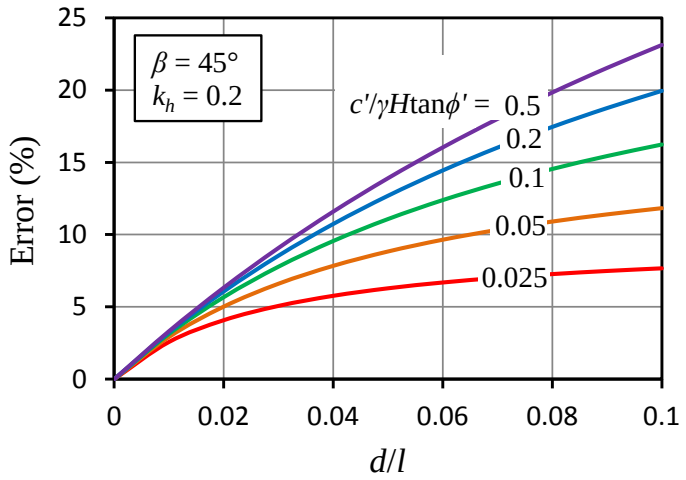

Figure 6.6 The error caused by pseudo-static infinite slope analysis

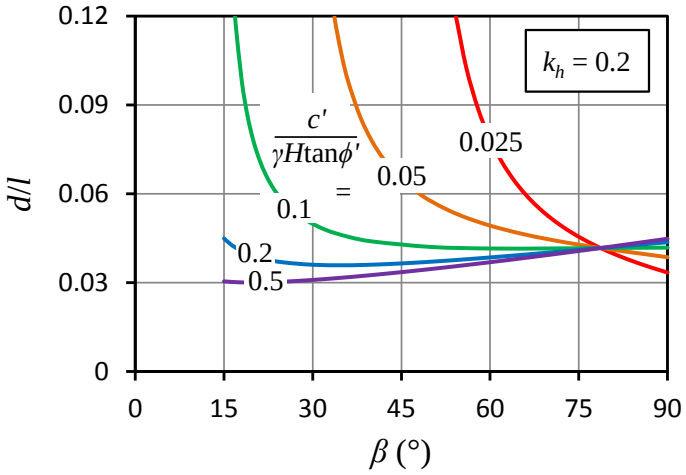

Figure 6.7 Limits of d/l for 10% error in pseudo-static infinite slope analysis

6.2.2.2 Yield Coefficient

The yield coefficient is equal to the pseudo-static coefficient (k_h) which could bring the slope to the limiting equilibrium (F = 1). For a cohesive slope with translational failure as the critical failure mode, the yield coefficient of the slope by infinite slope analysis can be obtained by rearranging Eq. (6.6):

$$k_{y.IS}^{\text{trl}} = \frac{\dfrac{c'}{\gamma z \cos^2 \beta} + \tan\phi' - \tan\beta}{1 + \tan\phi' \tan\beta} \tag{6.9}$$

By rearranging Eq. (6.7), the yield coefficient which has considered the boundary effects of the translational slip can be calculated by:

$$k_y^{\text{trl}} = \frac{\dfrac{c'}{\gamma H}\left[\dfrac{H}{z \sin\beta \cos\beta} + 5.0 \exp\left(-0.008\beta\right)\right] \tan\beta + \tan\phi' - \tan\beta}{1 + \tan\phi' \tan\beta} \tag{6.10}$$

The yield coefficient for translational failure mechanism can be rigorously calculated by upper bound limit analysis, the details of which can be found in Section 4.3.2. The stability curves of yield coefficients obtained by translational upper bound limit analysis [Eq. (4.73)], Eq. (6.10) and infinite slope model [Eq. (6.9)] for various β, ϕ' and z/H are compared in Figure 6.8. It is shown that both Eq. (6.10) and infinite slope model [Eq. (6.9)] perform well when z/H is small. With the increase in z/H, Eq. (6.10) may slightly underestimate k_y, while infinite slope model [Eq. (6.9)] may severely underestimate k_y.

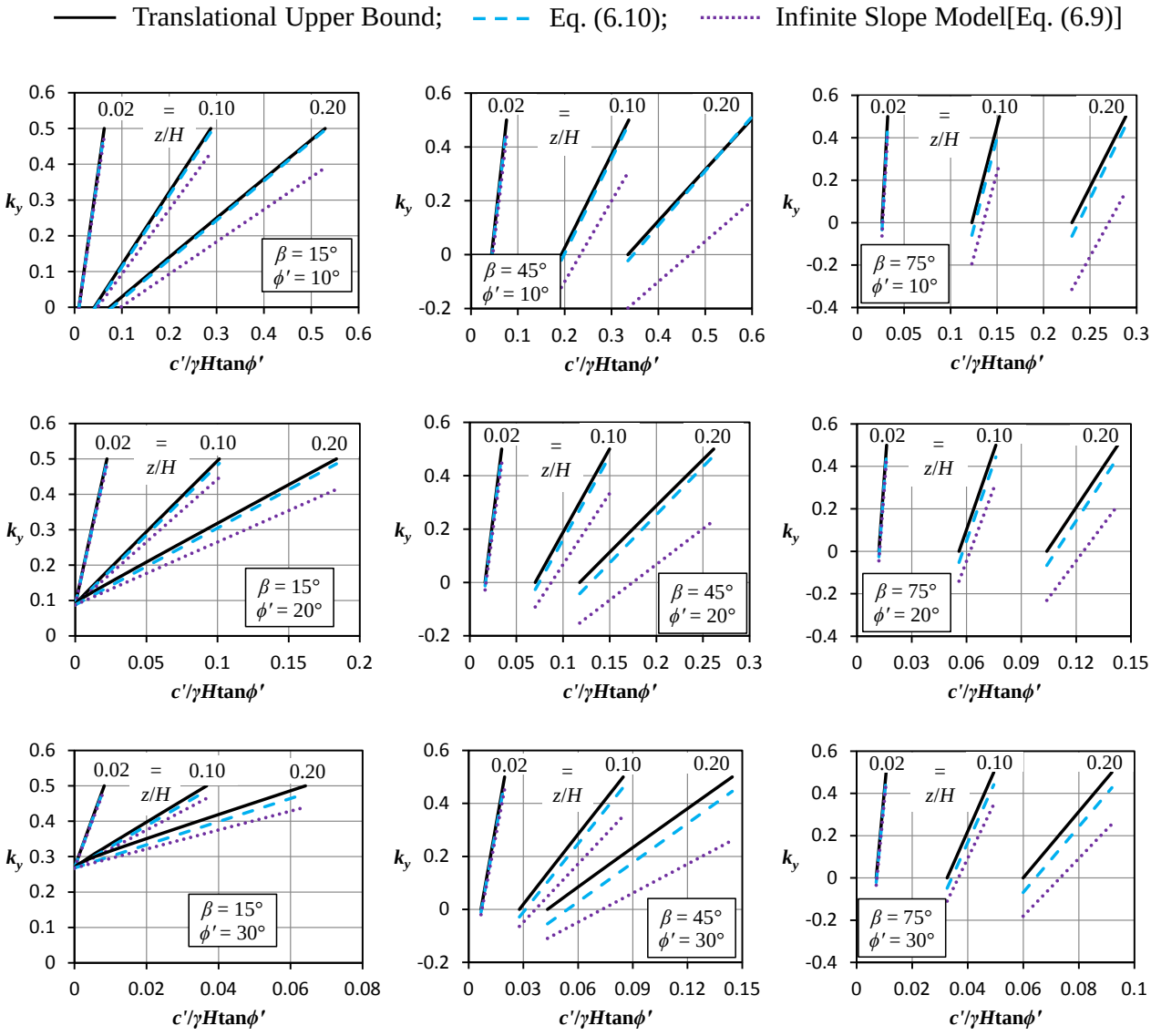

Figure 6.8 Charts of k_y for pseudo-static translational failure obtained by various methods

If the k_y obtained by Eq. (6.10) is treated as benchmark solution, the error (underestimation) caused by infinite slope analysis due to the neglect of boundary effects can be estimated by:

$$\text{Error}(\%)=\frac{k_y^{\text{trl}}-k_{y.IS}^{\text{trl}}}{k_y^{\text{trl}}}=\frac{5.0\exp(-0.008\beta)}{5.0\exp(-0.008\beta)+\dfrac{H}{z\sin\beta\cos\beta}+\dfrac{\gamma H\tan\phi'}{c'}\left(\dfrac{1}{\tan\beta}-\dfrac{1}{\tan\phi'}\right)} \tag{6.11}$$

From Eq. (6.11), it is obvious that the error caused by infinite slope model is negligible when z/H is small ($z/H \rightarrow 0$) or the soil is cohesionless ($c'/\gamma H \tan\phi' \rightarrow 0$). The influence of β on the error caused by infinite slope model is not obvious, as it appears in both the numerator and denominator of Eq. (6.11). Hence, parametric study was conducted to investigate the influence of β, and a typical result is shown in Figure 6.9.

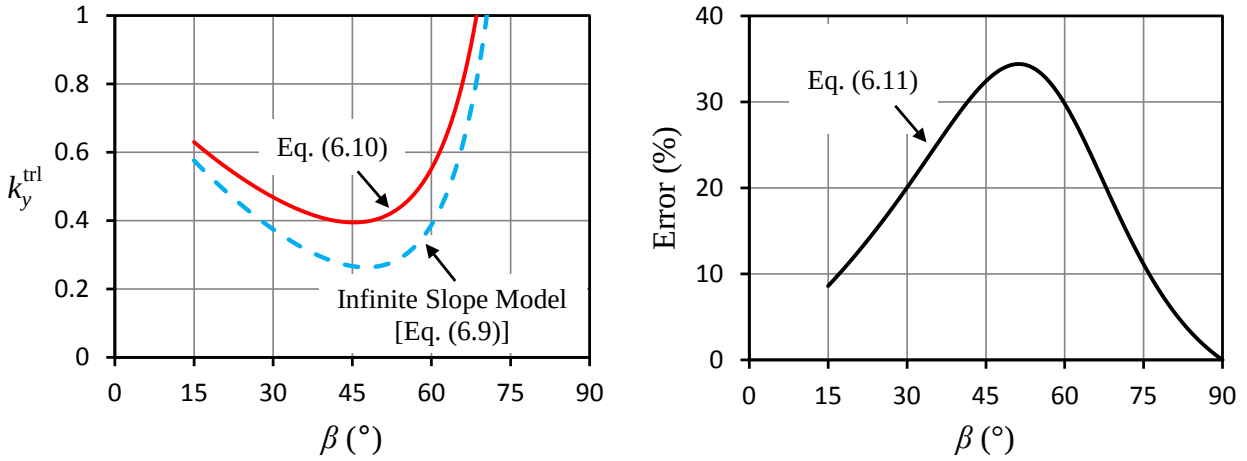

(a) k_y (b) Error (%)

Figure 6.9 Influence of β on the accuracy of k_y calculated by infinite slope model ($c'/\gamma H = 0.05$, $\phi' = 20°$, $z/H = 0.1$)

As shown in Figure 6.9(a), with the increase in β the k_y calculated by Eqs. (6.9) and (6.10) decreases at first and then increases. The k_y obtained by Eq. (6.10) is always larger than the k_y obtained by the infinite slope model [Eq. (6.9)], as the latter has neglected the boundary effects. The error caused by the infinite slope model is calculated by Eq. (6.11). As shown in Figure 6.9(b), the error increases first and then decreases with the increase in β.

6.3 Stability Equations for Unsaturated Soil Slopes under Seismic Loading

Dry soils can be considered as special unsaturated soils that have degree of saturation of zero. For an unsaturated soil slope with deep groundwater table [Figure 4.4(b)], if the contribution of matric suction to slope stability is neglected (i.e., $\gamma_w h_c \tan\phi^b = 0$), the unsaturated soil slope can be analyzed as a dry soil slope. Similarly, the stability equations developed for dry soil slopes can readily be extended to unsaturated soil slopes by replacing the effective cohesion (c') of dry soils with the total cohesion of unsaturated soils (c):

$$c = c' + \gamma_w h_c \tan\phi^b \tag{6.12}$$

This method is referred to as the "total cohesion" method by Fredlund and Rahardjo (1993).

The pseudo-static factor of safety and yield coefficient of dry soil slopes based on rotational failure mechanism can be calculated by Eq. (6.4) and Eq. (6.5), respectively. By using the "total cohesion" method, the pseudo-static factor of safety ($F_{\text{dyn}}^{\text{rot}}$) and yield coefficient (k_y^{rot}) of unsaturated soil slopes based on rotational failure mechanism can be calculated by:

$$F_{\text{dyn}}^{\text{rot}} = A_{\text{est}}\left(1 - \frac{k_h \tan\beta}{k_h + \tan\beta}\frac{60}{\beta}\right)\left(\frac{c' + \gamma_w h_c \tan\phi^b}{\gamma H \tan\phi'}\right)^{B_{\text{est}}} \tan\phi' + \frac{1 - k_h \tan\beta}{k_h + \tan\beta}\tan\phi' \tag{6.13}$$

$$k_y^{\text{rot}} = \frac{\dfrac{1}{\tan\beta} - \dfrac{1}{\tan\phi'} + A_{\text{est}}\left(\dfrac{c' + \gamma_w h_c \tan\phi^b}{\gamma H \tan\phi'}\right)^{B_{\text{est}}}}{1 + \dfrac{1}{\tan\beta\tan\phi'} + A_{\text{est}}\left(\dfrac{60}{\beta} - \dfrac{1}{\tan\beta}\right)\left(\dfrac{c' + \gamma_w h_c \tan\phi^b}{\gamma H \tan\phi'}\right)^{B_{\text{est}}}} \tag{6.14}$$

The pseudo-static factor of safety and yield coefficient of dry soil slopes based on translational failure mechanism can be calculated by Eq. (6.7) and Eq. (6.10), respectively. By using the "total

cohesion" method, the pseudo-static factor of safety ($F_{\text{dyn}}^{\text{trl}}$) and yield coefficient (k_y^{trl}) of unsaturated soil slopes based on translational failure mechanism can be calculated by:

$$F_{\text{trl}} = \frac{\dfrac{c' + \gamma_w h_c \tan \phi^b}{\gamma H}\left[\dfrac{H}{z \sin \beta \cos \beta} + 5.0 \exp\left(-0.008\beta\right)\right] \tan \beta + \left(1 - k_h \tan \beta\right) \tan \phi'}{k_h + \tan \beta} \tag{6.15}$$

$$k_y^{\text{trl}} = \frac{\dfrac{c' + \gamma_w h_c \tan \phi^b}{\gamma H}\left[\dfrac{H}{z \sin \beta \cos \beta} + 5.0 \exp\left(-0.008\beta\right)\right] \tan \beta + \tan \phi' - \tan \beta}{1 + \tan \phi' \tan \beta} \tag{6.16}$$

6.4 Summary

Under seismic loading saturated soils experience strength degradation, while dry and unsaturated soils experience densification and hardening. Stability charts and equations considering seismic loading may not be appropriate for saturated soil slopes, as the charts and equations may fail to take strength degradation into account and consequently overestimate the seismic stability. Stability charts and equations considering seismic loading are appropriate for dry and unsaturated soil slopes, as the error is on the safe side due to the cyclic hardening effect of dry and unsaturated soils. Hence, in this study stability equations considering seismic loading are only developed for dry and unsaturated soil slopes.

Through extension of the proposed stability equations for slopes under static loading and regression analysis of the pseudo-static stability numbers, stability equations were proposed for dry soil slopes under seismic loading [Eqs. (6.4), (6.5), (6.7) and (6.10)]. The proposed equations were validated with existing slope stability charts and upper bound limit analysis for a wide range of slope geometries and soil properties. By using the "total cohesion" method, the slope

stability equations proposed for dry soil slopes were extended to unsaturated soil slopes [Eqs. (6.13) - (6.16)].

Chapter 7: Summary and Application of the Proposed Slope Stability Equations

In this chapter, the proposed slope stability equations are summarized, the procedures to determine the required input parameters are explained, application of the proposed slope stability equations are discussed and illustrated.

7.1 Summary of the Proposed Slope Stability Equations

The slope stability equations proposed in Chapters 5 and 6 are summarized in Table 7.1. In the stability equations developed for rotational failure mechanism [Eqs. (5.4), (5.9), (5.26), (6.13) and (6.14)], the parameters A_{est} and B_{est} are functions of β and they can be calculated by Eq. (5.2) and Eq. (5.3), respectively.

7.2 Determination of the Input Parameters

The input parameters required by the slope stability equations are listed in Table 7.2. The basic input parameters required are slope angle (β), slope height (H), soil unit weight (γ), effective cohesion (c') and effective angle of internal friction (ϕ'). The parameters β and H can be measured directly. The determination of γ, c' and ϕ' would not be explained here, as the determination is well documented in textbooks on soil mechanics. The additional parameter for saturated soil slope stability analysis is the pore-water pressure ratio (r_u). The procedure to determine r_u can be found in Bishop and Morgenstern (1960).

Table 7.1 Summary of the proposed slope stability equations

Slope Conditions	Failure Mode	Equations	Source
Dry soil slopes	Rotational failure	$F_{\text{est}} = A_{\text{est}}\left(\dfrac{c'}{\gamma H \tan\phi'}\right)^{B_{\text{est}}} \tan\phi' + \dfrac{\tan\phi'}{\tan\beta}$	Eq. (5.4)
Unsaturated soil slopes under rainfall	Rotational failure	$F_{\text{rot}}^{\text{est}} = A_{\text{est}}\left(\dfrac{c'}{\gamma H \tan\phi'} - \dfrac{\gamma_w h_p \tan\phi'}{\gamma H \tan\phi'} + \zeta \dfrac{\gamma_w h_c^* \tan\phi^b}{\gamma H \tan\phi'}\right)^{B_{\text{est}}} \tan\phi' + \dfrac{\tan\phi'}{\tan\beta}$	Eq. (5.9)
	Translational failure	$F_{\text{trl}}^{\text{est}} = \left[\dfrac{H}{z_w \sin\beta\cos\beta} + 5.0\exp(-0.008\beta)\right]\dfrac{c'}{\gamma H} + \dfrac{\tan\phi'}{\tan\beta}$	Eq. (5.14)
Saturated Soil Slopes	Rotational failure	$F_{\text{est}} = \begin{cases} A_{\text{est}}\left(\dfrac{c'}{\gamma H \tan\phi'}\right)^{B_{\text{est}}} \tan\phi' + \dfrac{\tan\phi'}{\tan\beta} - \left(\dfrac{c'}{\gamma H}\dfrac{1}{\tan\beta} + \dfrac{\tan\phi'}{\sin\beta\cos\beta}\right) r_u, \text{ if } \beta \le 60^\circ \\ A_{\text{est}}\left(\dfrac{c'}{\gamma H \tan\phi'} - 0.5 r_u\right)^{B_{\text{est}}} \tan\phi' + \dfrac{\tan\phi'}{\tan\beta}, \text{ if } \beta > 60^\circ \end{cases}$	Eq. (5.26)
Unsaturated soil slopes under seismic loading	Rotational failure	$F_{\text{dyn}}^{\text{rot}} = A_{\text{est}}\left(1 - \dfrac{k_h \tan\beta}{k_h + \tan\beta}\dfrac{60}{\beta}\right)\left(\dfrac{c' + \gamma_w h_c \tan\phi^b}{\gamma H \tan\phi'}\right)^{B_{\text{est}}} \tan\phi' + \dfrac{1 - k_h \tan\beta}{k_h + \tan\beta}\tan\phi'$	Eq. (6.13)
		$k_y^{\text{rot}} = \dfrac{\dfrac{1}{\tan\beta} - \dfrac{1}{\tan\phi'} + A_{\text{est}}\left(\dfrac{c' + \gamma_w h_c \tan\phi^b}{\gamma H \tan\phi'}\right)^{B_{\text{est}}}}{1 + \dfrac{1}{\tan\beta\tan\phi'} + A_{\text{est}}\left(\dfrac{60}{\beta} - \dfrac{1}{\tan\beta}\right)\left(\dfrac{c' + \gamma_w h_c \tan\phi^b}{\gamma H \tan\phi'}\right)^{B_{\text{est}}}}$	Eq. (6.14)
	Translational failure	$F_{\text{dyn}}^{\text{trl}} = \dfrac{\dfrac{c' + \gamma_w h_c \tan\phi^b}{\gamma H}\left[\dfrac{H}{z\sin\beta\cos\beta} + 5.0\exp(-0.008\beta)\right]\tan\beta + (1 - k_h\tan\beta)\tan\phi'}{k_h + \tan\beta}$	Eq. (6.15)
		$k_y^{\text{trl}} = \dfrac{\dfrac{c' + \gamma_w h_c \tan\phi^b}{\gamma H}\left[\dfrac{H}{z\sin\beta\cos\beta} + 5.0\exp(-0.008\beta)\right]\tan\beta + \tan\phi' - \tan\beta}{1 + \tan\phi'\tan\beta}$	Eq. (6.16)

Table 7.2 Summary of the input parameters required by the stability equations

Slope Conditions	Failure Mode	Basic input parameters	Additional parameters
Dry soil slopes	Rotational failure	β, H, γ, c', ϕ'	-
Unsaturated soil slopes under rainfall	Rotational failure		h_p, h_c, ϕ^b, ζ
	Translational failure		z_w
Saturated Soil Slopes	Rotational failure		r_u
Unsaturated soil slopes under seismic loading	Rotational failure		k_h, h_c, ϕ^b
	Translational failure		k_h , z, h_c, ϕ^b

Rainfall reduces the stability of unsaturated soil slopes by producing a wetting front and decreasing the matric suction above the wetting front. Before the rainfall infiltration, the average positive and negative pore-water pressure heads on the critical rotational slip surface (Figure 5.5) are denoted as h_p and h_c, respectively. The increase of shear strength due to matric suction (i.e., absolute value of the negative pore-water pressure) is denoted as ϕ^b. The infiltration of rainwater gradually increases the depth of wetting front z_w, which decreases slope stability for both translational and rotational failure mechanisms. The critical translational slip surface is completely located in the saturated zone (Figure 5.10) where pore-water pressure is assumed to be zero. Hence, there is no contribution from matric suction to slope stability (translational failure mechanism), and factor of safety F_{trl} decreases due to the increase in z_w [Eq. (5.14)]. The critical rotational slip surface is gradually saturated by rainwater (Figure 5.5) with the wetting front moving downward. The degree of contribution of matric suction to slope stability (rotational failure mechanism) is denoted as ζ. The parameter ζ is equal to unity at no infiltration condition. The increase in z_w decreases the ζ, and consequently decreases the factor of safety F_{rot} [Eq. (5.9)].

Earthquake loading is cyclic in nature. Unsaturated soil is not susceptible to liquefaction or strength degradation under cyclic loading. On the contrary, unsaturated soils would experience densification and strength hardening under cyclic loading, as has been found by other researchers (Chu and Vucetic, 1992; Ishihara, 1996; Whang et al., 2004) and confirmed by the experiments conducted in Chapter 3. Hence, earthquake loading reduces the stability of unsaturated soil slopes by increasing the shearing stresses. The magnitude of the earthquake is represented by the pseudo-static coefficient k_h.

For the stability analysis of unsaturated soil slopes under rainfall, graphical procedures and charts are provided in Section 5.2.2 to determine h_p, h_c and ζ. The determination of z_w and ϕ^b will be given below. For the stability analysis considering seismic loading, the selection of pseudo-static coefficient k_h has been reviewed in Section 2.3.3.1. The shear strength parameters used for seismic slope stability analysis has been discussed in Section 3.6.

7.2.1 Depth of the Wetting front

The amount of matric suction loss due to rainfall is related to the depth of the wetting front z_w. The depth of the wetting front z_w needs to be known in order to calculate F_{trl} [Eq. (5.14)]. Besides, z_w determines the magnitude of ζ [Figure 5.7 or Eq. (5.8g)], which needs to be determined in order to calculate F_{rot} [Eq. (5.9)]. For a slope under rainfall of high intensity ($I > k_s$, where I is the rainfall intensity, k_s is the saturated permeability of the soil), z_w can be estimated by the two-stage model proposed by Mein and Larson (1973). If the intense rainfall ($I \geq k_s$) lasts a long period of time, z_w can be estimated by Eq. (7.1a) (Lumb, 1962), in which t is the rainfall

duration, n is the porosity of the soil, S_f is the final degree of saturation and S_o is the initial degree of saturation. If $I < k_s$, z_w can be estimated by Eq. (7.1b) (Sun et al., 1998).

$$z_w = \begin{cases} \dfrac{k_s t}{n(S_f - S_o)}, \text{ if } I \geq k_s & \text{(7.1a)} \\ \dfrac{It}{n(S_f - S_o)}, \text{ if } I < k_s & \text{(7.1b)} \end{cases}$$

Equations (7.1a) and (7.1b) implicitly assume that the infiltration capacity of the soil would converge to k_s or I, which may not be the case due to the entrapped air during the infiltration (Bouwer, 1966; Li et al., 2005; Rahardjo et al., 2005; Gavin and Xue, 2008). However, the error is on the safe side as it leads to the overestimation of z_w. The denominator in Eq. (7.1) [$n(S_f - S_o)$] is essentially the water storage capacity of the soil, and the parameters n, S_o and S_f can easily be determined by conventional laboratory tests. If the input parameters are reasonably determined, the z_w obtained by Eq. (7.1) generally agrees well with those obtained by finite element transient seepage analysis (Sun et al., 1998; Lee et al., 2009) and by field measurement (Li et al., 2005).

7.2.2 Determination of ϕ^b

The critical rotational slip surface (Figure 5.5) may only be partially saturated by rainwater ($\zeta > 0$). The matric suction in the unsaturated zone can increase the soil strength and hence factor of safety F_{rot} [Eq. (5.9)]. To incorporate matric suction in the stability analysis, the increase in shear strength due to matric suction ϕ^b needs to be known. In order to obtain ϕ^b, modified triaxial or direct shear test with matric suction (u_a - u_w) controlled or measured need to be performed on unsaturated soil specimens. The equipment and techniques used for testing unsaturated soils are

well documented in Fredlund and Rahardjo (1993) and Fredlund et al. (2012), and are not reported in this thesis.

The experimental determination of ϕ^b is costly, technically demanding and time-consuming (Vanapalli et al., 1996; Nam et al., 2011). Hence, a number of empirical procedures have been proposed in the literature to estimate ϕ^b, as summarized in Goh et al. (2010) and Sheng et al. (2011). The approach given by Vanapalli et al. (1996) is suitable for soils of different plasticity index (I_p):

$$\tan\phi^b = \left(\frac{\theta}{\theta_s}\right)^{\kappa} \tan\phi' \tag{7.2}$$

where θ is the volumetric water content, θ_s is the volumetric water content at a saturation of 100%, and κ is a function of I_p (Garven and Vanapalli, 2006):

$$\kappa = -0.0016 I_p^2 + 0.0975 I_p + 1 \tag{7.3}$$

If the groundwater table is shallow [Figure 5.5(b)] and the potential slip surface is mainly located in the capillary saturated zone or below (Figure 4.2), the volumetric water content θ in Eq. (7.2) approaches to θ_s. If the groundwater table is deep [Figure 5.5(a)], θ is the volumetric water content at the moisture discontinuous zone (i.e., $\theta = \theta_r$). If the groundwater table is moderately deep [Figure 5.5(c)], θ is a value between θ_r and θ_s.

7.3 Sigficance of the Proposed Slope Stability Equations

The slope stability equations [Eq. (5.4) and Eq. (5.26)] provide convenient alternatives to the existing slope stability charts (e.g., Taylor, 1937; Bishop and Morgenstern, 1960; Michalowski, 2002; Steward et al., 2011) for the stability analysis of dry and saturated soil slopes. Once the

slope stability equations are integrated into a computer program (e.g., excel spreadsheet), parametric study for different slope geometries (β, H), soil properties (γ, c', ϕ', ϕ^b), pore-water pressure conditions (r_u, h_c, h_p), seismic conditions (k_h), etc. can easily be carried out by changing the input data. In constrast, stability numbers always need to be read from or interpolated between stability curves if slope stability charts are used. This advantage is especially obvious if a large number of slope stability analyses need to be performed.

The slope stability equations [Eq. (5.9) and Eq. (5.14)] can readily be used for the stability analysis of unsaturated soil slopes under rainfall. The difficulties in obtaining unsaturated soil properties (e.g., SWCC and permeability function) and the complexity involved in the numerical analysis have limited the application of numerical seepage and slope stability analysis in practice (e.g., Vahedifard et al., 2016). As a result, the contribution of matric suction to slope stability is usually neglected in routine geotechnical design (Vanapalli et al., 1996; Zhang et al., 2004; Fredlund et al., 2012). To apply Eq. (5.9) and Eq. (5.14), the soil parameters required to calculate z_w (i.e., soil porosity n, initial degree of saturation S_o, and final degree of saturation S_f) can easily be determined by conventional laboratory tests, and the procedure to calculate F_{rot} and F_{trl} is straightforward. Hence, the availability of Eq. (5.9) and Eq. (5.14) will encourage practicing engineers to apply unsaturated soil mechanics principles when analyzing slope stability involving unsaturated soils.

The proposed equations can be efficiently used for regional landslide hazard mapping. Numerous slope stability analyses are required in a regional landslide hazard mapping, and currently infinite slope model seems to be the only feasible tool for regional slope stability analysis (e.g., Jibson et

al., 2000; Harp et al., 2006, 2009; Ho et al., 2012; Dreyfus et al., 2013; Park et al., 2013; Jibson, 2014). However, infinite slope model may be overly conservative due to the neglect of boundary effects, and infinite slope model can only assess slope stability based on translational failure mechanism. The proposed stability equations based on translational failure mechanism [Eq. (5.14), Eq. (6.15) and Eq. (6.16)] have considered the boundary effects, hence they can provide more accurate slope stability analysis than the infinite slope models. Besides, the stability equations based on rotational failure mechanism [Eq. (5.9), Eq. (5.26), Eq. (6.13), and Eq. (6.14)] may be used to identify potential rotational slides in regional landslide hazard mapping.

The slope stability equations can readily be extended to probabilistic slope stability analysis. In a probabilistic slope stability analysis it is desirable if the limit state surface, which separates the safe domain from the failure domain (i.e., $F = 1$), can be defined explicitly (e.g., Goh and Kulhawy, 2003). The slope stability equations shown in Table 7.1 enable explicit calculation of factors of safety, and the partial derivatives of factors of safety with respect to soil parameters (e.g., γ, c', ϕ') can be expressed analytically. Hence, the slope stability equations can readily be extended to probabilistic stability analysis using First Order Second Moment Method (e.g., Baecher and Christican, 2003; Griffiths et al., 2011b) or First Order Reliability Method (e.g., Low et al., 1998; Low, 2003).

7.4 Application of the Proposed Slope Stability Equations

As explained in Section 7.3, the proposed slope stability equations can be used for deterministic slope stability analysis, regional landslide hazard mapping and probabilistic slope stability analysis. In this section, the proposed equations are only used for deterministic slope stability analysis. Further research work needs to be conducted in order to incorporate the proposed slope stability equations into regional landslide hazard mapping and probabilistic slope stability analysis. In the following sections, the proposed slope stability equations are used to reanalyze slope stability problems that have been solved by numerical methods and back analysis of landslides reported in the literature.

7.4.1 Unsaturated Soil Slopes under Rainfall

For an unsaturated soil slope under rainfall infiltration, rotational or translational failure may occur due to the loss of matric suction. Factor of safety due to rotational failure can be estimated by Eq. (5.9). Factor of safety due to translational failure can be estimated by Eq. (5.14). The failure mode which gives the lower factor of safety is the governing failure mode. The application and effectiveness of Eqs. (5.9) and (5.14) are illustrated through three cases. In Cases 1 and 2, the solutions obtained by Eqs. (5.9) and (5.14) are compared with those obtained by numerical software SoilVision and Geostudio, respectively. In Case 3, Eqs. (5.9) and (5.14) are used to analyze a landslide that occurred at Langkawi, Malaysia. The given conditions for the three cases are summarized in Table 7.3.

Table 7.3 Summary of the parameters for unsaturated slope stability analyses

Case No.	Reference	Slope geometry	Soil properties		Groundwater table	Rainfall characteristics
1	Zhang et al. (2016)	β = 40° H = 20 m	γ = 18 kN/m^3 c' = 10 kPa ϕ' = 35° ϕ^b = 10°	n = 0.4 S_f = 1 S_o = 0.8	H_{wt} = 2 m i = 0° $h_n^{\max} = 5$ m	I is a variable $k_s = 1\times10^{-5}$ m/s t = 24 h
2	Rahardjo et al. (2007)	β = 45° H = 10 m	γ = 20 kN/m^3 c' = 10 kPa ϕ' = 26° ϕ^b = 26°	n = 0.45 S_f = 1 S_o = 0.84	H_{wt} = 5 m i = 7° $h_n^{\max} = 7.5$ m	$I = 1\times10^{-6}$ m/s $k_s = 1\times10^{-6}$ m/s t = 24 h
3	Huat et al. (2006)	β = 56° H = 60m	γ = 21 kN/m^3 c' = 11 kPa ϕ' = 25° ϕ^b = 18°	n = 0.5* S_f = 1* S_o = 0.2*, 0.5*, 0.8*	H_{wt} = 10 m i = 0° $h_n^{\max} = 10$ m	$I = 1\times10^{-6}$ m/s $k_s = 1\times10^{-6}$ m/s t = 24 h

(*denotes that the parameters are not given in the literature and they are assumed in this study)

Case 1: Compared with SoilVision

Zhang et al. (2016) conducted stability analysis of an unsaturated soil slope using *SVFLUX* and *SVSLOPE* (example 3.2 in their study). The slope geometry, soil properties and rainfall conditions are shown in Table 7.3 and Figure 7.1.

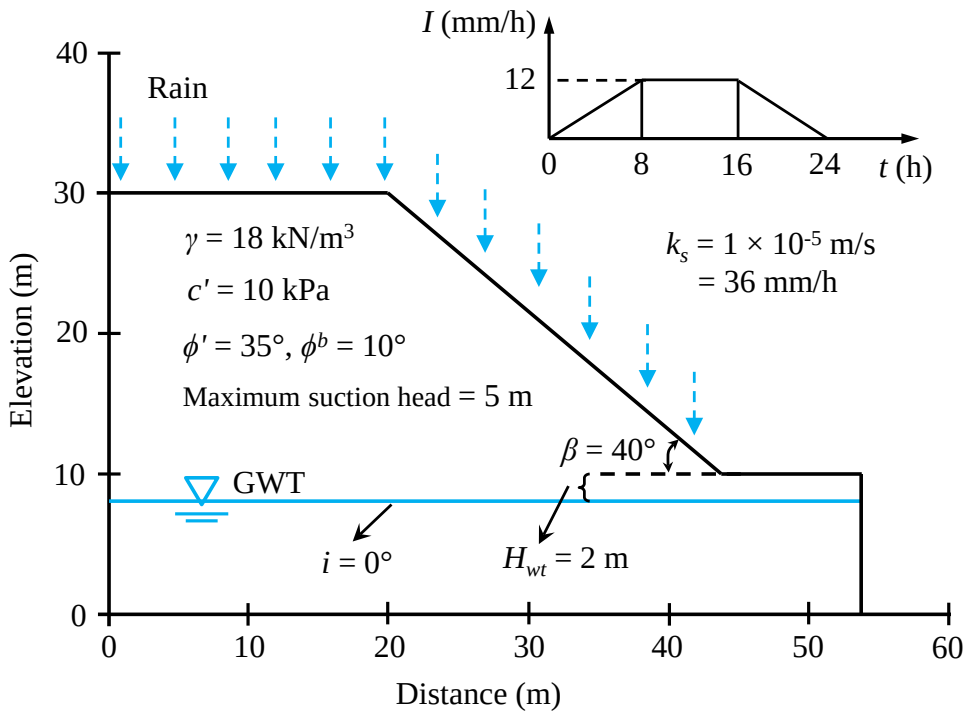

Figure 7.1 Slope geometry, soil properties and rainfall conditions (from Zhang et al., 2016)

According to the given conditions, the groundwater table is moderately deep [Figure 5.5(c)], $\bar{h}_p = 0$ m. The suction head ranges from 2 m to 5 m, and the average $\bar{h}_c$ is estimated as 3.5 m [Eq. (5.10a)]. The parameters n and S_o are not explicitly given, but they can be inferred from the soil-water characteristic curve (SWCC) provided in Zhang et al. (2016) (i.e., $n = \theta_s$, $S_o = \theta_o/n$, where θ_o denotes the initial volumetric water content corresponding to the average $\bar{h}_c$). The final degree of saturation S_f is assumed to be equal to 1. The rainfall intensity I is a variable that changes with time (Figure 7.1). Hence, z_w is estimated by a modified form of Eq. (7.1b):

$$z_w = \frac{\int I \, dt}{n(S_f - S_o)} \tag{7.4}$$

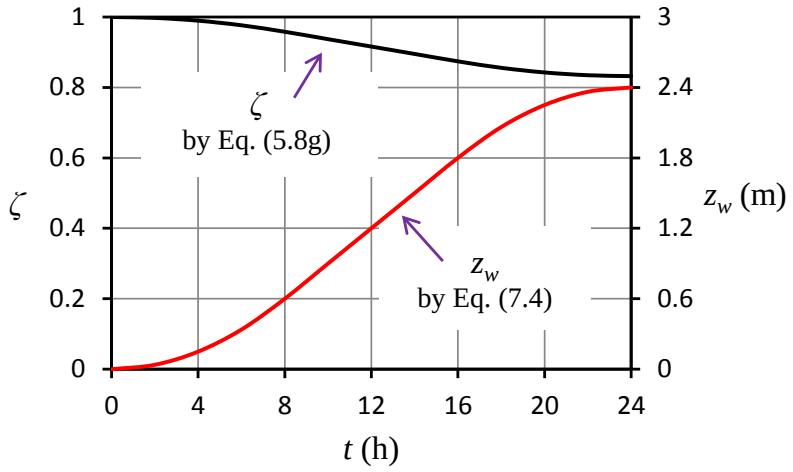

(a) Infiltration analysis

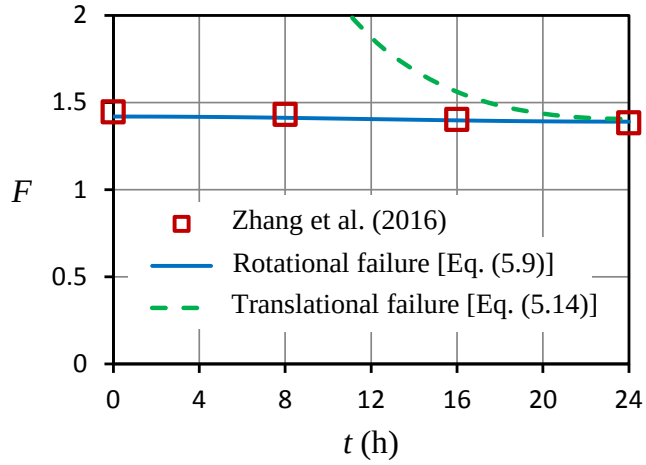

(b) Stability analysis

Figure 7.2 Unsaturated soil slope stability analysis using proposed equations – Case 1

For moderately deep groundwater table, Eq. (5.8g) provides a quick and conservative estimation of ζ; hence, it was used in the calculation. The obtained z_w and ζ are shown in Figure 7.2(a), and they are incorporated into Eq. (5.14) and Eq. (5.9), respectively, for stability analysis. As shown in Figure 7.2(b), the F obtained by Eq. (5.9) agree well with the F given by Zhang et al. (2016) who used General Limit Equilibrium method. At $t = 0$, $F_{rot} = 1.420$, while F_{trl} tends to infinity as $z_w = 0$. Hence, at no infiltration condition ($t = 0$) rotational failure is more critical than

translational failure. With the increase in t, F_{rot} only decreases slightly while F_{trl} decreases dramatically. At t = 24 h, F_{rot} = 1.391 and F_{trl} = 1.405, which reveals that translational failure mechanism is almost as critical as rotational failure mechanism. Zhang et al. (2016) also observed that the critical slip surface is deep rotational at no infiltration condition (t = 0), but it becomes shallower when the soils near the slope surface are saturated.

Case 2: Compared with GeoStudio

Rahardjo et al. (2007) conducted stability analysis on an unsaturated soil slope using *SEEP/W* and *SLOPE/W*. According to the given conditions shown in Table 7.3, the groundwater table is moderately deep [Figure 5.5(c)], $\bar{h}_p = 0$ m, $\bar{h}_c \approx 6$ m [Eq. (5.10a)]. Similar to Case 1, the parameters n = 0.45 and S_o = 0.84 are inferred from the SWCC provided in Rahardjo et al. (2007), and S_f is assumed to be equal to 1. For a specific rainfall duration t, z_w is estimated by Eq. (7.1a), ζ is estimated by Eq. (5.8g), and the results are summarized in Figure 7.3(a). The obtained z_w and ζ are incorporated into Eq. (5.14) and Eq. (5.9), respectively, for the stability analysis, as shown in Figure 7.3(b). The F obtained by Eq. (5.9) agrees well with the F given by Rahardjo et al. (2007) who used Bishop's simplified method with a circular slip surface for the slope stability analysis. Figure 7.3(b) also shows that rotational failure is more critical than translational failure when $t < 14.6$ h, while translational failure becomes more critical when $t > 14.6$ h. However, Bishop's simplified method fails to search for the shallow critical slip surface when $t > 14.6$ h. The phenomenon that limit equilibrium methods may fail to search for shallow critical slip surface was also reported by Lu et al. (2012).

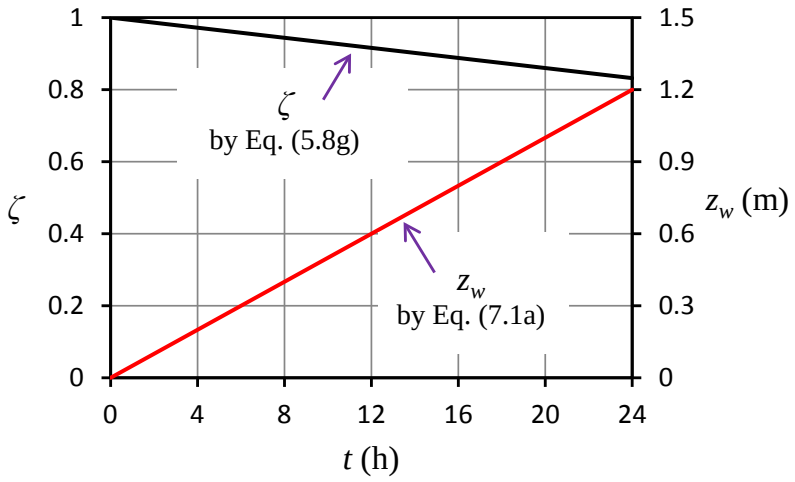

(a) Infiltration analysis

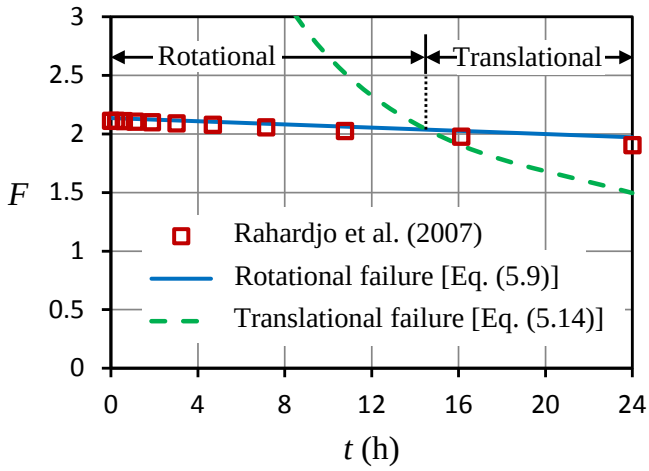

(b) Stability analysis

Figure 7.3 Unsaturated soil slope stability analysis using proposed equations – Case 2

Case 3: Slope failure at Langkawi, Malaysia

Case 3 is a back analysis of an actual slope failure reported by Huat et al. (2006). The residual soil slope failed on 14th November 2003 at the Island of Langkawi, Malaysia after a rainfall event, as shown in Figure 7.4. According to the given conditions shown in Table 7.3, the groundwater table can be considered as deep [Figure 5.5(a)], $h_p = 0$ m, $h_c = 10$ m. The

parameters n, S_f and S_o are not given in Huat et al. (2006). Lee et al. (2009) summarized the typical properties of the residual soil found in the Malaysian Peninsula, and reported that the porosity n typically ranges between 0.4 and 0.6. Hence, in the calculation n is assumed to be 0.5, S_f is assumed to be 1, and a parametric study with S_o = 0.2 (dry season), 0.5 and 0.8 (rainy season) is conducted. The infiltration and stability analysis results are summarized in Figure 7.5.

Figure 7.4 A deep rotational slide at Langkawi, Malaysia (from Huat et al., 2006)

For a specific rainfall duration t, the increase in initial degree of saturation S_o greatly increases the z_w [Figure 7.5(a)] and consequently greatly decrease the F_{trl} obtained by Eq. (5.14) [Figure 7.5(b)]. The height of the slope H = 60 m, which is much larger than the z_w (= 0 ~ 0.86 m). Hence, the ratios z_w/H are very small (0 ~ 0.014). As a result, ζ is only slightly reduced from unity due to the rainfall [Figure 7.5(a)], and the effects of t and S_o on the F_{rot} calculated by Eq. (5.9) can hardly be observed [Figure 7.5(b)]. At no infiltration condition (t = 0), F_{rot} = 0.695. The F_{rot} at t = 0 is supposed to be not less than 1, as the slope was stable before the infiltration. The

possible explanation could be the input shear strength parameters may have been underestimated, or the slope was stable because of the three-dimensional boundary effects.

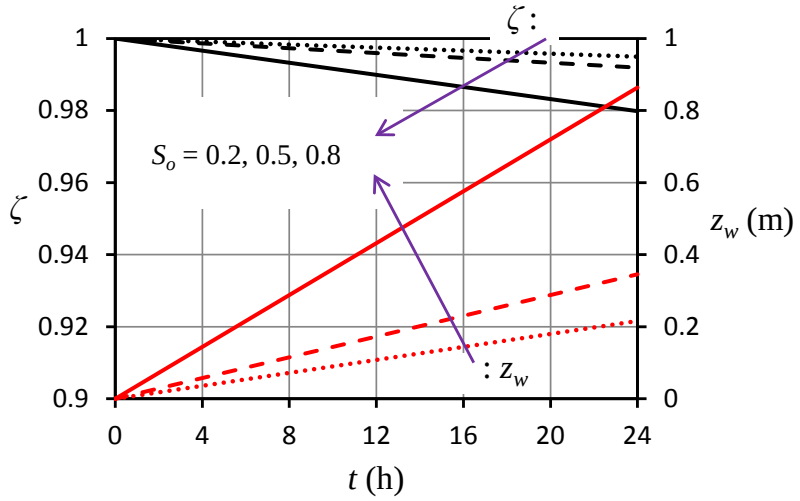

(a) Infiltration analysis

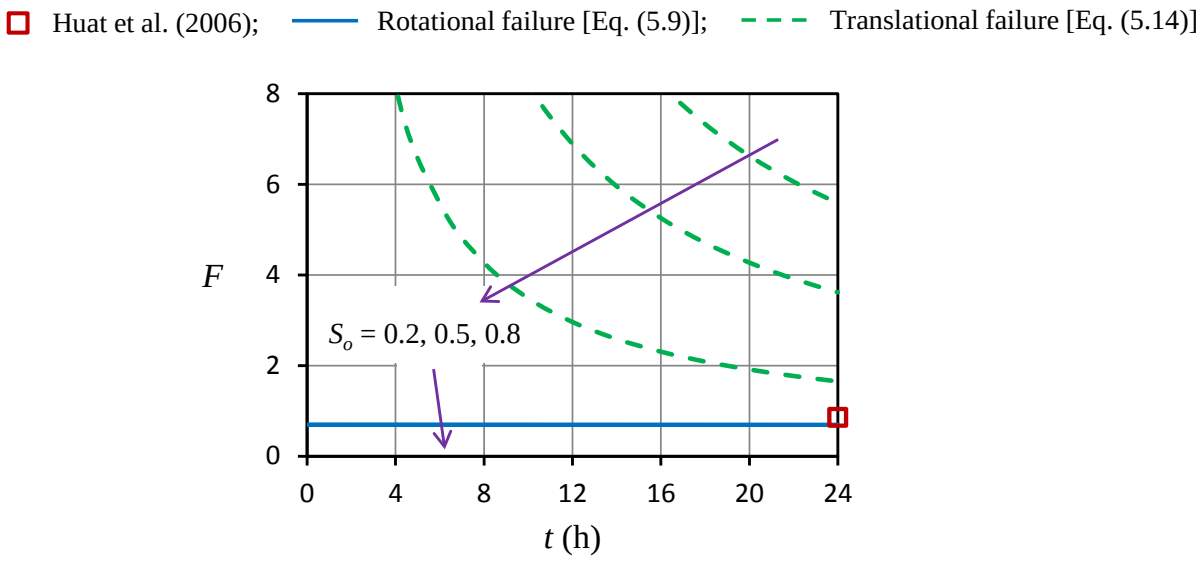

(b) Stability analysis

Figure 7.5 Back analysis of Langkawi slope failure using proposed equations – Case 3

At t = 24 h, the F_{rot} (= 0.69) obtained by Eq. (5.9) is generally consistent with the F (= 0.86) obtained by Huat et al. (2006) who used stability charts developed from *SEEP/W* and *SLOPE/W*. Figure 7.5(b) shows that F_{rot} calculated by Eq. (5.9) is less than F_{trl} calculated by Eq. (5.14) regardless of t and S_o, which reveals that rotational failure is more critical than translational failure. This was confirmed by the occurrence of the deep-seated rotational slide (Figure 7.4).

7.4.2 Saturated Soil Slopes

Equation (5.26) is used to analyze two landslide cases documented in the literature, as shown below.

Landslide at Selset, Yorkshire

Skempton and Brown (1961) presented a case study for a landslide in a boulder clay slope at Selset, Yorkshire. Details of the slope geometry are shown in Figure 7.6. The slope angle β is 28°, and height H is 12.8 m. The water level is practically at the ground surface except at the top of the slope. The bedrock is deep and would not affect the location of the critical slip surface. The soil properties of the boulder clay are: γ = 21.8 kN/m^3, c' = 8.6 kPa, and ϕ' = 32°. Skempton and Brown (1961) conducted stability analyses at two extreme pore-water pressure conditions: the groundwater flow is horizontal (r_u = 0.45) or parallel to the slope (r_u = 0.35). By using the stability charts developed by Bishop and Morgenstern (1960), Skempton and Brown (1961) estimated that the factor of safety for the slope was bound somewhere between 0.99 and 1.14.

The factors of safety of the Selset slope at various pore-water pressure ratios r_u can readily be calculated by Eq. (5.26). As shown in Figure 7.7, F_{est} = 1.66 at r_u = 0, and it decreases linearly

with the increase in r_u. If r_u increases from 0.35 to 0.45, F_{est} decreases from 1.12 to 0.96, compared to 1.14 and 0.99 obtained by Skempton and Brown (1961). To bring the slope to a state of limiting equilibrium (i.e., F_{est} = 1) requires that r_u = 0.42. The groundwater table shown in Figure 7.6 is very close to the ground surface. Hence, r_u = 0.42 is a reasonable estimate, and the back-calculation by Eq. (5.26) reasonably explains the failure of the slope.

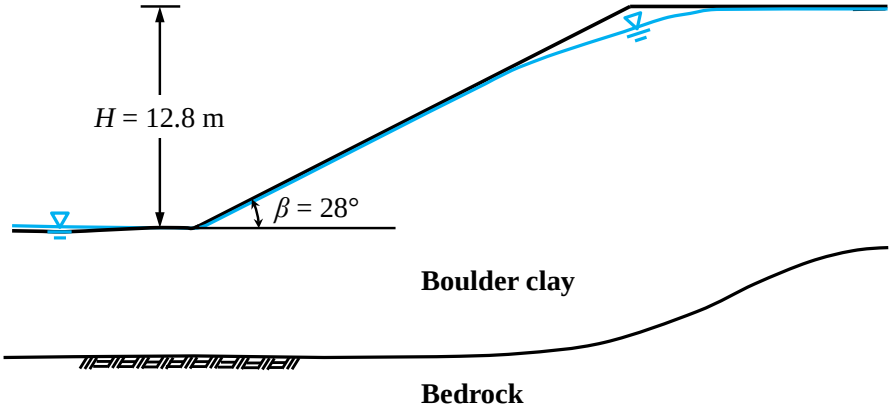

Figure 7.6 Cross-section of a slope at Selset before failure (from Skempton and Brown, 1961)

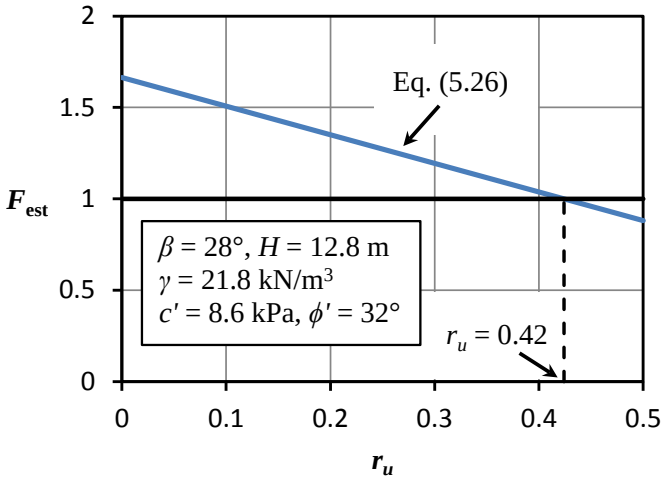

Figure 7.7 Stability analysis of the slope at Selset, Yorkshire

Landslide at Lodalen, Oslo

Sevaldson (1956) elaborately documented a slope failure that occurred in a railway cutting at Lodalen, Oslo. The central cross-section of the slope before failure is shown in Figure 7.8. The slope angle β is 26.6°, and height H is 17.3 m. The groundwater table is at shallow depth. The soil is relatively uniform and the soil properties are: γ = 18.7 kN/m^3, c' = 9.8 kPa, and ϕ' = 27.1°. Sevaldson (1956) conducted stability analysis using the limit equilibrium method proposed by Bishop (1955), and reported that the factor of safety for the central cross-section is exactly equal to unity.

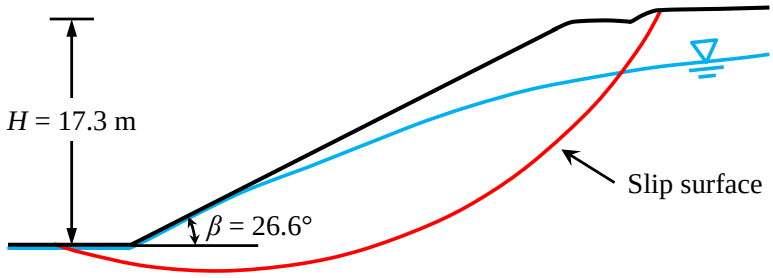

Figure 7.8 Central cross-section of a slope at Lodalen before failure (from Sevaldson, 1956)

If the groundwater level is at the ground surface and pore-water pressure is hydrostatic, $r_u = \gamma_w/\gamma$ = 0.52. For the groundwater level shown in Figure 7.8, the ratio of the area of submerged failure mass to the area of total failure mass is about 0.7. Hence, the r_u can be approximated by $0.52 \times 0.7 = 0.364$ according to the graphical procedure suggested by Bishop and Morgenstern (1960). The factors of safety F_{est} of the Lodalen slope at various r_u can readily be calculated by Eq. (5.26), as shown in Figure 7.9. At r_u = 0.364, the F_{est} is almost equal to unity. Hence, the back analysis is in good agreement with the analysis by Sevaldson (1956).

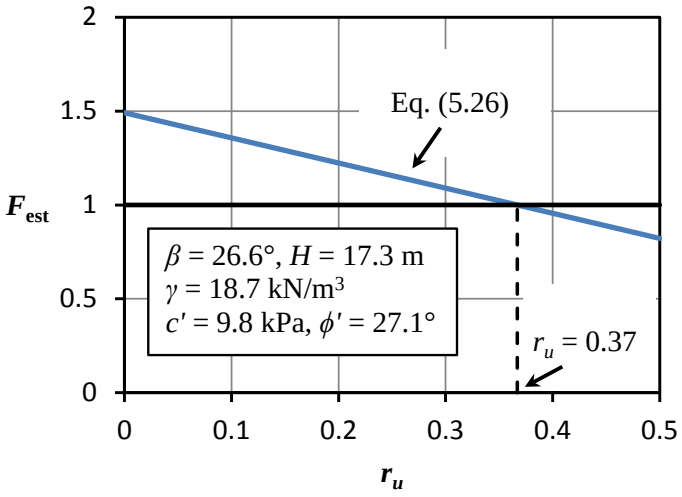

Figure 7.9 Stability analysis of the slope at Lodalen, Oslo

7.4.3 Dry and Unsaturated Soil Slopes under Seismic Loading

Dry Soil Slopes under Seismic Loading

Baker et al. (2006) presented two case studies for pseudo-static analysis of dry soil slopes. The given conditions for Case 1 are β = 40°, H = 7 m, γ = 18 kN/m^3, c' = 10 kPa and ϕ' = 28°. The given conditions for Case 2 are β = 26°, H = 5 m, γ = 18 kN/m^3, c' = 10 kPa and ϕ' = 12°. Since the slopes are dry, $\gamma_w h_c \tan\phi^b = 0$. Baker et al. (2006) calculated the factors of safety at static (k_h = 0) and pseudo-static (k_h = 0.2) conditions using variational approach. The factors of safety F_{est} for various pseudo-static coefficients k_h can readily be calculated by Eq. (6.13). As shown in Figure 7.10, F_{est} decreases nonlinearly with the increase in k_h. For Case 1, if k_h increases from 0 to 0.2, F_{est} decreases from 1.50 to 1.09, compared to 1.51 and 1.11 obtained by Baker et al. (2006). To bring the slope to a state of limiting equilibrium (i.e., F_{est} = 1) requires that k_h = 0.25 according to Eq. (6.14). For Case 2, if k_h increases from 0 to 0.2, F_{est} decreases from 1.50 to 1.00, compared to 1.47 and 0.96 obtained by Baker et al. (2006).

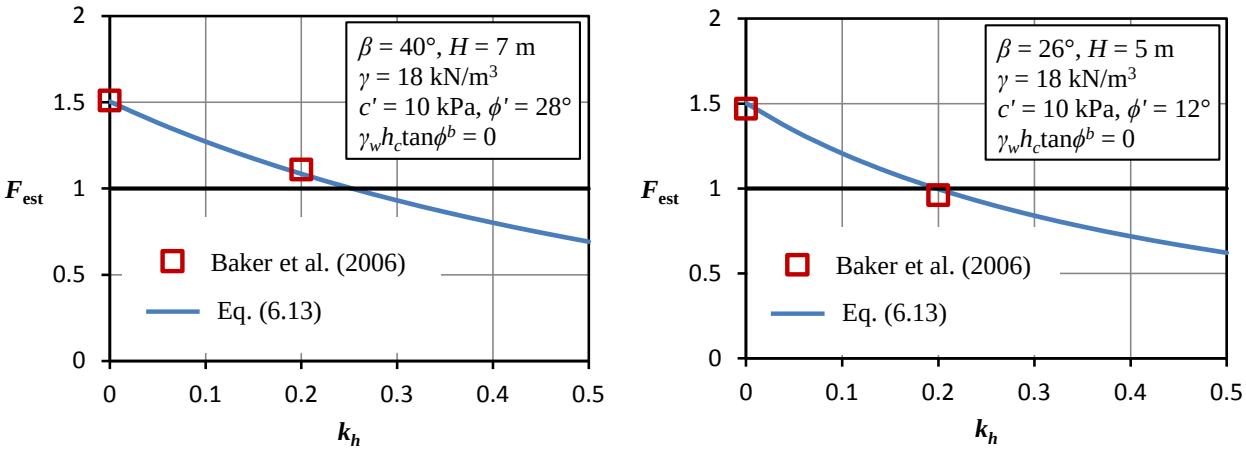

(a) Case 1 (b) Case 2

Figure 7.10 Seismic stability analysis of two dry soil slopes

Unsaturated Soil Slopes under Seismic Loading

Many soil slopes in arid and semi-arid regions are unsaturated with a deep groundwater table [Figure 4.4(b)]. By neglecting the contribution of matric suction to slope stability, unsaturated soil slopes with a deep groundwater table are conventionally analyzed as dry soil slopes. However, the neglect of matric suction may severely underestimate the factor of safety and lead to overly conservative geotechnical design. The incorporation of matric suction is straightforward in Eq. (6.13). To illustrate the improvement of factor of safety due to the consideration of matric suction, the two case studies presented in Figure 7.10 are reanalyzed with matric suction $\gamma_w h_c$ = 50 kPa and $\phi^b = 0.5\phi'$, and the results are shown in Figure 7.11. In order to illustrate the effect of matric suction clearly, the factors of safety for dry soil slopes (i.e., $\gamma_w h_c \tan\phi^b = 0$) shown in Figure 7.10 are also plotted in Figure 7.11 as dash curves. It can be seen that the stability curves move upward when the contribution of matric suction is considered. For Case 1, the factors of safety are increased by more than 50% due to the consideration of matric

suction ($\phi^b = 0.5\phi' = 14°$). For Case 2, the factors of safety are increased by about 30% due to the consideration of matric suction ($\phi^b = 0.5\phi' = 6°$). The case studies reveal that incorporating matric suction into unsaturated slope stability analysis could lead to more realistic stability assessment and consequently more economical design.

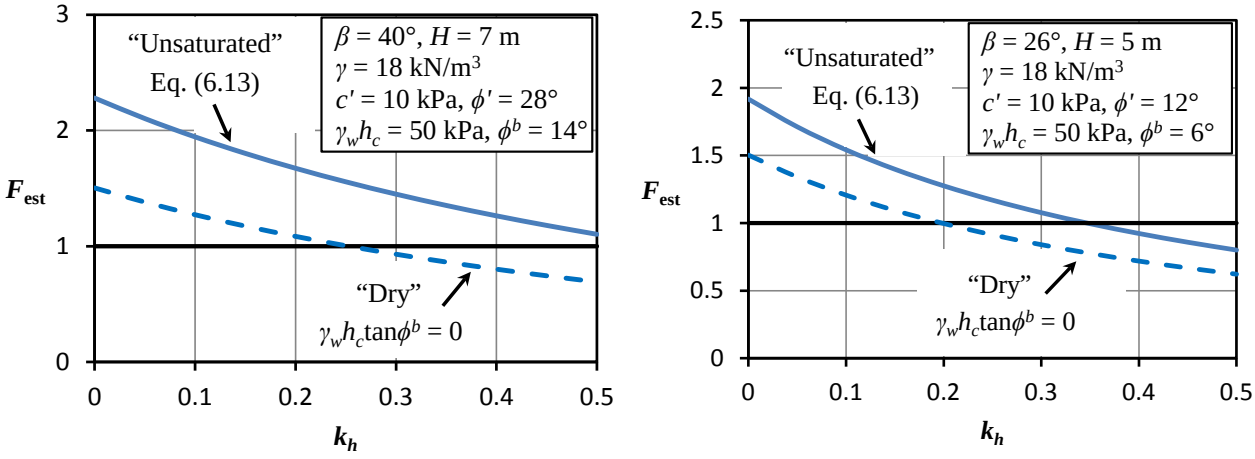

(a) Case 1 (b) Case 2

Figure 7.11 Seismic stability analysis of two unsaturated soil slopes

7.5 Summary

In this chapter, the slope stability equations proposed in Chapters 5 and 6 were summarized. The procedures to determine the required input parameters and potential applications of the slope stability equations were explained. Finally, the slope stability equations were used to reanalyze slope stability problems that have been solved by numerical methods and back analysis of landslides reported in the literature.

Chapter 8: Conclusions and Recommendations

8.1 Conclusions

The main conclusions drawn from this study are listed below.

1. **Simple shear tests on unsaturated soils.** The test program consists of two parts. In the first part, the effectiveness of lateral confinement methods for drained simple shear test was examined. It was found that constant K_o cell pressure would fail to ensure plane strain condition at large shear strain and consequently underestimate the shear strength. For the cyclic simple shear test confined by reinforced membrane, at small strain level the shear modulus may be underestimated if the soil specimen and reinforced membrane are not in good contact. Hence, in this study the soil specimens were confined by both reinforced membrane and cell pressure, so that these two confinement methods can complement each other. In the second part, the effect of cyclic loading on the shear strength of unsaturated soils was investigated through conducting cyclic, post-cyclic monotonic and monotonic simple shear tests on unsaturated residual soils. It was found that unsaturated soils would experience hardening under cyclic loading. More specifically, shear modulus of unsaturated soils would increase with the increase in number of cycles, and post-cyclic monotonic shear strength is larger than the monotonic shear strength. Hence, the static shear strength of unsaturated soils could be considered as a conservative estimate to the dynamic shear strength that should be used in seismic stability analysis.

2. **Upper bound limit analysis.** Log-spiral upper bound limit analysis has been widely used to develop slope stability charts for dry and saturated soil slopes due to its sound theoretical basis and high computational efficiency. In this study, the conventional log-spiral upper bound limit analysis for dry and saturated soil slopes was extended to analyze the rotational failure of unsaturated soil slopes under rainfall. More specifically, the equation to calculate the rate of work done by negative pore-water pressure was derived, the pore-water pressure profiles before and after rainfall infiltration were conceptualized, and the work rate balance equations for the log-spiral failure mechanism of unsaturated soil slopes were established. In addition, a kinematically admissible failure mode which can consider the boundary resistance of a translational slip was proposed to analyze the translational failure. Moreover, a procedure which can be incorporated into a computer program and enable automatic generation of dimensionless stability numbers was proposed.

3. **Slope stability equations.** Through regression analysis of the dimensionless stability numbers, a series of equations have been proposed for stability analysis of dry and saturated soil slopes, unsaturated soil slopes under rainfall and seismic loading, as summarized in Table 7.1. The proposed slope stability equations enable explicit calculation of factor of saefty and they can readily be integrated into computer program (e.g., excel spreadsheet) for parametric study; hence, the proposed slope stability equations provide convenient alternatives to existing slope stability charts. For the stability analysis of unsaturated soil slopes under rainfall, the parameters required by the proposed slope stability equations [Eq. (5.9) and Eq. (5.14)] (e.g., soil porosity n, initial degree of saturation S_o, and final degree of saturation S_f) are more easily determined than the parameters required for numerical seepage and slope stability analyses

(e.g., soil-water characteristic curve and permeability function). Hence, the availability of Eq. (5.9) and Eq. (5.14) will encourage practicing engineers to apply unsaturated soil mechanics principles when analyzing slope stability involving unsaturated soils. In addition, the proposed slope stability equations can readily be incorporated into regional landslide hazard mapping and probabilistic slope stability analysis. Application of the proposed slope stability equations has been discussed in Section 7.3 and illustrated with examples in Section 7.4.

4. **Controlling factors on the failure mode of unsaturated soil slopes under rainfall.** Through the dimensionless slope stability charts obtained by the upper bound limit analysis for both rotational and translational failure mechanisms, the governing failure mode of an unsaturated soil slope under rainfall was found to be closely related to the parameter group $c'/\gamma H\tan\phi'$. An unsaturated soil slope is increasingly prone to translational failure with the increase in infiltration depth and contribution of matric suction to soil strength in the unsaturated zone. Moderately steep slopes are more susceptible to translational failure than gentle and steep slopes, as the loss of matric suction is greater in moderately steep slopes than in gentle and steep slopes for a given amount of rainwater infiltration.

5. **Accuracy of the infinite slope model.** The stability equations for translational failure mechanism proposed in this study have considered the boundary effects. By benchmarking the factors of safety obtained by infinite slope models to the factors of safety obtained by the proposed stability equations, the errors caused by infinite slope models can be explicitly expressed as functions of depth/length ratio, slope geometry and soil properties. It was found that the accuracy of infinite slope models was not only affected by the depth/length ratio (d/l),

but also affected by the parameter group $c'/\gamma H\tan\phi'$. Infinite slope model is accurate if d/l or $c'/\gamma H\tan\phi'$ approaches zero, however, underestimation of the factor of safety increases with increasing d/l and $c'/\gamma H\tan\phi'$.

8.2 Limitations

The major limitation of slope stability charts and equations is that they are developed for simple conditions (e.g., simple slope geometry, homogeneous soil properties). Hence, if the slope geometry and soil properties deviate from simple conditions, approximations of the slope geometry and soil properties need to be performed. If the approximation can be made judiciously, the stability of the slope can still be assessed accurately (Duncan, 1996). For a slope with complex geometry and high soil heterogeneity, it may be difficult to approximate the slope geometry and soil properties. Consequently, the solutions obtained by the proposed slope stability equations may not be as accurate as those obtained by a more rigorous approach (e.g., numerical seepage and slope stability analysis).

There is a trade-off between a simplified approach and a rigorous approach (Jibson, 2011): a simplified approach requires less data and the procedure is simpler, while the results obtained may not be very accurate; a rigorous approach generally leads to accurate results, but it requires a significant amount of data and effort, consequently it is reserved for critical projects where substantial risk may be involved. The slope stability equations proposed in this study are suggested for use when the rigirous approaches (e.g., finite element analysis) are inaccessible or the data quality does not merit a rigorous analysis.

8.3 Recommendations for Further Research

The following research topics would be a logical continuation of the studies described in this thesis.

1) Slope failures are in fact three-dimensional rather than two-dimensional. The translational upper bound limit analysis proposed in this study is two-dimensional. It can be extended to three-dimensional by considering the slope width.

2) The slope stability equations listed in Table 7.1 are for two-dimensional slope stability analyses. They can be extended to three-dimensional slopes by considering the ratio of the slope width to the slope height.

3) The upper bound limit analysis and slope stability equations are only developed for simple conditions (e.g., simple slope geometry, homogeneous soil properties). They may be extended to consider more complicated conditions (e.g., layered slopes, slopes with tension cracks).

4) The slope stability equations enable explicit calculation of factors of safety. Hence, they can be incorporated into regional slope stability analysis and probabilistic slope stability analysis.

References

Acharya, B., and Airey, D. (2017). “Effect of Specimen Confinement Method on Simple Shear Test of Clay.” In: *Advances in Laboratory Testing and Modelling of Soils and Shales* (Ferrari & Laloui (eds)), Springer, Cham, 247-254.

Ahangar-Asr, A., Faramarzi, A., and Javadi, A. A. (2010). “A new approach for prediction of the stability of soil and rock slopes.” *Engineering Computations*, 27(7), 878-893.

Airey, D. W., and Wood, D. M. (1987). “An evaluation of direct simple shear tests on clay.” *Géotechnique*, 37(1), 25-35.

Alonso, E. E., Gens, A., and Delahaye, C. H. (2003). “Influence of rainfall on the deformation and stability of a slope in overconsolidated clays: a case study.” *Hydrogeology Journal*, 11(1), 174-192.

Ambraseys, N. N., and Menu, J. M. (1988). “Earthquake-induced ground displacements.” *Earthquake Engineering and Structural Dynamics*, 16(7), 985-1006.

Amer, M. I., Aggour, M. S., and Kovacs, W. D. (1984). “Size effect in simple shear testing.” Report NBS-GCR-84-478, National Bureau of Standards, U.S. Dept. of Commerce, Washington, DC, 65 pp.

Amer, M. I., Kovacs, W. D., and Aggour, M. S. (1987). “Cyclic simple shear size effects.” *Journal of Geotechnical Engineering*, 113(7), 693-707.

American Society for Testing and Materials (2007). *Standard Test Method for Consolidated Undrained Direct Simple Shear Testing of Cohesive Soils*, ASTM D 6528-07.

Andersen, K. H. (2015). “Cyclic soil parameters for offshore foundation design.” *3rd McClelland Lecture: Frontiers in Offshore Geotechnics III* (Meyer (ed.)), Taylor & Francis Group, Oslo, Norway, 5-82.

Baecher, G. B., and Christian, J. T. (2003). *Reliability and Statistics in Geotechnical Engineering*, John Wiley & Sons, New York.

Baker, R. (2003). “A second look at Taylor’s stability chart.” *Journal of Geotechnical and Geoenvironmental Engineering*, 129(12), 1102-1108.

Baker, R., and Garber, M. (1978). “Theoretical analysis of the stability of slopes.” *Géotechnique*, 28(4), 395-411.

Baker, R., Shukha, R., Operstein, V., and Frydman, S. (2006). “Stability charts for pseudo-static slope stability analysis.” *Soil Dynamics and Earthquake Engineering*, 26(9), 813-823.

Barnes, G. E. (1991). “A simplified version of the Bishop and Morgenstern slope stability charts.” *Canadian Geotechnical Journal*, 28(4), 630-637.

Baxter, C. D. P., A. S. Bradshaw, M. Ochoa-Lavergne, and R. Hankour. (2010). “DSS test results using wire-reinforced membranes and stacked rings.” In *GeoFlorida 2010: Advances in Analysis, Modeling & Design*, pp. 600-607.

Bell, J. M. (1966). “Dimensionless parameters for homogeneous earth slopes.” *Journal of the Soil Mechanics and Foundations Division*, 92(5), 51-65.

Bishop, A. W. (1955). “The use of the slip circle for the stability analysis of slopes.” *Géotechnique*, 5(1), 7–17.

Bishop, A. W., and Blight, G. E. (1963). “Some aspects of effective stress in saturated and partly saturated soils.” *Géotechnique*, 13(3), 177-197.

Bishop, A. W., and Morgenstern, N. (1960). “Stability coefficients for earth slopes.” *Géotechnique*, 10(4), 129-153.

Bjerrum, L., and Landva, A. (1966). “Direct simple-shear tests on a Norwegian quick clay.” *Géotechnique*, 16(1), 1-20.

Boulanger, R. W., Chan, C. K., Seed, H. B., Seed, R. B., and Sousa, J. (1993). "A Low-Compliance Bi-Directional Cyclic Simple Shear Apparatus," *Geotechnical Testing Journal,* 16(1): 36–45.

Boulanger, R. W., and Idriss, I. M. (2007). "Evaluation of cyclic softening in silts and clays." *Journal of Geotechnical and Geoenvironmental Engineering*, 133(6), 641-652.

Bouwer, H. (1966). "Rapid field measurement of air entry value and hydraulic conductivity of soil as significant parameters in flow system analysis." *Water Resource Research*, 2(4), 729-738.

Bray, J. D., and Travasarou, T. (2007). "Simplified procedure for estimating earthquake-induced deviatoric slope displacements." *Journal of Geotechnical and Geoenvironmental Engineering*, 133(4), 381-392.

Bray, J. D., and Travasarou, T. (2009). "Pseudostatic coefficient for use in simplified seismic slope stability evaluation." *Journal of Geotechnical and Geoenvironmental Engineering*, 135(9), 1336-1340.

Budhu, M. (1984). "Nonuniformities imposed by simple shear apparatus." *Canadian Geotechnical Journal*, 21(1), 125-137.

Cai, F., and Ugai, K. (2004). "Numerical analysis of rainfall effects on slope stability." *International Journal of Geomechanics*, 4(2), 69-78.

Cascini, L., Cuomo, S., Pastor, M., and Sorbino, G. (2010). "Modeling of rainfall-induced shallow landslides of the flow-type." *Journal of Geotechnical and Geoenvironmental Engineering*, 136(1), 85-98.

Chandler, R.J., Peiris, T.A. (1989). "Further extensions to the Bishop and Morgenstern slope stability charts." *Ground Engineering*, 22(4), 33-38.

Chang, C. J., Chen, W. F., and Yao, J. T. P. (1984). "Seismic displacements in slopes by limit analysis." *Journal of Geotechnical Engineering*, 110(7), 860-874.

Chen, W. F. (1975). *Limit Analysis and Soil Plasticity*, Elsevier Science, Amsterdam, the Netherlands.

Chen, W. F., Giger, M. W., and Fang, H. Y. (1969). "On the limit analysis of stability of slopes." *Soils and Foundations*, 9(4), 23-32.

Chen, Z., Wang, X., Haberfield, C., Yin, J. H., and Wang, Y. J. (2001). "A three-dimensional slope stability analysis method using the upper bound theorem Part I: Theory and methods." *International Journal of Rock Mechanics and Mining Sciences*, 38(3), 369-378.

Chien, Y. C., and Tsai, C. C. (2017). "Immediate Estimation of Yield Acceleration for Shallow and Deep Failures in Slope-Stability Analyses." *International Journal of Geomechanics*, 17(7), 04017009.

Chin, K. B. (2011). "Cyclic simple shear properties of unsaturated residual soils", PhD thesis, Nanyang Technological University, Singapore.

Chin, K. B., Leong, E. C., and Rahardjo, H. (2009). "Cyclic behaviour of unsaturated silt in suction-controlled simple shear apparatus," *Proceedings of the 4th Asia-Pacific Conference on Unsaturated Soils*, November 23-25, 2009, Newcastle, Australia, 65-70.

Chin, K. B., Leong, E. C., and Rahardjo, H. (2010). "A simplified method to estimate the soil-water characteristic curve." *Canadian Geotechnical Journal*, 47(12), 1382-1400.

Cho, S. E. (2009). "Infiltration analysis to evaluate the surficial stability of two-layered slopes considering rainfall characteristics." *Engineering Geology*, 105(1), 32-43.

Cho, S. E., and Lee, S. R. (2002). "Evaluation of surficial stability for homogeneous slopes considering rainfall characteristics." *Journal of Geotechnical and Geoenvironmental Engineering*, 128(9), 756-763.

Chu, H. H., and Vucetic, M. (1992). "Settlement of compacted clay in a cyclic direct simple shear device." *Geotechnical Testing Journal*, 15(4), 371-379.

Dai, F. C., Lee, C. F., and Wang, S. J. (2003). “Characterization of rainfall-induced landslides.” *International Journal of Remote Sensing*, 24(23), 4817-4834.

Dawson, E. M., Roth, W. H., and Drescher, A. (1999). Slope stability analysis by strength reduction. *Géotechnique*, 49(6), 835-840.

Deere, D. U., and Patton, F. D. (1971). “Slope stability in residual soils.” *Proceedings of 4th Pan-American Conference on Soil Mechanics and Foundation Engineering*, Puerto Rico, Vol. 1, pp. 87-170.

Dreyfus, D., Rathje, E. M., and Jibson, R. W. (2013). “The influence of different simplified sliding-block models and input parameters on regional predictions of seismic landslides triggered by the Northridge earthquake.” *Engineering Geology*, 163, 41-54.

Drucker, D. C., and Prager, W. (1952). “Soil mechanics and plastic analysis or limit design.” *Quarterly of Applied Mathematics*, 10(2), 157-165.

Duncan, J. M. (1996). “State of the art: limit equilibrium and finite-element analysis of slopes.” *Journal of Geotechnical Engineering*, 122(7), 577-596.

Duncan, J. M., Wright, S. G., and Brandon, T. L. (2014). *Soil Strength and Slope Stability*, John Wiley & Sons.

Eid, H. T. (2014). “Stability charts for uniform slopes in soils with nonlinear failure envelopes.” *Engineering Geology*, 168, 38-45.

FHWA (2011). *LRFD Seismic Analysis and Design of Transportation Geotechnical Features and Structural Foundations*, Geotechnical Engineering Circular No. 3, Report No. FHWA-NHI-11-032, Federal Highway Administration, Washington, DC.

Fourie, A. B. (1996). “Predicting rainfall-induced slope instability.” *Proceedings of the ICE-Geotechnical Engineering*, 119(4), 211-218.

Fourie, A. B., Rowe, D., and Blight, G. E. (1999). “The effect of infiltration on the stability of the slopes of a dry ash dump.” *Géotechnique*, 49(1), 1-13.

Franke, E., Kiekbusch, M., and Schuppener, B. (1979). “A new direct simple shear device.” *Geotechnical Testing Journal*, 2(4), 190-199.

Fredlund, D. G., and Morgenstern, N. R. (1976). “Constitutive relations for volume change in unsaturated soils.” *Canadian Geotechnical Journal*, 13(3), 261-276.

Fredlund, D. G., and Morgenstern, N. R. (1977). “Stress State Variables for Unsaturated Soils.” *Journal of the Geotechnical Engineering Division*, 103(5), 447-466.

Fredlund, D. G., Morgenstern, N. R., and Widger, R. A. (1978). “The shear strength of unsaturated soils.” *Canadian Geotechnical Journal*, 15(3), 313-321.

Fredlund, D. G., and Rahardjo, H. (1993). *Soil Mechanics for Unsaturated Soils*, Wiley, New York.

Fredlund, D. G., Xing, A., and Huang, S. (1994). “Predicting the permeability function for unsaturated soils using the soil-water characteristic curve”. *Canadian Geotechnical Journal*, 31(4), 533-546.

Fredlund, D. G., Rahardjo, H., and Fredlund, M. D. (2012). *Unsaturated Soil Mechanics in Engineering Practice*. John Wiley & Sons.

Fredlund, M. D., Wilson, G. W., and Fredlund, D. G. (2002). “Use of the grain-size distribution for estimation of the soil-water characteristic curve.” *Canadian Geotechnical Journal*, 39(5), 1103-1117.

Gan, J. K., and Fredlund, D. G. (1996). “Shear strength characteristics of two saprolitic soils.” *Canadian Geotechnical Journal*, 33(4), 595-609.

Gao, Y., Zhang, F., Lei, G. H., Li, D., Wu, Y., and Zhang, N. (2013). “Stability charts for 3D failures of homogeneous slopes.” *Journal of Geotechnical and Geoenvironmental Engineering*, 139(9), 1528-1538.

Gao, Y., Zhu, D., Zhang, F., Lei, G. H., and Qin, H. (2014). “Stability analysis of three-dimensional slopes under water drawdown conditions.” *Canadian Geotechnical Journal*, 51(11), 1355-1364.

Garven, E. A., and Vanapalli, S. K. (2006). “Evaluation of empirical procedures for predicting the shear strength of unsaturated soils.” In *Unsaturated Soils 2006*(pp. 2570-2592). ASCE.

Gasmo, J. M., Rahardjo, H., and Leong, E. C. (2000). “Infiltration effects on stability of a residual soil slope.” *Computers and Geotechnics,* 26(2), 145-165.

Gavin, K., and Xue, J. (2008). “A simple method to analyze infiltration into unsaturated soil slopes.” *Computer and Geotechnics*, 35(2), 223-230.

Gerscovich, D. M. S., Vargas, E. A., and De Campos, T. M. P. (2006). “On the evaluation of unsaturated flow in a natural slope in Rio de Janeiro, Brazil.” *Engineering Geology*, 88(1), 23-40.

Godt, J. W., B. Sener-Kaya, N. Lu, and R. L. Baum (2012). “Stability of infinite slopes under transient partially saturated seepage conditions.” *Water Resource Research*, 48, W05505.

Goh, A. T., and Kulhawy, F. H. (2003). “Neural network approach to model the limit state surface for reliability analysis.” *Canadian Geotechnical Journal*, 40(6), 1235-1244.

Goh, S. G., Rahardjo, H., and Leong, E. C. (2010). “Shear strength equations for unsaturated soil under drying and wetting.” *Journal of Geotechnical and Geoenvironmental Engineering*, 136(4), 594-606.

Green, W. H., and Ampt, G. A. (1911). “Studies on Soil Phyics I. The flow of air and water through soils.” *The Journal of Agricultural Science*, 4(1), 1-24.

Griffiths, D. V., and Lu, N. (2005). “Unsaturated slope stability analysis with steady infiltration or evaporation using elasto-plastic finite elements.” *International Journal for Numerical and Analytical Methods in Geomechanics*, 29(3), 249-267.

Griffiths, D. V., Huang, J., and Dewolfe, G. F. (2011a). “Numerical and analytical observations on long and infinite slopes.” *International Journal for Numerical and Analytical Methods in Geomechanics*, 35(5), 569-585.

Griffiths, D. V., Huang, J., and Fenton, G. A. (2011b). “Probabilistic infinite slope analysis.” *Computer and Geotechnics*, 38(4), 577-584.

Harder, L. S., Jr. (1991). “Performance of earth dams during the Loma Prieta earthquake.” *Proc. 2nd International conference on Recent Advances in Geotechnical Earthquake Engineering and Soil Dynamics*, University of Missouri-Rolla, Rolla, Missouri, Vol. 3, 1663-1679.

Harp, E. L., Michael, J. A., Laprade, W. T. (2006). “Shallow-landslide hazard map of Seattle, Washington.” U.S. Geological Survey Open-File Report 2006-1139. 20 pp.

Harp, E. L., Reid, M. E., McKenna, J. P., Michael, J. A. (2009). “Mapping of hazard from rainfall-triggered landslides in developing countries: examples from Honduras and Micronesia.” *Engineering Geology*, 104(3), 295-311.

Ho, J. Y., Lee, K. T., Chang, T. C., Wang, Z. Y., Liao, Y. H. (2012). “Influences of spatial distribution of soil thickness on shallow landslide prediction.” *Engineering Geology*, 124, 38–46.

Hsu, C. C., and Vucetic, M. (2004). “Volumetric threshold shear strain for cyclic settlement.” *Journal of Geotechnical and Geoenvironmental Engineering*, 130(1), 58-70.

Huang, M., and Jia, C. Q. (2009). “Strength reduction FEM in stability analysis of soil slopes subjected to transient unsaturated seepage.” *Computer and Geotechnics*, 36(1), 93-101.

Huat, B. B., Ali, F. H., and Rajoo, R. S. K. (2006). “Stability analysis and stability chart for unsaturated residual soil slope.” *American Journal of Environmental Science*, 2(4), 154-160.

Hubler, J. F., Athanasopoulos-Zekkos, A., and Zekkos, D. (2017). “Monotonic, cyclic, and postcyclic simple shear response of three uniform gravels in constant volume conditions.” *Journal of Geotechnical and Geoenvironmental Engineering*, 143(9), 04017043.

Hynes-Griffin, M. E., and Franklin, A. G. (1984). “Rationalizing the seismic coefficient method.” U.S. Army Corps of Engineers Waterways Experiment Station, Miscellaneous Paper GL-84-13.

Idriss, I. M., Dobry, R., and Singh, R. D. (1978). “Nonlinear behavior of soft clays during cyclic loading.” *Journal of Geotechnical Engineering, ASCE*, 104(GT12), 1427-1447.

Ishihara, K. (1996). *Soil Behavior in Earthquake Geotechnics*, Clarendon Press, Oxford.

Iverson, R. M. (2000). “Landslide triggering by rain infiltration.” *Water Resources Research*, 36(7), 1897-1910.

Jafarzadeh, F., and Sadeghi, H. (2012). “Experimental study on dynamic properties of sand with emphasis on the degree of saturation.” *Soil Dynamics and Earthquake Engineering*, 32(1), 26-41.

Jiang, J. C., and Yamagami, T. (2006). “Charts for estimating strength parameters from slips in homogeneous slopes.” *Computer and Geotechnics*, 33(6), 294-304.

Jibson, R. W. (1993). “Predicting earthquake-induced landslide displacements using Newmark's sliding block analysis.” *Transportation Research Record 1411*, 9-17.

Jibson, R. W. (2007). “Regression models for estimating coseismic landslide displacement.” *Engineering Geology*, 91(2), 209-218.

Jibson, R. W. (2011). “Methods for assessing the stability of slopes during earthquakes—A retrospective.” *Engineering Geology*, 122(1), 43-50.

Jibson, R. W. (2014). “Mapping seismic landslide hazards in Anchorage, Alaska.” *Tenth U.S. National Conference on Earthquake Engineering*, July 21-25, 2014, Anchorage, Alaska.

Jibson, R. W., Harp, E. L., and Michael, J. A. (2000). “A method for producing digital probabilistic seismic landslide hazard maps.” *Engineering Geology*, 58(3), 271-289.

Joer, H. A., Erbrich, C. T., and Sharma, S. S. (2011). “A new interpretation of the simple shear test.” *Proceedings Frontiers in Offshore Geotechnics II, Perth*, 353-358.

Kang, X., Cheng, Y., and Ge, L. (2015). “Radial strain behaviors and stress state interpretation of soil under direct simple shear.” *Journal of Testing and Evaluation*, 43(6), 1594-1601.

Kang, X., Ge, L., Chang, K. T., and Kwok, A. O. L. (2016). “Strain-controlled cyclic simple shear tests on sand with radial strain measurements.” *Journal of Materials in Civil Engineering*, 28(4), 04015169.

Keaton, J. R., Wartman, J., Anderson, S., Benoît, J., deLaChapelle, J., Gilbert, R., and Montgomery, D. R. (2014). “The 22 March 2014 Oso Landslide, Snohomish County, Washington.” Geotechnical Extreme Event Reconnaissance (GEER), National Science Foundation, Arlington, VA.

Keefer, D. K. (1984). “Landslides caused by earthquakes.” *Geological Society of America Bulletin*, 95(4), 406-421.

Keefer, D. K. (2002). “Investigating landslides caused by earthquakes–a historical review.” *Surveys in Geophysics*, 23(6), 473-510.

Kim, J., Salgado, R., and Yu, H. S. (1999). “Limit analysis of soil slopes subjected to pore-water pressures.” *Journal of Geotechnical and Geoenvironmental Engineering*, 125(1), 49-58.

Kisch, M. (1959). “The theory of seepage from clay-blanketed reservoirs.” *Géotechnique*, 9(1), 9-21.

Kjellman, W. (1951). “Testing the shear strength of clay in Sweden.” *Géotechnique*, 2(3), 225-232.

Koo, Y. C. (1998). “Some important aspects of design of soil slopes in Hong Kong”. In *Slope Engineering in Hong Kong* (Li, Kay & Ho (eds)), Balkema, Rotterdam, the Netherlands, pp. 21-29.

Kostić, S., Vasović, N., and Sunarić, D. (2016). “Slope stability analysis based on experimental design.” *International Journal of Geomechanics*, 16(5), 04016009.

Kovacs, W. D., and Leo, E. (1981). “Cyclic simple shear of large scale samples: Effects of diameter to height ratio.” *International Conference on Recent Advances in Geotechnical Earthquake Engineering*, Univ. of Missouri, Rolla, Mo., 897 - 904.

Kramer, S.L. (1996). *Geotechnical Earthquake Engineering*, Prentice Hall, NJ.

Kwan, W. S., and El Mohtar, C. (2014). “Comparison between Shear Strength of Dry Sand Measured in CSS Device Using Wire-Reinforced Membranes and Stacked Rings.” In *Geo-Congress 2014: Geo-characterization and Modeling for Sustainability*, pp. 1111-1119.

Ladd, C. C , and Edgers, L. (1972). “Consolidated-undrained direct simple shear tests on saturated clays.” Research Report R72-82, Dept. of Civ. Engrg., MIT, Cambridge, Mass.

Lambe, T. W. (1951). “Capillary phenomenon in cohesionless soils.” *Transactions of the American Society of Civil Engineers*, 116(1), 401-423.

Le, T. M. H., Gallipoli, D., Sánchez, M., and Wheeler, S. (2015). “Stability and failure mass of unsaturated heterogeneous slopes.” *Canadian Geotechnical Journal*, 52(11), 1747-1761.

Lee, L. M., Gofar, N., and Rahardjo, H. (2009). “A simple model for preliminary evaluation of rainfall-induced slope instability.” *Engineering Geology*, 108(3), 272-285.

Lefebvre, G., and Pfendler, P. (1996). “Strain rate and preshear effects in cyclic resistance of soft clay.” *Journal of Geotechnical Engineering, ASCE,* 122(1), 21-26.

Leong, E. C., and Rahardjo, H. (1997a). “Review of soil-water characteristic curve equations.” *Journal of Geotechnical and Geoenvironmental Engineering*, 123(12), 1106-1117.

Leong, E. C., and Rahardjo, H. (1997b). “Permeability functions for unsaturated soils.” *Journal of Geotechnical and Geoenvironmental Engineering*, 123(12), 1118-1126.

Leshchinsky, D., and San, K. C. (1994). “Pseudostatic seismic stability of slopes: Design charts.” *Journal of Geotechnical Engineering*, 120(9), 1514-1532.

Li, A. G., Yue, Z. Q., Tham, L. G., Lee, C. F., and Law, K. T. (2005). “Field-monitored variations of soil moisture and matric suction in a saprolite slope.” *Canadian Geotechnical Journal*, 42(1), 13-26.

Li, X., Li, J. H., and Zhang, L. M. (2014). “Predicting bimodal soil–water characteristic curves and permeability functions using physically based parameters.” *Computers and Geotechnics*, 57, 85-96.

Lin, J. S., and Whitman, R. V. (1983). “Decoupling approximation to the evaluation of earthquake-induced plastic slip in earth dams.” *Earthquake Engineering and Structural Dynamics*, 11(5): 667-678.

Loukidis, D., Bandini, P., and Salgado, R. (2003). “Stability of seismically loaded slopes using limit analysis.” *Géotechnique*, 53(5), 463-480.

Low, B.K. (2003). Practical probabilistic slope stability analysis. 12th Panamerican Conference on Soil Mechanics and Geotechnical Engineering and 39th U.S. Rock Mechanics Symposium, M.I.T., Cambridge, Massachusetts, Vol. 2, 2777-2784.

Low, B. K., Gilbert, R. B., and Wright, S. G. (1998). “Slope reliability analysis using generalized method of slices.” *Journal of Geotechnical and Geoenvironmental Engineering*, 124(4), 350-362.

Lu, N., and Likos, W. J. (2006). “Suction stress characteristic curve for unsaturated soil.” *Journal of Geotechnical and Geoenvironmental Engineering*, 132(2), 131-142.

Lu, N., and Godt, J. (2008). “Infinite slope stability under steady unsaturated seepage conditions.” *Water Resource Research*, 44(11), W11404.

Lu, N., Şener-Kaya, B., Wayllace, A., and Godt, J. W. (2012). “Analysis of rainfall-induced slope instability using a field of local factor of safety.” *Water Resource Research*, 48(9), W09524.

Lumb, P. (1962). “Effect of rain storms on slope stability.” *Proc. Symp. on Hong Kong Soils*, Hong Kong, pp. 73-87.

Makdisi, F. I., and Seed, H. B. (1978). “Simplified procedure for estimating dam and embankment earthquake-induced deformations.” *Journal of the Geotechnical Engineering Division*, ASCE, 104(GT7), 849-867.

Manouchehrian, A., Gholamnejad, J. and Sharifzadeh, M. (2014). “Development of a model for analysis of slope stability for circular mode failure using genetic algorithm.” *Environmental Earth Science*, 71(3), 1267-1277.

McGuire, S. T. (2011). “Comparison of direct simple shear confinement methods on clay and silt specimens”, Master thesis, University of Rhode Island.

Mein, R. G., and Larson, C. L. (1973). “Modeling infiltration during a steady rain.” *Water Resource Research*, 9(2), 384-394.

Michalowski, R. L. (1989). “Three-dimensional analysis of locally loaded slopes.” *Géotechnique*, 39(1), 27-38.

Michalowski, R. L. (1995). “Slope stability analysis: a kinematical approach.” *Géotechnique*, 45(2), 283-293.

Michalowski, R. L. (2002). “Stability charts for uniform slopes.” *Journal of Geotechnical and Geoenvironmental Engineering*, 128(4), 351-355.

Michalowski, R. L., and Nadukuru, S. S. (2013). “Three-dimensional limit analysis of slopes with pore pressure.” *Journal of Geotechnical and Geoenvironmental Engineering*, 139(9), 1604-1610.

Milledge, D. G., Griffiths, D. V., Lane, S. N., and Warburton, J. (2012). “Limits on the validity of infinite length assumptions for modelling shallow landslides.” *Earth Surface Processes and Landforms*, 37(11), 1158-1166.

Miller, T. W., and Hamilton, J. M. (1989). “A new analysis procedure to explain a slope failure at the Martin Lake mine.” *Géotechnique*, 39(1), 107-123.

Miller, T. W. and Hamilton, J. H. (1990). “A new analysis procedure to explain a slope failure at the Martin Lake mine.” Discussion by R. L. Michalowski, *Géotechnique*, 40(1), 145-147.

Moregenstern, N. (1963). “Stability charts for earth slopes during rapid drawdown.” *Géotechnique*, 13(2), 121-131.

Morgenstern, N.R., and Price, V.E. (1965). “The analysis of the stability of general slip surfaces.” *Géotechnique*, 15(1), 79-93.

Nam, S., Gutierrez, M., Diplas, P., and Petrie, J. (2011). “Determination of the shear strength of unsaturated soils using the multistage direct shear test.” *Engineering Geology*, 122(3), 272-280.

Newmark, N. M. (1965). “Effects of earthquakes on dams and embankments.” *Géotechnique*, 15(2), 139-160.

Neuman, S. P. (1976). “Wetting front pressure head in the infiltration model of Green and Ampt.” *Water Resources Research*, 12(3), 564-566.

Ng, C. W. W., and Shi, Q. (1998). “A numerical investigation of the stability of unsaturated soil slopes subjected to transient seepage.” *Computer and Geotechnics*, 22(1), 1-28.

O’Connor, M. J., and Mitchell, R. J. (1977). “An extension of the Bishop and Morgenstern slope stability charts.” *Canadian Geotechnical Journal*, 14(1), 144-151.

Park, H. J., Lee, J. H., and Woo, I. (2013). “Assessment of rainfall-induced shallow landslide susceptibility using a GIS-based probabilistic approach.” *Engineering Geology*, 161, 1-15.

Perera, Y. Y., Zapata, C. E., Houston, W. N., and Houston, S. L. (2005). “Prediction of the soil-water characteristic curve based on grain-size-distribution and index properties.” *Proceedings of Geo-Frontiers 2005 Congress, ASCE*, Jan. 24-26, Austin, TX.

Pradel, D., and Raad, G. (1993). “Effect of permeability on surficial stability of homogeneous slopes.” *Journal of Geotechnical Engineering*, 119(2), 315-332.

Philip, J. R. (1957). “The theory of infiltration: 4. Sorptivity and algebraic infiltration equations.” *Soil Science*, 84(3), 257-264.

Rahardjo, H., Lim, T. T., Chang, M. F., and Fredlund, D. G. (1995). “Shear-strength characteristics of a residual soil.” *Canadian Geotechnical Journal*, 32(1), 60-77.

Rahardjo, H., Leong, E. C., Deutcher, M. S., Gasmo, J. M., and Tang, S. K. (2000). “Rainfall-induced slope failures.” *Geotechnical Engineering Monograph 3*, NTU-PWD Geotechnical Research Centre, Nanyang Technological Univ., Singapore, 1-86.

Rahardjo, H., Lee, T. T., Leong, E. C., and Rezaur, R. B. (2005). “Response of a residual soil slope to rainfall.” *Canadian Geotechnical Journal*, 42(2), 340-351.

Rahardjo, H., Ong, T. H., Rezaur, R. B., and Leong, E. C. (2007). “Factors controlling instability of homogeneous soil slopes under rainfall.” *Journal of Geotechnical and Geoenvironmental Engineering*, 133(12), 1532-1543.

Rahardjo, H., Nio, A. S., Leong, E. C., and Song, N. Y. (2010). “Effects of groundwater table position and soil properties on stability of slope during rainfall.” *Journal of Geotechnical and Geoenvironmental Engineering*, 136(11), 1555-1564.

Rahimi, A., Rahardjo, H., and Leong, E. C. (2011). “Effect of antecedent rainfall patterns on rainfall-induced slope failure.” *Journal of Geotechnical and Geoenvironmental Engineering*, 137(5), 483-491.

Rathje, E. M., and Bray, J. D. (1999). “An examination of simplified earthquake-induced displacement procedures for earth structures.” *Canadian Geotechnical Journal*, 36(1), 72-87.

Rathje, E. M., and Bray, J. D. (2000). “Nonlinear coupled seismic sliding analysis of earth structures.” *Journal of Geotechnical and Geoenvironmental Engineering*, 126(11), 1002-1014.

Rathje, E. M., and Antonakos, G. (2011). “A unified model for predicting earthquake-induced sliding displacements of rigid and flexible slopes.” *Engineering Geology*, 122(1), 51-60.

Reyno, A. J., Airey, D., and Taiebat, H. A. (2005). “Influence of height and boundary conditions in simple shear tests.” In *International Symposium on Frontiers in Offshore Geotechnics*. Taylor & Francis/Balkema.

Richards, L. A. (1931). “Capillary conduction of liquids through porous mediums.” *Journal of Applied Physics*, 1(5), 318-333.

Robinson, J. D., Vahedifard, F., and AghaKouchak, A. (2017). “Rainfall-triggered slope instabilities under a changing climate: comparative study using historical and projected precipitation extremes.” *Canadian Geotechnical Journal*, 54(1), 117-127.

Rodríguez, C. E., Bommer, J. J., and Chandler, R. J. (1999). "Earthquake-induced landslides: 1980–1997." *Soil Dynamics and Earthquake Engineering*, 18(5), 325-346.

Romeo, R. (2000). "Seismically induced landslide displacements: a predictive model." *Engineering Geology*, 58(3), 337-351.

Roscoe, K. H. (1953). "An apparatus for the application of simple shear to soil samples." Proceedings of the 3rd International Conference on Soil Mechanics and Foundations Engineering, Zurich, vol. 1, pp. 186-191.

Rutherford, C. J., and Biscontin, G. (2013). "Development of a Multidirectional Simple Shear Testing Device." *Geotechnical Testing Journal*, 36(6), 1-9.

Sah, N. K., Sheorey, P. R., Upadhyaya, L. N. (1994). "Maximum likelihood estimation of slope stability." *International Journal of Rock Mechanics and Mining Science*, 31(1), 47-53.

Saygili, G., and Rathje, E. M. (2008). "Empirical predictive models for earthquake-induced sliding displacements of slopes." *Journal of Geotechnical and Geoenvironmental Engineering*, 134(6), 790-803.

Seed, H. B. (1979). "Considerations in the earthquake-resistant design of earth and rockfill dams." *Géotechnique*, 29(3), 215-263.

Seed, H. B., and Chan, C. K. (1959). “Structure and strength characteristics of compacted clays.” *Journal of the Soil Mechanics and Foundations Division*, 85(SM5), 87-128.

Seed, H. B., and Chan, C. K. (1966). “Clay strength under earthquake loading conditions.” *Journal of the Soil Mechanics and Foundations Division, ASCE*, 92(SM2), 53-78.

Seed, H. B., and Lee, K. L. (1966). “Liquefaction of saturated sands during cyclic loading.” *Journal of the Soil Mechanics and Foundations Division, ASCE*, 92(SM6), 105-134.

Seed, H. B., Makdisi, F. I., and De Alba, P. (1978). “The Performance of earth dams during earthquakes.” *Journal of the Geotechnical Engineering Division*, ASCE, 104(GT7), 967-994.

Seed, H. B., and Martin, G. R. (1966). “The seismic coefficient in earth dam design.” *Journal of the Soil Mechanics and Foundations Division*, ASCE, 92(SM3), 25 - 58.

SEEP/W [Computer software]. Geo-Slope International, Calgary, Canada.

Sevaldson, R. A. (1956). “The slide in Lodalen, October 6th, 1954.” *Géotechnique*, 6(4), 167-182.

Sheng, D. (2011). “Review of fundamental principles in modelling unsaturated soil behaviour.” *Computers and Geotechnics*, 38(6), 757-776.

Sheng, D., Zhou, A., and Fredlund, D. G. (2011). “Shear strength criteria for unsaturated soils.” *Geotechnical and Geological Engineering*, 29(2), 145-159.

Silver, M. L., and Seed, H. B. (1971). “Deformation characteristics of sands under cyclic loading.” *Journal of Soil Mechanics and Foundations Division, ASCE*, 97(8), 1081-1098.

Skempton, A. W., and DeLory, F. A. (1957). “Stability of natural slopes in London clay.” *Proceedings of the 4th International Conference on Soil Mechanics and Foundation Engineering*, London, Vol. 2, 378-381.

Skempton, A. W., and Brown, J. D. (1961). “A landslide in boulder clay at Selset, Yorkshire.” *Géotechnique*, 11(4), 280-293.

Sloan, S. W. (2013). “Geotechnical stability analysis.” *Géotechnique*, 63(7), 531-572.

SLOPE/W [Computer software]. Geo-Slope International, Calgary, Canada.

Spencer, E. (1967). “A method of analysis of the stability of embankments assuming parallel inter-slice forces.” *Géotechnique*, 17(1), 11-26.

Steward, T., Sivakugan, N., Shukla, S. K., and Das, B. M. (2011). “Taylor’s slope stability charts revisited.” *International Journal of Geomechanics*, 11(4), 348-352.

Stewart, J. P., Blake, T. F., and Hollingsworth, R. A. (2003). “A screen analysis procedure for seismic slope stability.” *Earthquake Spectra*, 19(3), 697-712.

Stewart, J. P., Smith, P. M., Whang, D. H., and Bray, J. D. (2004). “Seismic compression of two compacted earth fills shaken by the 1994 Northridge earthquake.” *Journal of Geotechnical and Geoenvironmental Engineering*, 130(5), 461-476.

Sun, H. W., Wong, H. N., and Ho, K. K. S. (1998). “Analysis of infiltration in unsaturated ground.” In *Slope Engineering in Hong Kong* (Li, Kay & Ho (eds)), Balkema, Rotterdam, the Netherlands, pp. 101-109.

SVFLUX[Computer software]. SoilVision Sytem Ltd, Saskatoon, Canada.

SVSLOPE[Computer software]. SoilVision Sytem Ltd, Saskatoon, Canada.

Taylor, D. W. (1937). “Stability of earth slopes.” *J. Boston Soc. Civil Eng*., 24(3), 197-246.

Taylor, D. W. (1948). *Fundamentals of Soil Mechanics*, Wiley, New York.

Terzaghi, K. (1936). “The shearing resistance of saturated soils and the angle between planes of shear.” *Proceedings of the First International Conference on Soil Mechanics and Foundation Engineering*, Vol. 1, 54-56.

Terzaghi, K. (1943). *Theoretical Soil Mechanics*, Wiley, New York.

Terzaghi, K. (1950). "Mechanism of Landslides". The Geological Society of America, Engineering Geology (Berkeley) Volume.

Terzaghi, K., Peck, R. B., and Mesri, G. (1996). *Soil Mechanics in Engineering Practice*. John Wiley & Sons.

Thiers, G. R., and Seed, H. B. (1969). "Strength and stress-strain characteristics of clays subjected to seismic loading conditions." *Symposium on Vibration Effects of Earthquakes on Soils and Foundations*, American Society for Testing and Materials, STP 450, 3-56.

Toll, D. G. (2001). "Rainfall-induced landslides in Singapore." *Proceedings of the Institution of Civil Engineers: Geotechnical Engineering*, 149(4), 211-216.

Travis, Q. B., Houston, S. L., Marinho, F. A., and Schmeeckle, M. (2010). "Unsaturated infinite slope stability considering surface flux conditions." *Journal of Geotechnical and Geoenvironmental Engineering*, 136(7), 963-974.

Tsaparas, I., Rahardjo, H., Toll, D. G., and Leong, E. C. (2002). "Controlling parameters for rainfall-induced landslides." *Computers and Geotechnics*, 29(1), 1-27.

Tu, X. B., Kwong, A. K. L., Dai, F. C., Tham, L. G., and Min, H. (2009). “Field monitoring of rainfall infiltration in a loess slope and analysis of failure mechanism of rainfall-induced landslides.” *Engineering Geology*, 105(1), 134-150.

Vahedifard, F., Leshchinsky, D., Mortezaei, K., and Lu, N. (2016). “Effective stress-based limit-equilibrium analysis for homogeneous unsaturated slopes.” *International Journal of Geomechanics*, 16(6), D4016003.

Vanapalli, S. K., Fredlund, D. G., Pufahl, D. E., and Clifton, A. W. (1996). “Model for the prediction of shear strength with respect to soil suction.” *Canadian Geotechnical Journal*, 33(3), 379-392.

Viratjandr, C., and Michalowski, R. L. (2006). “Limit analysis of submerged slopes subjected to water drawdown.” *Canadian Geotechnical Journal*, 43(8), 802-814.

Vo, T., and Russell, A. R. (2017). “Stability charts for curvilinear slopes in unsaturated soils.” *Soils and Foundations*, 57(4), 543-556.

Vucetic, M., and Dobry, R. (1988). “Degradation of marine clays under cyclic loading.” *Journal of Geotechnical Engineering, ASCE*, 114(2), 133-149.

Whang, D. H., Bray, J. D., and Stewart, J. P. (2004). “Effect of compaction conditions on the seismic compression of compacted fill soils.” *Geotechnical Testing Journal*, 27(4), 1 - 9.

Wilson, R. C., and Keefer, D. K. (1983). “Dynamic analysis of a slope failure from the 6 August 1979 Coyote Lake, California, earthquake.” *Bulletin of the Seismological Society of America*, 73(3), 863-877.

Wroth, C. P. (1984). “The interpretation of in situ soil tests.” *Géotechnique*, 34(4), 449-489.

Yang, C. X., Tham, L. G., Feng, X. T., Wang, Y. J., and Lee, P. K. K. (2004). “Two-stepped evolutionary algorithm and its application to stability analysis of slopes.” *Journal of Computing in Civil Engineering*, 18(2), 145-153.

Yu, H. S., Salgado, R., Sloan, S. W., and Kim, J. M. (1998). “Limit analysis versus limit equilibrium for slope stability”. *Journal of Geotechnical and Geoenvironmental Engineering*, 124(1), 1-11.

Zhai, Q., and Rahardjo, H. (2015). “Estimation of permeability function from the soil–water characteristic curve.” *Engineering Geology*, 199, 148-156.

Zhan, T. L., Ng, C. W., and Fredlund, D. G. (2007). “Field study of rainfall infiltration into a grassed unsaturated expansive soil slope.” *Canadian Geotechnical Journal*, 44(4), 392-408.

Zhang, F., and Fredlund, D. G. (2015). “Examination of the estimation of relative permeability for unsaturated soils.” *Canadian Geotechnical Journal*, 52(12), 2077-2087.

Zhang, L. L., Fredlund, D. G., Zhang, L. M., and Tang, W. H. (2004). “Numerical study of soil conditions under which matric suction can be maintained.” *Canadian Geotechnical Journal*, 41(4), 569-582.

Zhang, L. L., Zhang, J., Zhang, L. M., and Tang, W. H. (2011). “Stability analysis of rainfall-induced slope failure: a review.” *Proceedings of the Institution of Civil Engineers: Geotechnical Engineering*, 164(5), 299-316.

Zhang, L., Li, J., Li, X., Zhang, J., and Zhu, H. (2016). *Rainfall-Induced Soil Slope Failure: Stability Analysis and Probabilistic Assessment*. CRC Press.

Zizioli, D., Meisina, C., Valentino, R., and Montrasio, L. (2013). “Comparison between different approaches to modeling shallow landslide susceptibility: a case history in Oltrepo Pavese, Northern Italy.” *Natural Hazards and Earth System Sciences*, 13(3), 559-573.

Appendix A: Calibration of LVDT and Load Cells for Simple Shear Tests

The linear variable differential transformers (LVDT) used to measure the shear displacements of simple shear tests were calibrated with LVDT calibrators, as shown in Figure A.1. The calibration data are shown in Figure A.2. The normal and shear load cells were calibrated with a proof ring, as shown in Figure A.3. The calibration data are shown in Figure A.4.

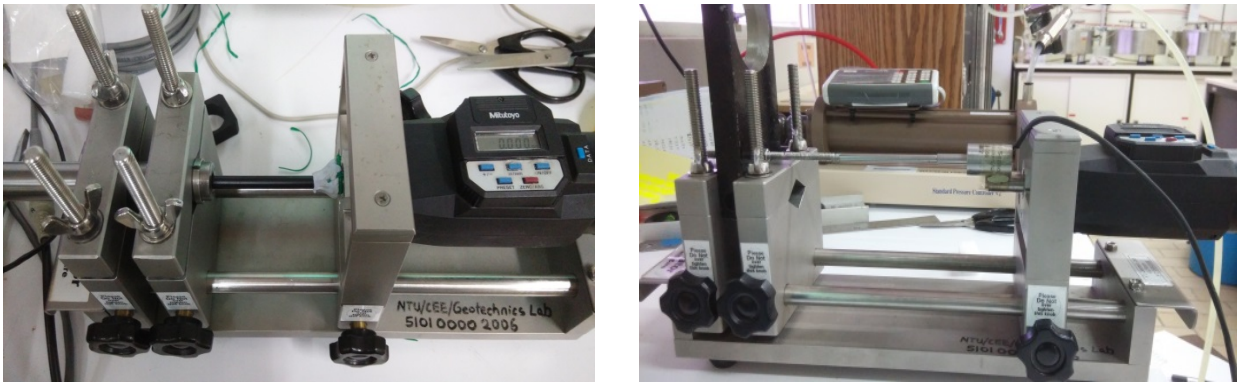

(a) LVDT (high-range) (b) LVDT (low-range)

Figure A.1 Calibrating LVDT with LVDT calibrator

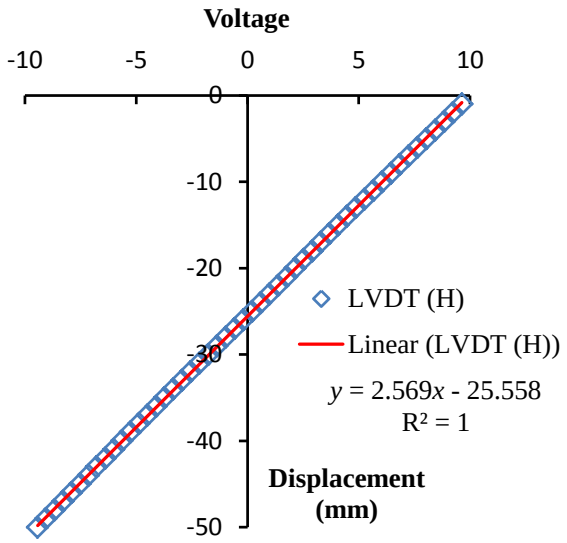

(a) LVDT (50 mm) for shear displacement

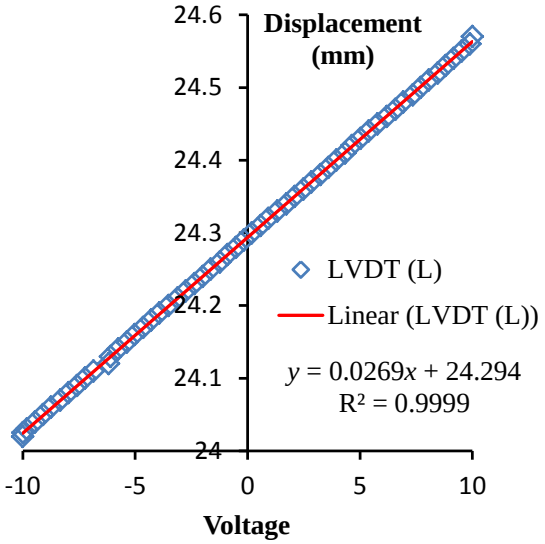

(b) LVDT (0.5 mm) for shear displacement

Figure A.2 LVDT calibration results

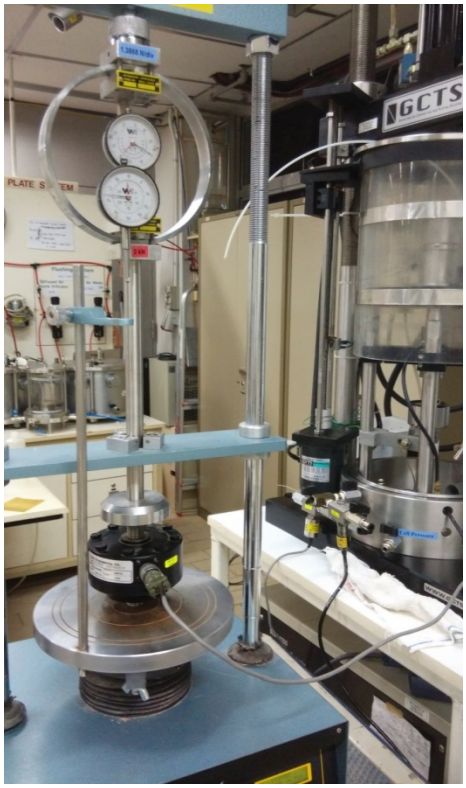

Figure A.3 Set-up for calibrating load cell with proofing ring

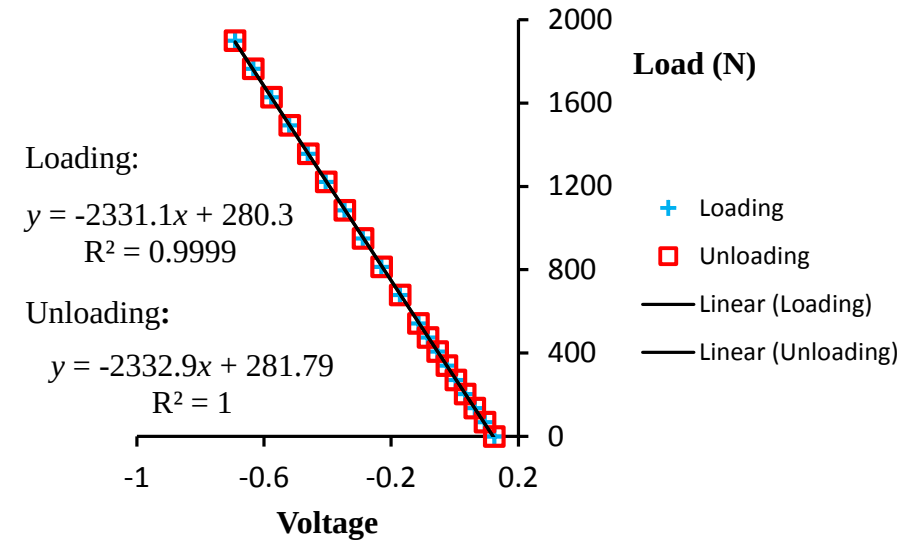

(a) Normal load cell

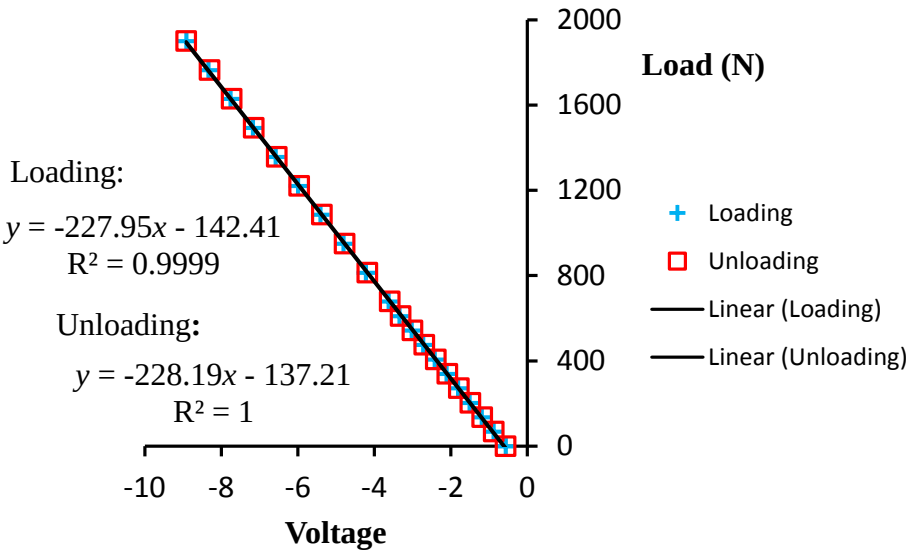

(b) Shear load cell

Figure A.4 Calibration results for load cells

Appendix B: Excel Spreadsheet and Visual Basic Application Code used in This Study

A typical spreadsheet used to perform the upper bound limit analysis (rotational failure mechanism with hydrostatic pore-water pressure distribution) and develop stability charts is shown in Figure A.5. The formulation of the upper bound limit analysis can be found in Sections 4.2 and 4.3. The procedure used to develop stability charts can be found in Section 4.4. The analysis is performed through Subroutines and User-defined Functions, which are created by using Visual Basic Application (VBA) programming language. The relevant VBA codes are attached.

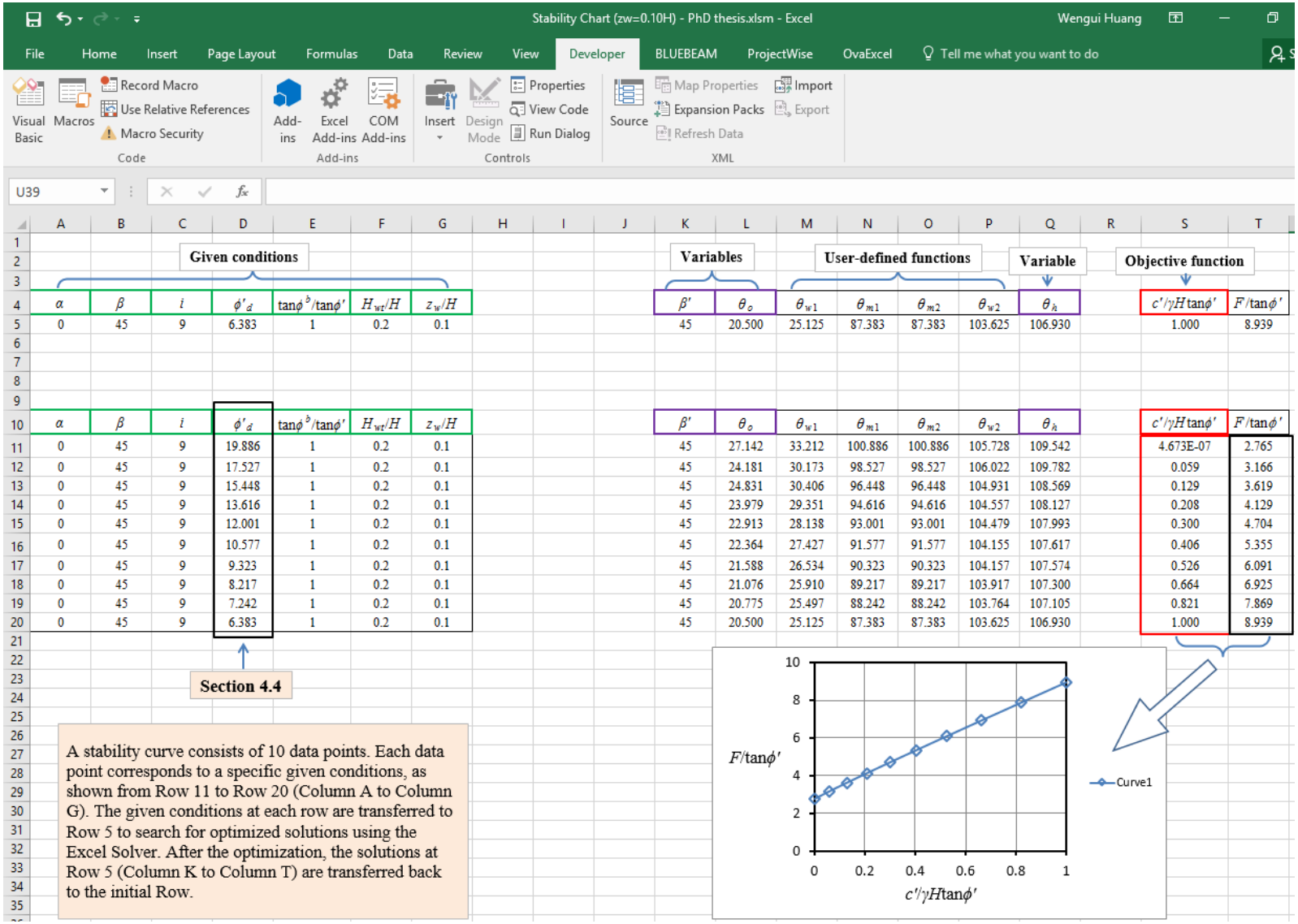

Figure A.5 Excel Spreadsheet used to perform upper bound limit analysis and develop slope stability chart

B.1 Subroutines Used to Perform the Analysis

```
Sub Calculation()

Dim s As Integer, n As Integer, i As Integer

s = 11 ' The row number of the starting row to calculate
n = 10 ' The number of rows need to calculate

Call InitiatePhi

For i = 1 To n

    ' Start the calculation
    Cells(5, 17).Value = Cells(s + i - 1, 17).Value
    Range("A5:L5").FormulaR1C1 = Range(Cells(s + i - 1, 1), Cells(s + i - 1, 12)).FormulaR1C1
    Call RotationalFailure

    ' Transfer the data
    Range(Cells(s + i - 1, 11), Cells(s + i - 1, 28)).Value = Range("K5:AB5").Value

Next i

End Sub
```

```
Sub InitiatePhi()

Dim s As Integer, n As Integer, i As Integer
Dim phi_max As Double, phi_min As Double
Dim a As Double, b As Double

s = 11 ' The row number of the starting row to calculate
n = 10 ' The number of rows need to calculate

' Initiate the MaxPhi
Cells(5, 17).Value = Cells(s, 17).Value
Range("A5:L5").FormulaR1C1 = Range(Cells(s, 1), Cells(s, 12)).FormulaR1C1

Call MaxPhi

Range(Cells(s, 1), Cells(s, 9)).FormulaR1C1 = Range("A5:I5").FormulaR1C1
Range(Cells(s, 11), Cells(s, 24)).Value = Range("K5:X5").Value

' Initiate the MinPhi
```

```
Cells(5, 17).Value = Cells(s + n - 1, 17).Value
Range("A5:L5").FormulaR1C1 = Range(Cells(s + n - 1, 1), Cells(s + n - 1, 12)).FormulaR1C1

Call MinPhi

Range(Cells(s + n - 1, 1), Cells(s + n - 1, 9)).FormulaR1C1 = Range("A5:I5").FormulaR1C1
Range(Cells(s + n - 1, 11), Cells(s + n - 1, 28)).Value = Range("K5:AB5").Value

'To assign the initial phi values

phi_max = Cells(s, 4).Value  ' Maximum phi value
phi_min = Cells(s + n - 1, 4).Value  ' Minimum phi value

a = phi_max ^ (n / (n - 1)) / phi_min ^ (1 / (n - 1))
b = 1 / (n - 1) * Log(phi_min / phi_max)

For i = 1 To n
   Cells(s + i - 1, 4).Value = a * Exp(b * i)
Next i

End Sub
```

```
Sub MaxPhi()

Dim phi_lb As Double, phi_ub As Double, ObjectValue() As Double
Dim Counter As Integer, Zero_Num As Double

Counter = 0
Zero_Num = 0.000001

Call RotationalFailure

If Cells(5, 19).Value > Zero_Num Then
   Do
   Cells(5, 4).Value = Cells(5, 4).Value + 0.5
   Call RotationalFailure
   Loop Until Cells(5, 19).Value < 0

   phi_ub = Cells(5, 4).Value
   phi_lb = Cells(5, 4).Value - 0.5

ElseIf Cells(5, 19).Value < 0 Then
   Do
   Cells(5, 4).Value = Cells(5, 4).Value - 0.5
   Call RotationalFailure
```

```
    Loop Until Cells(5, 19).Value > 0

    phi_ub = Cells(5, 4).Value + 0.5
    phi_lb = Cells(5, 4).Value

Else
    phi_ub = Cells(5, 4).Value
    phi_lb = Cells(5, 4).Value

End If

Do
    Counter = Counter + 1
    ReDim ObjectValue(Counter)
    ObjectValue(Counter) = Cells(5, 19).Value

    Cells(5, 4).Value = (phi_ub + phi_lb) / 2
    Call RotationalFailure

    If Cells(5, 19).Value < 0 Then
        phi_ub = Cells(5, 4).Value
    ElseIf Cells(5, 19).Value > Zero_Num Then
        phi_lb = Cells(5, 4).Value
    End If

    If Counter > 1 And Abs(Cells(5, 19).Value - ObjectValue(Counter)) < Zero_Num / 1000 Then
        Call MaxPhi
        Exit Sub
    End If

Loop Until Cells(5, 19).Value >= 0 And Cells(5, 19).Value <= Zero_Num

End Sub
```

```
Sub MinPhi()

Dim phi_lb As Double, phi_ub As Double, ObjectValue() As Double
Dim Counter As Integer, Zero_Num As Double

Counter = 0
Zero_Num = 0.000001

Call RotationalFailure

If Cells(5, 19).Value > 1 + Zero_Num Then
```

```
    Do
    Cells(5, 4).Value = Cells(5, 4).Value + 0.5
    Call RotationalFailure

    Loop Until Cells(5, 19).Value < 1

    phi_ub = Cells(5, 4).Value
    phi_lb = Cells(5, 4).Value - 0.5

ElseIf Cells(5, 19).Value < 1 - Zero_Num Then
    Do
    Cells(5, 4).Value = Cells(5, 4).Value - 0.5
    Call RotationalFailure

    Loop Until Cells(5, 19).Value > 1

    phi_ub = Cells(5, 4).Value + 0.5
    phi_lb = Cells(5, 4).Value

Else
    phi_ub = Cells(5, 4).Value
    phi_lb = Cells(5, 4).Value

End If

Do
    Counter = Counter + 1
    ReDim ObjectValue(Counter)
    ObjectValue(Counter) = Cells(5, 19).Value

    Cells(5, 4).Value = (phi_ub + phi_lb) / 2
    Call RotationalFailure

    If Cells(5, 19).Value < 1 - Zero_Num Then
        phi_ub = Cells(5, 4).Value
    ElseIf Cells(5, 19).Value > 1 + Zero_Num Then
        phi_lb = Cells(5, 4).Value
    End If

    If Abs(Cells(5, 19).Value - 1) > Zero_Num And Abs(Cells(5, 19).Value -
ObjectValue(Counter)) < Zero_Num / 1000 Then
        Call MinPhi
        Exit Sub
    End If

Loop Until Abs(Cells(5, 19).Value - 1) <= Zero_Num
```

```
End Sub
```

```
Sub RotationalFailure()

Application.ScreenUpdating = False

    SolverReset
    SolverOk SetCell:="$S$5", MaxMinVal:=1, ValueOf:=0, ByChange:="$K$5,$L$5,$Q$5" _
       , Engine:=1, EngineDesc:="GRG Nonlinear"
    SolverAdd CellRef:="$K$5", Relation:=3, FormulaText:="0.4*$B$5"
    SolverAdd CellRef:="$K$5", Relation:=1, FormulaText:="$B$5"
    SolverAdd CellRef:="$L$5", Relation:=3, FormulaText:="$D$5"
    SolverAdd CellRef:="$L$5", Relation:=1, FormulaText:="90+$D$5-$A$5"
    SolverAdd CellRef:="$L$5", Relation:=1, FormulaText:="$Q$5-0.1"
    SolverAdd CellRef:="$Q$5", Relation:=3, FormulaText:="90+$D$5-$B$5"
    SolverAdd CellRef:="$Q$5", Relation:=1, FormulaText:="180+$D$5"
    SolverSolve True

End Sub
```

B.2 User-defined Functions Used to Perform the Analysis

```
Function ObjectFun_RotateFail(alpha, beta, inclination, beta_prime, theta_0, theta_w1, theta_m1,
theta_m2, theta_w2, theta_h, phi, phi_b, m)

'Angles are input as degrees, and they are transformed into radians through following definition

alphar = WorksheetFunction.Radians(alpha)
betar = WorksheetFunction.Radians(beta)
beta_primer = WorksheetFunction.Radians(beta_prime)
theta_0r = WorksheetFunction.Radians(theta_0)
theta_hr = WorksheetFunction.Radians(theta_h)
phir = WorksheetFunction.Radians(phi)
phi_br = WorksheetFunction.Radians(phi_b)

' Toe failure or base failure is assumed
r0 = 1  ' r0=1 is a fictious number, it can be equal to any number
H = r0 * Sin(beta_primer) / Sin(beta_primer - alphar) * (Sin(theta_hr + alphar) * Exp((theta_hr -
theta_0r) * Tan(phir)) - Sin(theta_0r + alphar))
```

```
L = r0 * (Sin(beta_primer + theta_0r) / Sin(beta_primer - alphar) - Sin(theta_hr + beta_primer) / Sin(beta_primer - alphar) * Exp((theta_hr - theta_0r) * Tan(phir)))

f1 = 1 / (3 * (1 + 9 * Tan(phir) ^ 2)) * ((Sin(theta_hr) + 3 * Tan(phir) * Cos(theta_hr)) * Exp(3 * (theta_hr - theta_0r) * Tan(phir)) - (Sin(theta_0r) + 3 * Tan(phir) * Cos(theta_0r)))
f2 = 1 / 6 * L / r0 * (2 * Cos(theta_0r) - L / r0 * Cos(alphar)) * Sin(theta_0r + alphar)
f3 = 1 / 6 * Exp((theta_hr - theta_0r) * Tan(phir)) * (Sin(theta_hr - theta_0r) - L / r0 * Sin(theta_hr + alphar)) * (Cos(theta_0r) - L / r0 * Cos(alphar) + Cos(theta_hr) * Exp((theta_hr - theta_0r) * Tan(phir)))
f4 = ((H / r0) ^ 2) * Sin(betar - beta_primer) / (2 * Sin(betar) * Sin(beta_primer)) * (Cos(theta_0r) - L / r0 * Cos(alphar) - 1 / 3 * H / r0 * (1 / Tan(beta_primer) + 1 / Tan(betar)))

'*********************************************
If theta_m2 - theta_m1 > 0.1 Then  ' There is intersection between groundwater table and slip surface
   If theta_w1 > theta_m1 Then
      theta_w1 = theta_m1
   End If
   If theta_w2 < theta_m2 Then
      theta_w2 = theta_m2
   End If
End If
'*********************************************

f5 = Tan(phi_br) * (f5u_wt(theta_w2, alpha, beta, inclination, beta_prime, theta_0, theta_h, phi, m) - f5u_wt(theta_w1, alpha, beta, inclination, beta_prime, theta_0, theta_h, phi, m)) + (Tan(phir) - Tan(phi_br)) * (f5u_wt(theta_m2, alpha, beta, inclination, beta_prime, theta_0, theta_h, phi, m) - f5u_wt(theta_m1, alpha, beta, inclination, beta_prime, theta_0, theta_h, phi, m))

tem = H / r0 * (Exp(2 * (theta_hr - theta_0r) * Tan(phir)) - 1) / 2

ObjectFun_RotateFail = (f1 - f2 - f3 - f4 + f5) / tem

End Function
```

```
Function f5u_wt(theta, alpha, beta, inclination, beta_prime, theta_0, theta_h, phi, m)

' m among the input parameters represent the ratio Hwt/H

alphar = WorksheetFunction.Radians(alpha)
betar = WorksheetFunction.Radians(beta)
ir = WorksheetFunction.Radians(inclination)
beta_primer = WorksheetFunction.Radians(beta_prime)
theta_0r = WorksheetFunction.Radians(theta_0)
theta_hr = WorksheetFunction.Radians(theta_h)
```

```
phir = WorksheetFunction.Radians(phi)
thetar = WorksheetFunction.Radians(theta)

gamma_w = 9.81  'Unit weight of water
gamma = 2 * gamma_w  'Both unit weight and saturated weight of soil are assumed to be 2 * 9.81

'Toe failure or base failure is assumed
r0 = 1  ' r0=1 is a fictious number, it can be equal to any number
H = r0 * Sin(beta_primer) / Sin(beta_primer - alphar) * (Sin(theta_hr + alphar) * Exp((theta_hr - theta_0r) * Tan(phir)) - Sin(theta_0r + alphar))
Hwt = m * H
L = r0 * (Sin(beta_primer + theta_0r) / Sin(beta_primer - alphar) - Sin(theta_hr + beta_primer) / Sin(beta_primer - alphar) * Exp((theta_hr - theta_0r) * Tan(phir)))
x0 = -r0 * Exp((theta_hr - theta_0r) * Tan(phir)) * Cos(theta_hr) - H * Sin(betar - beta_primer) / (Sin(betar) * Sin(beta_primer))

f5u_wt = gamma_w * ((Cos(ir)) ^ 2) / (gamma * r0) * (x0 * Tan(ir) - (Hwt + H + L * Sin(alphar) + r0 * Sin(theta_0r))) * Exp(2 * (thetar - theta_0r) * Tan(phir)) / (2 * Tan(phir)) + gamma_w / gamma * Sin(ir) * Cos(ir) / (1 + 9 * Tan(phir) ^ 2) * (Sin(thetar) + 3 * Tan(phir) * Cos(thetar)) * Exp(3 * (thetar - theta_0r) * Tan(phir)) + gamma_w / gamma * (Cos(ir) ^ 2) / (1 + 9 * Tan(phir) ^ 2) * (-Cos(thetar) + 3 * Tan(phir) * Sin(thetar)) * Exp(3 * (thetar - theta_0r) * Tan(phir))

End Function
```

```
Function theta_w1(alpha, beta, beta_prime, theta_0, theta_h, phi, n)

Dim thetaW As Double, thetaB As Double, theta_w11 As Double, theta_w12 As Double, theta_w13 As Double, theta_w14 As Double
Dim thetaW1Trial() As Double, Counter As Integer, Accuracy As Double

Counter = 0
Accuracy = 0.001 'Accuracy of the calculated angle, unit: degree

thetaW = theta_w(beta, phi)
thetaB = theta_b(alpha, beta_prime, theta_0, theta_h, phi)

If Hzw_s1(thetaB, alpha, beta, beta_prime, theta_0, theta_h, phi, n) > 0 Then
    theta_w11 = theta_0
    theta_w12 = thetaB

    Do
    Counter = Counter + 1
    ReDim thetaW1Trial(Counter)
    thetaW1Trial(Counter) = theta_w12
```

```
    theta_w1 = (theta_w11 + theta_w12) / 2
        If Hzw_s1(theta_w1, alpha, beta, beta_prime, theta_0, theta_h, phi, n) * Hzw_s1(theta_w12,
alpha, beta, beta_prime, theta_0, theta_h, phi, n) <= 0 Then
            theta_w11 = theta_w1
        Else
            theta_w12 = theta_w1
        End If
    Loop Until Abs(theta_w1 - thetaW1Trial(Counter)) < Accuracy  'The accuracy is set as 0.01
degree.

ElseIf Hzw_s2(thetaW, alpha, beta, beta_prime, theta_0, theta_h, phi, n) > 0 Then
    theta_w13 = thetaB
    theta_w14 = thetaW

    Do
    Counter = Counter + 1
    ReDim thetaW1Trial(Counter)
    thetaW1Trial(Counter) = theta_w14

    theta_w1 = (theta_w13 + theta_w14) / 2
        If Hzw_s2(theta_w1, alpha, beta, beta_prime, theta_0, theta_h, phi, n) * Hzw_s2(theta_w14,
alpha, beta, beta_prime, theta_0, theta_h, phi, n) <= 0 Then
            theta_w13 = theta_w1
        Else
            theta_w14 = theta_w1
        End If
    Loop Until Abs(theta_w1 - thetaW1Trial(Counter)) < Accuracy

Else
    theta_w1 = thetaW
End If

End Function
```

```
Function theta_w2(alpha, beta, beta_prime, theta_0, theta_h, phi, n)

Dim thetaW As Double, thetaC As Double, theta_w21 As Double, theta_w22 As Double,
theta_w23 As Double, theta_w24 As Double
Dim thetaW2Trial() As Double, Counter As Integer, Accuracy As Double
Counter = 0
Accuracy = 0.001 'Accuracy of the calculated angle, unit: degree

thetaW = theta_w(beta, phi)
thetaC = theta_c(alpha, beta, beta_prime, theta_0, theta_h, phi)
```

```
If Hzw_s2(thetaW, alpha, beta, beta_prime, theta_0, theta_h, phi, n) <= 0 Then
   theta_w2 = thetaW
ElseIf Hzw_s2(thetaC, alpha, beta, beta_prime, theta_0, theta_h, phi, n) <= 0 Then
   theta_w21 = thetaW
   theta_w22 = thetaC

   Do
   Counter = Counter + 1
   ReDim thetaW2Trial(Counter)
   thetaW2Trial(Counter) = theta_w21

   theta_w2 = (theta_w21 + theta_w22) / 2
      If Hzw_s2(theta_w2, alpha, beta, beta_prime, theta_0, theta_h, phi, n) * Hzw_s2(theta_w22,
alpha, beta, beta_prime, theta_0, theta_h, phi, n) <= 0 Then
         theta_w21 = theta_w2
      Else
         theta_w22 = theta_w2
      End If
   Loop Until Abs(theta_w2 - thetaW2Trial(Counter)) < Accuracy

ElseIf Hzw_s3(theta_h, alpha, beta_prime, theta_0, theta_h, phi, n) <= 0 Then
   theta_w23 = thetaC
   theta_w24 = theta_h

   Do
   Counter = Counter + 1
   ReDim thetaW2Trial(Counter)
   thetaW2Trial(Counter) = theta_w23

   theta_w2 = (theta_w23 + theta_w24) / 2
      If Hzw_s3(theta_w2, alpha, beta_prime, theta_0, theta_h, phi, n) * Hzw_s3(theta_w24,
alpha, beta_prime, theta_0, theta_h, phi, n) <= 0 Then
         theta_w23 = theta_w2
      Else
         theta_w24 = theta_w2
      End If
   Loop Until Abs(theta_w2 - thetaW2Trial(Counter)) < Accuracy

End If
End Function
```

```
Function theta_m1(alpha, beta, inclination, beta_prime, theta_0, theta_h, phi, m)

Dim thetaM As Double, theta_m11 As Double, theta_m12 As Double
```

```
Dim thetaM1Trial() As Double, Counter As Integer, Accuracy As Double

Counter = 0
Accuracy = 0.001 'Accuracy of the calculated angle, unit: degree

thetaM = theta_m(inclination, phi)

If Hws_2(thetaM, alpha, beta, inclination, beta_prime, theta_0, theta_h, phi, m) <= 0 Then
   theta_m1 = thetaM
ElseIf Hws_2(theta_0, alpha, beta, inclination, beta_prime, theta_0, theta_h, phi, m) <= 0 Then
   theta_m11 = theta_0
   theta_m12 = thetaM

   Do
   Counter = Counter + 1
   ReDim thetaM1Trial(Counter)
   thetaM1Trial(Counter) = theta_m12

   theta_m1 = (theta_m11 + theta_m12) / 2
      If Hws_2(theta_m1, alpha, beta, inclination, beta_prime, theta_0, theta_h, phi, m) *
Hws_2(theta_m12, alpha, beta, inclination, beta_prime, theta_0, theta_h, phi, m) <= 0 Then
         theta_m11 = theta_m1
      Else
         theta_m12 = theta_m1
      End If
   Loop Until Abs(theta_m1 - thetaM1Trial(Counter)) < Accuracy

   If theta_m1 > theta_h Then
      theta_m1 = theta_h
   End If

End If

End Function
```

```
Function theta_m2(alpha, beta, inclination, beta_prime, theta_0, theta_h, phi, m)

Dim thetaM As Double, theta_m21 As Double, theta_m22 As Double
Dim thetaM2Trial() As Double, Counter As Integer, Accuracy As Double

Counter = 0
Accuracy = 0.001  ' Accuracy of the calculated angle, unit: degree

thetaM = theta_m(inclination, phi)
```

```
If Hws_2(thetaM, alpha, beta, inclination, beta_prime, theta_0, theta_h, phi, m) <= 0 Then
   theta_m2 = thetaM
ElseIf Abs(Hws_2(theta_h, alpha, beta, inclination, beta_prime, theta_0, theta_h, phi, m)) <
0.000001 Then
   theta_m2 = theta_h
ElseIf Hws_2(theta_h, alpha, beta, inclination, beta_prime, theta_0, theta_h, phi, m) < 0 Then
   theta_m21 = thetaM
   theta_m22 = theta_h

   Do
   Counter = Counter + 1
   ReDim thetaM2Trial(Counter)
   thetaM2Trial(Counter) = theta_m21

   theta_m2 = (theta_m21 + theta_m22) / 2
      If Hws_2(theta_m2, alpha, beta, inclination, beta_prime, theta_0, theta_h, phi, m) *
Hws_2(theta_m22, alpha, beta, inclination, beta_prime, theta_0, theta_h, phi, m) <= 0 Then
         theta_m21 = theta_m2
      Else
         theta_m22 = theta_m2
      End If
   Loop Until Abs(theta_m2 - thetaM2Trial(Counter)) < Accuracy

   If theta_m2 > theta_h Then
      theta_m2 = theta_h
   End If

End If

End Function
```

```
Function theta_b(alpha, beta_prime, theta_0, theta_h, phi)

Dim theta_b1 As Double, theta_b2 As Double
Dim thetaB_Trial() As Double, Counter As Integer, Accuracy As Double

Counter = 0
Accuracy = 0.01 'Accuracy of the calculated angle, unit: degree

theta_b1 = theta_0
theta_b2 = theta_h

If fb(theta_0, alpha, beta_prime, theta_0, theta_h, phi) > 0 Then
   Do
   Counter = Counter + 1
```

```
    ReDim thetaB_Trial(Counter)
    thetaB_Trial(Counter) = theta_b1

    theta_b = (theta_b1 + theta_b2) / 2
        If fb(theta_b, alpha, beta_prime, theta_0, theta_h, phi) * fb(theta_b1, alpha, beta_prime,
theta_0, theta_h, phi) <= 0 Then
            theta_b2 = theta_b
        Else
            theta_b1 = theta_b
        End If
    Loop Until Abs(theta_b - thetaB_Trial(Counter)) < Accuracy
Else
    theta_b = theta_0
End If

End Function
```

```
Function theta_c(alpha, beta, beta_prime, theta_0, theta_h, phi)

Dim theta_c1 As Double, theta_c2 As Double
Dim thetaC_Trial() As Double, Counter As Integer, Accuracy As Double

Counter = 0
Accuracy = 0.01 'Accuracy of the calculated angle, unit: degree

If beta_prime = beta Then
    theta_c = theta_h
ElseIf beta_prime < beta Then
    theta_c1 = theta_0
    theta_c2 = theta_h

    Do
    Counter = Counter + 1
    ReDim thetaC_Trial(Counter)
    thetaC_Trial(Counter) = theta_c2

    theta_c = (theta_c1 + theta_c2) / 2
        If fc(theta_c, alpha, beta, beta_prime, theta_0, theta_h, phi) * fc(theta_c2, alpha, beta,
beta_prime, theta_0, theta_h, phi) <= 0 Then
            theta_c1 = theta_c
        Else
            theta_c2 = theta_c
        End If
    Loop Until Abs(theta_c - thetaC_Trial(Counter)) < Accuracy
End If
```

```
End Function
```

```
Function theta_w(beta, phi)

theta_w = 90 + phi - beta

End Function
```

```
Function theta_m(inclination, phi)

theta_m = 90 + phi - inclination

End Function
```

```
Function fb(theta, alpha, beta_prime, theta_0, theta_h, phi)

alphar = WorksheetFunction.Radians(alpha)
beta_primer = WorksheetFunction.Radians(beta_prime)
theta_0r = WorksheetFunction.Radians(theta_0)
theta_hr = WorksheetFunction.Radians(theta_h)
phir = WorksheetFunction.Radians(phi)
thetar = WorksheetFunction.Radians(theta)

r0 = 1  ' r0=1 is a fictious number, it can be equal to any number
L = r0 * (Sin(beta_primer + theta_0r) / Sin(beta_primer - alphar) - Sin(theta_hr + beta_primer) /
Sin(beta_primer - alphar) * Exp((theta_hr - theta_0r) * Tan(phir)))

fb = r0 * Exp((thetar - theta_0r) * Tan(phir)) * Cos(thetar) - (r0 * Cos(theta_0r) - L *
Cos(alphar))

End Function
```

```
Function fc(theta, alpha, beta, beta_prime, theta_0, theta_h, phi)

alphar = WorksheetFunction.Radians(alpha)
betar = WorksheetFunction.Radians(beta)
beta_primer = WorksheetFunction.Radians(beta_prime)
theta_0r = WorksheetFunction.Radians(theta_0)
theta_hr = WorksheetFunction.Radians(theta_h)
phir = WorksheetFunction.Radians(phi)
thetar = WorksheetFunction.Radians(theta)
```

```
'Toe failure or base failure is assumed
r0 = 1  ' r0=1 is a fictious number, it can be equal to any number
L = r0 * (Sin(beta_primer + theta_0r) / Sin(beta_primer - alphar) - Sin(theta_hr + beta_primer) /
Sin(beta_primer - alphar) * Exp((theta_hr - theta_0r) * Tan(phir)))
H = r0 * Sin(beta_primer) / Sin(beta_primer - alphar) * (Sin(theta_hr + alphar) * Exp((theta_hr -
theta_0r) * Tan(phir)) - Sin(theta_0r + alphar))

fc = r0 * Exp((thetar - theta_0r) * Tan(phir)) * Cos(thetar) - (r0 * Cos(theta_0r) - L * Cos(alphar)
- H / Tan(betar))

End Function
```

```
Function Hws_2(theta, alpha, beta, inclination, beta_prime, theta_0, theta_h, phi, m)
' Vertical distance between groundwater table and slip surface

alphar = WorksheetFunction.Radians(alpha)
betar = WorksheetFunction.Radians(beta)
ir = WorksheetFunction.Radians(inclination)
beta_primer = WorksheetFunction.Radians(beta_prime)
theta_0r = WorksheetFunction.Radians(theta_0)
theta_hr = WorksheetFunction.Radians(theta_h)
phir = WorksheetFunction.Radians(phi)
thetar = WorksheetFunction.Radians(theta)

'Toe failure or base failure is assumed
r0 = 1  ' r0=1 is a fictious number, it can be equal to any number
L = r0 * (Sin(beta_primer + theta_0r) / Sin(beta_primer - alphar) - Sin(theta_hr + beta_primer) /
Sin(beta_primer - alphar) * Exp((theta_hr - theta_0r) * Tan(phir)))
H = r0 * Sin(beta_primer) / Sin(beta_primer - alphar) * (Sin(theta_hr + alphar) * Exp((theta_hr -
theta_0r) * Tan(phir)) - Sin(theta_0r + alphar))
Hwt = m * H
x0 = -r0 * Exp((theta_hr - theta_0r) * Tan(phir)) * Cos(theta_hr) - H * Sin(betar - beta_primer) /
(Sin(betar) * Sin(beta_primer))

Hws_2 = (x0 + r0 * Exp((thetar - theta_0r) * Tan(phir)) * Cos(thetar)) * Tan(ir) - Hwt - (H + L *
Sin(alphar) + r0 * Sin(theta_0r) - r0 * Exp((thetar - theta_0r) * Tan(phir)) * Sin(thetar))

End Function
```

```
Function Hzw_s1(theta, alpha, beta, beta_prime, theta_0, theta_h, phi, n)

' Vertical distance between wetting front 1 (right one) and slip surface
```

```
alphar = WorksheetFunction.Radians(alpha)
betar = WorksheetFunction.Radians(beta)
beta_primer = WorksheetFunction.Radians(beta_prime)
theta_0r = WorksheetFunction.Radians(theta_0)
theta_hr = WorksheetFunction.Radians(theta_h)
phir = WorksheetFunction.Radians(phi)
thetar = WorksheetFunction.Radians(theta)

'Toe failure or base failure is assumed
r0 = 1 'r0=1 is a fictious number, it can be equal to any number
L = r0 * (Sin(beta_primer + theta_0r) / Sin(beta_primer - alphar) - Sin(theta_hr + beta_primer) /
Sin(beta_primer - alphar) * Exp((theta_hr - theta_0r) * Tan(phir)))
H = r0 * Sin(beta_primer) / Sin(beta_primer - alphar) * (Sin(theta_hr + alphar) * Exp((theta_hr -
theta_0r) * Tan(phir)) - Sin(theta_0r + alphar))
zw = n * H  'Depth of wetting front
x0 = -r0 * Exp((theta_hr - theta_0r) * Tan(phir)) * Cos(theta_hr) - H * Sin(betar - beta_primer) /
(Sin(betar) * Sin(beta_primer))

Hzw_s1 = (H - zw + (x0 + r0 * Exp((thetar - theta_0r) * Tan(phir)) * Cos(thetar) - H / Tan(betar))
* Tan(alphar)) - (H + L * Sin(alphar) + r0 * Sin(theta_0r) - r0 * Exp((thetar - theta_0r) *
Tan(phir)) * Sin(thetar))

End Function
```

```
Function Hzw_s2(theta, alpha, beta, beta_prime, theta_0, theta_h, phi, n)

' Vertical distance between wetting front 2 (middle one) and slip surface

alphar = WorksheetFunction.Radians(alpha)
betar = WorksheetFunction.Radians(beta)
beta_primer = WorksheetFunction.Radians(beta_prime)
theta_0r = WorksheetFunction.Radians(theta_0)
theta_hr = WorksheetFunction.Radians(theta_h)
phir = WorksheetFunction.Radians(phi)
thetar = WorksheetFunction.Radians(theta)

'Toe failure or base failure is assumed
r0 = 1  ' r0=1 is a fictious number, it can be equal to any number
L = r0 * (Sin(beta_primer + theta_0r) / Sin(beta_primer - alphar) - Sin(theta_hr + beta_primer) /
Sin(beta_primer - alphar) * Exp((theta_hr - theta_0r) * Tan(phir)))
H = r0 * Sin(beta_primer) / Sin(beta_primer - alphar) * (Sin(theta_hr + alphar) * Exp((theta_hr -
theta_0r) * Tan(phir)) - Sin(theta_0r + alphar))
zw = n * H  'Depth of wetting front
x0 = -r0 * Exp((theta_hr - theta_0r) * Tan(phir)) * Cos(theta_hr) - H * Sin(betar - beta_primer) /
(Sin(betar) * Sin(beta_primer))
```

```
Hzw_s2 = (x0 + r0 * Exp((thetar - theta_0r) * Tan(phir)) * Cos(thetar)) * Tan(betar) - zw - (H + L * Sin(alphar) + r0 * Sin(theta_0r) - r0 * Exp((thetar - theta_0r) * Tan(phir)) * Sin(thetar))

End Function
```

```
Function Hzw_s3(theta, alpha, beta_prime, theta_0, theta_h, phi, n)

' Vertical distance between wetting front 3 (left one) and slip surface

alphar = WorksheetFunction.Radians(alpha)
beta_primer = WorksheetFunction.Radians(beta_prime)
theta_0r = WorksheetFunction.Radians(theta_0)
theta_hr = WorksheetFunction.Radians(theta_h)
phir = WorksheetFunction.Radians(phi)
thetar = WorksheetFunction.Radians(theta)

' Toe failure or base failure is assumed
r0 = 1  ' r0=1 is a fictious number, it can be equal to any number
L = r0 * (Sin(beta_primer + theta_0r) / Sin(beta_primer - alphar) - Sin(theta_hr + beta_primer) / Sin(beta_primer - alphar) * Exp((theta_hr - theta_0r) * Tan(phir)))
H = r0 * Sin(beta_primer) / Sin(beta_primer - alphar) * (Sin(theta_hr + alphar) * Exp((theta_hr - theta_0r) * Tan(phir)) - Sin(theta_0r + alphar))
zw = n * H   ' Depth of wetting front

Hzw_s3 = -zw - (H + L * Sin(alphar) + r0 * Sin(theta_0r) - r0 * Exp((thetar - theta_0r) * Tan(phir)) * Sin(thetar))

End Function
```

Appendix C: Analytical Solutions to the Graphical Parameters of Log-Spiral Failure Mechanism

For unsaturated slope stability analysis based on rotational failure mechanism, graphical approaches can be used to estimate the average positive (h_p) and negative (h_c) pore-water pressure heads on the critical slip surface before the rain infiltration and degree of contribution of matric suction to slope stability (ζ) during the rainfall infiltration, as explained in Section 5.2.2. If the critical rotational slip surface is a log-spiral, the graphical parameters can be obtained analytically. The analytical expressions of the graphical parameters are shown below.

1. Constant negative pore-water pressure distribution

The degree of contribution of matric suction (constant) to the slope stability, ζ_c^g, can be calculated by:

$$\zeta_c^g = \frac{l_{\widehat{\mathrm{DE}}}}{l_{\widehat{\mathrm{AC'}}}} = \frac{\int_{\theta_{w1}}^{\theta_{w2}} \sqrt{r^2(\theta)+r'^2(\theta)}\,\mathrm{d}\theta}{\int_{\theta_o}^{\theta_h} \sqrt{r^2(\theta)+r'^2(\theta)}\,\mathrm{d}\theta} = \frac{\exp\left[(\theta_{w2}-\theta_o)\tan\phi'\right]-\exp\left[(\theta_{w1}-\theta_o)\tan\phi'\right]}{\exp\left[(\theta_h-\theta_o)\tan\phi'\right]-1} \tag{A1}$$

2. Hydrostatic pore-water pressure distribution

The average positive pore-water pressure head can be graphically calculated by:

$$\bar{h}_p^g = \frac{A_{\mathrm{GMF}}}{l_{\mathrm{GF}}}\cos i \tag{A2}$$

The average negative pore-water pressure head before the infiltration, $\bar{h}_c^g$, can be calculated by:

$$\bar{h}_c^g = \frac{A_{\mathrm{C'GK}} + A_{\mathrm{AFH}}}{l_{\mathrm{KG}} + l_{\mathrm{FH}}} \cos i \tag{A3}$$

The degree of contribution of matric suction (hydrostatic) to the slope stability, ζ_h^g, during the infiltration can be calculated by:

$$\zeta_h^g = \frac{A_{\mathrm{EGJ}} + A_{\mathrm{DFI}}}{A_{\mathrm{C'GK}} + A_{\mathrm{AFH}}} \tag{A4}$$

In the above equations, the area of regions and the length of plane can be calculated by:

$$A_{\mathrm{GMF}} = \mathrm{Area}(\theta_{m1}) - \mathrm{Area}(\theta_{m2}) \tag{A5}$$

$$A_{\mathrm{C'GK}} = \mathrm{Area}(\theta_{m2}) - \mathrm{Area}(\theta_h) - \frac{1}{2}[H_{ws}(\theta_h)]^2 \sin i \cos i \tag{A6}$$

$$A_{\mathrm{AFH}} = \mathrm{Area}(\theta_o) - \mathrm{Area}(\theta_{m1}) + \frac{1}{2}[H_{ws}(\theta_o)]^2 \sin i \cos i \tag{A7}$$

$$A_{\mathrm{EGJ}} = \mathrm{Area}(\theta_{m2}) - \mathrm{Area}(\theta_{w2}) - \frac{1}{2}[H_{ws}(\theta_{w2})]^2 \sin i \cos i \tag{A8}$$

$$A_{\mathrm{DFI}} = \mathrm{Area}(\theta_{w1}) - \mathrm{Area}(\theta_{m1}) + \frac{1}{2}[H_{ws}(\theta_{w1})]^2 \sin i \cos i \tag{A9}$$

$$l_{\mathrm{GF}} = \frac{x_s(\theta_{m1}) - x_s(\theta_{m2})}{\cos i} \tag{A10}$$

$$l_{\mathrm{KG}} = \frac{x_s(\theta_{m2}) - x_s(\theta_h) - |H_{ws}(\theta_h)| \sin i \cos i}{\cos i} \tag{A11}$$

$$l_{\mathrm{FH}} = \frac{x_s(\theta_o) - x_s(\theta_{m1}) + |H_{ws}(\theta_o)| \sin i \cos i}{\cos i} \tag{A12}$$

where $\mathrm{Area}(\theta)$ is a function of θ and it can be calculated by:

$$\begin{aligned}\text{Area}(\theta) &= \int [y_s(\theta) - w_t(\theta)]\mathrm{d}x_s(\theta) \\ &= (y_o + H_{wt} - x_o \tan i) r(\theta)\cos\theta - \frac{(\tan i - \tan\phi')\cos\phi'\cos(2\theta+\phi')}{4} r^2(\theta) \\ &\quad + \frac{2 - \cos 2\theta + \cos 2(\theta+\phi')}{8\tan\phi'} r^2(\theta) - \frac{2 + \cos 2\theta - \cos 2(\theta+\phi')}{8} r^2(\theta)\tan i\end{aligned} \tag{A13}$$

The functions $H_{ws}(\theta)$ [Eq. (4.40)], $x_s(\theta)$ [Eq. (4.33)], $y_s(\theta)$ [Eq. (4.34)], $w_t(\theta)$ [Eq. (4.37)] and $r(\theta)$ [Eq. (4.1)] can be found in Chapter 4.